Draft version 1.5

ATLAS NOTE

September 5, 2013

Measurement of the Zb and $Zb\bar{b}$ cross sections with $4.6\,\mathrm{fb}^{-1}$ of 7 TeV ATLAS data

Aaron Bundock[a], Gabriele Chiodini[b], Peter Davison[c], Dennis Hellmich[d], Gavin Hesketh[c], Sonja Hillert[d], Eric Jansen[c], Paul Laycock[a], Nicola Orlando[e,f], Michiel Sanders[g], Stefania Spagnolo[f], Mark Tibbetts[h], Dan Vladoiu[g]

[a]*University of Liverpool*
[b]*INFN Lecce*
[c]*University College London*
[d]*University of Bonn*
[e]*CERN*
[f]*INFN Lecce and Dipartimento di Matematica e Fisica "Ennio De Giorgi", University of Salento*
[g]*Ludwig Maximilians Universität München*
[h]*Lawrence Berkeley National Laboratory*

Abstract

The differential cross sections for associated production of a Z boson and at least one $(Z+b)$ and at least two $(Z+b\bar{b})$ b-jets have been measured as function of Z boson and b jet kinematic observables. Differential measurements of the $Z+b$ event-level cross section as function of Z boson p_{T} and rapidity are made, together with jet-level cross sections measured as a function of b-jet p_{T}, rapidity and the angular distances ΔR, $\Delta\phi$, Δy and y_{boost} between the Z boson and the b-jet. The fiducial $Z+b\bar{b}$ cross section times branching ratio of the Z into electrons or muons is measured to be

$$\sigma(Z+b\bar{b})\cdot BR(Z\rightarrow ee,\mu\mu) = 0.54 \pm 0.02(\mathrm{stat.})^{+0.06}_{-0.06}(\mathrm{syst.}) \pm 0.01(\mathrm{lumi.})pb$$

A differential measurement of the $Z+b\bar{b}$ cross section as function of Z boson p_{T}, rapidity, invariant mass of the pair of b-jets and the angular distance ΔR between them is also performed.

Contents

1 Updates from previous version

1.1 To Do

- split the b-tagging systematic into eigenvectors
- evaluate remaining systematics - MET, pileup, zvtx (small), MC statistics on unfolding ($Z + b$)
- (re)run aMC@NLO in the Atlas framework ($Z + b$)

1.2 Cross checks in the pipeline

- cross check unfolding using sherpa
- electron vs muon channel also for the Zb analysis, plots need to be remade
- cross check different b-tagging OPs for $Z + b$

1.3 updates from v1.3

- Major: added the Z+b part of the analysis back in (yield extraction, unfolding and theory comparison).

1.4 Reminder of updates in 1.3 compared to v1.2

- QCD background estimate is now final (common to Z+b and Z+bb)
- Reweighting of b-hadron decays to EvtGen is now final (common to Z+b and Z+bb)
- text clarified and reorganised
- extensive appendix on ee-mumu differences observed in the double tag sample
- Final non-perturbative corrections for MCFM, and updated aMC@NLO predictions.

1.5 Updates from 1.4

- New Z+b differential distributions dy and yboost
- MEt cut changed from 30 to 70 GeV
- electron vs muon channel Z+bb appendix B completely rewritten
- added Z rapidity in Z+bb, and Δy and y_{boost} variables in Z+b.
- updated theory comparisons
- Final breakdown of b-tag and JES systematics
- MPI and gluon splitting uncertainty calculated for Z+b analysis
- electron muon comparisons added for Z+b
- TODO: add appendix detailing the MV1 60% scale factor issues.

- TODO: add appendix detailing Zb unfolding statistical uncertainty closure test for the Bayesian method
- TODO: correlated MC stat uncertainties for Zb unfolding

2 Introduction

In the complex environment of a hadron collider like the LHC, the electron and muon decay modes of the Z provide a very clear experimental signature of Z production. The two leptons are generally high transverse momentum (p_{T}), and isolated from other activity in the event. This provides an ideal signature for both triggering and reconstruction. Combining the leptons gives a clear mass peak centred on M_Z, and selecting only events close to this peak greatly reduces the backgrounds, which come mainly from semi-leptonic decays of top pairs, and real or fake leptons from multi-jets events.

Events containg Z bosons are an ideal testing ground for QCD predictions. Several calculations exist for predicting such final states, from parton level pQCD calculations such as MCFM [1], through to full event generators. These event generators typically combine a parton shower model with matrix elements for Z production at leading order (LO) ($2 \rightarrow 1$ at tree level), such as PYTHIA [2] and HERWIG [3], next-to-leading order (NLO) matrix-element, such as MC@NLO [4], or with multi-leg tree level matrix elements, such as ALPGEN [5] or SHERPA [6].

The production cross section for a Z boson in association with at least one b jet was measured previously at the Tevatron [7, 8] and the LHC [9, 10], where the Tevatron measurements were normalised to the cross section for inclusive Z + jets production. Generally the data are well described by pQCD models.

With the increased statistics of the ATLAS 2011 data set, corresponding to an integrated luminosity of 4.6 fb^{-1}, both a higher precision inclusive cross section measurement and the measurement of differential cross sections become feasible.

For this analysis, true b jets were defined by matching weakly decaying b hadrons to AntiKt $R = 0.4$ jets at particle level. At reconstruction level, b tagged jets were required to pass the MV1 tagger cut corresponding to the 75 % efficiency operating point. In all analyses, the yield of b jets was extracted from template fits of a b discriminant, $\ln(pb/pc)$.

In final states with a Z boson and at least 1 b jet, the following measurements were performed: differential cross sections were measured as a function of the jet-based observables b jet p_{T} and y and the angular quantities $\Delta\phi(Z, b)$, $\Delta R(Z, b)$ between the Z boson and the b jet with the highest p_{T} in the event. Also, the event based differential cross section as a function of Z boson p_{T} was determined.

For final states with a Z boson and at least two b jets, the inclusive cross section was measured. In the same final state, differential cross section measurements were performed as a function of the event based observables Z boson p_{T}, Z boson $|y|$, the mass m_{bb} of the di-b system and ΔR_{bb} between the b jets.

Results from these analyses are compared to NLO predictions, permitting constraints to be placed on theoretical models of heavy flavour production in hadron collisions.

This document is structured as follows: The data and MC samples used are given in Section 3. To obtain the final result, both electron and muon decay modes of the Z were used. The event selection is described in detail in Section 4. A correction to the description of b hadron decays in the Monte Carlo simulation is described in Section 5. The determination of the data-driven multi-jet background is covered in Section 7. The extraction of the numbers of $Z + b\bar{b}$ events using an extended likelihood fit method, are presented in Section 10 and 12. Section 10 also covers the scale factors needed to match the heavy flavour component in the Monte Carlo to data. Section 13 describes how fiducial cross section results were obtained from the fit results. Systematic uncertainties are covered in Section 14, and the final result compared to theoretical predictions in Section 16. Finally, the conclusions are given in Section 17.

3 Data and Monte Carlo Samples

3.1 The data set used

The analysis uses the data taken between 13th March and 30th October 2011. Due to the nearly exponential increase in LHC instantaneous luminosity over the year, the trigger menu had to be adjusted to deal with the increasing trigger rate. The analysis uses the unprescaled triggers recommended by the W/Z group for 2011 analyses. For the electron channel, di-electron triggers were used, while for the muon channel single lepton triggers were used, as shown in table 1. Run periods B-K1 were taken with version 2 of the trigger menu, while from run period K2 version 3 was used. See [11] for further documentation of the menus.

Z decay channel	data periods	trigger	integrated luminosity after GRL [fb^{-1}]
$Z \to ee$	D-J	`EF_2e12_medium`	1.66
$Z \to ee$	K	`EF_2e12T_medium`	0.58
$Z \to ee$	L-M	`EF_2e12Tvh_medium`	2.40
$Z \to ee$	D-M		4.64
$Z \to \mu\mu$	D-I	`EF_mu18_MG`	1.44
$Z \to \mu\mu$	J-M	`EF_mu18_MG_medium`	3.20
$Z \to \mu\mu$	D-M		4.64

Table 1: Triggers used and integrated luminosities collected during 2011 data taking periods.

The good runs list (GRL) was produced centrally [1]. The names of the triggers are listed in Table 1, along with the data taking periods during which they were used for this analysis and the integrated luminosity collected after applying the GRL. Resulting integrated luminosities for the entire period D-M data set considered are also shown.

3.2 Monte Carlo samples

To decribe $Z+$jets events, including the Zb and Zbb signal, the ALPGEN [5] matrix element MC generator, version 2.13, has been used. It was interfaced to HERWIG version 6.520 [3] which describes parton shower and hadronisation effects, and to JIMMY version 4.31 [3] for generating multiple parton interactions. Matrix element and parton shower results were matched via the MLM approach [12]. Event generation was based on generator tune AUET2-CTEQ6L1 [13] and the CTEQ6L1 PDF set [14].

The same combination of generators was also used to describe the backgrounds from $W+$ jets final states. Backgrounds from $t\bar{t}$ and single top production, as well as diboson final states, were generated using the MC@NLO program [4], version 3.41, interfaced to HERWIG + JIMMY and to PDF set CT10 [15, 16].

Tables 2 and 3 list the MC samples used for the description of the $Z+b\bar{b}$ signal, the Standard Model background samples and samples used for systematic studies, respectively. For each sample, the ATLAS ID, a short description, the cross section, k-factor and number of events generated are shown.

The analysis was based on the `MC11c` samples, with reconstruction tag `r3043_r2993`, for which conditions used in the reconstruction corresponded to the optimised parameter set matched to the entire 2011 LHC data. The D3PD files were prepared by the Standard Model WZ physics group (`*NTUP_SMWZ*`) corresponding to production tag `p1035`.

[1]GRL data11_7TeV.periodAllYear_DetStatusv36pro10_CoolRunQuery000408_WZjets_allchannels_DtoM.xml was used

ID	description	MC generator(s)	$\epsilon_F \cdot \sigma$ [pb]	k-factor	N_{evts}
109300	$Zb\bar{b}$+0 part., $Z \to ee$	ALPGEN+JIMMY	6.57	1.25	409999
109301	$Zb\bar{b}$+1 part., $Z \to ee$	ALPGEN+JIMMY	2.48	1.25	160000
109302	$Zb\bar{b}$+2 part., $Z \to ee$	ALPGEN+JIMMY	0.89	1.25	60000
109303	$Zb\bar{b}$+3 part., $Z \to ee$	ALPGEN+JIMMY	0.39	1.25	30000
107650	Z+0 part., $Z \to ee$	ALPGEN+JIMMY	668.32	1.25	6618284
107651	Z+1 part., $Z \to ee$	ALPGEN+JIMMY	134.36	1.25	1334897
107652	Z+2 part., $Z \to ee$	ALPGEN+JIMMY	40.54	1.25	2004195
107653	Z+3 part., $Z \to ee$	ALPGEN+JIMMY	11.16	1.25	549949
107654	Z+4 part., $Z \to ee$	ALPGEN+JIMMY	2.88	1.25	149948
107655	Z+5 part., $Z \to ee$	ALPGEN+JIMMY	0.83	1.25	50000
109305	$Zb\bar{b}$+0 part., $Z \to \mu\mu$	ALPGEN+JIMMY	6.56	1.25	409949
109306	$Zb\bar{b}$+1 part., $Z \to \mu\mu$	ALPGEN+JIMMY	2.47	1.25	160000
109307	$Zb\bar{b}$+2 part., $Z \to \mu\mu$	ALPGEN+JIMMY	0.89	1.25	60000
109308	$Zb\bar{b}$+3 part., $Z \to \mu\mu$	ALPGEN+JIMMY	0.39	1.25	29999
107660	Z+0 part., $Z \to \mu\mu$	ALPGEN+JIMMY	668.68	1.25	6615230
107661	Z+1 part., $Z \to \mu\mu$	ALPGEN+JIMMY	134.14	1.25	1334296
107662	Z+2 part., $Z \to \mu\mu$	ALPGEN+JIMMY	40.3	1.25	1999941
107663	Z+3 part., $Z \to \mu\mu$	ALPGEN+JIMMY	11.19	1.25	309899
107664	Z+4 part., $Z \to \mu\mu$	ALPGEN+JIMMY	2.75	1.25	35000
107665	Z+5 part., $Z \to \mu\mu$	ALPGEN+JIMMY	0.77	1.25	50000

Table 2: Signal MC samples, filter efficiency times cross section, k-factor and number of events.

3.3 Overlap removal between samples using the HFOR tool

The ALPGEN generator can calculate exact matrix-elements for processes involving e.g. a lepton pair, a pair of bottom quarks (where the mass of the bottom quark is taken into account) and optionally extra light partons. In this analysis, samples based on these ALPGEN matrix-elements are used (see Table 2), where the showering of the partons is modeled by HERWIG . However, events with a lepton pair and a pair of bottom quarks can also appear from an ALPGEN lepton-pair with gluon final state, where the gluon splits into a bottom-quark pair in the parton shower (as in the Z + parton samples listed in Table 3, where the additional partons are gluons or light quarks, including charm). This implies that there is a potential event overlap between the ALPGEN $Z + b\bar{b}$ and Z+light-parton samples.

The Heavy Flavour Overlap Removal (HFOR) tool removes this overlap based on the assumption that for small angle gluon splitting (i.e., a small angular separation ΔR between the b and $\bar{b}$ quarks), the parton shower gives a more correct description of the kinematics and the yield, whereas for large angle splitting, the exact matrix-element calculation in ALPGEN is more correct.

For this, the HFOR tool first classifies the b-quarks in an event as coming from the ALPGEN matrix-element calculation (ME), from gluon splitting in the parton shower (GS), from the underlying event or multi-parton-interactions (MPI), or from the b-quark content of the colliding protons (PDF). The PDF $b/\bar{b}$-quarks participate in the hard-scattering, but the parton shower restores flavour conservation by inserting a $\bar{b}/b$-quark in the event. This last category of b-quarks only appears from the MPI contribution because ALPGEN does not consider the b-PDF. Moreover, they are not relevant for the overlap removal.

To remove the overlap between Z+light-parton and $Z + b\bar{b}$ samples, events are then classified as follows, using the final state b-quarks in the event.

- If in a Z+light-parton sample, a $b\bar{b}$-pair from the parton shower with $\Delta R < 0.4$ is found, the event

ID	description	MC generator(s)	$\epsilon_F \cdot \sigma$ [pb]	k-factor	N_{evts}
105200	$t\bar{t}$	MC@NLO+Jimmy	79.01	1.146	14983835
108346	Wt inclusive	MC@NLO+Jimmy	14.59	1.079	899694
108344	Wt s-channel	MC@NLO+Jimmy	0.47	1.064	299998
108341	Wt t-channel	MC@NLO+Jimmy	7.12	0.979	299999
105930	ZZ, $\ell\ell qq$	MC@NLO+Jimmy	0.559	-	25000
105942	W^+Z, $qq\ell\ell$	MC@NLO+Jimmy	0.5415	-	24950
105972	W^-Z, $qq\ell\ell$	MC@NLO+Jimmy	0.2944	-	100000
107680	W+0 part., $W \to e\nu$	Alpgen+Jimmy	6930.50	1.196	10495000
107681	W+1 part., $W \to e\nu$	Alpgen+Jimmy	1305.30	1.196	7570000
107682	W+2 part., $W \to e\nu$	Alpgen+Jimmy	378.13	1.196	3770000
107683	W+3 part., $W \to e\nu$	Alpgen+Jimmy	101.86	1.196	1010000
107684	W+4 part., $W \to e\nu$	Alpgen+Jimmy	25.68	1.196	1075000
107685	W+5 part., $W \to e\nu$	Alpgen+Jimmy	6.99	1.196	1000000
107690	W+0 part., $W \to \mu\nu$	Alpgen+Jimmy	6932.40	1.195	10495000
107691	W+1 part., $W \to \mu\nu$	Alpgen+Jimmy	1305.90	1.195	7500000
107692	W+2 part., $W \to \mu\nu$	Alpgen+Jimmy	378.07	1.195	3770000
107693	W+3 part., $W \to \mu\nu$	Alpgen+Jimmy	101.85	1.195	1010000
107694	W+4 part., $W \to \mu\nu$	Alpgen+Jimmy	25.72	1.195	1000000
107695	W+5 part., $W \to \mu\nu$	Alpgen+Jimmy	7.00	1.195	1000000
107280	$Wb\bar{b}$+0 part., $W \to \ell\nu$	Alpgen+Jimmy	47.35	1.2	1000000
107281	$Wb\bar{b}$+1 part., $W \to \ell\nu$	Alpgen+Jimmy	35.76	1.2	1240000
107282	$Wb\bar{b}$+2 part., $W \to \ell\nu$	Alpgen+Jimmy	17.33	1.2	175000
107283	$Wb\bar{b}$+3 part., $W \to \ell\nu$	Alpgen+Jimmy	7.61	1.2	700000

Table 3: Background MC samples, cross section and number of events.

is kept; otherwise the event is rejected.

- If in a $Z + b\bar{b}$ sample, a $b\bar{b}$-pair from the alpgen matrix-element calculation, with $\Delta R > 0.4$ is found, the event is kept; otherwise the event is rejected.

In the present analysis, HFOR is applied to the $Z + b\bar{b}$ and Z+light-parton samples. Since it is not certain whether the parton-shower approach really gives a better description of small-angle b-quark-pair production than the full matrix-element calculation, a systematic uncertainty due to HFOR is estimated (see Section 14).

Further details regarding the technical implementation of the HFOR procedure and its effect on relevant quantities can be found in Appendix A.

4 Object and event selection

Event vertex definition	vertex with max $\left(\sum p_{\mathrm{T}}^2\,(track)\right)$
Event vertex quality	≥ 3 tracks assigned to event vertex
Electron selection criteria	author 1 or 3 *egammaPID* :: *ElectronMediumPP* passed crack region $1.37 < \|\eta_e\| < 1.52$ excluded $\|\eta_e < 2.47$ electron track $z_0 < 1$ mm, $\|d_0/\sigma(d_0)\| < 10$
$Z \to ee$ selection	2 oppositely charged selected electrons no further e or μ in event $76 < M_{ee}($ GeV$) < 106$
Muon selection criteria	use STACO combined muons $z_0(\mu) < 1$ mm, $\|d_0/\sigma(d_0)\| < 3$ $\|\eta_\mu < 2.4$, $p_T(\mu) > 20$ GeV isolation: $\Sigma p_{\mathrm{T}}(ID)/p_{\mathrm{T}} < 0.1$
$Z \to \mu\mu$ selection	2 oppositely charged selected muons no selected e with $\Delta R(e, \mu) > 0.1$ $76 < M_{\mu\mu}($ GeV$) < 106$
Event selection based on $E_{\mathrm{T}}^{\mathrm{miss}}$ (to suppress top background)	pass “looser” $E_{\mathrm{T}}^{\mathrm{miss}}$ cleaning $E_{\mathrm{T}}^{\mathrm{miss}} < 70$ GeV, using `MET_RefFinal` recalculated with calibrated jets and leptons.
Jet selection criteria	Anti-k_T jets, built from topo-clusters, $R = 0.4$ p_T(jet) > 20 GeV $\|y(\text{jet})\| < 2.4$ ΔR(jet signal ℓ) > 0.5 $JVF > 0.75$ pass “looser” cleaning requirements jet not in LAr hole When constructing jet observables (eg $\Delta R(b, b)$, the two leading tagged jets are used.
Jet flavour (in MC)	Jets matched to a weakly-decaying b-hadron with $p_T > 5$ GeV based on a simple $\Delta R < 0.3$ matching are labelled as b-jets. If no b hadron is found, the same criteria are applied using charmed hadrons. If still no match is found, the jet is labelled as a light flavour jet.

Table 4: Object and event selection criteria used for reconstructed events.

The object definition and event selection criteria are listed in Table 4. They largely follows the baseline WZ group selection [2] with a few exceptions. A narrower dilepton mass window is used to reject background from top decays, and multi jet production, which have an approximately flat distribution in the dilepton invariant mass. A maximum MEt cut is also used to reject more top background. Jet rapidity is used instead of pseudo-rapidity, and the $|y|$ and jet p_{T} ranges utilise the full range available for heavy flavour tagging.

[2] https://twiki.cern.ch/twiki/bin/viewauth/AtlasProtected/WZElectroweakCommonTopics2011

For the electron selection criteria, the cluster η is used for the crack region removal and η kinematic cut. In the following steps, electron candidate kinematics use either cluster or track-based quantities depending on the number of hits in the ID, as standard. In the definition of muon isolation, the variable $p_{\mathrm{T}}(ID)$ denotes the transverse momentum sum of inner detector tracks in a R < 0.2 cone around the muon. Jets are corrected to the EM+JES scale with offset and beam-spot corrections.

The MV1 algorithm is used to tag a jet as a candidate b-jet. MV1 is a neural network-based algorithm that uses the output weights of IP3D, SV1 and JetFitterCombNN as inputs [17] (see Section 5 for more details on b-tagging variables). The MV1 tagger is used at the 75% efficiency operating point, corresponding to a cut of w(MV1)> 0.404219, where w(MV1) is the MV1 weight.

4.1 Monte Carlo Corrections

Simulated events are required to pass the (simulated) trigger requirements as used in data, and the same detector level event selection. Small η and p_{T} dependent scale factors are applied to correct the lepton reconstruction efficiency in simulation to match the data (an average correction of 0.99 in the electron channel, 0.98 in the muon channel). The electron and muon resolutions are also smeared in the simulation to match the data, using the standard prescriptions described in the WZ Baseline [3]. A further scale factor (which averages to approximately 1.05) is applied to bring the efficiency of the MV1 cut (w(MV1)> 0.404219) into agreement with data (applied per jet, using the standard BTagging Calibration Interface). For the corrections, standard tools are used, as listed in Table 5.

Purpose	Package, Version
Muon Trigger Recommendations 2011	TrigMuonEfficiency-00-02-32
Muon Efficiency Correction	MuonEfficiencyCorrections-02-01-12
Muon momentum correction	MuonMomentumCorrections-00-08-07
Electron corrections	egammaAnalysisUtils-00-04-22
Electron scale factors	ElectronEfficiencyCorrection-00-00-13
Pileup Reweighting	PileupReweighting-00-02-09
Jet Calibration	ApplyJetCalibration-00-03-03
JES uncertainty provider	JetUncertainties-00-08-05
JER provider	JetResolution-01-00-00
Advanced B-tagger	JetTagAlgorithms-00-00-01
B-tag calibration interface	CalibrationDataInterface-00-02-01
MET utility	MissingETUtility-01-01-04-01

Table 5: Versions used of common packages for obtaining scale factors and event reweighting prescriptions, as far as these need to be applied at the analysis stage.

4.2 Particle Level Selection

To extract the cross section, the signal must be defined at the particle level. This is done matching as closely as possible the detector level selection, to minimise the introduction of theoretical model-dependent corrections. Details are given in Table 6.

[3] https://twiki.cern.ch/twiki/bin/viewauth/AtlasProtected/WZElectroweakCommonTopics2011

Lepton dressing	Dressed leptons are constructed using all photons in a cone $\Delta R < 0.1$ around any stable (status=1) muon or electron
Lepton selection	The two highest pT dressed, same flavour leptons are then used. They are required to have $p_{\mathrm{T}} > 20$ GeV, $\lvert\eta\rvert < 2.5$, be opposite-charge, and have a dilepton mass $76 < M < 106$ GeV.
Jet Selection	All other stable particles are passed to the jet finder (the Antikt4TruthWZ collection is used). Jets are required to have $p_{\mathrm{T}} > 20$ GeV and $\lvert y\rvert < 2.4$. Any jets within $\Delta R < 0.5$ of a signal lepton are discarded.
Jet flavour	Jets matched to a weakly-decaying *b*-hadron with $p_T > 5$ GeV based on a simple $\Delta R < 0.3$ matching are labelled as *b*-jets. If no *b* hadron is found, the same criteria are applied using charm quarks. If still no match is found, the jet is labelled as a light flavour jet. When constructing jet observables (eg $\Delta R(b, b)$, the two leading b-jets are used.

Table 6: Object and event selection criteria used for particle level events.

5 B-Hadron Decay Modelling in Herwig

The results presented in this document are based on extended maximum likelihood fits to data using probability templates derived from MC simulations. Variables chosen to form the templates are those which discriminate jets containing heavy flavour b hadron decays from those without such decays. To ensure the fit results are not significantly systematically biased it is essential to validate that the shapes of templates in MC for a given jet flavour accurately represent the shape expected in data for that jet flavour. This section describes validation of templates representing jets containing b hadron decays. These are investigated using a data control region enriched in such jets, specifically top quark decay candidate events with a lepton (muon or electron) and four or more jets in the final state of which exactly two pass the MV1 algorithm 75% tagging requirement. Discussion of the selection criteria for the control region and corrections which need to be applied to correct the top MC in that region so that it accurately represents the data are described in appendix E. The chosen control region has previously been use to investigate the properties of b-jets by the ATLAS 2011 $W+b$ analysis [18] and top group b-jet efficiency measurements [19].

Mismodelling of heavy flavour sensitive variables can originate from the production, decays and reconstruction of b hadron daughters in the MC data. For the validation to be applicable to the signal region it follows that the MC in the control region must have the same parton showering, hadronisation and b hadron decay tables as the signal region. In these analyses such processes are modelled by HERWIG 6 in the signal region so a top MC generator interfaced to HERWIG 6 must be chosen for the control region. The same MC@NLO sample used to model the top background in the signal region is therefore used. It is also important to identify and understand whether corrections in the control region can be directly applied to the signal region due to the different underlying physics processes. For top pair events the majority of b-jets originate from top decays and are well isolated, with a residual contribution from gluon splitting and CKM suppressed W boson decays. In an inclusive signal sample of a Z boson with at least one b-jet the majority of b-jets originate from gluon splitting (or equivalently from the b PDF) in the initial state which typically results in well isolated b-jet(s) in the final state. Only around 5% of b-jets at truth level originate from gluon splitting in the final state, although this does increase for a selection requiring two or more b-jets. It follows that, for the most part, isolated b-jets from top decays are a reasonable cross-check of the physics of isolated b-jets in the signal region. However, the kinematics of b-jets in the signal and control samples do differ, with top decays having a harder spectrum on average. It is therefore necessary to understand how any mismodelling in the control region behaves differentially in b-jet p_T so that the different kinematics are accounted for when corrections are applied to the signal MC samples.

5.1 Evidence for Template Mismodelling

Figures 1 and 2 show the distributions of analysis fit variables based on outputs of the JetFitterCOMBNN algorithm, $\ln(pb/pu)$ and $\ln(pb/pc)$ respectively, for the control region with muon and electron channels combined. It can be seen that there is a difference in shape between the lead and sublead tagged jet indicating the p_T dependence of these variables. Furthermore, in the pure b-jet region at higher values the MC underestimates the data for both variables. The normalisation in MC is fixed to match that in data, therefore, this difference is interpreted as a shape distortion due to a mismodelling of the NN algorithm response in the MC.

The JetFitterCOMBNN algorithm has seven inputs listed in Table 7. Six input variables originate from the JetFitter algorithm which aims to reconstruct secondary vertices from weak heavy flavour decays; three of the inputs are continuous and three discrete. The final input originates from the IP3D algorithm which assigns weights to preselected tracks associated to a given jet depending on their three dimensional impact parameter significance. The neural net algorithm is trained independently for b, c

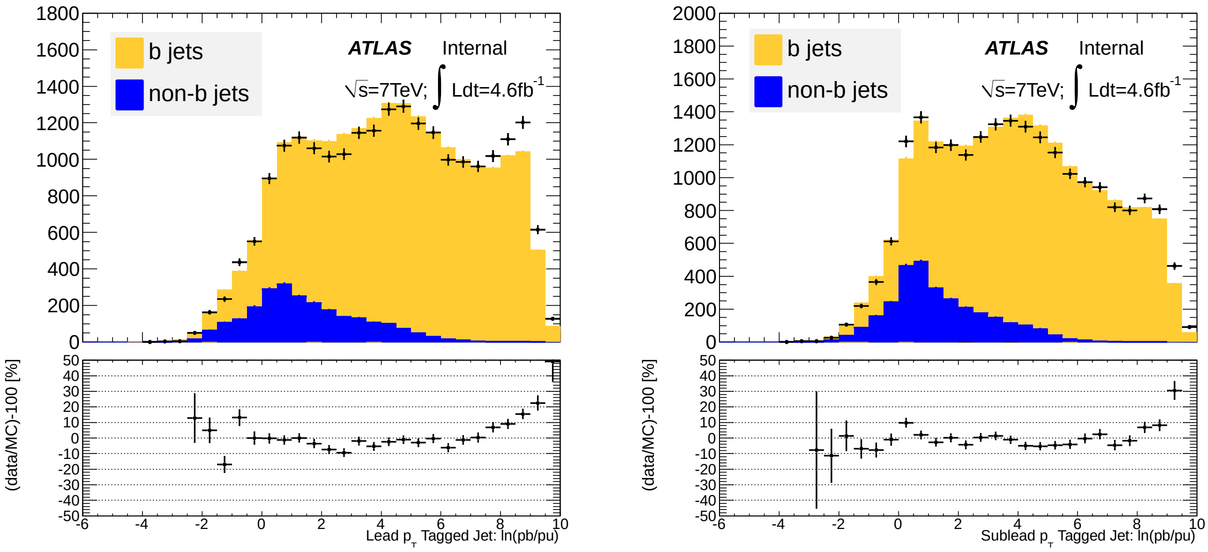

(a) (b)

Figure 1: Comparison of $\ln(pb/pu)$ distribution shape in the two tagged jet control region showing (a) the lead p_T and (b) the sublead p_T tagged jet.

and light jets giving the three response distributions *pb*, *pc* and *pu* respectively; these responses define the $\ln(pb/pu)$ and $\ln(pb/pc)$ variables used extensively in these analyses. Figure 3 shows the six JetFitter input variables for the lead p_T tagged jet with the muon and electron channels combined. It can be seen that the agreement between data and MC is not perfect for a number of the variables. The equivalent plot for the IP3D weight is shown in Figure 4 where again there is systematic difference observed between data and MC. In order to determine whether the disagreement of the NN response output is a direct consequence of mismodelling in the input variables, each input variable is reweighted in the top MC so the overall MC distribution matches the data and the difference between data and MC of the NN output is examined for any improvement. Figure 5 shows ratios of data and MC for both NN output variables from the lead tagged jet in the muon channel with each input variable reweighted individually. It can be seen that the largest improvement comes from the variable nTrkAtVtx and the IP3D weight with a larger improvement from the former. Figure 6 shows the effect of reweighting these two variables separately and then together (nTrkAtVtx first then IP3D weight) for the same sample; it can be seen that the combined reweighting gives little improvement over just reweighting nTrkAtVx. Figure 7 shows the applied nTrkAtVtx weight as a function of number of tracks for the lead and sublead tagged jets in each control region channel; the correction weight is seen to be largely sample independent, although this breaks down somewhat for higher track multiplicities where statistics become limited in both the data and MC.

5.2 Study of *b* Hadron Decay Properties

The variable nTrkAtVtx represents the number of reconstructed tracks used in secondary vertex fits by the JetFitter algorithm. Its mismodelling in the MC can derive from either different track and vertex selection and reconstruction efficiencies compared to data or from incorrect modelling *b* hadron properties in the MC giving rise to an incorrect average number of stable charged particles from their decays. The contribution of *b* hadron decay tables to the latter effect can be investigated by comparing the number of charged particles from *b* hadron decays in the default HERWIG 6 sample to those in an identical sample but where the decays after hadronisation are implemented by the EvtGen package. The advantage of such

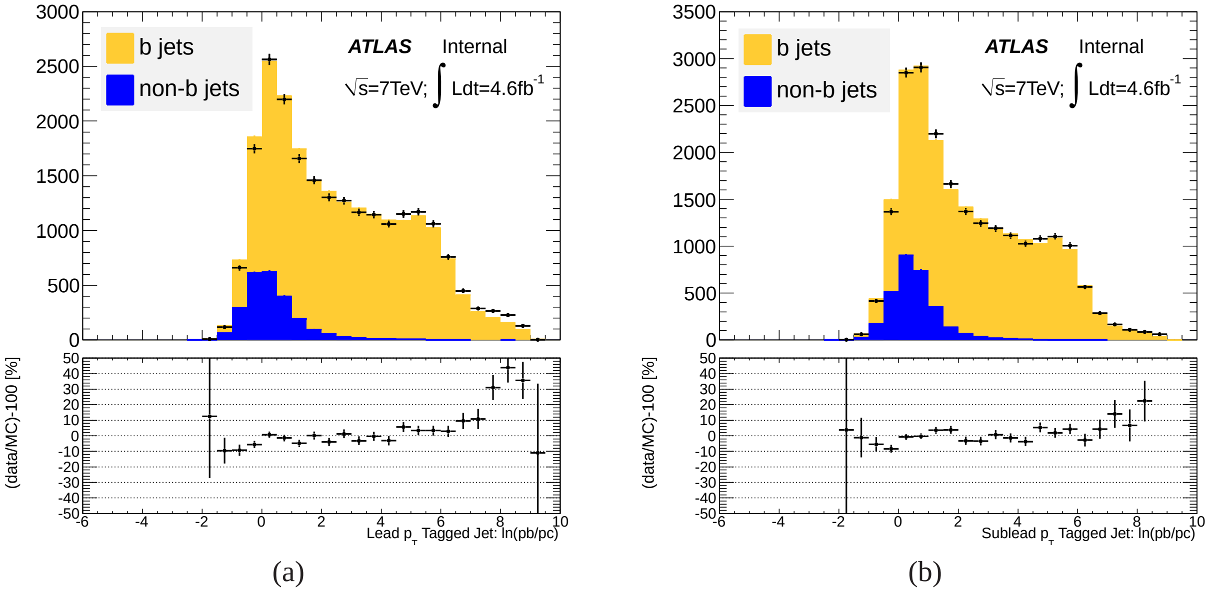

Figure 2: Comparison of $\ln(pb/pc)$ distribution shape in the two tagged jet control region showing (a) the lead p_T and (b) the sublead p_T tagged jet.

a comparison is it factorises the effect of decay tables from fragmenation and hadronisation modelling, and it can be made at generator level without requiring full simulation of the ATLAS detector response. To this end modified job options using the EvtGen 'afterburner' based on those used by the W+b 2011 analysis group are implemented. Table 8 lists the samples generated with the EvtGen job options; the samples are centrally produced and have official ATLAS dataset identification numbers which are given in the table.

Figure 8 compares the stable charge particle multiplicity of b hadron decays for MC@NLO top events with and without EvtGen decays. It can be seen that on average HERWIG 6 underestimates the number of charged particles with respect to EvtGen. EvtGen decay tables are based on PDG measurements and so are more likely to give a better representation of the response expected in data. Figure 9 shows a subset of the same distributions with kinematic cuts of particle p_T >500 MeV and particle $|\eta| < 2.5$ to mimic ATLAS track acceptance. Significantly, with these kinematic cuts applied, the underestimate at generator level by HERWIG 6 is consistent with the phenomenological mismodelling seen in the JetFitter nTrkAtVtx distribution. This suggests that a dominant component in the mismodellling of the nTrkAtVtx distribution in data, and hence to a large extent the NN output response, is due to incorrect b hadron decay tables in HERWIG 6. This conclusion has also been reached by the W+b 2011 analysis group in their independent study of the same data control region [18]. Additional comparisons of b and c hadron decay properties between HERWIG 6 and EvtGen have been studied and no other significant differences beyond the decay multiplicities are observed so these studies will not be discussed here.

Given the above contribution to the mismodelling of b-jet templates in HERWIG 6 it is desirable to correct the MC before performing template fits to data. A natural choice for this correction is to apply event by event weights based on the charged particle multiplicity of b hadron decays in an event; each b hadron decay is assigned a weight equal to the ratio of HERWIG 6 to EvtGen for that hadron's charge particle multiplicity and the overall event weight is the product of all individual b hadron weights in an event. The result is HERWIG 6 MC decays which emulate the EvtGen charge particle multiplicities. However, this procedure is complicated by the desire to apply weights derived from EVNT samples to their D3PD equivalents where some of the information is lost in the transform and where decays and material interactions simulated by GEANT4 have been added to the truth record. Comparisons of the

Algorithm	Name	Nature	Description
JetFitter	Mass	Continuous	Invariant mass of secondary vertex fitted tracks.
JetFitter	eFrac	Continuous	Fraction of energy of fitted tracks relative to all tracks in jet.
JetFitter	3D $d0$ sig.	Continuous	3D impact parameter significance of secondary vertex.
JetFitter	nVtx	Discrete	Number of fitted vertices with two or more tracks.
JetFitter	n1TrkVtx	Discrete	Number of vertices where single track crosses fitted b hadron line of flight.
JetFitter	nTrkAtVtx	Discrete	Total number of tracks in the secondary vertex.
IP3D	IP3D Weight	Partially Continuous	Output of the IP3D tagging algorithm.
JetFitterCOMBNN	pb	0.0-1.0	Neural net response to b jets
JetFitterCOMBNN	pc	0.0-1.0	Neural net response to c jets
JetFitterCOMBNN	pu	0.0-1.0	Neural net response to light jets
JetFitterCOMBNN	$\ln(pb/pu)$	–	Discriminates b-jets from light jets
JetFitterCOMBNN	$\ln(pb/pc)$	–	Discriminates b-jets from c-jets

Table 7: Definitions for JetFitter and IP3D inputs and subsequent response variables of the JetFitter-COMBNN algorithm.

charge particle multiplicity of b hadron decays between EVNT, AOD and D3PD have been made. A residual difference between EVNT and AOD is found, the origin of which appears to be attributable to the ATLAS software not perfectly preserving b hadron decay GenVertex structure between these formats. There is a more significant difference between AOD and D3PD which turns out to be due to the relevant D3PD branches (`mchfpart_`) not storing daughters in the b hadron decay tree which have p_T <200 MeV or $|\eta|$ >5.0. Applying these cuts at AOD level largely recovers this. Due to these kinematic cuts, it is necessary to apply the particle level selection of pT >200 MeV and $|\eta|$ <5.0 to the EVNT samples when deriving weights so they can be directly applied to D3PD samples. Weights are constructed as a function of number of b hadron decay stable charged particles[4] passing the kinematic cuts. Charged particles from GEANT4 (barcode>200000) are explicitly excluded when counting charged particles in the D3PDs.

5.3 Systematic Effects from EvtGen Reweighting

Weights which emulate b hadron decay charged particle multiplicities from EvtGen in HERWIG 6 samples are derived to correct the b-jet template distributions in MC used in fits to extract the b-jet yields. Figures 10 and 11 show the impact of applying weights to the top MC sample in the two tagged jet control region for the lead and sublead b-tagged jets respectively in both $\ln(pb/pu)$ and $\ln(pb/pc)$ distributions. The agreement does improve with respect to the distributions observed in figures 1 and 2 but there is a slight over correction of the template shape in the pure b-jet region. This is likely consequent of an additional mismodelling in either b hadronisation or reconstruction efficiency mismodelling of charged b decay daughters. Rather than investigate these effects directly, systematic variations to the templates are applied based on the top control region as described in the next subsection.

[4] status=1

MC Name	HERWIG DSID	HERWIG nEvts (EVNT)	HERWIG e-Tag	EvtGen DSID	EvtGen nEvts (EVNT)	EvtGen e-Tag
AlpgenJimmyZeebbNp0	109300	410000	e835	129460	410000	e1431
AlpgenJimmyZeebbNp1	109301	160000	e835	129461	160000	e1431
AlpgenJimmyZeebbNp2	109302	60000	e835	129462	50000	e1431
AlpgenJimmyZeebbNp3	109303	30000	e835	129463	30000	e1431
AlpgenJimmyZmumubbNp0	109305	410000	e835	129464	405000	e1431
AlpgenJimmyZmumubbNp1	109306	160000	e835	129465	160000	e1431
AlpgenJimmyZmumubbNp2	109307	60000	e835	129466	50000	e1431
AlpgenJimmyZmumubbNp3	109308	30000	e385	129467	30000	e1431
AlpgenJimmyZeeccNp0	126414	605000	e1008	129468	605000	e1431
AlpgenJimmyZeeccNp1	126415	260000	e1008	129469	255000	e1431
AlpgenJimmyZeeccNp2	126416	110000	e1008	129470	110000	e1431
AlpgenJimmyZeeccNp3	126417	40000	e1008	129471	40000	e1431
AlpgenJimmyZmumuccNp0	126418	600000	e1008	129472	600000	e1431
AlpgenJimmyZmumuccNp1	126419	265000	e1008	129473	250000	e1431
AlpgenJimmyZmumuccNp2	126420	115000	e1008	129474	115000	e1431
AlpgenJimmyZmumuccNp3	126421	40000	e1008	129475	40000	e1431
T1_McAtNlo_Jimmy	105200	14995000	e835	129476	1275000	e1431

Table 8: List of mc11 datasets reprocessed at generator level from 7 TeV four vector files implementing EvtGen decays. The original HERWIG and new EvtGen ATLAS dataset identifications (DSIDs) are given along with the number of generated events for each sample.

At reconstruction level, applying the weights in the signal region results in a 2% increase in b jet tagging efficiency for MV1 75%; no change in efficiency is observed for c and light jets as expected. Figure 12 shows the MV1 75% efficiency for jets matched to b hadrons in the signal MC as a function of jet p_T and rapidity. It can seen that the MV1 75% efficiency scale factor uncertainties provided by the b-tagging CP group are larger than the 2% increase observed from applying the EvtGen weights. An additional study has been made which corrects the MC efficency component of the b-tagging efficiency and inefficiency scale factors by this observed 2%. When unfolding with the EvtGen weights applied and applying this efficency correction the result is found to be identical to unfolding without the EvtGen weights applied and using the default uncorrected scale factors. As the two approaches are equivalent we choose not to apply the EvtGen weights in the unfolding but instead only apply them when forming templates containing b-jets to be used in fits to data.

5.4 Alternative Reweighting Scheme for b Templates

As noted above, application of EvtGen weights in the top pair control region slightly over corrects the $\ln(pb/pc)$ shape used extensively in analysis fits. An alternative reweighting scheme derived directly from the control region and used as a systematic variation for b template shapes is described in this section. All selected b-jets in the top pair control region are combined into a single $\ln(pb/pc)$ distribution and a functional form of the resulting data/MC ratio is determined. Figure 13 shows the resulting fitted ratio. The fit range is restricted to the b-jet dominated region of (2.0,9.0) and a 3rd order polynomial is found to give a good fit to these data with χ^2/DoF=14.13/10. Table 9 shows the fitted parameters for the polynomial. To determine if this functional correction is kinematically independent and thus directly applicable to the signal MC the integrated distribution used to derived the function is split into bins of jet p_T and the χ^2/DoF of the data/MC ratio in each bin with respect to the derived function is calculated. Table 10 lists the calculated χ^2 values. It can be seen that within the statistics available in the control region the assumption of kinematic independence of the ratio holds. It is therefore directly applied to the signal region as described in section 14.5.

Parameter	Fitted Value
p0	0.689±0.152
p1	0.213±0.105
p2	−0.051±0.022
p3	0.004±0.001

Table 9: Fitted polynomial parameters derived from the inclusive b-jet top pair control region data/MC ratio of $\ln(pb/pc)$.

p_T Range [GeV]	χ^2/DoF
20-30	16.32/10
30-50	16.71/10
50-75	8.68/10
75-110	13.37/10
110-200	17.63/10
200-500	15.19/10

Table 10: Calculated χ^2/DoF in bins of b-jet p_T for the data/MC ratio in that bin with respect to the fitted function derived from the inclusive b-jet top pair control region data/MC ratio of $\ln(pb/pc)$.

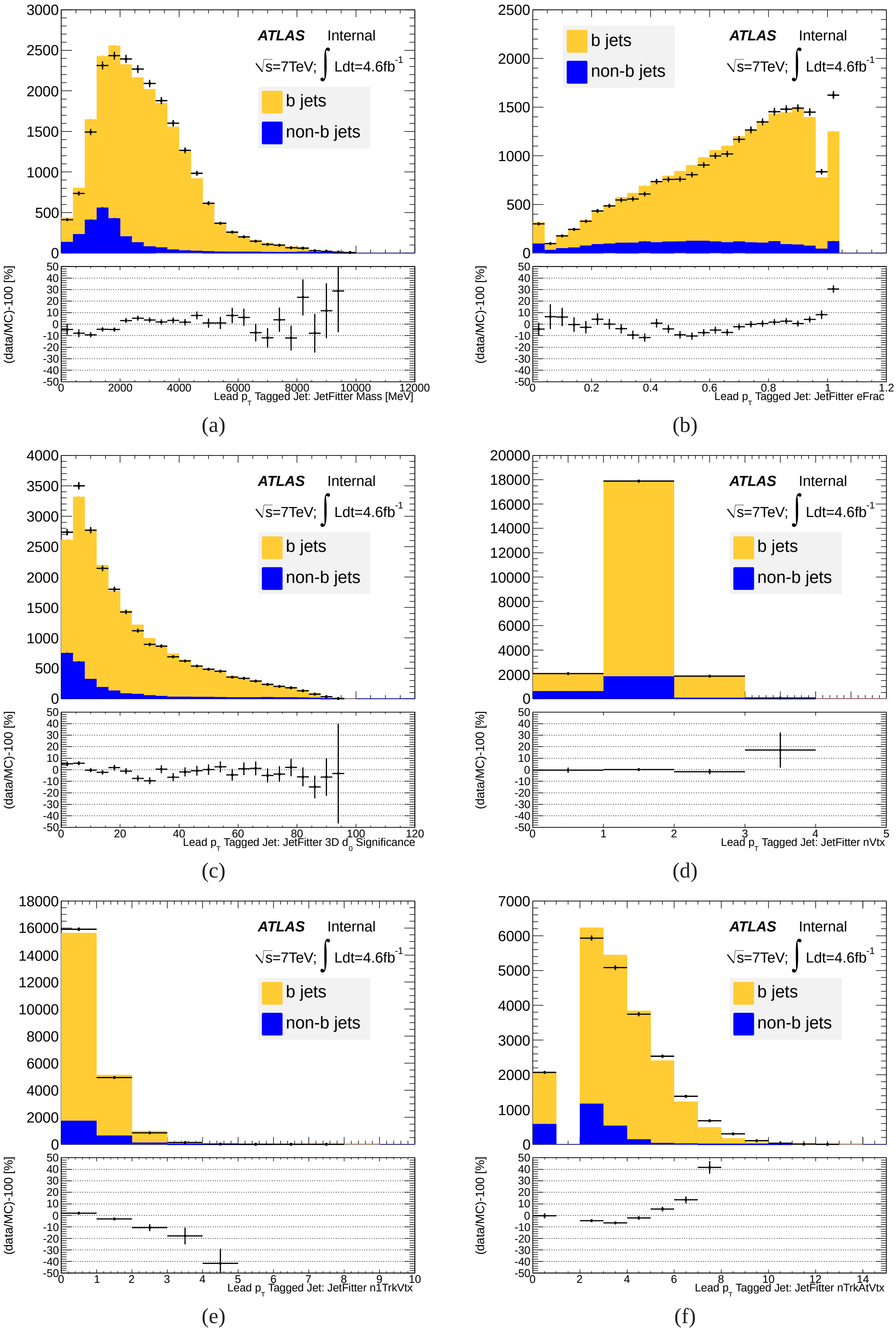

Figure 3: Comparisons of data to MC of the JetFitter based inputs to the JetFitterCOMBNN algorithm for the lead p_T tagged jet in the two tagged jet control region. The inputs are (a) Mass, (b) eFrac, (c) 3D $d0$ sig., (d) nVtx, (e) n1TrkVtx and (f) nTrkAtVtx.

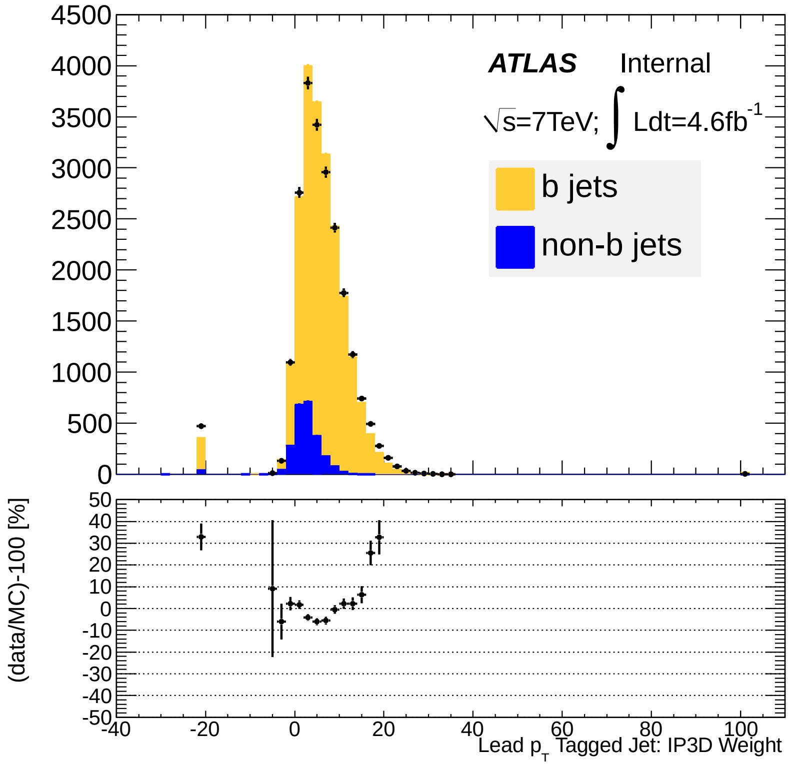

Figure 4: Comparison of data to MC of the IP3D weight input to the JetFitterCOMBNN algorithm for the lead p_T tagged jet in the two tagged jet control region.

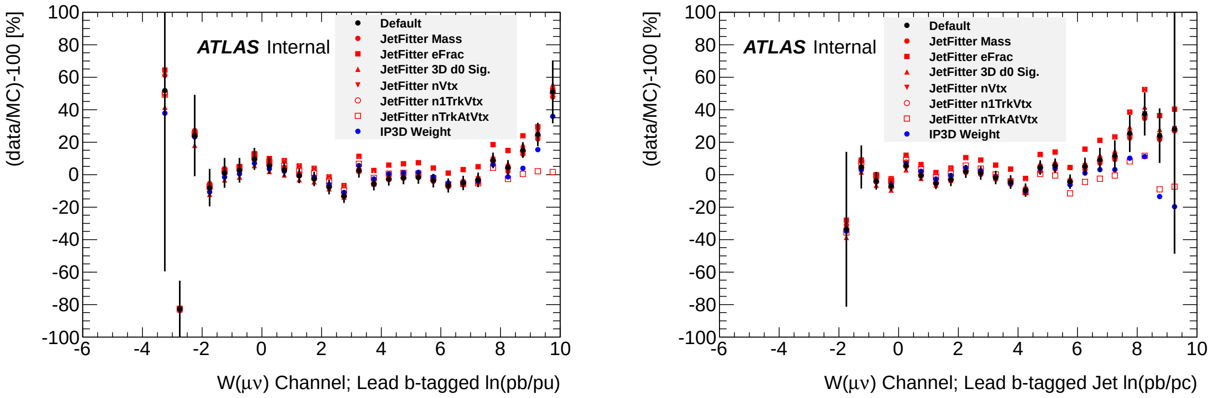

(a) (b)

Figure 5: Impact on JetFitterCOMBNN response for (a) $\ln(pb/pu)$ and (b) $\ln(pb/pc)$ as a consequence of reweighting an individual input variable in the top MC so that MC and data match in that variable. Plots are for the lead p_T tagged jet in the $W(\mu\nu)$ channel two tagged jet control region.

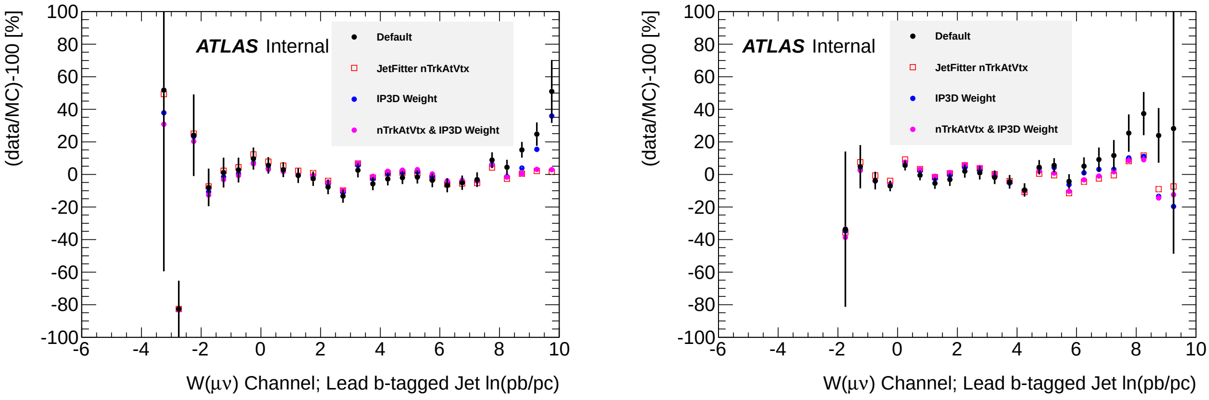

(a) (b)

Figure 6: Comparison of the impact of data to MC ratio for (a) $\ln(pb/pu)$ and (b) $\ln(pb/pc)$ when reweighting nTrkAtVtx and IP3D weight individually and when reweighting nTrkAtVtx then IP3D weight consecutively. Plots are for the lead p_T tagged jet in the muon channel two tagged jet control region.

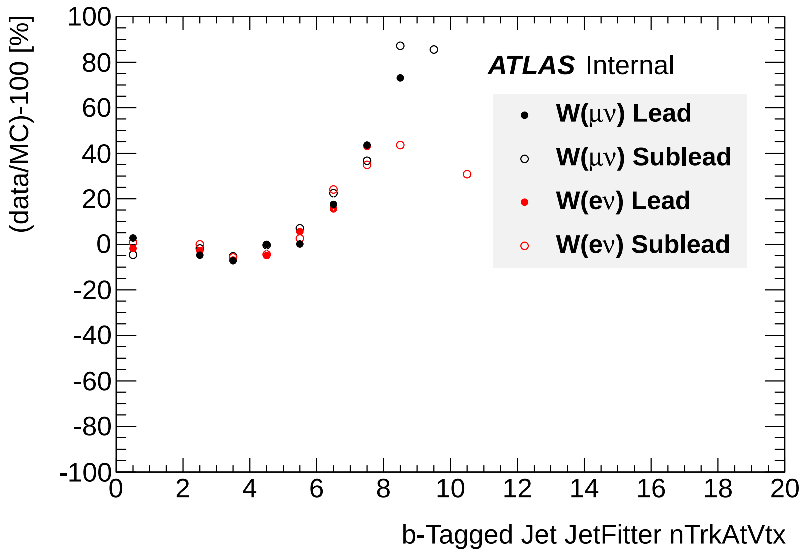

Figure 7: Data to MC ratios of the JetFitter nTrkAtVtx input to the JetFitterCOMBNN algorithm.

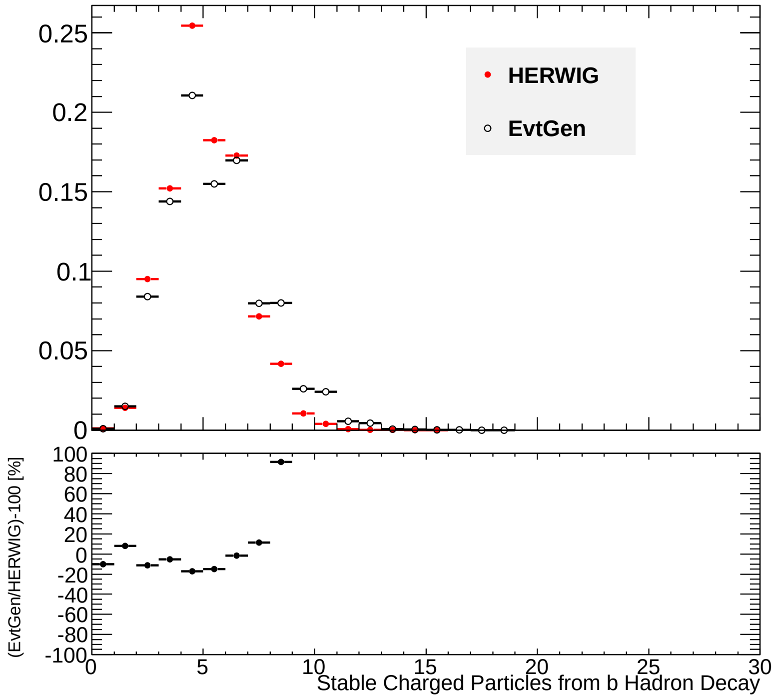

Figure 8: Normalised comparison of the total number of stable charged particles from b hadron decays in top MC with the hadron decays implemented by HERWIG 6 and EvtGen.

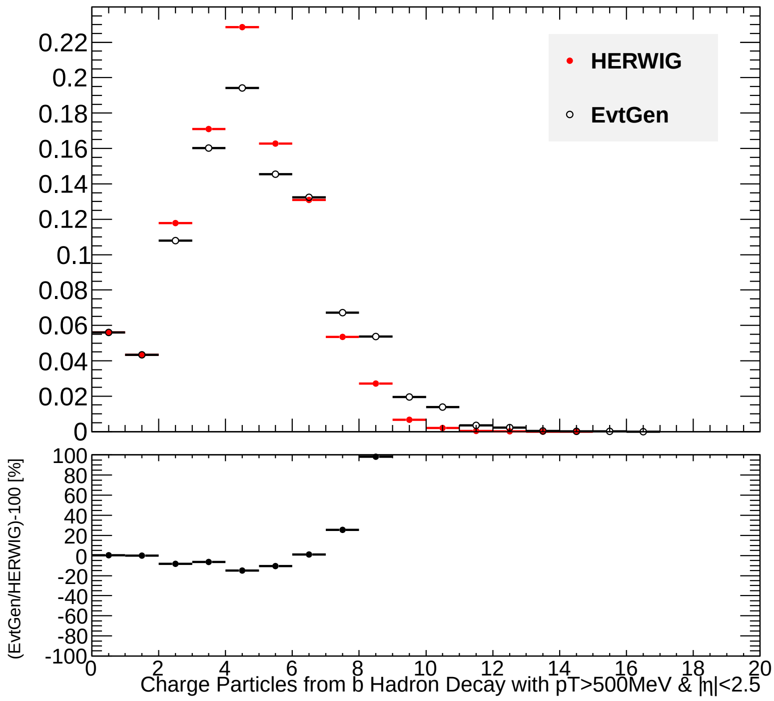

Figure 9: Normalised comparison of the number of stable charged particles from b hadron decays in top MC with the hadron decays implemented by HERWIG 6 and EvtGen. A kinematic cut of p_T >200 MeV and $|\eta|$ <2.5 is applied to the charged particles to emulate the ATLAS tracking acceptance.

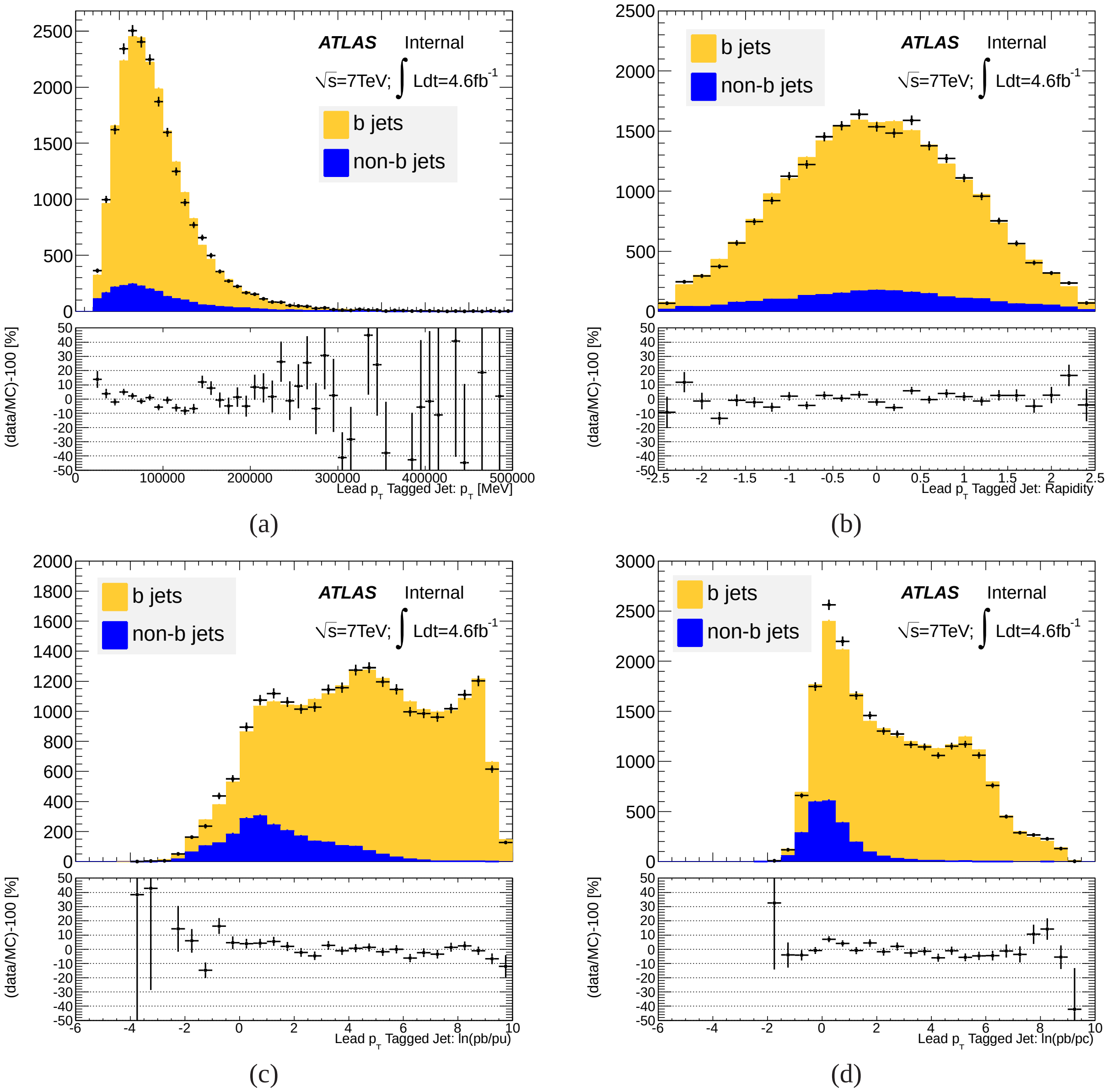

Figure 10: Control region two tag bin lead p_T tagged jet: (a) p_T; (b) rapidity; (c) $\ln(pb/pu)$; (d) $\ln(pb/pc)$.

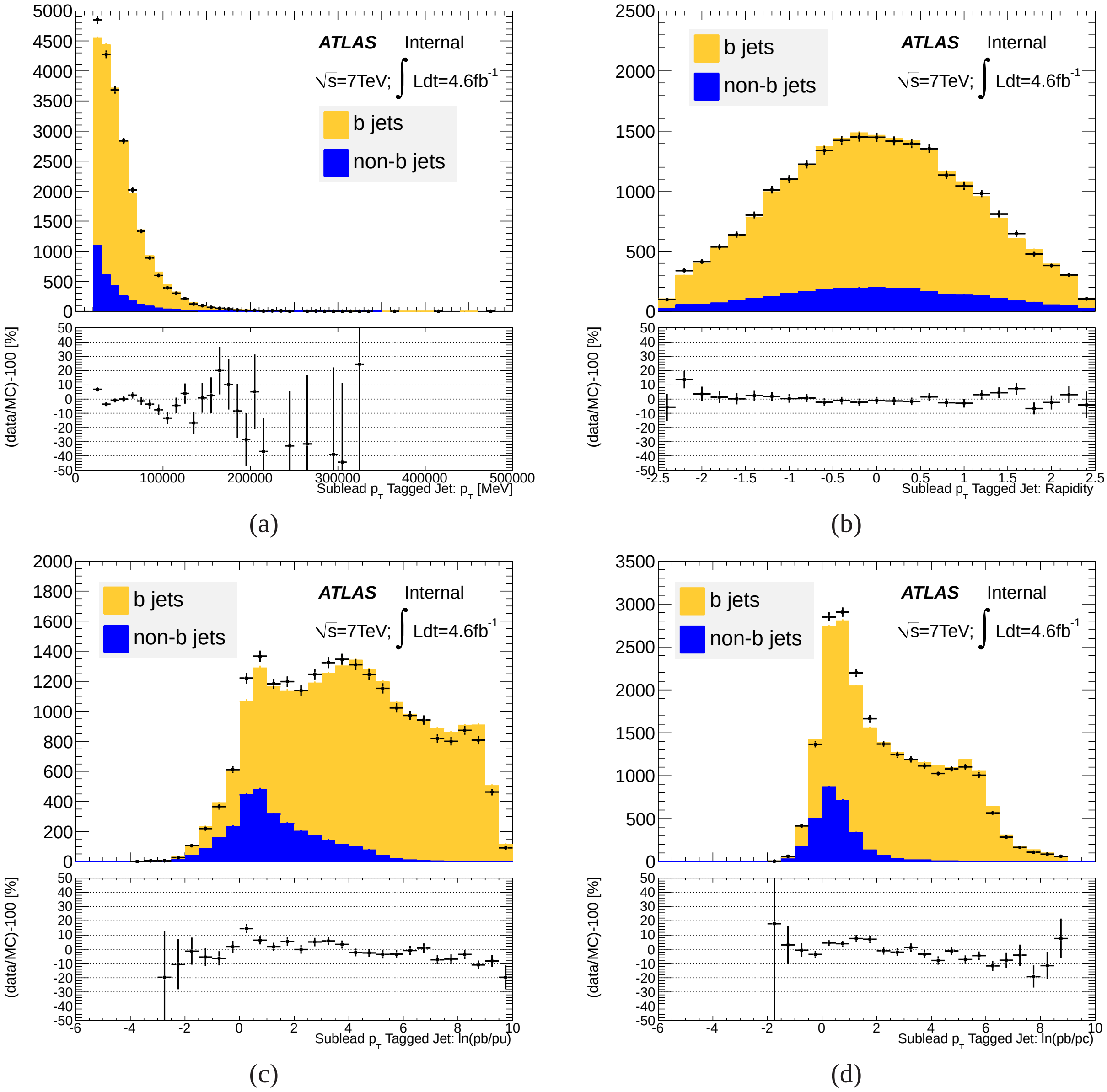

Figure 11: Control region two tag bin sublead p_T tagged jet: (a) p_T; (b) rapidity; (c) $\ln(pb/pu)$; (d) $\ln(pb/pc)$.

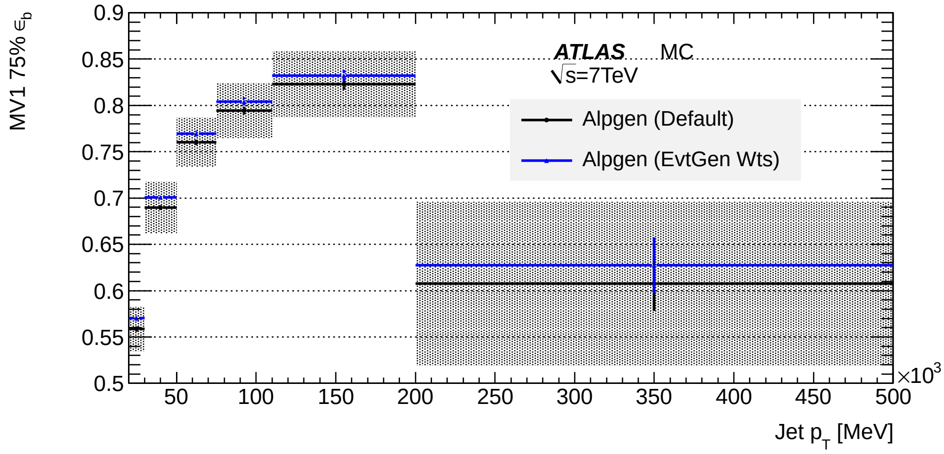

(a)

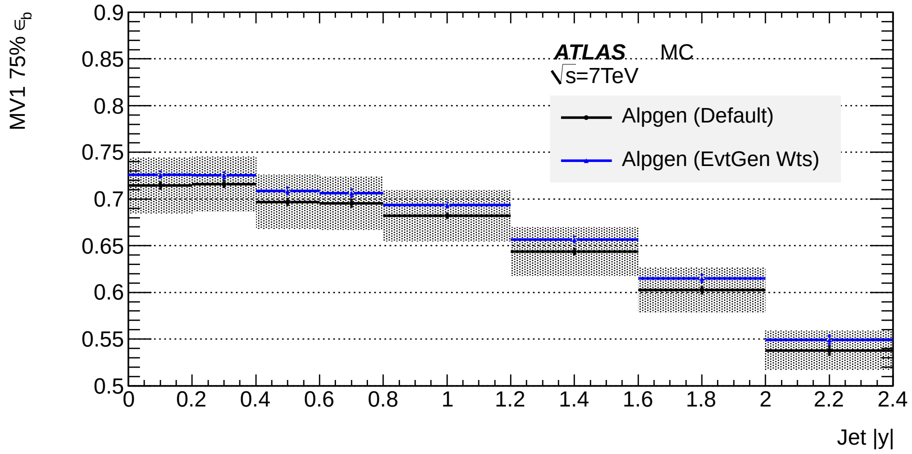

(b)

Figure 12: Signal MC MV1 75% *b*-jet efficiency as a function of (a) jet p_T and (b) jet rapidity. It can be seen that the application of EvtGen weights to the signal results in a 2% increase in the *b*-jet efficiency, independent of the jet kinematics, and that this increase is well withing the existing MV1 75% CP uncertainties.

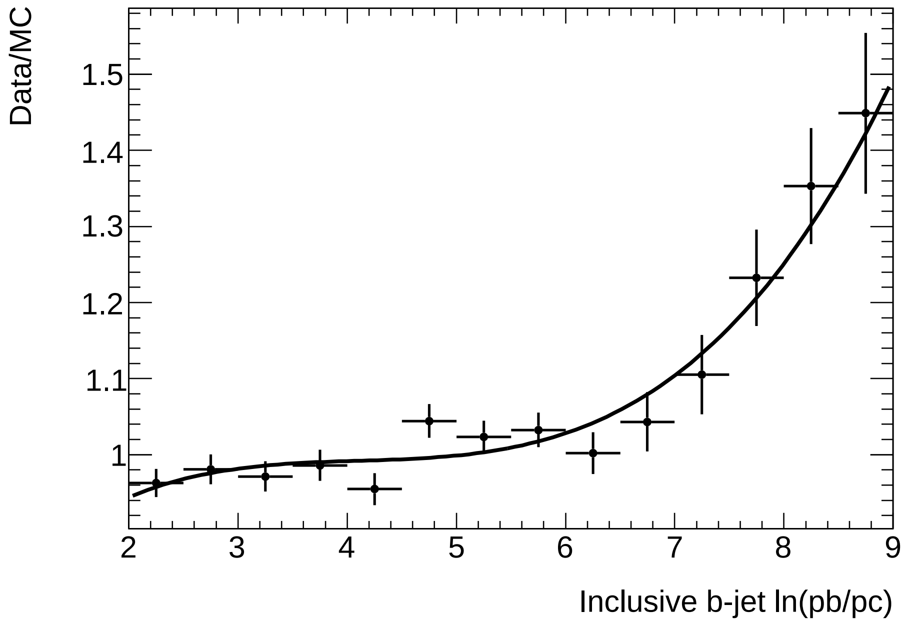

Figure 13: Inclusive b-jet top pair control region data/MC ratio of $\ln(pb/pc)$ fitted with a third order polynomial.

6 Data - Monte Carlo comparison

This Section shows a comparison between the data and Monte Carlo for several important kinematic distributions. The comparison is made between the data and Monte Carlo with the standard k-factors and CP group smearing and scale factors, and and reweighting of B-hadron decays described in Section 5. It is known that the Alpgen+Herwig Z+jets simulation underestimates the heavy flavour contribution, but no corrections are applied here, in order to give a sense of the scale of the issue.

Applying all selections up to and including the Z boson mass cut, kinematic variables of the Z boson are plotted in Fig. 14, separately for the electron and muon decay channels. For these plots, no requirements are made on number of jets and $E_{\mathrm{T}}^{\mathrm{miss}}$. Note that no multijet background is included here, which can lead to an excess of data over Monte Carlo. The multijet background is derived in a data-driven way in Section 7. This background is known to be larger for the electron than it is for the muon channel.

Additionally applying the $E_{\mathrm{T}}^{\mathrm{miss}}$ cut, the jet multiplicity is shown in Fig. 15. Requiring at least one jet, the multiplicity of tagged jets is shown in the same Figure. The transverse momentum and rapidity of tagged jets in the sample with at least 1 tagged jet are shown in Fig. 16. For the sample containing at least two b tagged jets, the transverse momentum of the leading and sub-leading b jet as well as their rapidities are presented in Fig. 17. Again, the Monte Carlo heavy flavour prediction is taken “out of the box”, with no additional scaling.

Fig. 18 shows the distributions used in the differential $Z + bb$ measurement with the same binning as used in the fit. q The fit variables used in the two analyses are displayed in Fig. 19. All flavour combinations are shown individually as they are implemented in the signal MC. Parts (a) and (b) show the leading b jet $\ln(pb/pc)$ distribution in the sub-sample with at least one b tagged jet, parts (c) and (d) the sum of the $\ln(pb/pc)$ values for the two b jets with highest p_{T} in the sub-sample with at least two b tags.

It can be seen throughout that the Monte Carlo underestimates the heavy flavour contribution to the data sample. It can also be see (for example in Fig. 15 (c) and (d), and Fig. 18) that there is a difference in the data-MC agreement for double-tagged events in the electron and muon channels. This is investigated in detail in Appendix B.

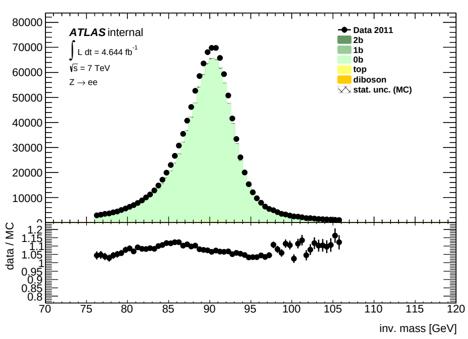

(a)

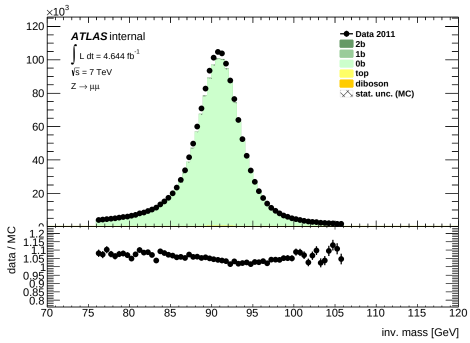

(b)

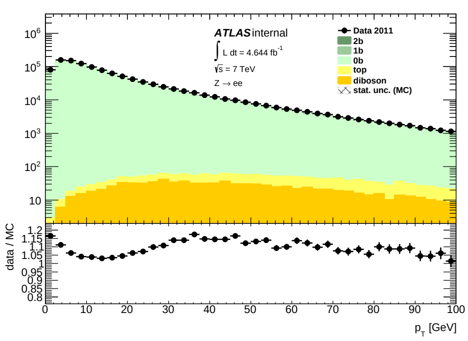

(c)

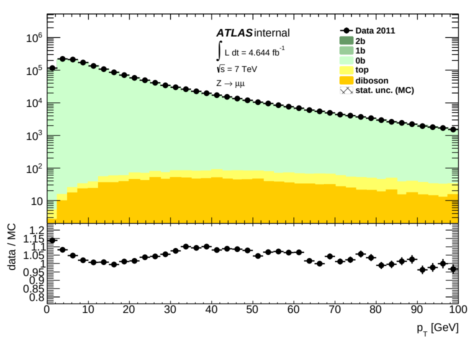

(d)

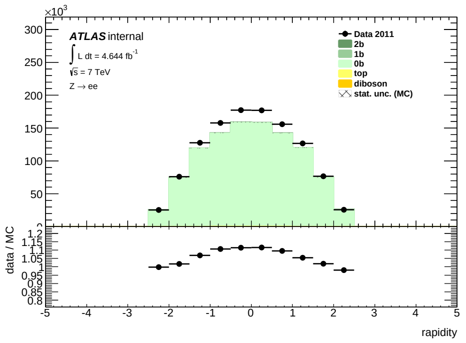

(e)

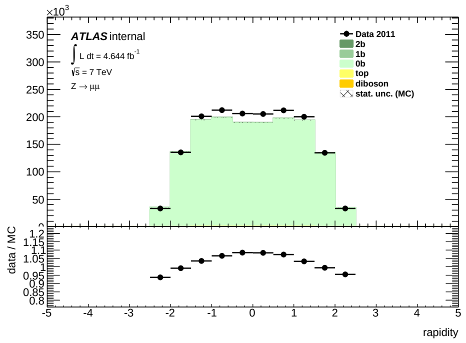

(f)

Figure 14: Kinematic distributions of the Z boson in electron and muon decay channel. Shown are Z mass, p_{T}, and y. No jet requirements or MEt cut are applied.

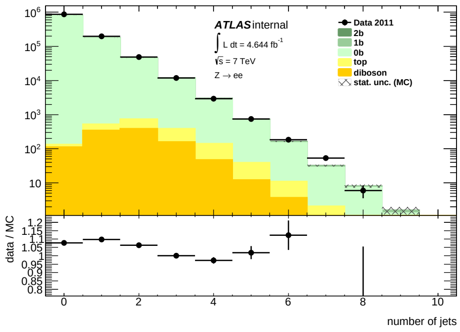

(a)

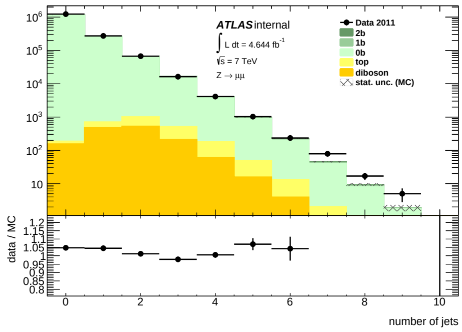

(b)

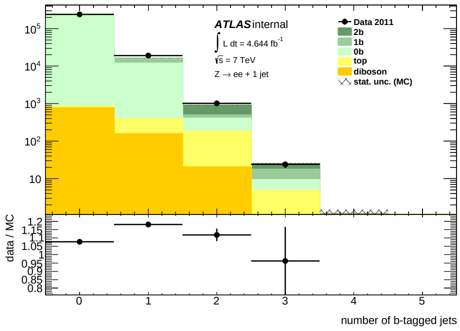

(c)

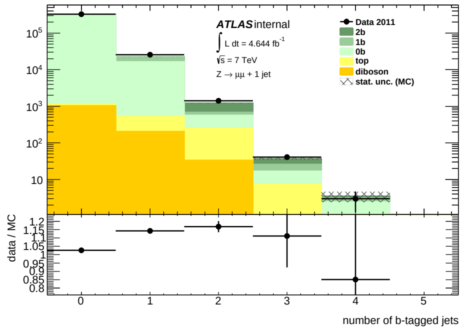

(d)

Figure 15: Inclusive jet multiplicity (a-b) and tagged jet multiplicity in the sub-sample with at least one jet (c-d).

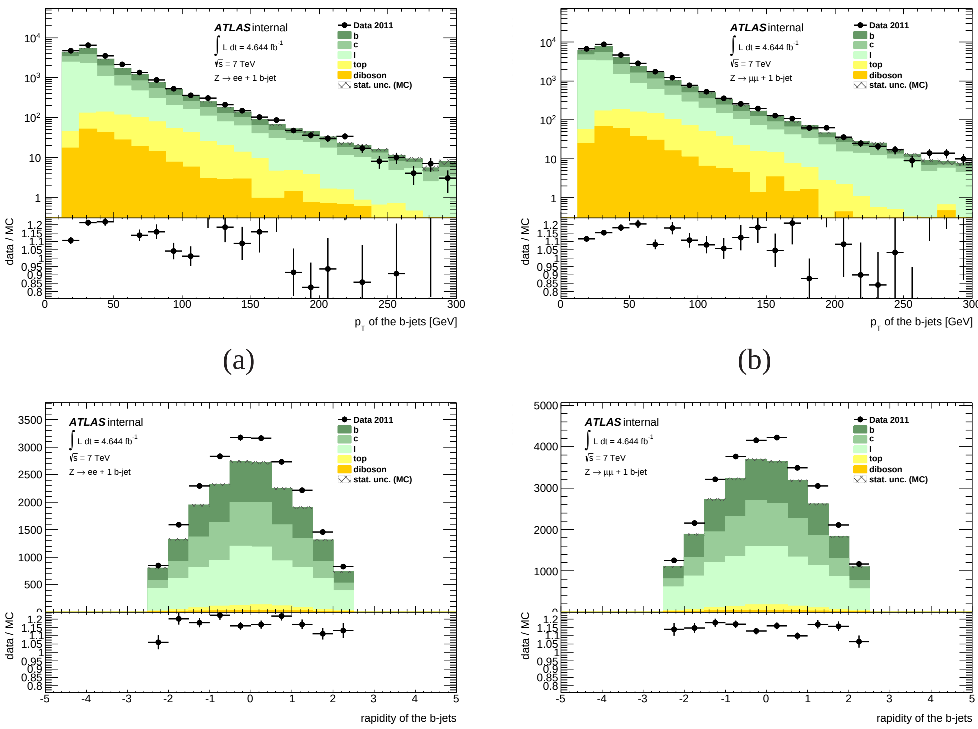

(a) (b)

(c) (d)

Figure 16: Transverse momentum (a-b) and rapidity (c-d) of tagged jets for the sample with at least one tagged jets, shown for the electron and muon channel separately.

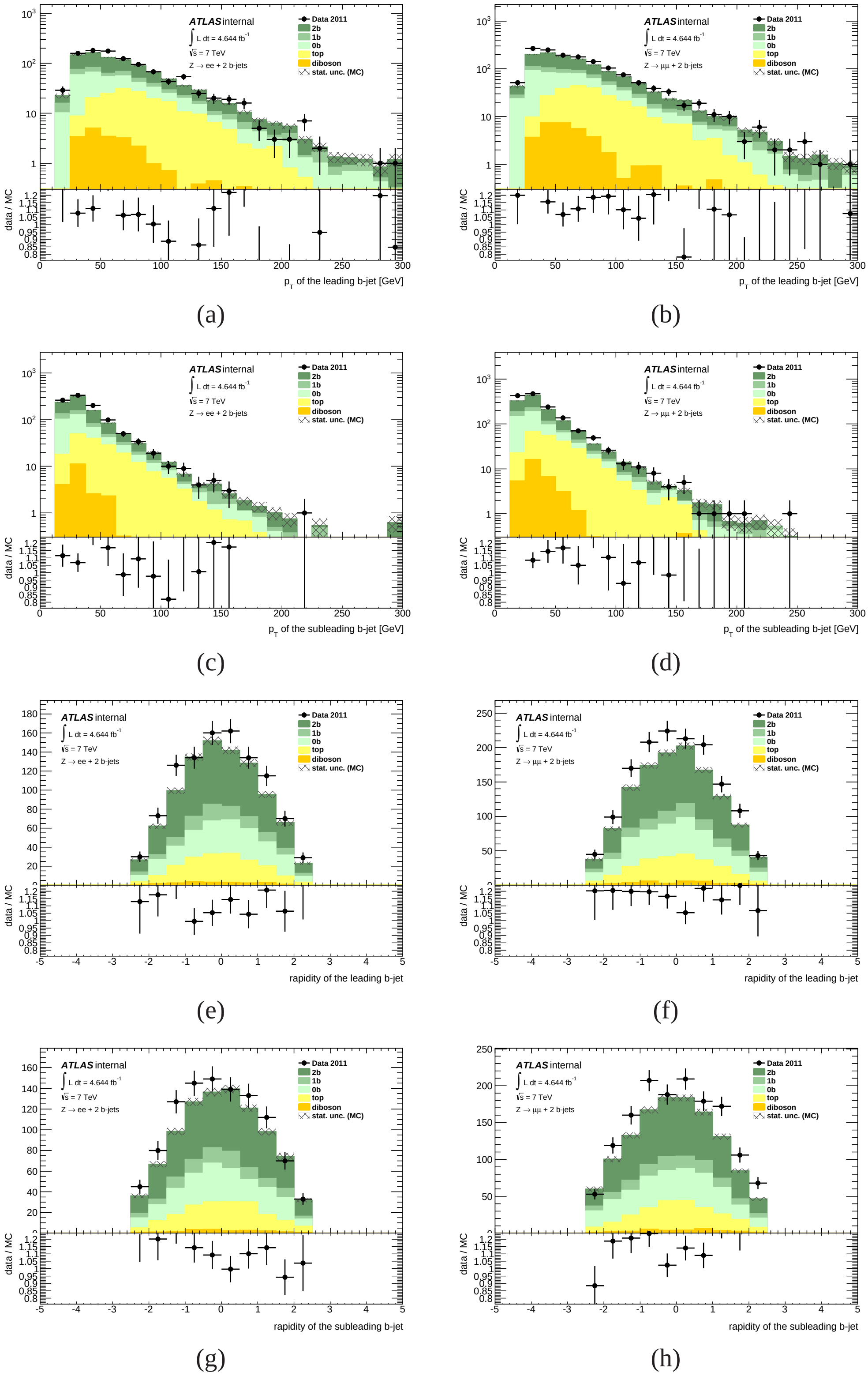

Figure 17: Transverse momentum leading and sub-leading tagged jet (a-d) and rapidity for the leading and sub-leading jets (e-h) for the sample with at least two tagged jets, shown in the electron and muon channels.

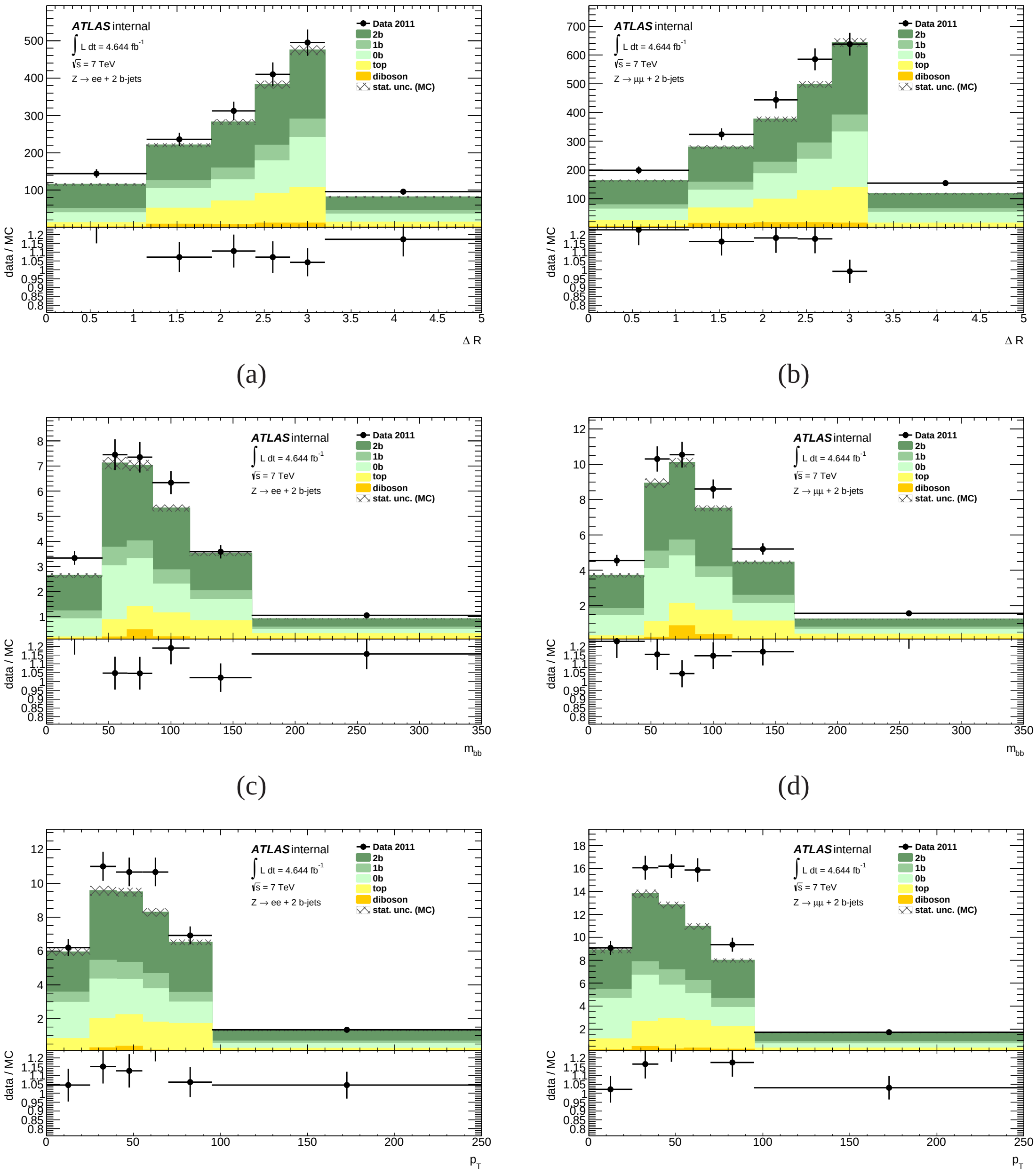

(a) (b) (c) (d) (e) (f)

Figure 18: Distributions of the variables in which the differential $Z + bb$ measurement is performed.

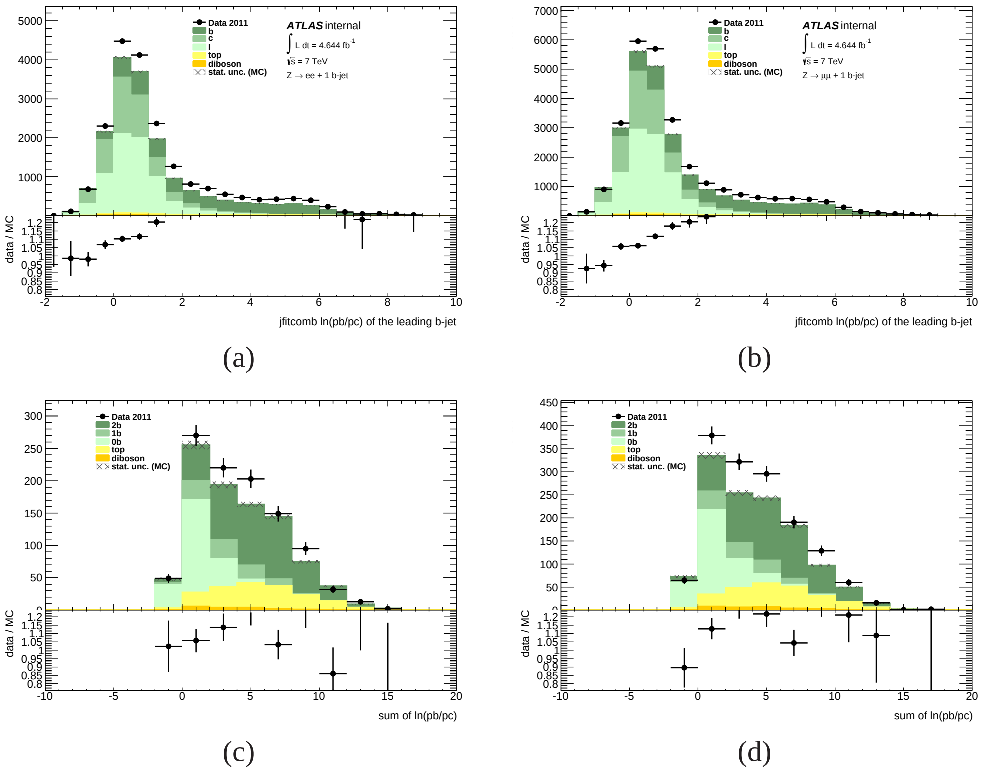

Figure 19: Variables used in determining the flavour composition. (a,b) show $\ln(pb/pc)$ of b-tagged jets in the sub-sample with at least 1 b tag required. (c,d) show the sum of the $\ln(pb/pc)$ values for the sub-sample selected by requiring 2 b tags. The various jet flavour templates are individually shown using the normalisation from the Monte Carlo, before the fit is performed.

7 Backgrounds

7.1 Determination of multijet background in the Zb and Zbb selection

The contamination from multi-jet events in the inclusive Zb selection and in the Zbb selection is estimated with a data driven method. The motivations for this choice are the limited statistics of the available simulated background samples and the uncertainty on the modeling of the rate of misidentification of jets as leptons.

The procedure uses the shape of the di-lepton invariant mass to discriminate the multi-jet background from the signal and the other physics processes with at least one real lepton passing the selection. For each lepton channel ($l = e, \mu$) the shape of the overall distribution, after all cuts are applied, can be modeled with

$$M(m_{ll}; \alpha_l, N_{\overline{mj},l}, N_{mj,l}) = N_{\overline{mj},l}\, g_l(m_{ll}) + N_{mj,l}\, f(m_{ll}; \alpha_{l,j}) \quad (1)$$

where the $g_l(m_{ll})$ represents the normalized distribution of the signal and non multi-jet background events, $f(m_{ll}; \alpha_l)$ is the normalized distribution for the multi-jet events and $N_{\overline{mj},l}$ and $N_{mj,l}$ are the number of events in the two samples. The distribution of the signal and non multi-jet events is estimated from MC simulations, relying on the simulated lineshape modeling and on the relative aboundances of the various processes which are summed in a single template with unitary normalization. The shape of the fake di-lepton invariant mass in multi-jet events (analitic expression and parameters $\alpha_{l,j}$) is derived from a fit to data in a control region, defined as a sample of events selected with criteria similar to those defining the selection but not overlapping with the selection and enriched of multi-jet background events. It has been observed that a suitable analitic expression for the shape of the invariant mass of multi-jet events $f(m_{ll}; \alpha_l)$ is an exponentially decaying function with decay parameter α_l. The exponential modeling was verified to be valid in several control regions with different background contaminations that will be described later.

The number of multi-jet events passing the selection $N_{mj,l}$ is obtained by fitting the observed m_{ll} distribution in data with equation 1. In the fit the total number of signal and non multi-jet background events $N_{\overline{mj},l}$ is also treated as a free parameter.

The selection of the background enriched control regions, the determination of the shape of the multi-jet background and the extraction of the background normalization are described in the following for the two lepton channels.

7.1.1 Electron channel control regions

A multi-jet enriched Z+jets control region is obtained by applying all event and object selection requirements described in section 4, with the exception of the b-tagging, and with the following different criteria:

- the e^+e^- invariant mass range is 70-120 GeV;
- one of the two electrons is an object in the electron container not satisfying the *egammaPID* :: *ElectronMediumPP* quality criterion.

The selection was applied to events pre-selected online by a single electron trigger with a transverse energy threshold of 20 GeV (`EF_e20_medium`). This trigger was unprescaled only in the first part of the 2011 data set for an integrated luminosity of 1.7 fb − 1. The b-tagging request was not applied in order to have a large statistics and because the flavor of the third jet is not expected to impact on the shape of the invariant mass built with two jets identified as electrons.

The e^+e^- invariant mass distribution obtained in the control sample is shown in Fig. 20(a). The same selection is applied to simulated samples of non multi-jet events that can contribute to the selection with

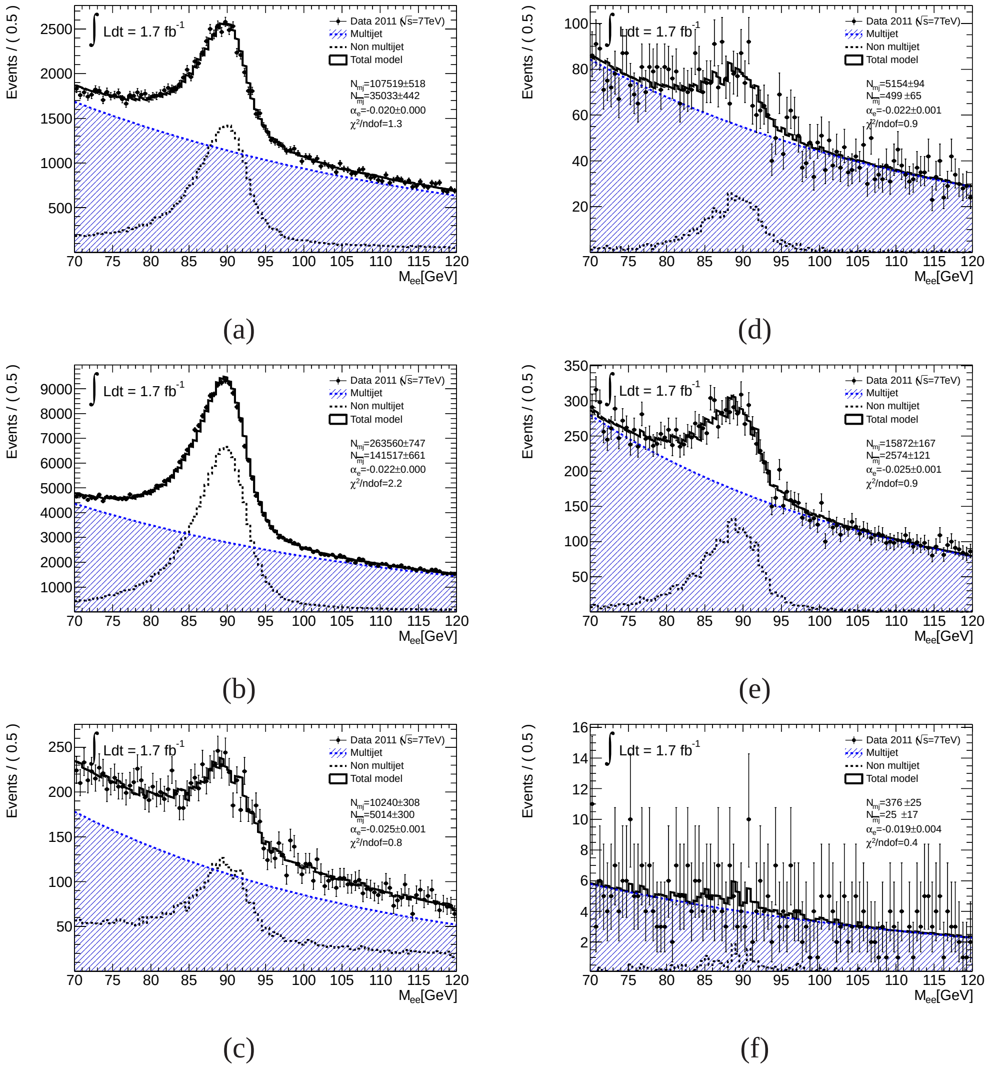

Figure 20: Invariant mass fit in the multi-jet enriched nominal control region for the electron channel (a), corresponding to a Z+jets selection, in a wider control region (b), corresponding to an inclusive Z selection, and in a region with a Z and one b-tagged jet (c). The fit results in a variation of the selections above with both electrons failing the *MediumPP* quality requirement but satisfying the *LoosePP* criterion: Z+jets (d), inclusive Z (e) and Z+b-tagged jet (f) selection.

Control region	α	$N_{\overline{mj}}$	N_{mj}
Z+jets, $(M, \overline{M})$	-0.020 ± 0.001	35033 ± 442	107519 ± 518
Z+jets, $(L_{\overline{M}}, L_{\overline{M}})$	-0.022 ± 0.001	499 ± 65	5154 ± 94
Z, $(M, \overline{M})$	-0.022 ± 0.000	141517 ± 661	263560 ± 748
Z, $(L_{\overline{M}}, L_{\overline{M}})$	-0.025 ± 0.001	2574 ± 121	15872 ± 167
Z+b-jet, $(M, \overline{M})$	-0.025 ± 0.001	5014 ± 300	10240 ± 308
Z+b-jet, $(L_{\overline{M}}, L_{\overline{M}})$	-0.019 ± 0.004	25 ± 17	376 ± 25

Table 11: Results of the fit to the e^+e^- invariant mass in various multi-jet enriched control regions: decay constant and normalization of multi-jet and non multi-jet event samples. The notation (Q, Q') refers to the identification quality requirements satisfied by the two electrons in the pair: M = MediumPP, $\overline{\text{M}}$ = electron failing MediumPP and $\text{L}_{\overline{\text{M}}}$ = LoosePP but not MediumPP.

Control region	Data	Z	$t\bar{t}$	Di-boson	single-top
Z+jets, $(M, \overline{M})$	142552.0	35558.6	6855.7	7181.7	1298.0
Z+jets, $(L_{\overline{M}}, L_{\overline{M}})$	5653.0	778.2	14.7	20.5	3.1
Z, $(M, \overline{M})$	405077.0	168289.9	7391.2	7780.4	1539.6
Z, $(L_{\overline{M}}, L_{\overline{M}})$	18446.0	3912.2	15.6	22.7	3.4
Z+b-jet, $(M, \overline{M})$	15254.0	1923.9	3511.2	3553.4	653.4
Z+b-jet, $(L_{\overline{M}}, L_{\overline{M}})$	401.0	40.5	7.4	9.0	1.9

Table 12: Composition, according to simulation, of the non multi-jet contribution to the selections for the various control regions. The notation (Q, Q') is defined in table 11. The sum of the non multi-jet contributions predicted by the MC is consistent with the overall normalization from the fit to the the data reported in 11.

real leptons. The data are well described by the sum of the various non-multijet contributions (from production of Z, top and pairs of gauge bosons), with total normalization adjusted to the data in the fit, and an exponentially decaying distribution, which represents the contribution of multi-jet events to the control sample, with normalization and decay parameter obtained from the fit to the data. An inclusive Z selection, where the electrons satisfy the same quality requirements as in the control region has been studied. The invariant mass distribution obtained and the fit, with the sum of the exponential distribution and the non multi-jet backgrounds, are reported in Fig. 20(b). The robusteness of the exponential modeling and the stability of the parameter α_e were tested by studying an alternative multi-jet enriched control sample,with a larger contamination. This was obtained by selecting both electrons as passing the *LoosePP* electron identification criteria but failing the *mediumPP* requirement. The invariant mass distribution and the fit obtained in the Z+jets selection and in the inclusive Z selection are shown in Fig.s 20(d) and 20(e) respectively. As a cross check, a third control region was derived from the nominal one, after requiring that the jet is b-tagged. The low statistics distributions of the di-electron invariant mass are shown in Fig.s 20(c) and 20(f). They show that in a b-jet enriched sample of multi-jet events faking the signal, the slope of the exponentially decaying background is stable with respect to a sample dominated by light jets.

The results of the fit are summarized in table 11, while table 12 shows the contributions of non multi-jet events in the background enriched selections as predicted by the simulation.

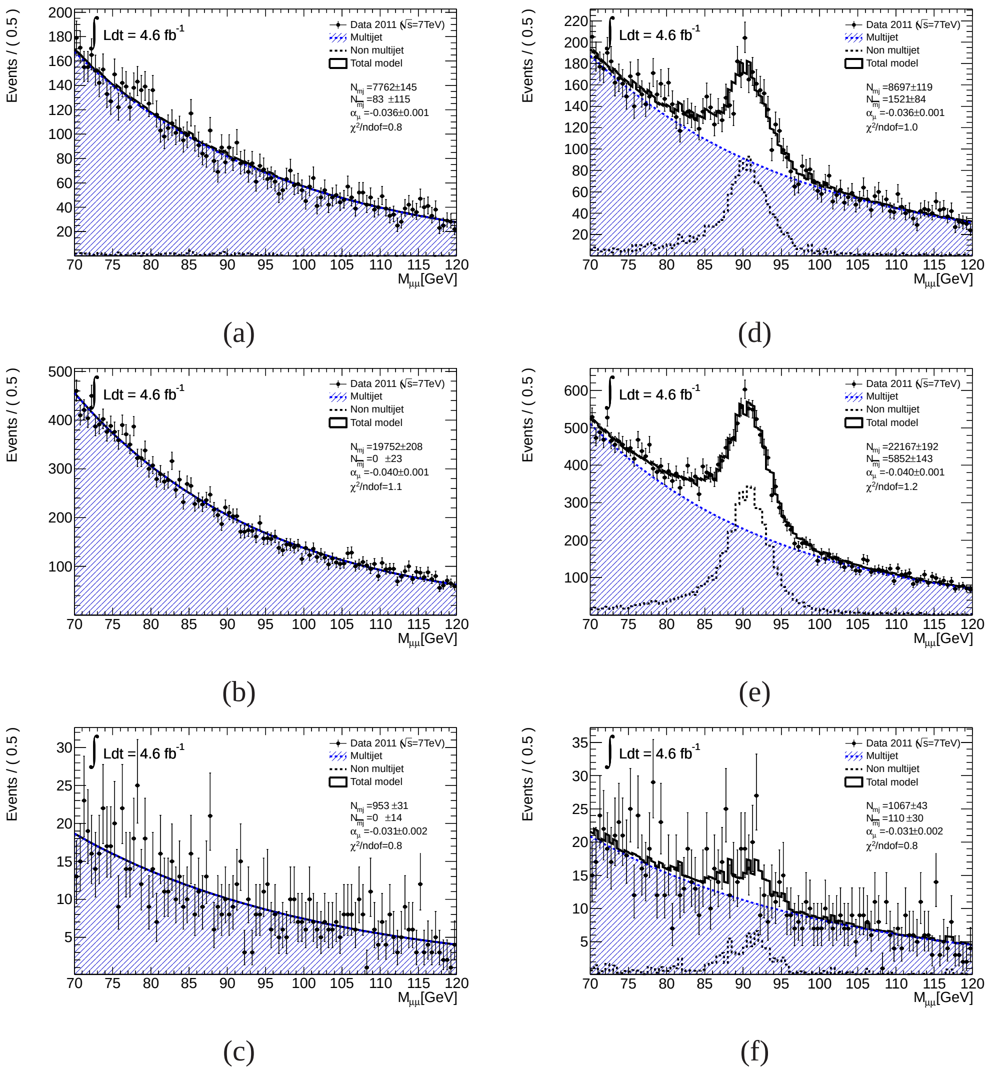

Figure 21: Invariant mass fit in the multi-jet enriched nominal control region for the muon channel (a), corresponding to a Z+jets selection, in a wider control region (b), corresponding to an inclusive Z selection, and in a region with a Z and a b-tagged jet (c). The fit results in a variation of the selections above based on quasi anti-solated muons: Z+jets (d), inclusive Z (e) and Z+b-tagged jet (f) selection.

Control region	α	$N_{\overline{mj}}$	N_{mj}
Z+jets, anti-Iso	-0.036 ± 0.001	83 ± 115	7762.4 ± 144.7
Z+jets, quasi anti-Iso	-0.036 ± 0.001	1520.7 ± 84.1	8698 ± 119
Z, anti-Iso	-0.040 ± 0.001	0.0 ± 22.6	19752.0 ± 208
Z, quasi anti-Iso	-0.040 ± 0.001	5852.1 ± 143.0	22167 ± 192
Z+b-jet, anti-Iso	-0.031 ± 0.002	0.0 ± 14	953.0 ± 30.9
Z+b-jet, quasi anti-Iso	-0.031 ± 0.002	110.0 ± 29.8	1066.9 ± 43.0

Table 13: Results of the fit to the $\mu^+\mu^-$ invariant mass in various multi-jet enriched control regions: decay constant and normalization of multi-jet and non multi-jet event samples.

Control region	Data	Z	$t\bar{t}$	Di-boson	single-top
Z+jets, anti-Iso	7845.0	30.5	11.3	0.2	2.0
Z+jets, quasi anti-Iso	10219.0	1140.3	32.4	45.7	6.6
Z, anti-Iso	19752.0	90.0	12.0	0.5	2.5
Z, quasi anti-Iso	28019.0	4525.7	34.2	7.6	48.8
Z+b-jet, anti-Iso	953.0	2.1	3.6	0.2	0.2
Z+b-jet, quasi anti-Iso	1177.0	68.4	15.0	0.9	2.3

Table 14: Composition, according to simulation, of the non multi-jet contribution to the selections for the various control regions in the muon channel. The sum of the non multi-jet contributions predicted by the MC is consistent with the overall normalization from the fit to the the data reported in 13.

7.1.2 Muon channel control regions

In the muon channel a multi-jet enriched control region can be obtained by reverting the isolation requirement. In particular, the Z+jets selection applied to fit the shape of the $\mu^+\mu^-$ invariant mass distribution from multi-jet events differs from the nominal selection, described in section 4, for these features:

- as in the electron channel, the $\mu^+\mu^-$ invariant mass range is 70-120 GeV;
- the muons are not required to satisfy impact parameter cuts;
- both the muons are anti-isolated, i.e. $\Sigma p_{\mathrm{T}}(ID)/p_{\mathrm{T}} > 0.1$.

Also in this case, an inclusive Z selection based on the same muon definition was studied in addition to the Z+jets selection defined above. Similarly, a low-statistic cross check was performed, by selecting the sub-sample of the nominal control region with the jet tagged as b-jet. The selections have a large multi-jet contamination and very small contribution from processes with real leptons. An exponentially decaying distribution provides a suitable description of the contribution to the di-muon invariant mass from multi-jet events, also in the muon channel, as shown in Fig. 21(a), 21(b) and 21(c). The distribution is fit, as in the electron channel, to the sum of the MC templates for the non multi-jet processes with floating total normalization, and the exponential function with decay constant and normalization free in the fit. In order to check the consistency of the multi-jet m_{ll} shape in a sample much closer to the standard signal selection, a new multi-jet enriched selection has been defined for the three selections of inclusive Z, Z+jets and Z+b-tagged jets. The features of the di-muon pair in this case are:

- $70 < M_{\mu^+\mu^-}(GeV) < 120$ and no impact parameter cuts;
- both the muons are quasi anti-isolated, i.e. $\Sigma p_{\mathrm{T}}(ID)/p_{\mathrm{T}} > 0.01$.

The invariant mass distribution obtained with this selection is reported in Fig. 21(d), 21(e) and 21(f) for the Z+jets, inclusive Z and Z+b-tagged jet respectively. In all cases the fit is reliable and the results summarized in table 13, show that the determination of the slope of the multi-jet invariant mass spectrum is stable with the background level and flavor composition. Table 14 shows the predicted non multi-jet contributions in the various control regions.

7.2 Multi-Jet background estimates in the Zb and Zbb signal region

The slope parameter α_l measured in the control region for each lepton channel is used to define the multi-jet model in a fit to the invariant mass distribution in the signal region. The fit to the di-lepton distributions from the nominal selection are shown, for both lepton channels, in Fig. 22 for the sample of events with one or more jets tagged as b-jets (top), the sample with at least two b-tags (center) and finally the sample of events with two jets passing the selection and only one of them passing the b-tagging requirement (bottom). The contamination of multi-jet events in the inclusive b-jet + Z selection is found to be very small (of the order of 1% of the non multi-jet selected events) and in the double tag selection it is found to be negligible. The method allows to derive the normalization of this background on the whole sample of events selected with a relative error close to 100%. All the results are summarized in table 15. Repeating the fit with variations of the value of the α_l parameter obtained from different control regions, has been shown to lead to negligible differences in the value of $N_{mj,l}$ (a few percents) with respect to the statistical error.

An attempt to fit the multi-jet background contribution in each bin of the analysis, e.g. in bins of b-jet p_{T}, as been done. The results are shown in figures 23 and 24 for the electron and muon channels, respectively. They are consistent, affected by rather large fluctuations, due to the very low statistics. However, within the statistical errors, the ratio between the multi-jet contamination and the non-multijet events passing the selection appers to be constant over the entire range of the variables studied.

Therefore, in each bin of the Zb inclusive selection, the final estimate of the number of multi-jet events will use the fit result in the total signal region to determine the overall fractional multi-jet background contamination.

To cover the systematic uncertainties from the choice of the control region or from the stability of the shape of the exponential model for the multi-jet background and to account for the statistical error on the final background normalization a 100% systematic uncertainty will be assigned to the fractional rate of multi-jet events.

Finally, a template for the distribution of the b-flavor discriminant $\ln(pb/pc)$ in multi-jet background events must be determined from data and used as input for the b-jet yeld extraction. The selection that has been used to derive the $\ln(pb/pc)$ distribution is based on the selection of the control region with the addition of the requirement that one jet is tagged as b-jet. In the muon case, both leptons are anti-isolated; in the electron channel, both leptons are failing the MediumPP criteron. The templates obtained for both lepton channels are shown in figure 25.

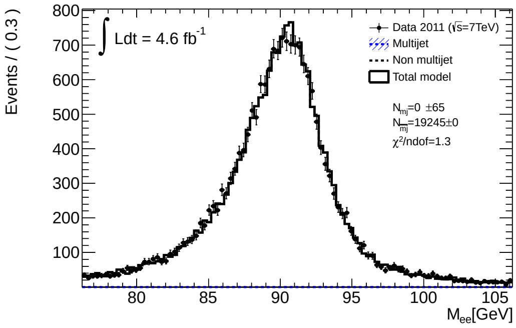

(a)

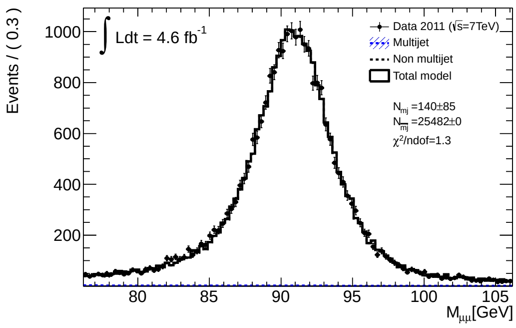

(b)

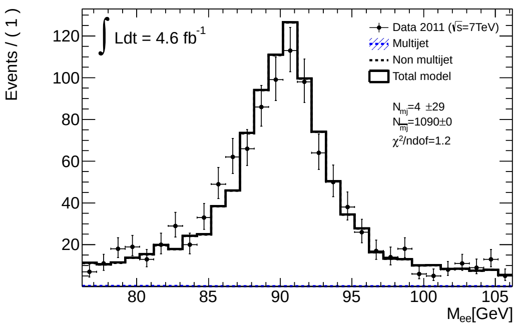

(c)

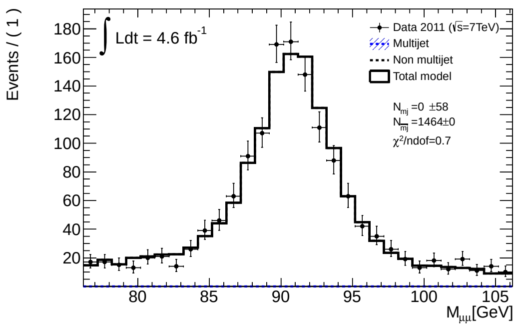

(d)

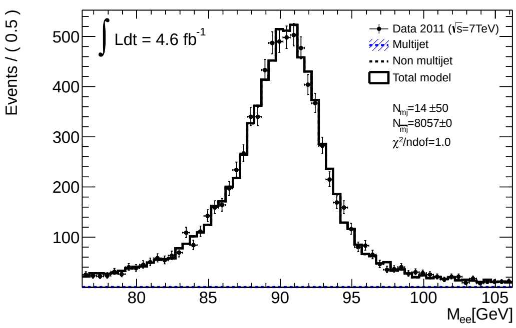

(e)

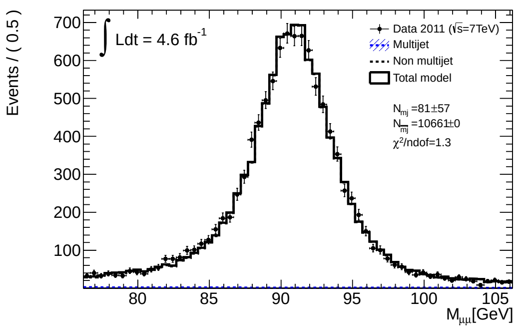

(f)

Figure 22: Extraction of the multi-jet background in the signal regions, corresponding to the nominal selection, from the fit to the di-lepton invariant mass: inclusive Zb selection (a and b), and Zbb selection (c and d). Plots on the left refer to the electron channel and plots on the right refer to the muon channel. The control sample corresponding to the selection of a Z, one b-jet and a second jet failing the b-tagging selection are shown in (e) and (f).

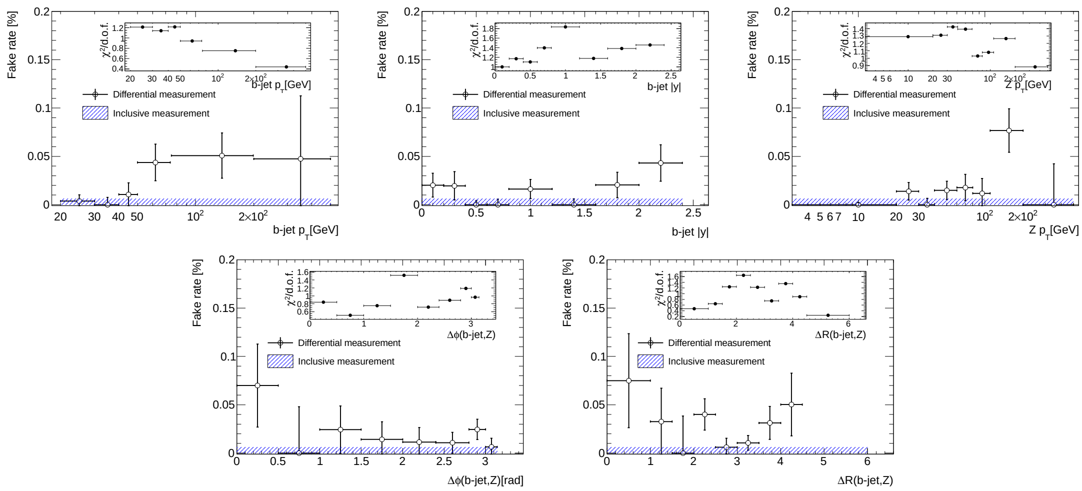

Figure 23: The results of the QCD background estimate fits in the signal regions in bins of observables studied in the analysis, for the electron channel. The histogram shows the result of a fit to the whole signal region.

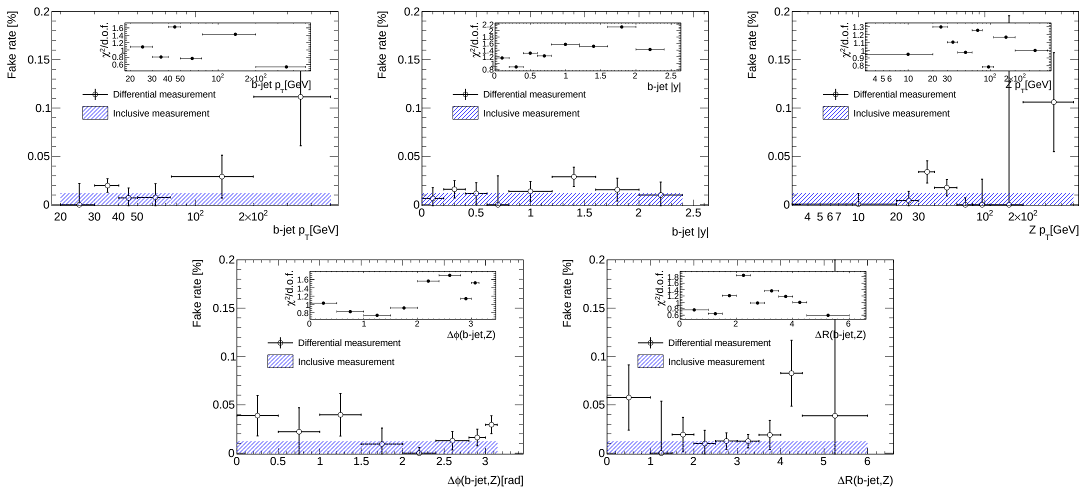

Figure 24: The results of the QCD background estimate fits in the signal regions in bins of observables studied in the analysis, for the muon channel. The histogram shows the result of a fit to the whole signal region.

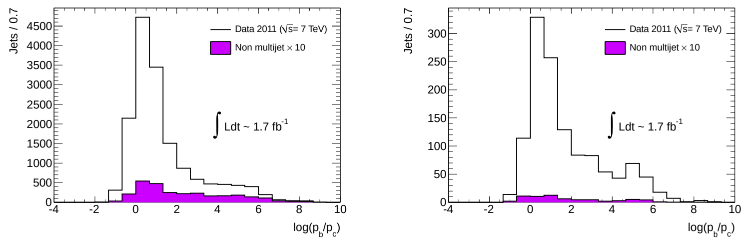

(a) (b)

Figure 25: The $\ln(pb/pc)$ template from multi-jet events as obtained from a modified control region demanding at least one tagged jet, for the electron (a) and muon (b) channel.

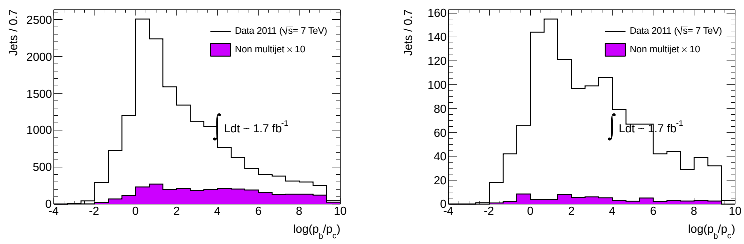

(c) (d)

Figure 26: The $\ln(pb/pl)$ template from multi-jet events as obtained from a modified control region demanding at least one tagged jet, for the electron (c) and muon (d) channel.

selection	α_e	$N_{\overline{mj},e} \pm \sigma(N_{\overline{mj},e})$	$N_{mj,e} \pm \sigma(N_{mj,e})$
≥ 1 b-tag	−0.020 ± −1.000	19244.5	0.0 ± 65.0
≥ 1 b-tag	−0.022 ± −1.000	19244.5	0.0 ± 62.7
≥ 1 b-tag	−0.025 ± −1.000	19244.5	0.0 ± 59.5
≥ 1 b-tag	−0.019 ± −1.000	19244.5	0.0 ± 66.4
≥ 2 b-tags	−0.020 ± −1.000	1089.7	4.4 ± 28.6
≥ 2 b-tags	−0.022 ± −1.000	1089.7	4.6 ± 27.5
≥ 2 b-tags	−0.025 ± −1.000	1089.7	4.9 ± 25.8
≥ 2 b-tags	−0.019 ± −1.000	1089.7	4.4 ± 29.3
1 b-tag and ≥ 2 jets	−0.020 ± −1.000	8057.3	14.2 ± 49.7
1 b-tag and ≥ 2 jets	−0.022 ± −1.000	8057.3	12.9 ± 49.8
1 b-tag and ≥ 2 jets	−0.025 ± −1.000	8057.3	11.1 ± 56.6
1 b-tag and ≥ 2 jets	−0.019 ± −1.000	8057.3	14.8 ± 49.6
selection	α_μ	$N_{\overline{mj},\mu} \pm \sigma N_{\overline{mj},\mu}$	$N_{mj,\mu} \pm \sigma N_{mj,\mu}$
≥ 1 b-tag	−0.036 ± −1.000	25482.2	140.1 ± 85.3
≥ 1 b-tag	−0.036 ± −1.000	25482.2	140.1 ± 85.3
≥ 1 b-tag	−0.031 ± −1.000	25482.2	135.4 ± 86.3
≥ 1 b-tag	−0.031 ± −1.000	25482.2	135.4 ± 86.3
≥ 2 b-tags	−0.036 ± −1.000	1463.9 ± 0.0	0.0 ± 58.1
≥ 2 b-tags	−0.036 ± −1.000	1463.9 ± 0.0	0.0 ± 58.1
≥ 2 b-tags	−0.031 ± −1.000	1463.9 ± 0.0	0.0 ± 85.2
≥ 2 b-tags	−0.031 ± −1.000	1463.9 ± 0.0	0.0 ± 85.2
1 b-tag and ≥ 2 jets	−0.036 ± −1.000	10661.1 ± 0.0	80.8 ± 57.3
1 b-tag and ≥ 2 jets	−0.036 ± −1.000	10661.1 ± 0.0	80.8 ± 57.3
1 b-tag and ≥ 2 jets	−0.031 ± −1.000	10661.1 ± 0.0	77.8 ± 58.0
1 b-tag and ≥ 2 jets	−0.031 ± −1.000	10661.1 ± 0.0	77.8 ± 58.0

Table 15: Estimate of the multi-jet background contamination of the sample of events passing the nominal selection, in both lepton channels.

8 Extraction of differential Zb yields

8.1 Flavour fit in the Zb analysis

The reconstruction-level criteria detailed in table 4 are used to select a sample of events with a Z boson candidate and at least one tagged jet (passing the MV1 cut at 75% efficiency). The number of b-jets, N_b and the number of events with a Z boson and a b jet, N_{Zb} are extracted from the data using flavour template fits to a variable which shows good flavour separation. An extended maximum likelihood binned fit using Roofit is used. For jet-level observables, all tagged jets enter the flavour templates. For event-level distributions, the leading (in p_{T}) tagged jet is used in the flavour templates.

The jet-level variable $\ln(p_b/p_c)$ is used as the baseline flavour discriminant. This variable was found to give the best precision on N_b compared to e.g. SV0 mass, used in the 2010 analysis. This precision is attributed to the low correlation (around 20-25%) of the *beauty* template with the *light* and *charm* templates. Two dimensional combinations of variables (e.g. $\ln(p_b/p_c)$ vs $\ln(p_b/p_u)$) were also studied, but did not yield superior results and tended to be slightly less stable especially when looking at differential fits in e.g. b-jet p_{T}.

A feature of the $\ln(p_b/p_c)$ discriminant is that the *light* and *charm* templates are almost entirely correlated ($> 98\%$) and so in the default fit, the *charm* and *light* flavour templates are combined. Thus the two variables floated free in the fit are the *beauty* and the (*charm* + *light*) template normalisations, where the flavour of the template is determined using the last criteria shown in table 4 (i.e. only the b-jet flavour definition is used). The QCD multi-jet background is subtracted from data for each distribution using the estimation provided by the method detailed in Section 7.1. The other backgrounds are taken from MC normalised according to table 3.

For the central results, the electron and muon channels are first combined for each distribution by simply adding the two sets of data, flavour templates and backgrounds together. The procedure is shown to improve the statistical precision and is robust against systematic effects related to flavour discriminant shapes and unfolding. A cross-check of the individual electron and muon channels is also performed and gives consistent yields. Two independent analyses are used to check the yield results and the agreement is in general at the per mille and better than 0.5% in all bins.

The combined data are compared to MC after the template fit results have been used to alter the normalisation of the *beauty* and *charm* + *light* templates, for all of the differential bins of the analysis, in figures 27 to 34.

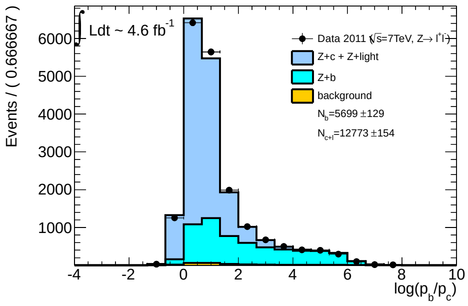

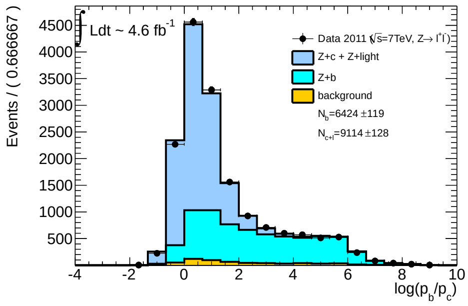

(a) (b)

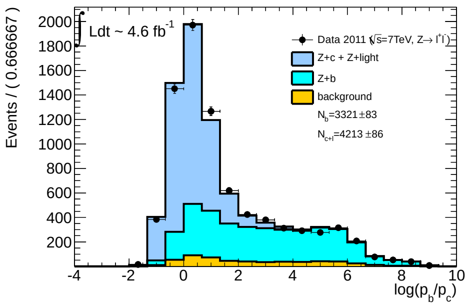

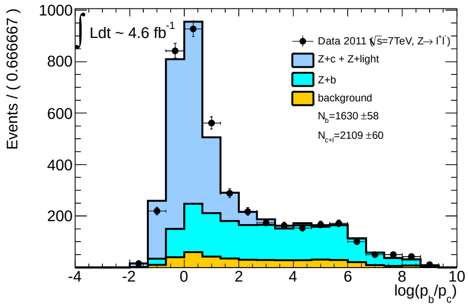

(c) (d)

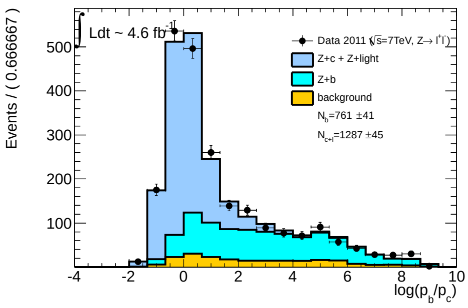

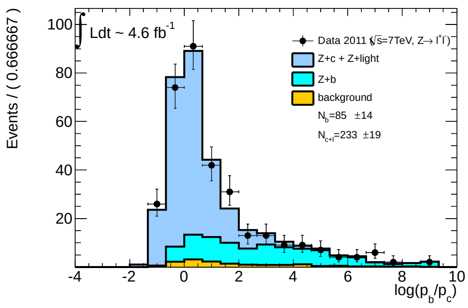

Figure 27: Flavour fit in the bins 20 ≤b-jet p_{T}[GeV]< 30 (a), 30 ≤b-jet p_{T}[GeV]< 50 (b), 50 ≤b-jet p_{T}[GeV]< 75 (c), 75 ≤b-jet p_{T}[GeV]< 110 (d), 110 ≤b-jet p_{T}[GeV]< 200 (e) and 200 ≤b-jet p_{T}[GeV]≤ 500 (f).

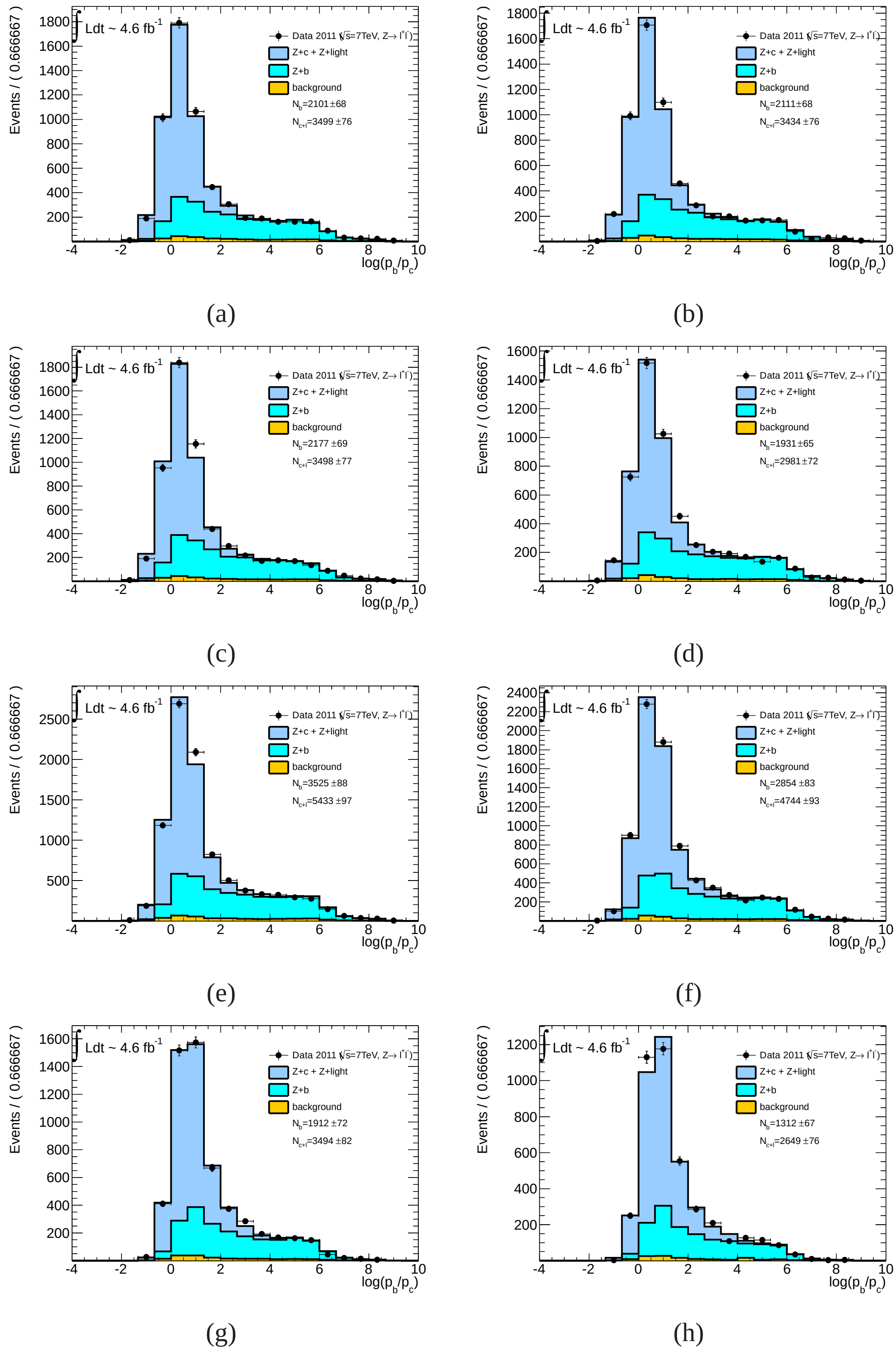

Figure 28: Flavour fit in the bins 0 ≤b-jet $|y| < 0.2$ (a), 0.2 ≤b-jet $|y| < 0.4$ (b), 0.4 ≤b-jet $|y| < 0.6$ (c), 0.6 ≤b-jet $|y| < 0.8$ (d), 0.8 ≤b-jet $|y| < 1.2$ (e), 1.2 ≤b-jet $|y| \leq 1.6$ (f), 1.6 ≤b-jet $|y| \leq 2.0$ (g) and 2.0 ≤b-jet $|y| \leq 2.4$ (h).

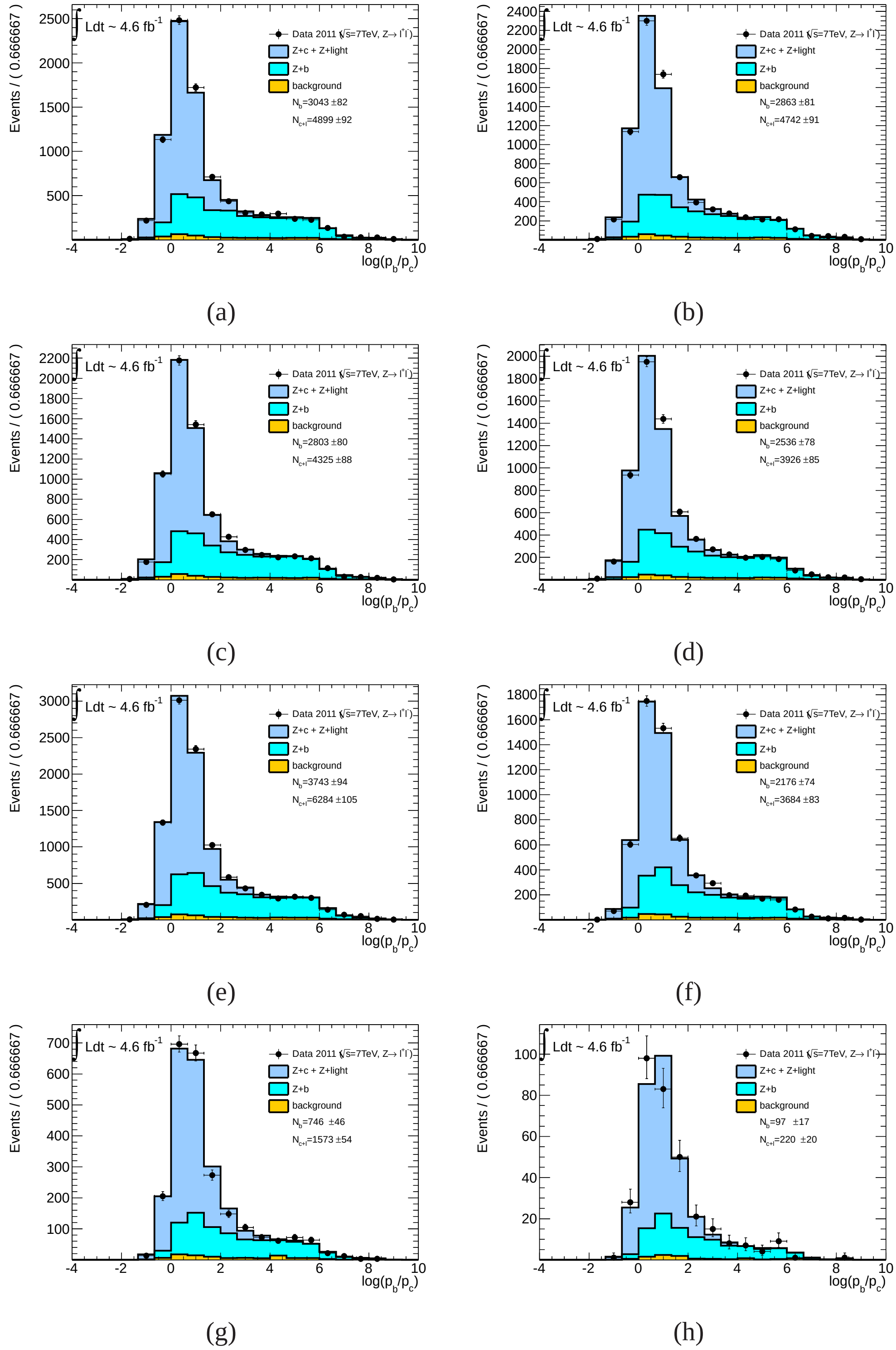

Figure 29: Flavour fit in the bins $0 \leq y^{\star} < 0.2$ (a), $0.2 \leq y^{\star} < 0.4$ (b), $0.4 \leq y^{\star} < 0.6$ (c), $0.6 \leq y^{\star} < 0.8$ (d), $0.8 \leq y^{\star} < 1.2$ (e), $1.2 \leq y^{\star} \leq 1.6$ (f), $1.6 \leq y^{\star} \leq 2.0$ (g) and $2.0 \leq y^{\star} \leq 2.5$ (h).

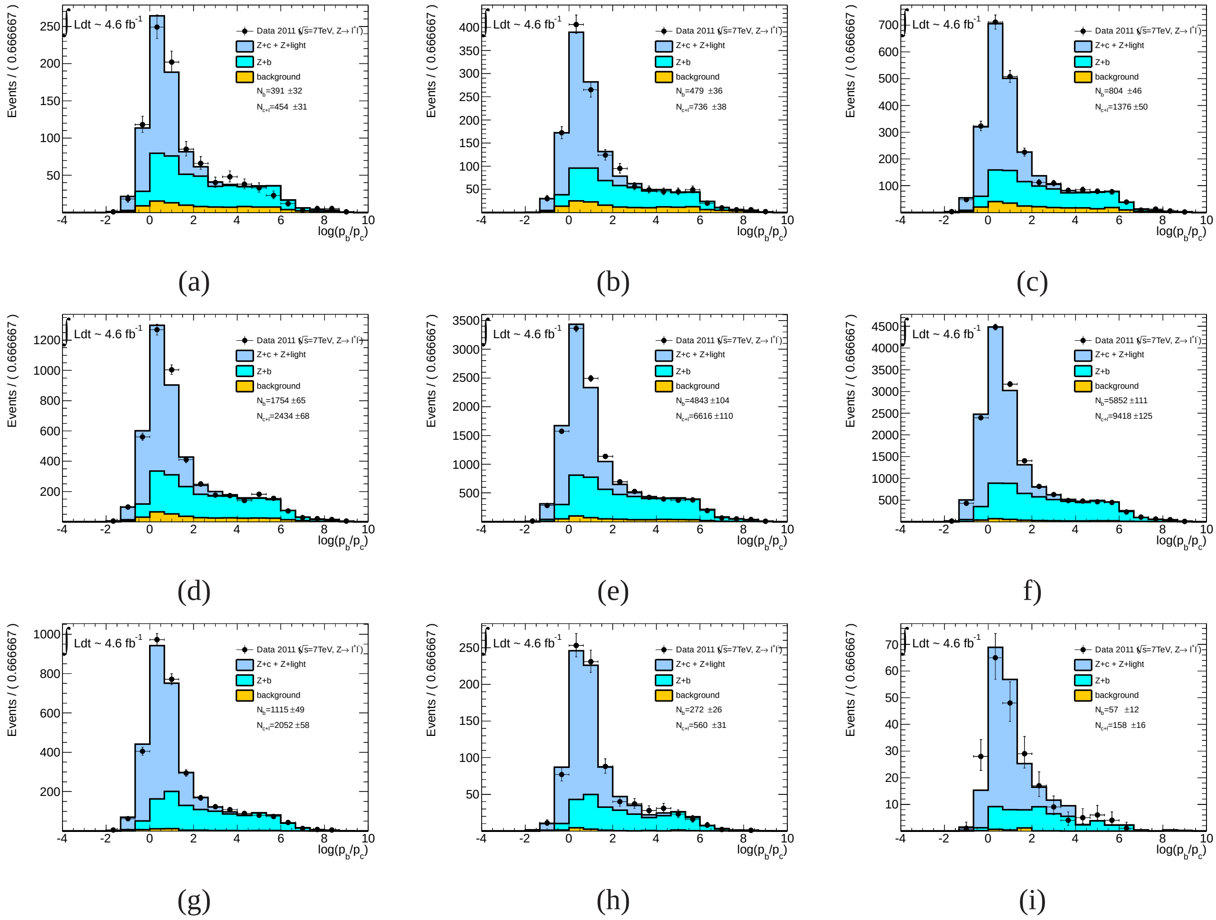

Figure 30: Flavour fit in the bins $0.0 \leq \Delta R(Z, b - jet) < 1.0$ (a), $1.0 \leq \Delta R(Z, b - jet) < 1.5$ (b), $1.5 \leq \Delta R(Z, b - jet) < 2.0$ (c), $2.0 \leq \Delta R(Z, b - jet) < 2.5$ (d), $2.5 \leq \Delta R(Z, b - jet) < 3.0$ (e), $3.0 \leq \Delta R(Z, b - jet) \leq 3.5$ (f), $3.5 \leq \Delta R(Z, b - jet) \leq 4.0$ (g), $4.0 \leq \Delta R(Z, b - jet) \leq 4.5$ (h) and $4.5 \leq \Delta R(Z, b - jet) \leq 6.0$ (i).

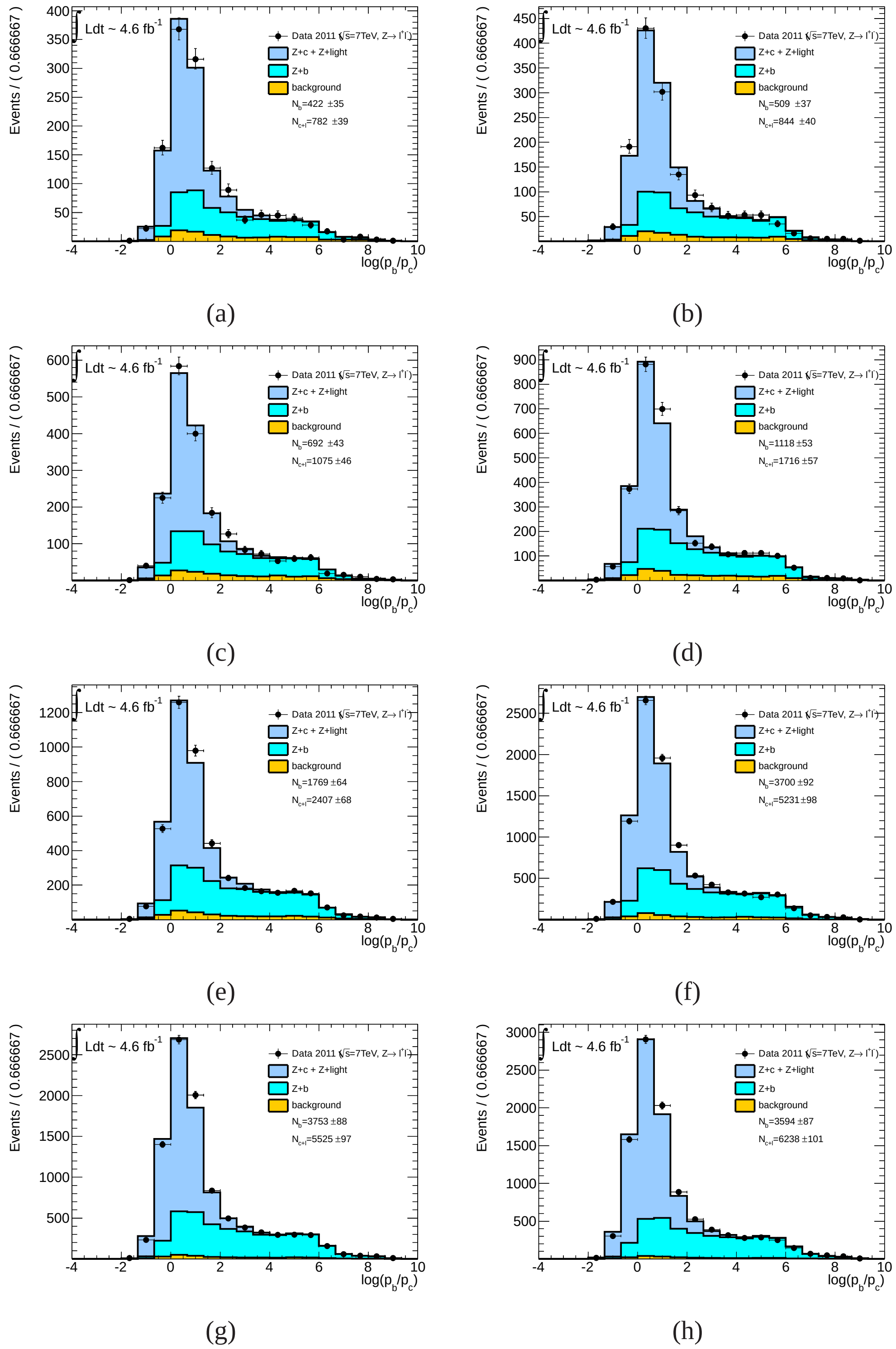

Figure 31: Flavour fit in the bins $0 \leq \Delta\phi(Z, b-jet) < 0.5$ (a), $0.5 \leq \Delta\phi(Z, b-jet) < 1.0$ (b), $1.0 \leq \Delta\phi(Z, b-jet) < 1.5$ (c), $1.5 \leq \Delta\phi(Z, b-jet) < 2.0$ (d), $2.0 \leq \Delta\phi(Z, b-jet) < 2.4$ (e), $2.4 \leq \Delta\phi(Z, b-jet) \leq 2.8$ (f) $2.8 \leq \Delta\phi(Z, b-jet) \leq 3.0$ (f) and $3.0 \leq \Delta\phi(Z, b-jet) \leq \pi$ (h).

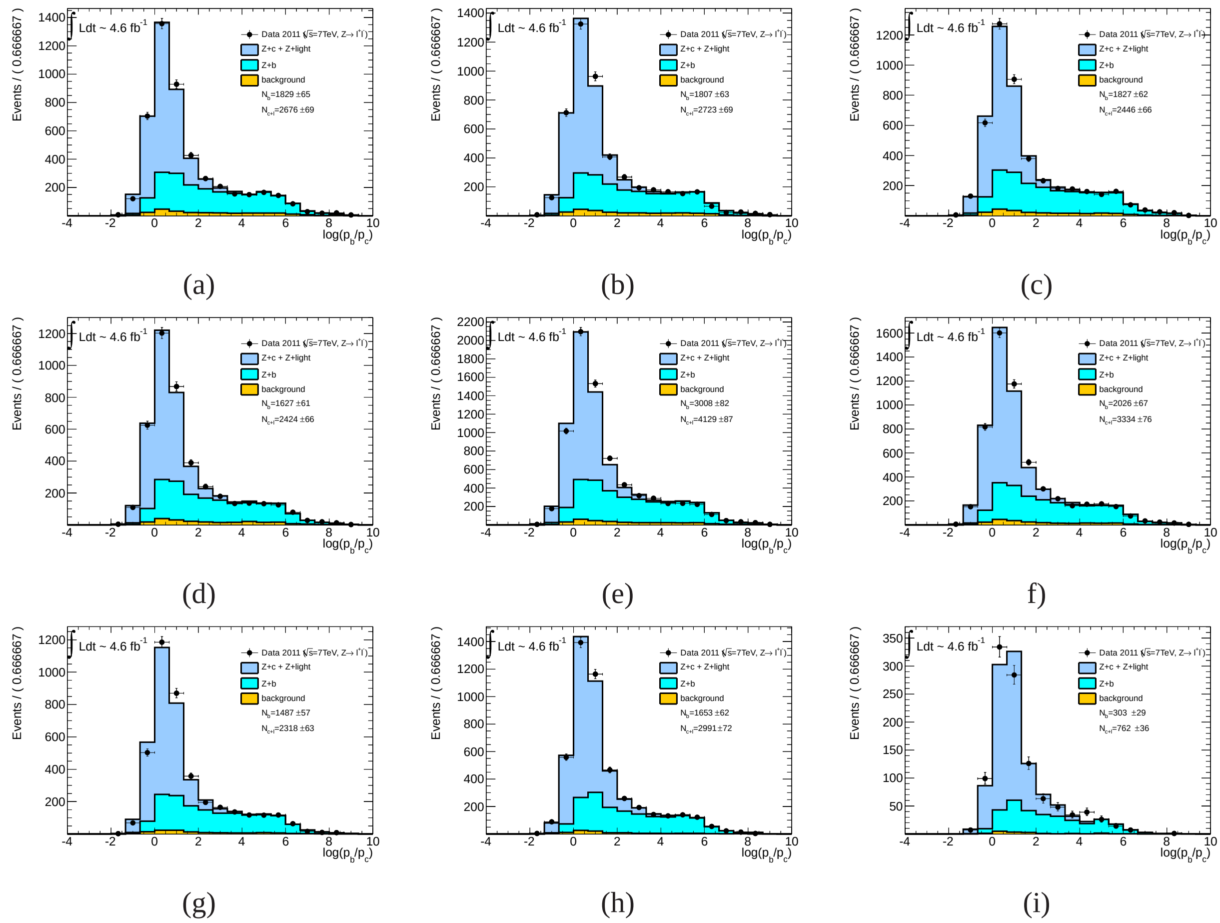

Figure 32: Flavour fit in the bins $0.0 \leq \Delta y(Z, b-jet) < 1.0$ (a), $1.0 \leq \Delta y(Z, b-jet) < 1.5$ (b), $1.5 \leq \Delta y(Z, b-jet) < 2.0$ (c), $2.0 \leq \Delta y(Z, b-jet) < 2.5$ (d), $2.5 \leq \Delta y(Z, b-jet) < 3.0$ (e), $3.0 \leq \Delta y(Z, b-jet) \leq 3.5$ (f), $3.5 \leq \Delta y(Z, b-jet) \leq 4.0$ (g), $4.0 \leq \Delta y(Z, b-jet) \leq 4.5$ (h) and $4.5 \leq \Delta y(Z, b-jet) \leq 6.0$ (i).

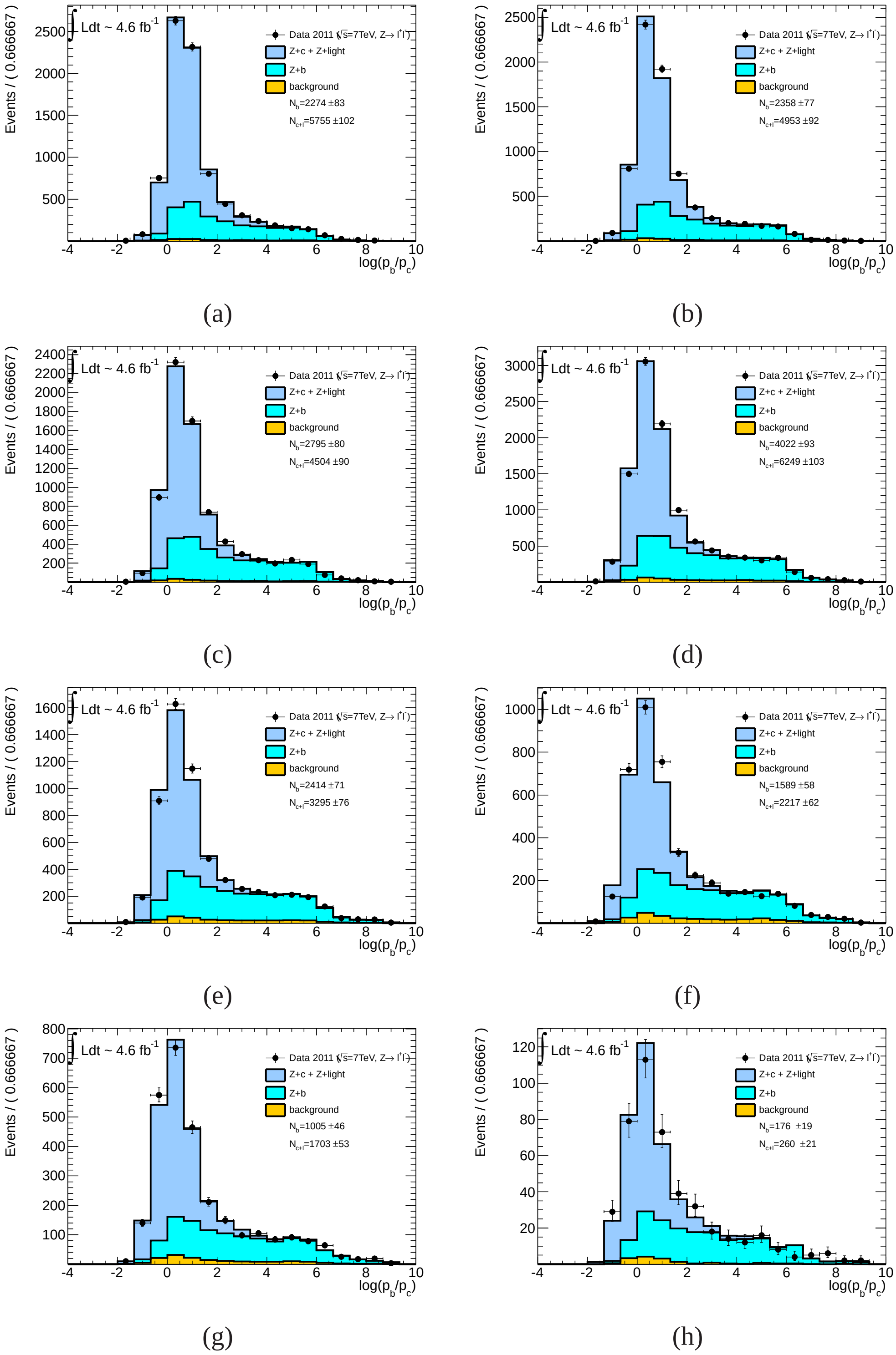

Figure 33: Flavour fit in the bins 0 ≤Z p_T[GeV]< 20 (a) 20 ≤Z p_T[GeV]< 30 (b), 30 ≤Z p_T[GeV]< 40 (c), 40 ≤Z p_T[GeV]< 60 (d), 60 ≤Z p_T[GeV]< 80 (e), 80 ≤Z p_T[GeV]< 110 (f), 110 ≤Z p_T[GeV]≤ 200 (g) and 200 ≤Z p_T[GeV]< 500 (h).

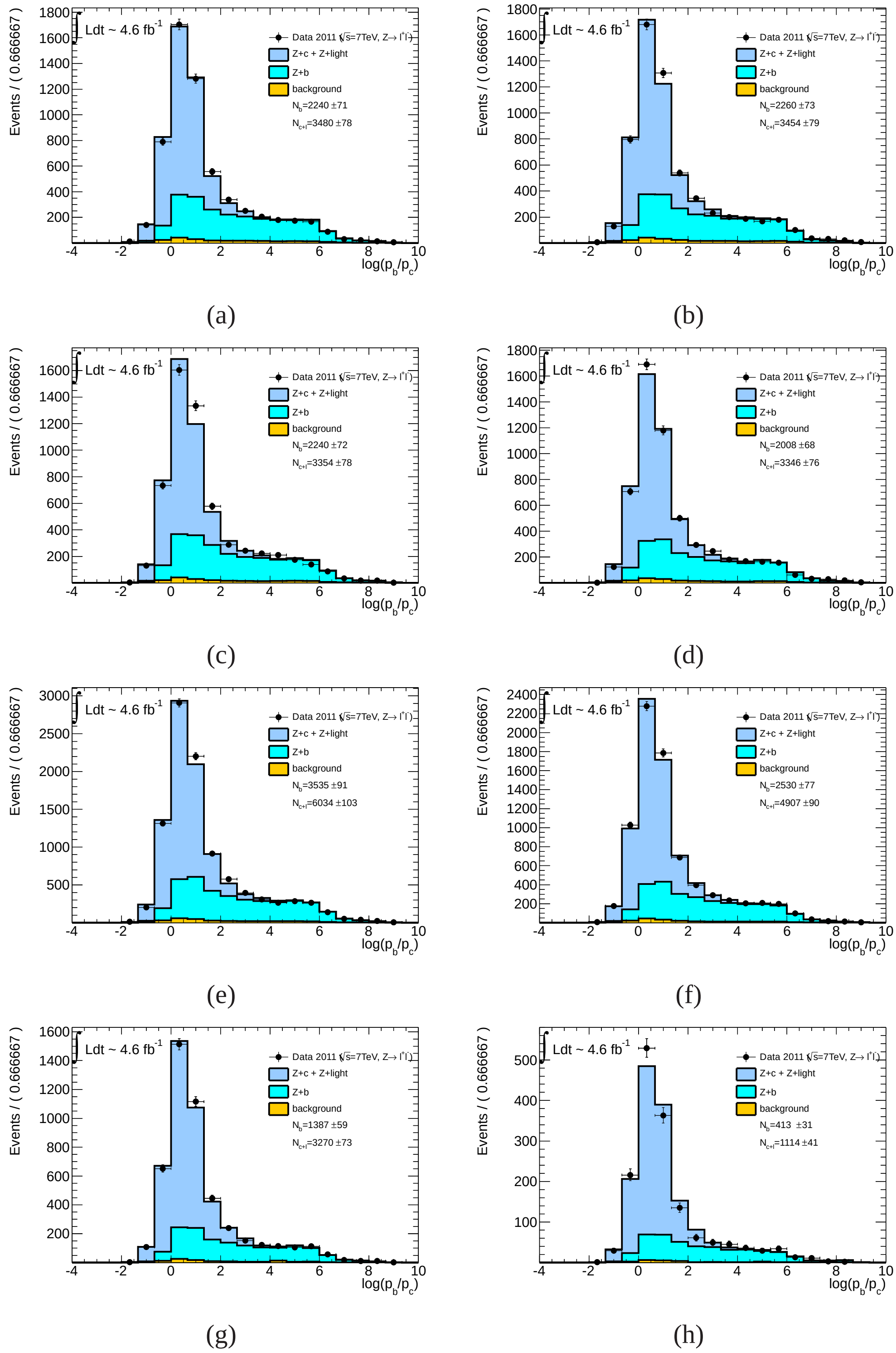

Figure 34: Flavour fit in the bins $0 \leq Z|y| < 0.2$ (a) $0.2 \leq Z|y| < 0.4$ (b), $0.4 \leq Z|y| < 0.6$ (c), $0.6 \leq Z|y| < 0.8$ (d), $0.8 \leq Z|y| < 1.2$ (e), $1.2 \leq Z|y| < 1.6$ (f), $1.6 \leq Z|y| \leq 2.0$ (g) and $2.0 \leq Z|y| < 2.5$ (h).

8.2 Comparison of extracted yields with ALPGEN

The fit results are shown at the reconstructed level for all observables differentially in figure 35 compared to the ALPGEN simulation.

8.3 Goodness of fit

The fit bias in the estimation of the number of b-jets is checked with a toy Monte-Carlo ensemble test. A set of pseudo-data is generated according to the flavour composition estimated in data; then a flavour fit is performed to each pseudo-dataset. The procedure is repeated separately in each analysis bin. The previous version of this study is summarised in figures showing the pull mean and width for all differential distributions, shown in Fig. 36 and 37.

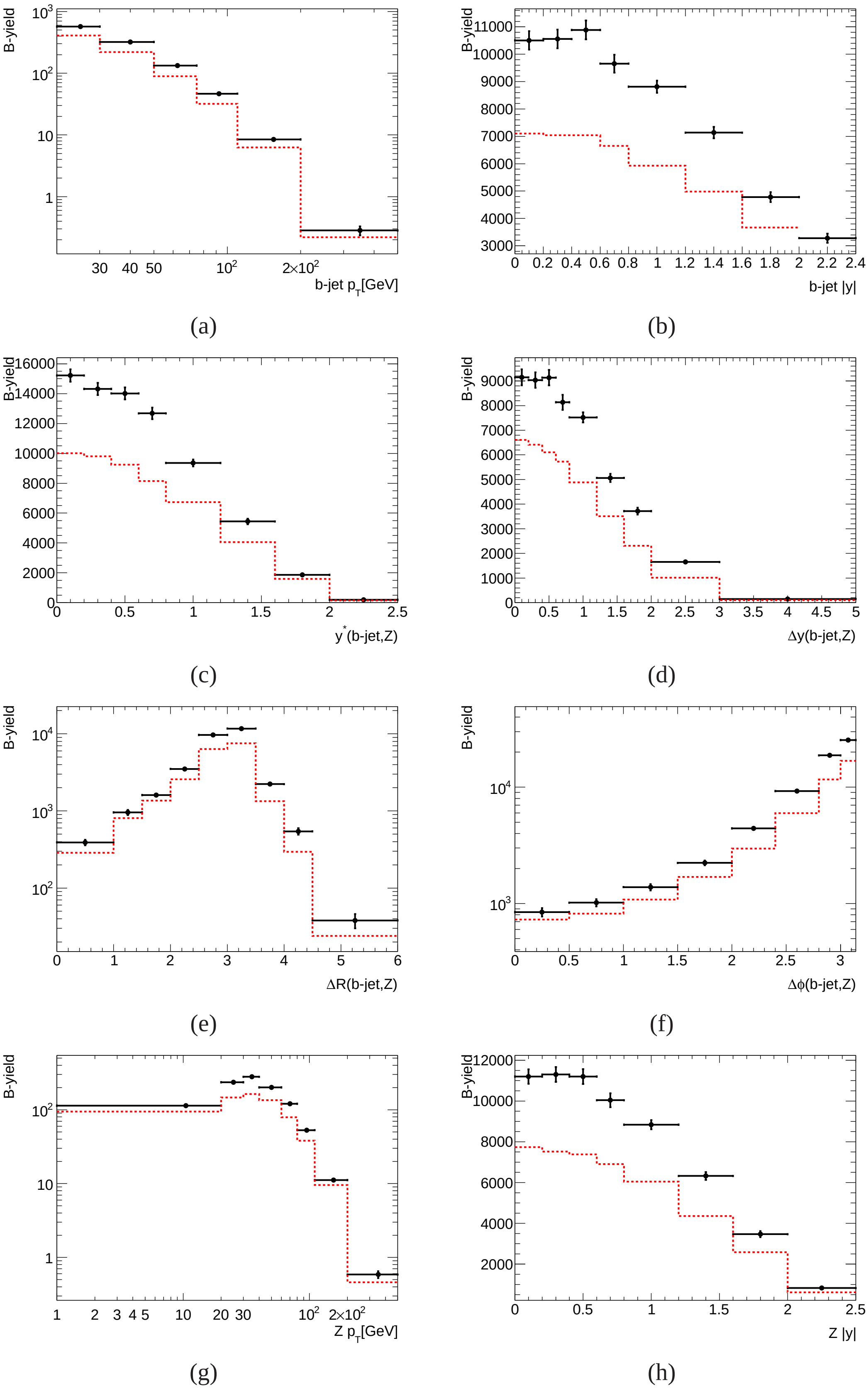

Figure 35: The number of b-jets at the reconstructed level as determined from flavour template fits, shown differentially in b-jet p_{T}(a), b-jet rapididty (b), $y^{\star}$ (c), $\Delta y(Z, b-jet)$ (d), $\Delta y(Z, b-jet)$ (e) and $\Delta\phi(Z, b-jet)$ (f). The number of events with a Z boson and at least one b-jet at the reconstructed level are shown differentially in $Z p_{\mathrm{T}}$(g) and Z rapidity (h). The reconstructed level data are compared to the ALPGEN model.

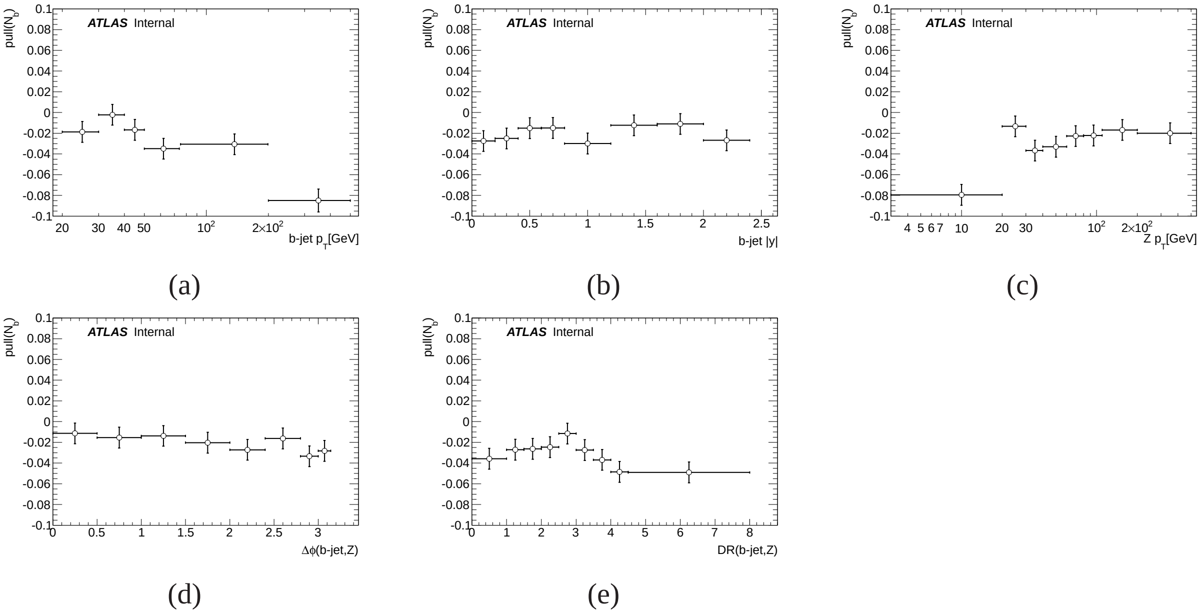

Figure 36: Pull mean as function of jet-p_T (a), jet-y (b), Z-p_T (c), $\Delta\phi(Z, b\text{−jet})$ (d) and $\Delta R(Z, b\text{−jet})$ (e).

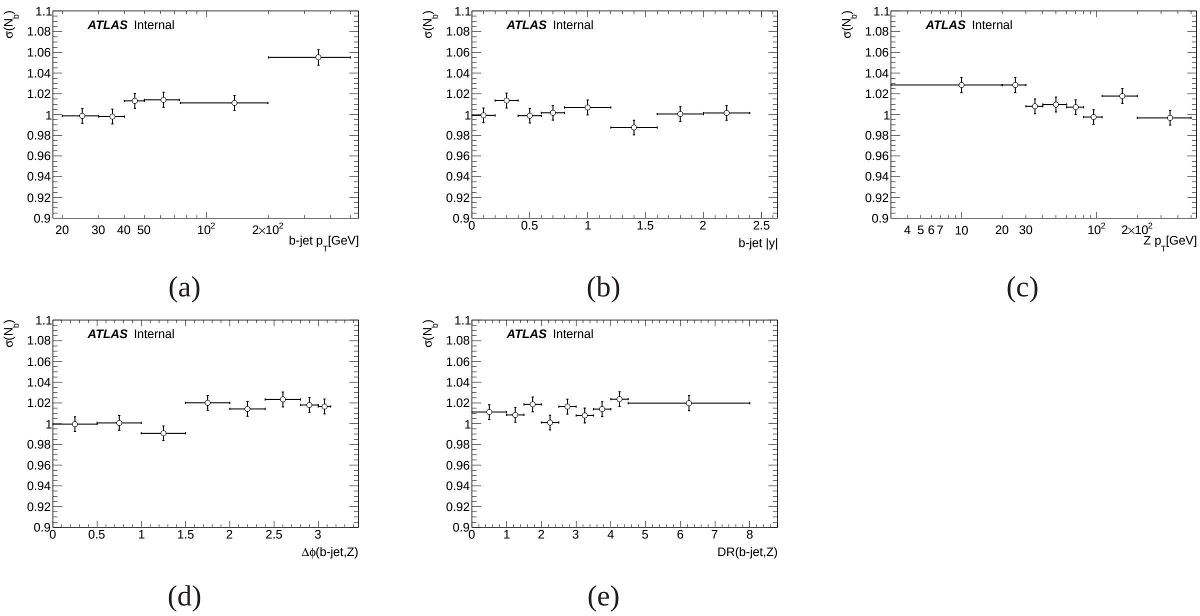

Figure 37: Pull width as function of jet-p_T (a), jet-y (b), Z-p_T (c), $\Delta\phi(Z, b\text{−jet})$ (d) and $\Delta R(Z, b\text{−jet})$ (e).

9 Unfolding the differential Zb yields

The jet and event yields N_b and N_{Zb}, extracted using the method in section 8, are next corrected for detector effects. The Bayesian unfolding method, as implemented in RooUnfold with covariance errors, is used as the baseline unfolding method, with the bin-by-bin method used as a cross-check.

A two dimensional histogram is filled for each observable, with a reconstructed level variable on the x-axis and a particle level variable on the y axis. If a reconstructed level b-jet is matched with a particle level b-jet using a simple $\Delta R < 0.4$ matching, then it enters the two dimensional histogram. A reconstructed or particle level b-jet is one that matches with a stable B hadron using the same criteria used for defining the flavour templates and given in table 4. For the b-jet p_T variable two additional truth jet bins are added: 10−15GeVand 15−20GeV. This corrects inefficiency in matching due to migration below the fiducial truth p_T cut and significantly increases the Accetance (defined below) in the lowest recontruction bin of this variable.

One dimensional histograms of the reconstructed and particle level variables are also filled, but with no matching requirement. The Acceptance and Efficiency are then defined as

$$Acceptance = \frac{N(matched)}{N(reconstructed)} \quad Efficiency = \frac{N(matched)}{N(particle)} \tag{2}$$

and in it simplest incarnation, the corrected number is just $N(data)*Acceptance/Efficiency$. Bayesian iterative unfolding is used to take into account the small correlations beteen bins, and 4 iterations is found to give a stable result.

The two dimensional matrix, the Acceptance and the Efficiency, are shown for each observable in figures 38 to 45. The Acceptance is in general high, while the Efficiency is approximately 30%.

Observables are grouped into pairs that have the same integrated cross section. The Z boson must have rapidity $|y| < 2.5$ and $p_{\mathrm{T}} < 500$ GeV for all distributions. The jets must have $p_{\mathrm{T}} < 500$ GeV for all jet-based observables. Finally, for the angular jet-level variables, ΔR, Δy and $\Delta\phi$, $Z\,p_{\mathrm{T}} > 20$ GeV in order to have a well defined ϕ of the Z, and $\Delta R(Z, b\mathrm{-jet}) < 6.0$.

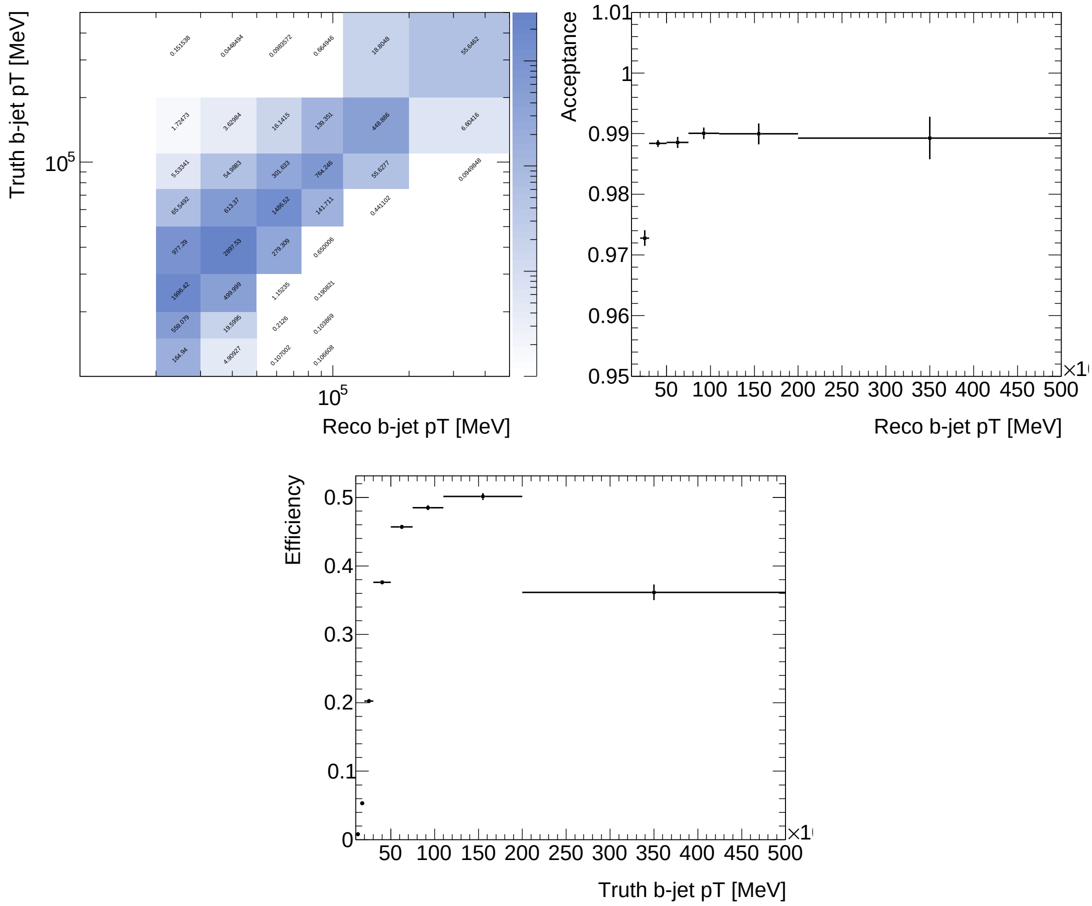

Figure 38: The unfolding matrix, the acceptance correction and the efficiency correction for b-jet p_{T}.

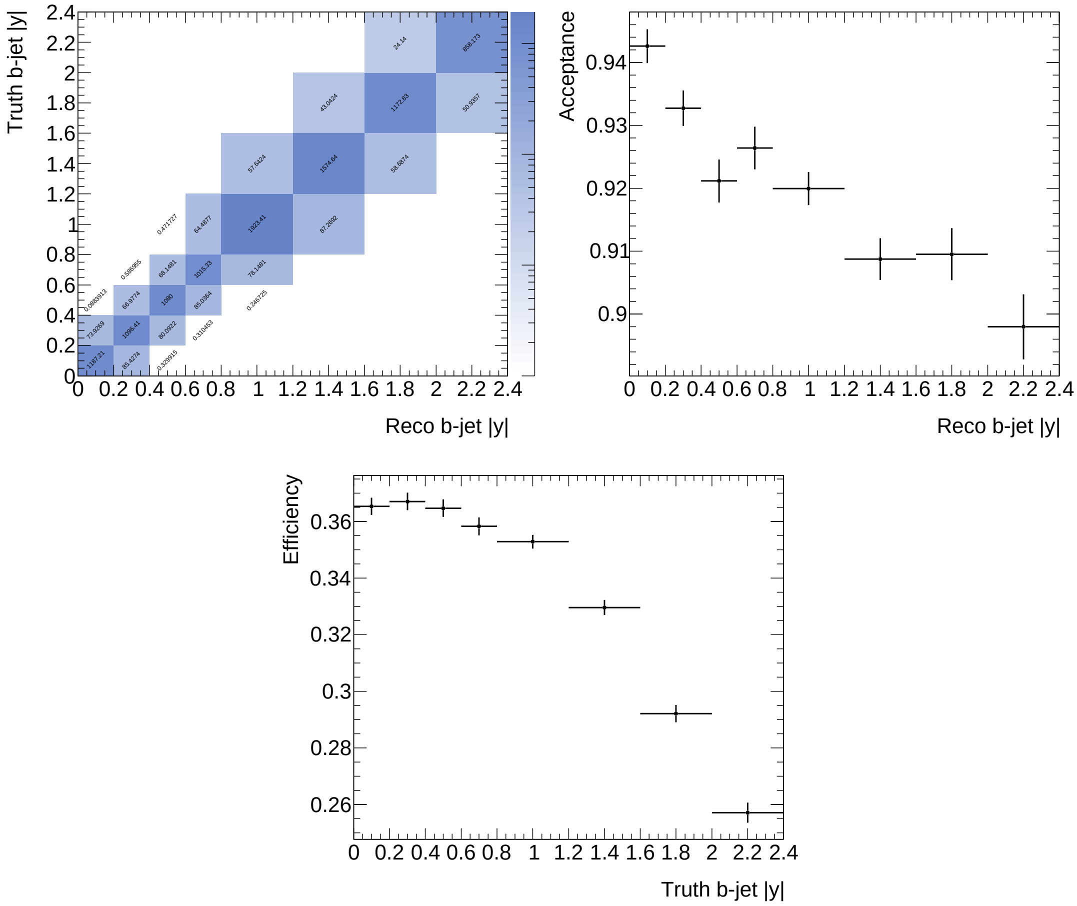

Figure 39: The unfolding matrix, the acceptance correction and the efficiency correction for b-jet rapidity.

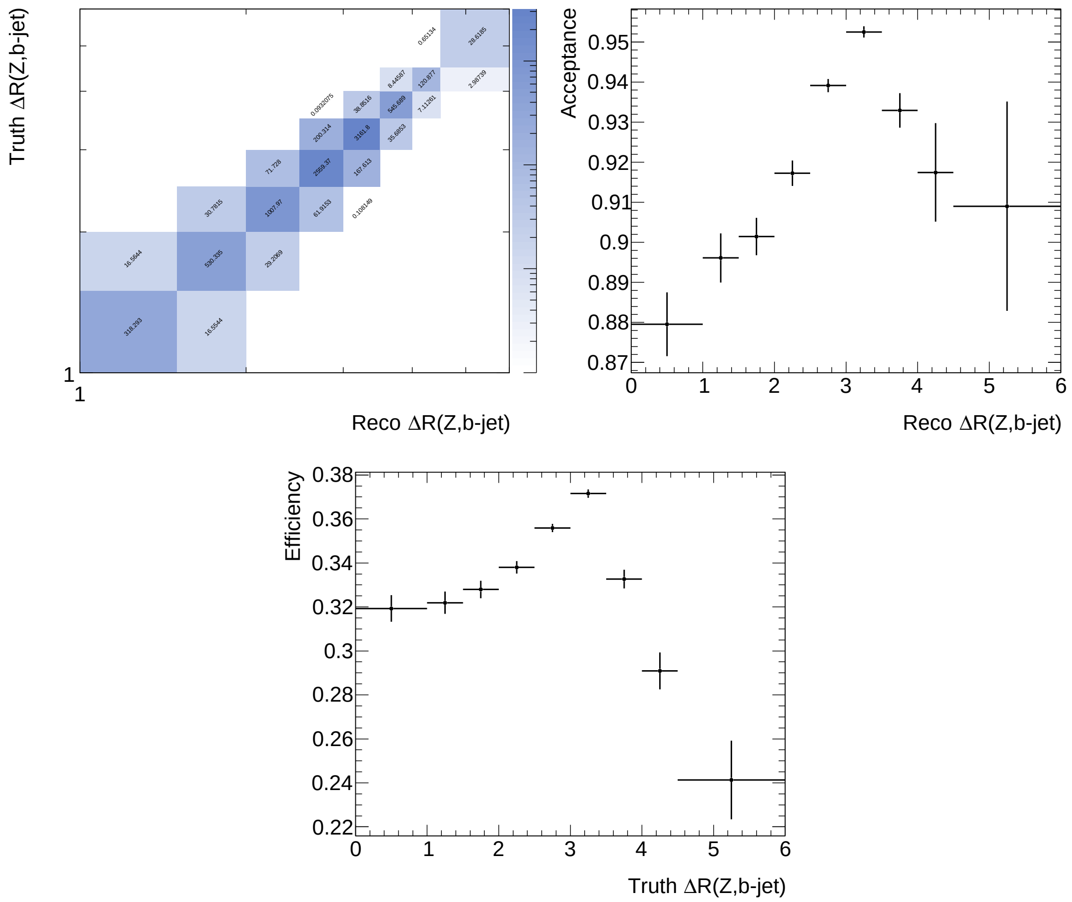

Figure 40: The unfolding matrix, the acceptance correction and the efficiency correction for $\Delta R(Z, b{-}\text{jet})$.

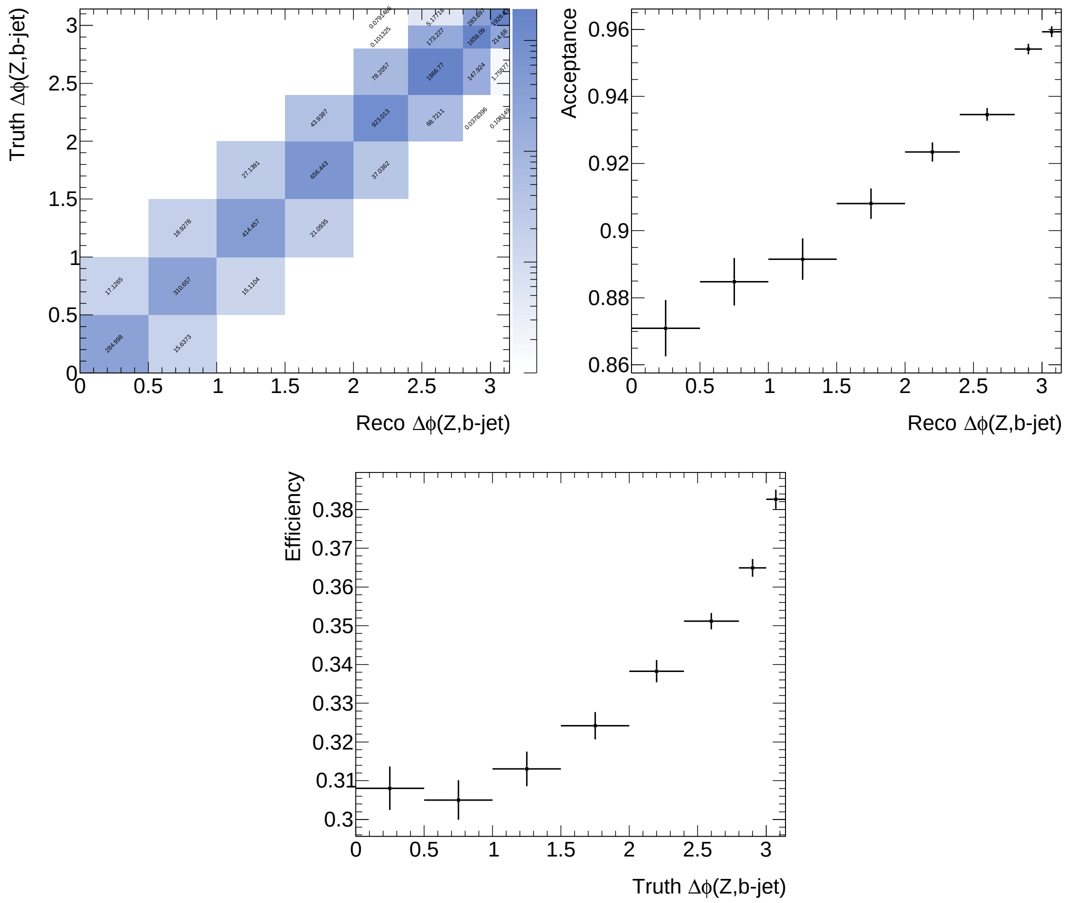

Figure 41: The unfolding matrix, the acceptance correction and the efficiency correction for $\Delta\phi(Z, b\text{−jet})$.

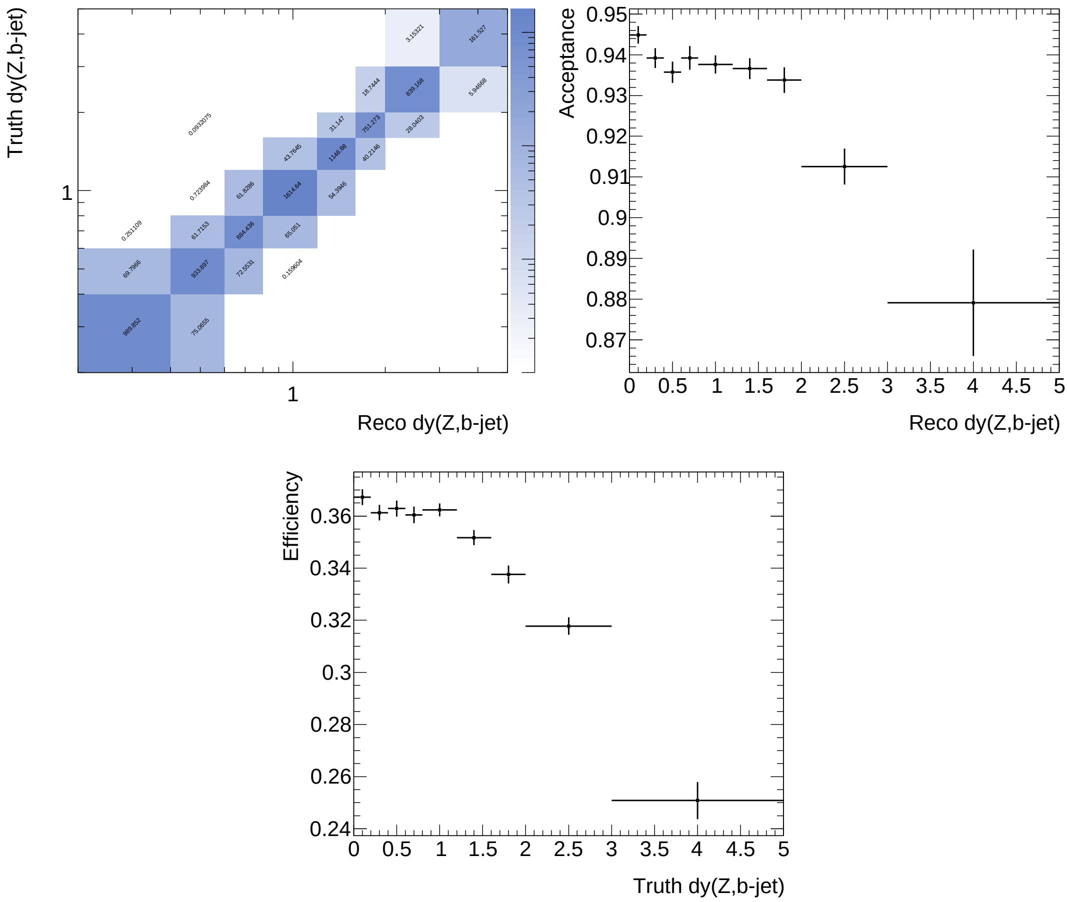

Figure 42: The unfolding matrix, the acceptance correction and the efficiency correction for $|\Delta y(Z, b\mathrm{-jet})|$.

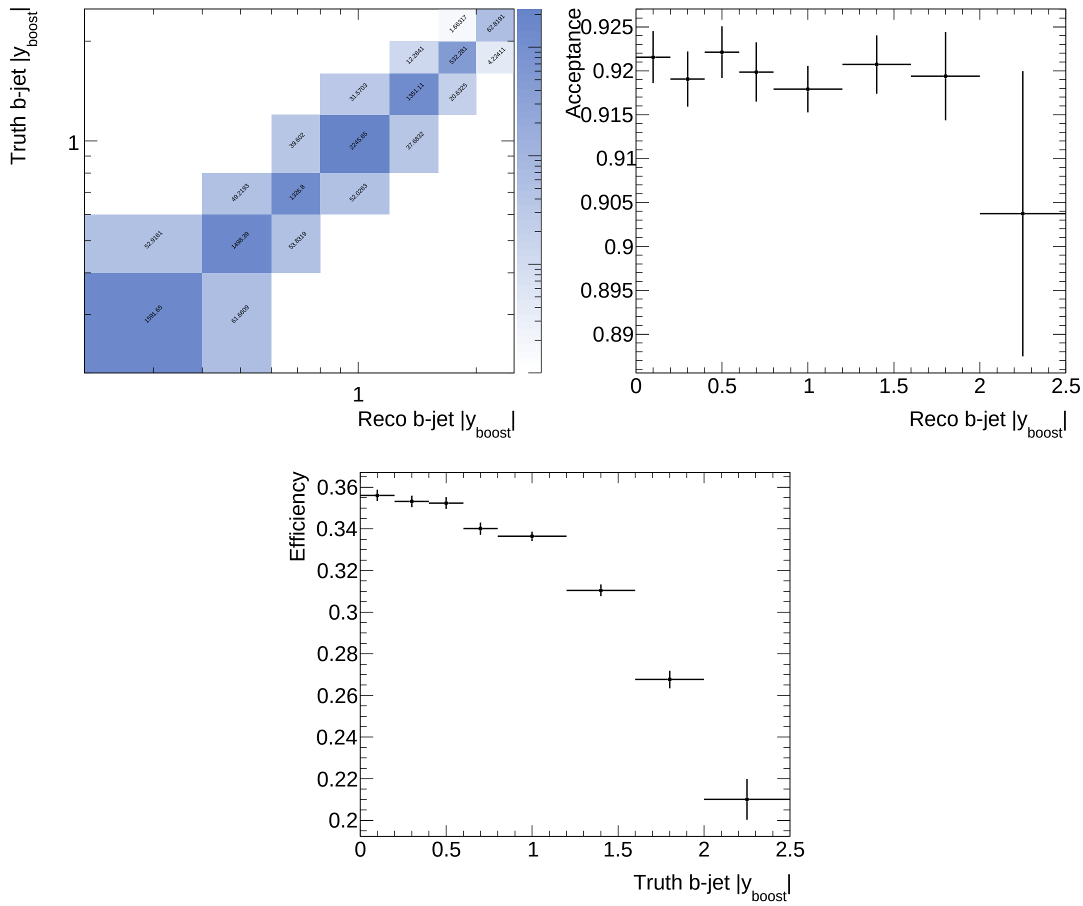

Figure 43: The unfolding matrix, the acceptance correction and the efficiency correction for b-jet $|y_{boost}|$.

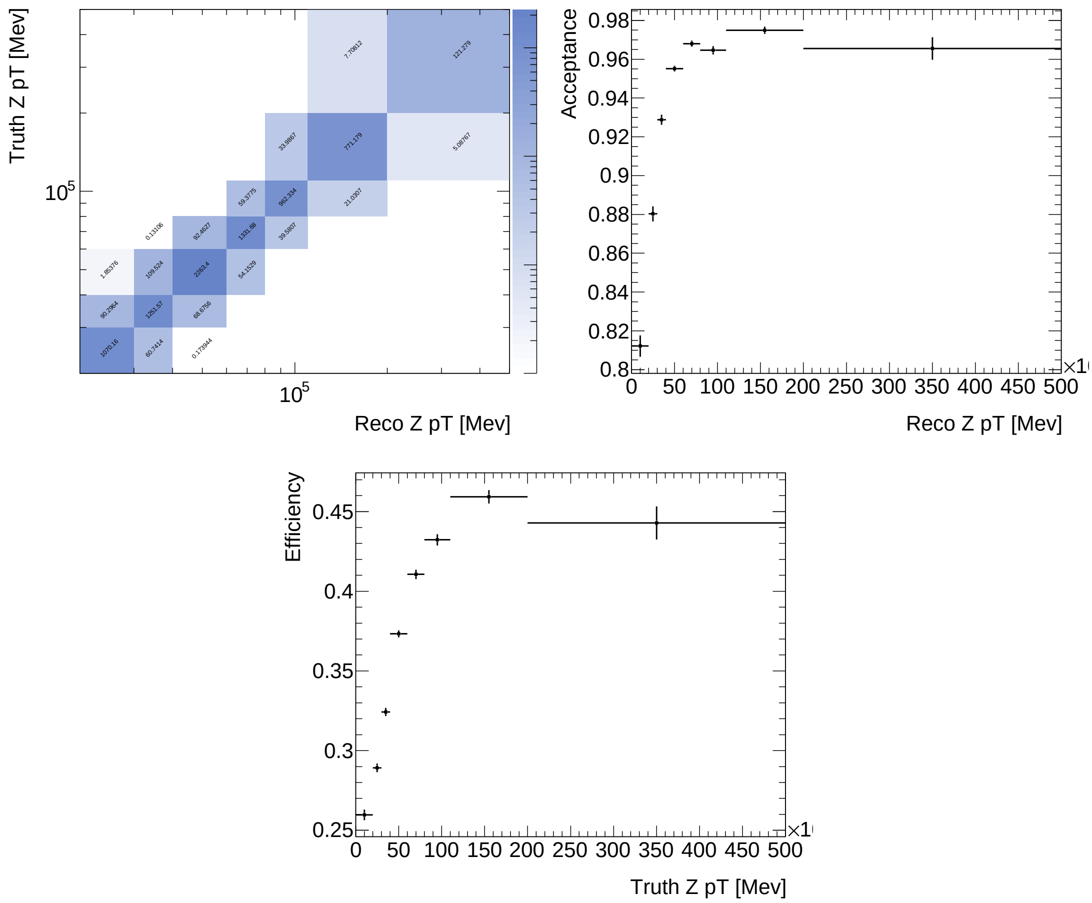

Figure 44: The unfolding matrix, the acceptance correction and the efficiency correction for Z p_{T}.

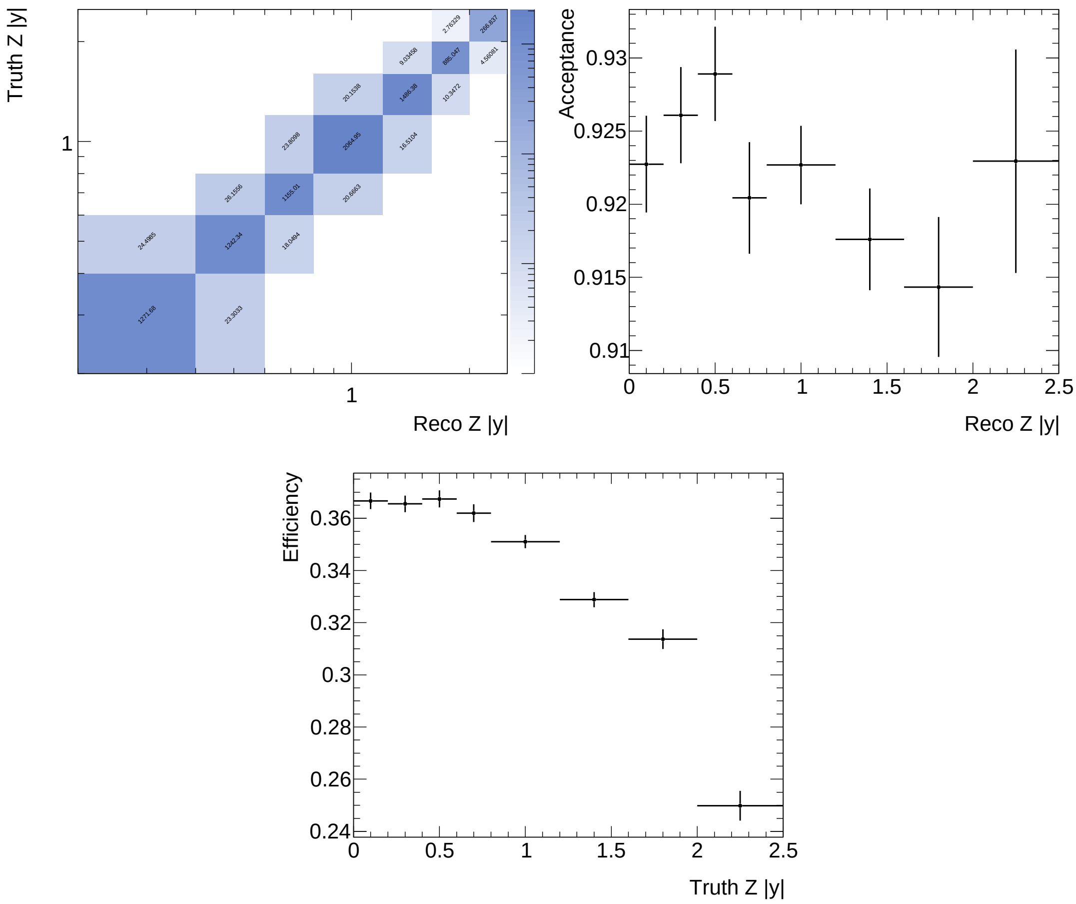

Figure 45: The unfolding matrix, the acceptance correction and the efficiency correction for Z rapidity.

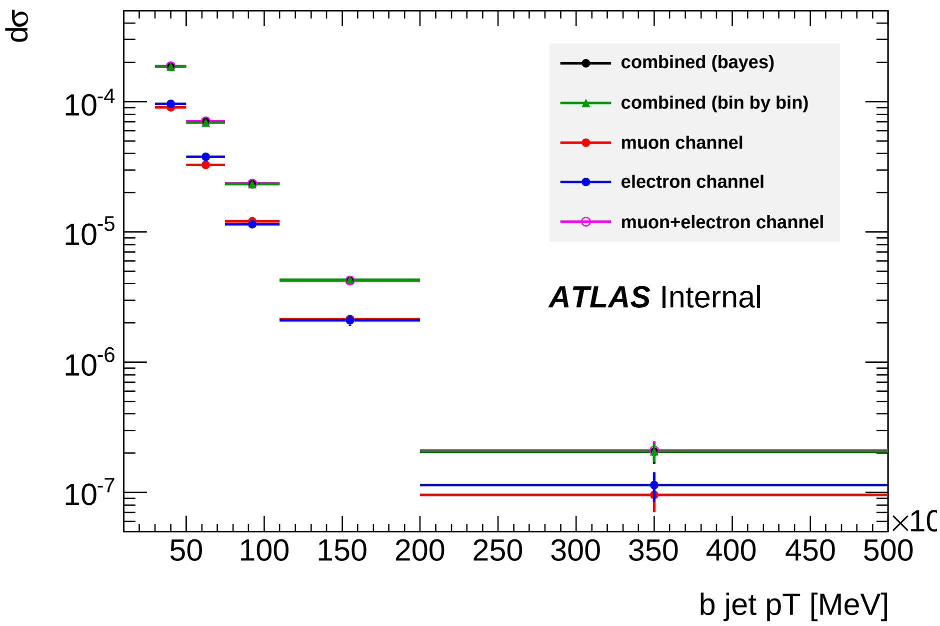

Figure 46: Comparison of b-jet p_T unfolded cross-sections using the bayesian and bin by bin methods, cross-sections for the indivdual electron and muon channels as well as their sum are also shown.

9.1 *Zb* unfolding cross checks

Various cross-checks are made for the eight unfolded *Zb* distributions:

The unfolding is performed using the bayesian method and cross-checked with the bin by bin method with excellent consistency observed. The full analysis chain of fits and bayesian unfolding is repeated separately for the electron and muons channel for all variables. This allows two important cross-checks. Firstly the electron and muon differential cross-sections, expected to be identical, can be directly compared and checked for consistency; for the most part this consistency is within the statistical uncertainties although the electron cross-section does fluctuate high in some bins relative to the muon cross-section. Secondly the individual analysese of electron and muon channel can be added after unfolding and compared to the cross-section obtained when the channels are combined in the fits and unfolding. Excellent agreement is observed validating the analysis procedure of combining the channels.

The above checks are displayed in figures 46 to 53 which show the unfolded cross-sections described above.

In addition to these checks, toy experiments using the bootstrap method are performed for the Bayesian unfolding procedure to validate the statistical uncertainties returned from RooUnfold. These toys will be documented in an appendix in the next version of this note before approval is requested.

One further appendix is in preparation detailing a cross-check whereby the *Zb* analysis was performed with an alternative cut on the MV1 tagger output (60% working point instead of 75%). With the default efficiency corrections from the b-tagging group a ∼5% difference in unfolded cross-section was observed. More detailed investigation has pointed to the dijet effiency methods causing this tension and in particular the tension occurs for the tighter working point and not the default working point used in this analysis. For this reason we do not currently change our central analysis or add an additional uncertainty due to this effect.

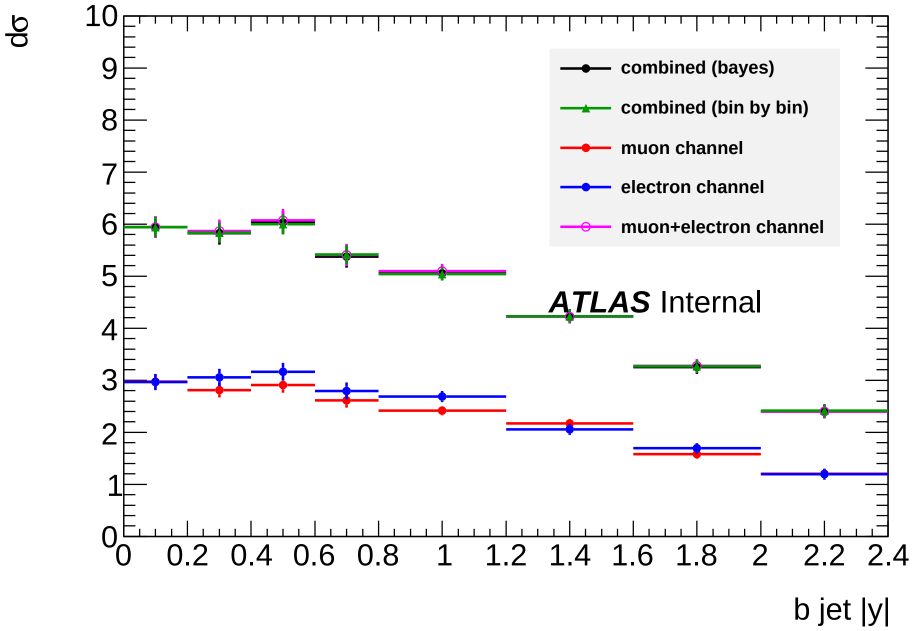

Figure 47: Comparison of b-jet $|y|$ unfolded cross-sections using the bayesian and bin by bin methods, cross-sections for the indivdual electron and muon channels as wellas their sum are also shown.

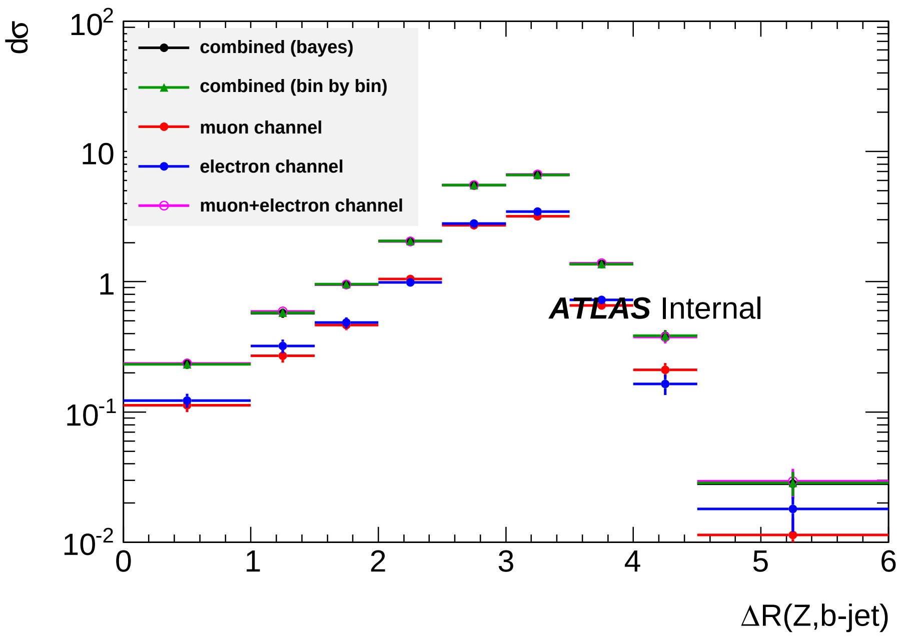

Figure 48: Comparison of $\Delta R(Z, b - jet)$ unfolded cross-sections using the bayesian and bin by bin methods, cross-sections for the indivdual electron and muon channelsas wellas their sum are also shown.

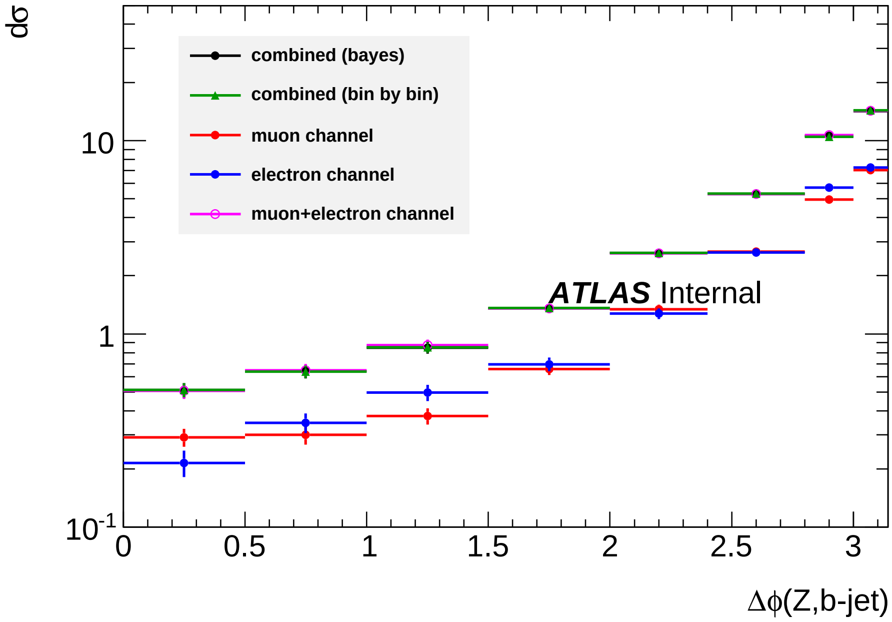

Figure 49: Comparison of $\Delta\phi(Z, b - jet)$ unfolded cross-sections using the bayesian and bin by bin methods, cross-sections for the indivdual electron and muon channelsas wellas their sum are also shown.

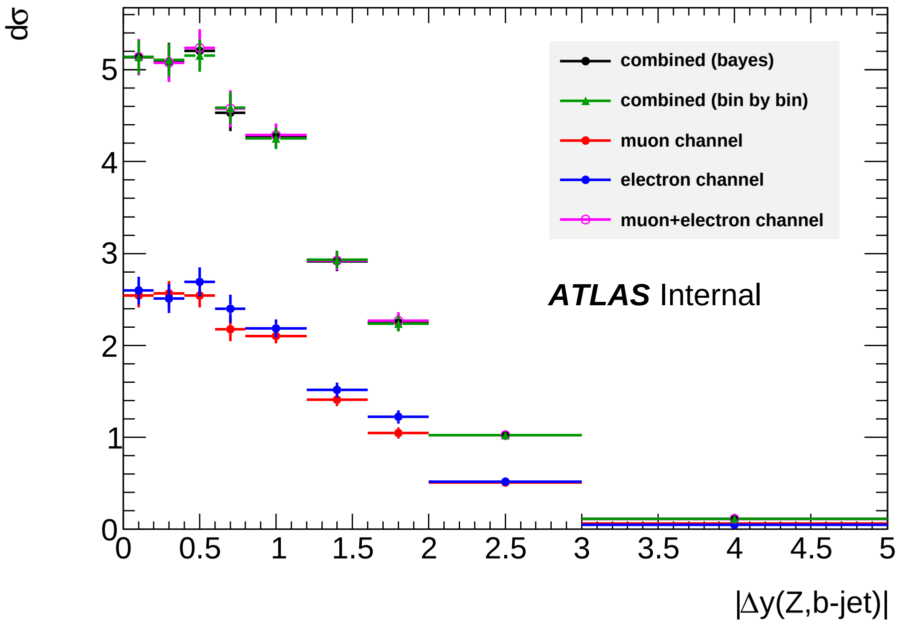

Figure 50: Comparison of $\Delta y(Z, b - jet)$ unfolded cross-sections using the bayesian and bin by bin methods, cross-sections for the indivdual electron and muon channelsas wellas their sum are also shown.

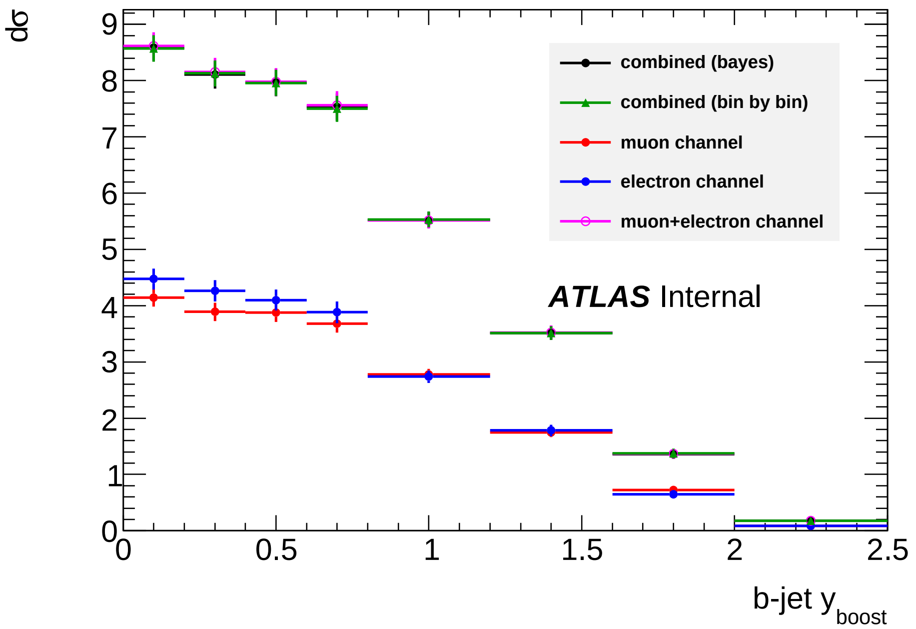

Figure 51: Comparison of b-jet $|y_{boost}|$ unfolded cross-sections using the bayesian and bin by bin methods, cross-sections for the indivdual electron and muon channelsas wellas their sum are also shown.

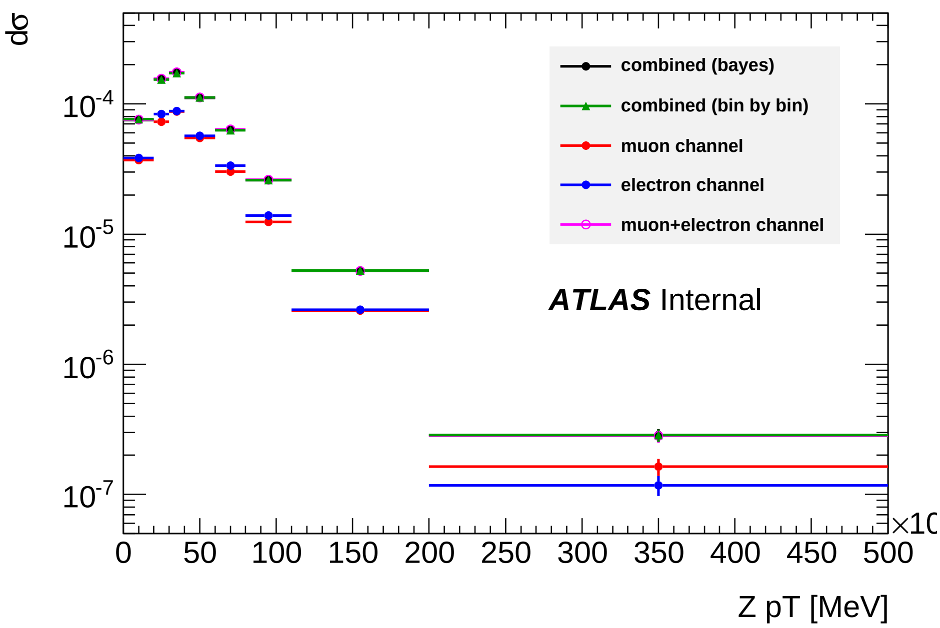

Figure 52: Comparison of Z p_T unfolded cross-sections using the bayesian and bin by bin methods, cross-sections for the indivdual electron and muon channelsas wellas their sum are also shown.

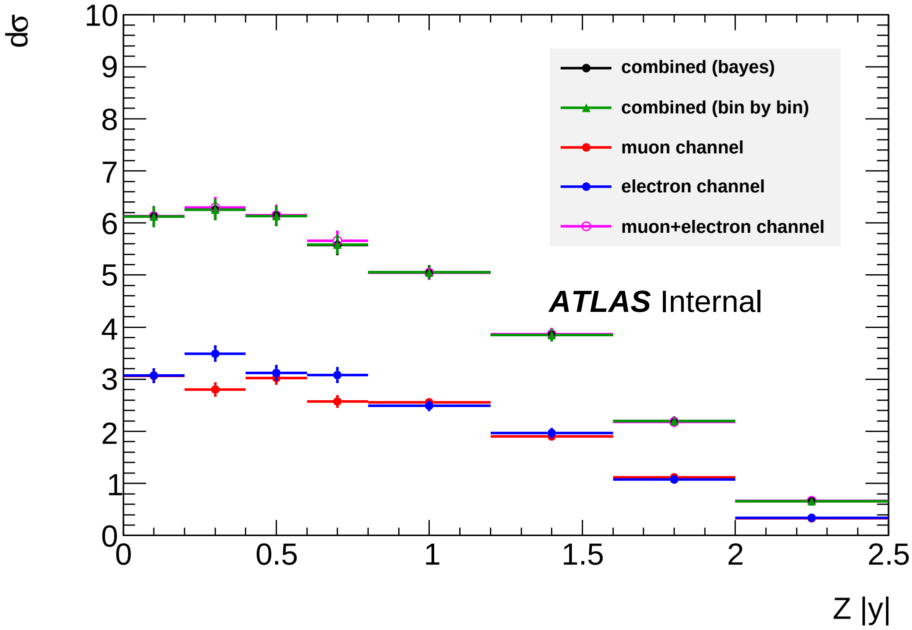

Figure 53: Comparison of Z $|y|$ unfolded cross-sections using the bayesian and bin by bin methods, cross-sections for the indivdual electron and muon channelsas wellas their sum are also shown.

10 Inclusive fit for Zbb

To extract the $Z + bb$ yield from the sample of Z+2 tagged jets, the data are fitted using templates from Monte Carlo, in a variable which provides discrimination between the different jet flavours (b, charm, light). To improve the statistics, the electron and muon decay channels of the Z boson are combined before performing the fit by adding the channels for each of the distributions. This fit is first done inclusively, as described in this Section, then differentially (see Section 12).

Section 10.1 gives an overview of different possible approaches to the fit that have been explored, as well as describing the baseline that was chosen for the cross section measurement. The results of a toy MC based fit validation study are summarised in Subsection 10.4.

10.1 Comparison of different fit methods

The number of true bb-pairs in the double b-tagged sample is extracted using a template fit. The fit procedure uses an extended likelihood fit based on MINUIT. To obtain the best fit performance, we must select the appropriate variable to fit, and the number and type of templates to be used in the fit.

For the fit variable, two options were compared, motivated by the resulting correlations between the fitted b, c and light jet contributions. These are the sum of $\ln(pb/pu)$ and the sum of $\ln(pb/pc)$, where the sum runs over the two leading p_{T} tagged jets.

Several combinations of the jet flavour are possible for the two tagged jets that enter the fit, namely: bb, bc, bu, cc, cu, uu (where u stands for any type of light flavour or gluon jet). The limited statistics and degenerate shapes of these templates means that several of the background templates are combined together before the fit is performed. The following combination options have been compared, where the parentheses indicate which of the combinations enter a common template T_i:

- (a) 2 templates: T_1: bb, T_2: (bc, bu, cc, cu, uu) ;
- (b) 3 templates: T_1: bb, T_2: (bc, bu), T_3: (cc, cu, uu) ;
- (c) 3 templates: T_1: bb, T_2: (bc, cc), T_3: (bu, cu, uu) ;
- (d) 3 templates: T_1: bb, T_2: cc, T_3: (bc, bu, cu, uu) ;
- (e) 3 templates: T_1: bb, T_2: (bc, bu, cc, cu), T_3: uu.

In addition to the templates explicitly listed above, a background template is formed from the combination of the background Monte Carlos (top, diboson, multijet, etc - see Section 3). This background template is not allowed to float in the fit.

An overview of the statistics available for each of the templates is provided in Table 16. The different ways to group the different Z + jets background templates have also been compared in terms of template correlations. Table 17 gives an overview of the results.

Given the limited statistics for the Z + jets templates corresponding to events with less than two true b's for options (b) — (e), the simplest grouping of templates, option (a), was chosen as the baseline.

fit	$N(T_1)$, raw	$N(T_2)$, raw	$N(T_3)$, raw
(a)	10536	5128	-
(b)	10536	2092	3036
(c)	10536	2187	2941
(d)	10536	1411	3717
(e)	10536	4332	796

Table 16: Overview of fit template statistics in terms of unweighted MC events contributing to each of the templates.

fit option	template combination	ln (pb/pu)	ln (pb/pc)
(a)	*bb*, (*bc*, *bu*, *cc*, *cu*, *uu*)	-0.50	-0.55
(b)	*bb*, (*bc*, *bu*)	-0.77	-0.86
	bb, (*cc*, *cu*, *uu*)	+0.51	+0.62
	(*bc*, *bu*), (*cc*, *cu*, *uu*)	-0.84	-0.84
(c)	*bb*, (*bc*, *cc*)	-0.60	+0.53
	bb, (*bu*, *cu*, *uu*)	+0.38	-0.63
	(*bc*, *cc*), (*bu*, *cu*, *uu*)	-0.89	-0.97
(d)	*bb*, *cc*	-0.18	+0.64
	bb, (*bc*, *bu*, *cu*, *uu*)	+0.00	-0.77
	cc, (*bc*, *bu*, *cu*, *uu*)	-0.94	-0.93
(e)	*bb*, (*bc*, *bu*, *cc*, *cu*)	-0.66	-0.18
	bb, *uu*	+0.47	+0.03
	(*bc*, *bu*, *cc*, *cu*), *uu*	-0.88	-0.96

Table 17: Correlations between the fit templates, for the different ways of grouping the Z + jets backgrounds.

10.2 Single-b Scale Factor

In the default fit method, the templates *bc*, *bu*, *cc*, *cu* and *uu* are combined before the fit into a general non-*bb* template. This assumes the Monte Carlo correctly describes the relative proportion of each of these samples. However, we know the Alpgen+Herwig samples underestimate the amount of $Z + b$, so this template must be scaled up before the combination in order to obtain the correct shape for the non-*b* template.

To derive the scale factors, the following fits are performed:

1. Fit to $\ln(pb/pl)$ in a sample of Z+2 jets with exactly one tag, to mimic the *bl* configuration. This fit is used to derive the default charm and *b* scale factors.

2. Fit to $\ln(pb/pl)$ in the inclusive $Z+ \geq 1$ tagged jet sample, to study kinematic dependence of the charm and *b* scale factors and set a systematic uncertainty.

3. Fit to $\ln(pb/pc)$ in a sample of Z+2 jets with exactly one tag, to validate the *b*-jet scale factor in the variable used in the final analysis. The charm scale factor cannot reliably be obtained in this fit, due to the degeneracy of the charm and light templates in $\ln(pb/pc)$.

4. Fit to $\ln(pb/pc)$ in the inclusive $Z+ \geq 1$ tagged jet sample, again to cross check the *b* scale factor.

The results of these fits can be seen in Fig. 54 for $\ln(pb/pl)$, and 55 for the validation in $\ln(pb/pc)$.

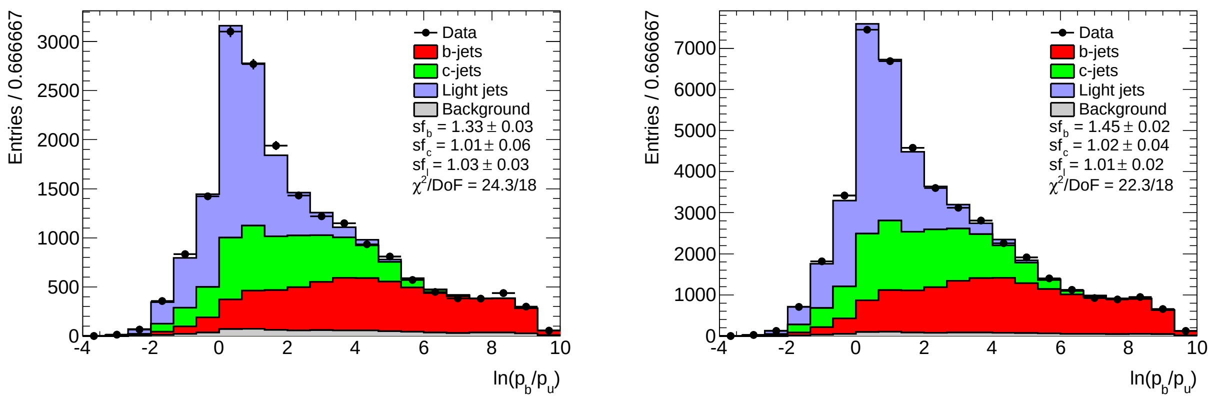

Figure 54: Extracting *b* and *c* jet scale factors from fits to $\ln(pb/pl)$ in (a) the Z+tagged jet + non-tagged jet sample, and (b) the inclusive Z+tagged jet sample.

In the main fit region (1), shown in Fig. 54 (a), we obtain a *b* scale factor of 1.29. In the more inclusive fit region, we see a *b* scale factor of 1.44. We therefore assign a 15% systematic uncertainty to this *b* scale factor. These results are consistent with those in the $\ln(pb/pc)$ fits.

We also observe a charm scale factor greater than unity. However, in the final fit variable ($\ln(pb/pc)$), the charm and light templates are essentially degenerate, and scaling up/down the charm contribution to the non-*b* template has negligble effect. So, we take a charm scale factor of unity with again a 15% systematic to cover any possible effects.

Hence, when building the non-*bb* template to fit the double-tagged sample, we apply the following scaling:

1. light-light, light-charm and charm-charm are not changes (scale factor of 1.0)

2. light-*b* and charm-*b* are scaled up by 1.29.

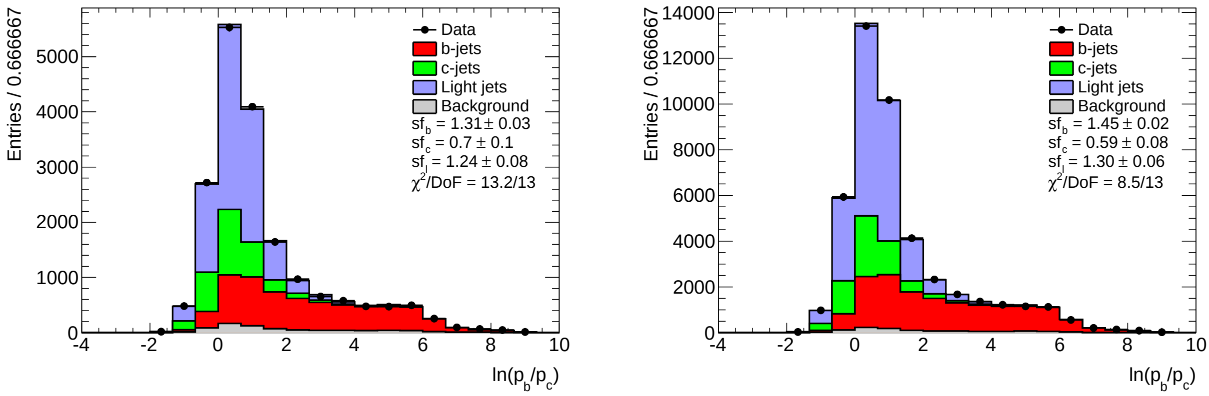

(a) (b)

Figure 55: Validating the b jet scale factors with fits to $\ln(pb/pc)$ in (a) the Z+tagged jet + non-tagged jet sample, and (b) the inclusive Z+tagged jet sample.

10.3 Inclusive Fit Results

The fit results corresponding to the baseline option are shown in Figure 56 for $\ln(pb/pc)$, comprising separate fit results for the electron and muon channel as well as the combined fit result used in the cross section measurement. Table 18 gives an overview of the corresponding numbers as well as a comparison to results obtained from the $\ln(pb/pu)$ variable. The data are reasonably well described in both cases. Results obtained from the two variables compared are in excellent agreement with each other. Also results of the combined fit of electron and muon channels are consistent with those obtained by fitting the individual channels.

variable	$Z \to ee$	$Z \to \mu\mu$	combined fit
$\ln(pb/pc)$	483 ± 34	727 ± 43	1207 ± 55
$\ln(pb/pu)$	480 ± 33	706 ± 41	1189 ± 53

Table 18: Overview of fit results for both fit variables considered, separately for electron and muon decay channel, and for the combined fit of both.

For completeness, the fit results obtained without the reweighting of b-decays obtained in Section 5 are shown in Table 19. It can be seen that the χ^2/ndf for the fits is higher without the reweighting, corresponding to a poorer description of the data. It can be seen also that the $\ln(pb/pc)$ and $\ln(pb/pu)$ results are in slightly worse agreement without the reweighting. Since only the statistical uncertainty of the fit result is shown in the table, no impact of the reweighting on the uncertainty is seen.

variable	result, no rew.	fit χ^2/ndf, no rew.	result, with rew.	fit χ^2/ndf, with rew.
$\ln(pb/pc)$	0 ± 0	0.0/0	1207 ± 55	8.8/6
$\ln(pb/pu)$	0 ± 0	0.0/0	1189 ± 53	12.1/8

Table 19: Effect of reweighting on combined fit results for both fit variables considered.

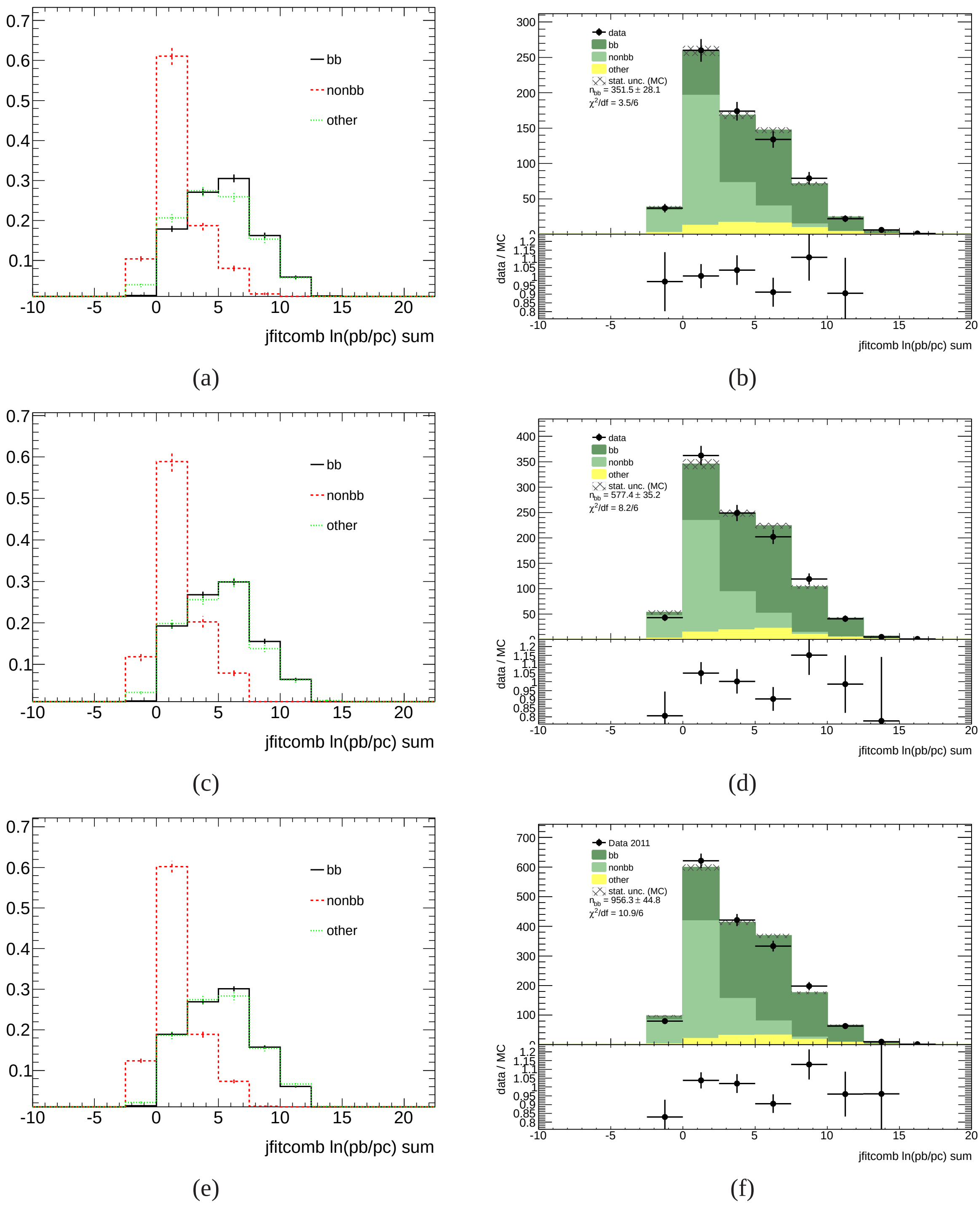

Figure 56: Templates and fit result obtained for the baseline fit approach, for (a, b) the electron and (c, d) the muon decay channel of the Z boson, respectively, as well as (e, f) for the combination of these as used in the cross section measurement. The baseline variable, based on $\ln(pb/pc)$, is used.

10.4 Validation of the fit procedure

For the technical implementation of the fit, the RooFit software [20], as provided within the Root package [21], was used. The fit was validated using 5 million toy MC events. As a closure test, the pull P

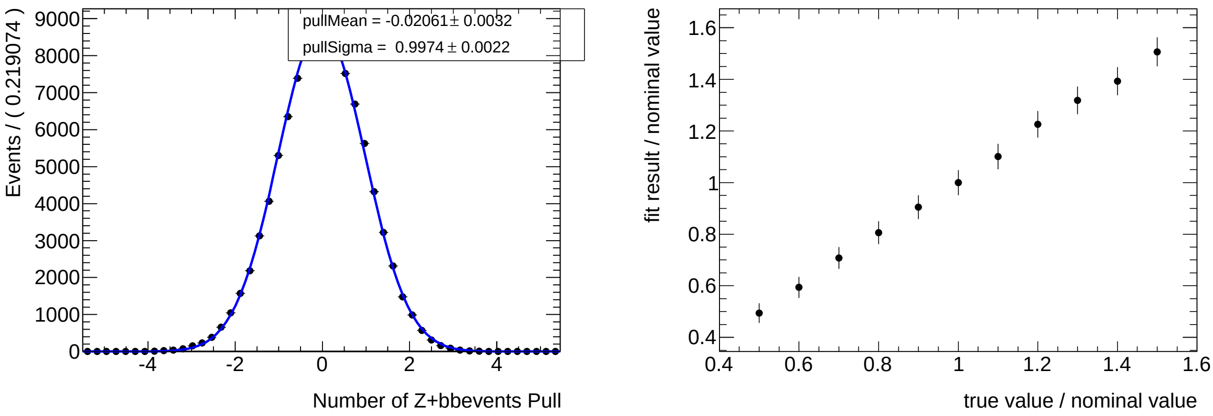

(a) (b)

Figure 57: Fit validation: (a) shows the pull distribution, (b) the linear response of the fit when varying the true fraction of signal in the toy MC sample.

defined as

$$P = \frac{x_{\text{fitted}} - x_{\text{true}}}{\sigma_{\text{fitted}}}$$

was calculated for each toy experiment. For the fit to pass the closure test the pull distribution is expected to have a mean value close to 0 and a width $\sigma \approx 1$. In order to test the linearity of the fit, the fraction of true $Z + bb$ events was systematically varied in steps of 10 % of the nominal fit value from 50 % to 150 % of the nominal. At each step, 100,000 toy experiments were performed. The mean and RMS of each set of toy experiments was plotted as function of the true $Z + bb$ fraction. The fits show a linear behaviour within statistical uncertainties, in agreement with the expectation. The Pull distribution and a plot showing the linear behaviour of the fits are shown in Figure 57.

11 Data - Monte Carlo comparison After Scaling

Having determined the need to scale up the heavy flavour contribution in the Monte Carlo, we now present a further data-Monte Carlo comparison after applying these scale factors. The scales applied are:

- in the inclusive Z+tagged jet sample, the *b*-jet contribution is scaled up by 1.45.
- in the Z+ 2xtagged jet sample, the *b*+non-*b*-jet contribution is scaled up by 1.33. The *bb* contribution is scaled up by 1.23.

All of these scale factors are simple normalisation changes; there is no dependence on kinematic variables. The difference in the two-tag sample between electron and muon channels is still visible. Taking into account only statistical errors, this is a 1.6σ effect. Again, a more detailed investigation into this difference is presented in Appendix B.

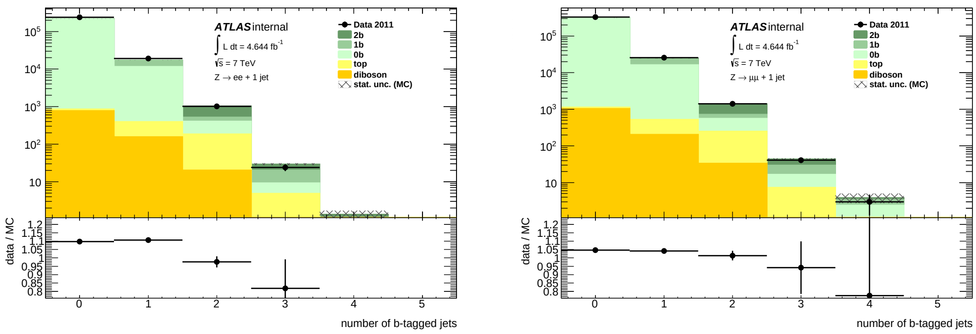

(a) (b)

Figure 58: Inclusive tagged jet multiplicity in the subsample with at least one jet.

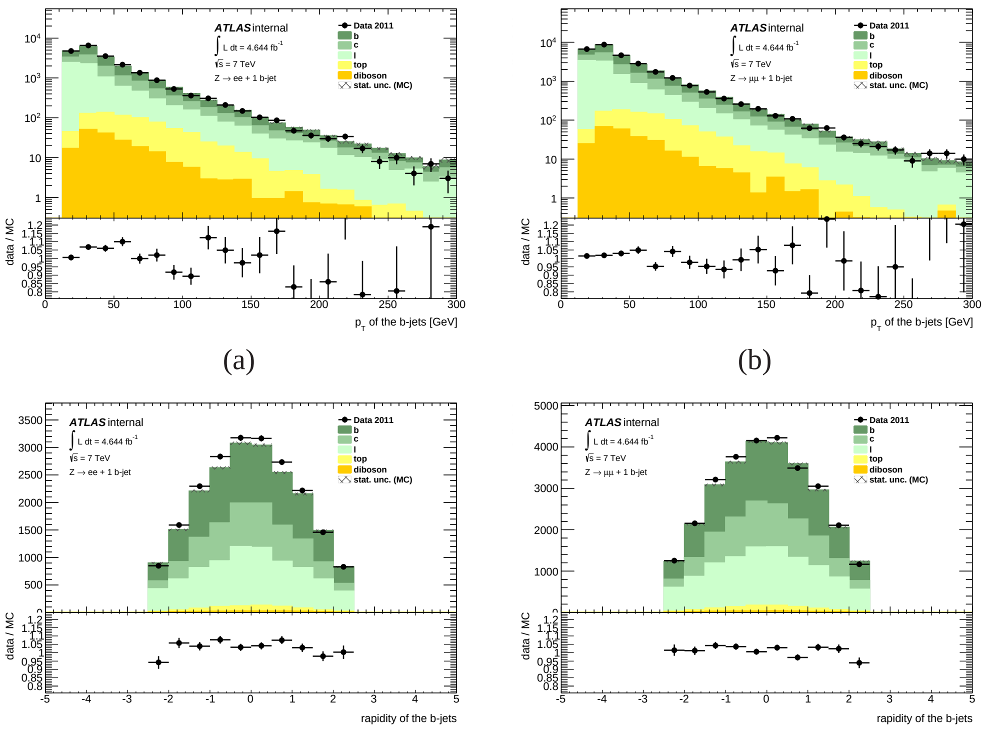

(a) (b) (c) (d)

Figure 59: Transverse momentum (a-b) and rapidity (c-d) of tagged jets for the sample with at least one tagged jets, shown for the electron and muon channel separately.

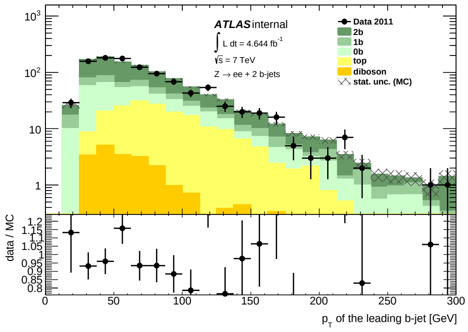

(a)

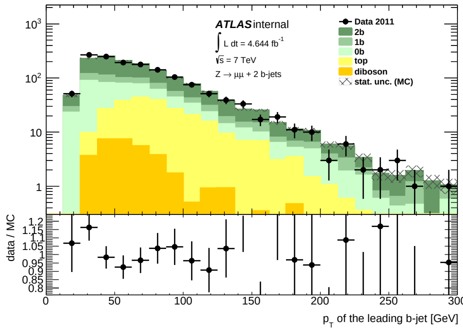

(b)

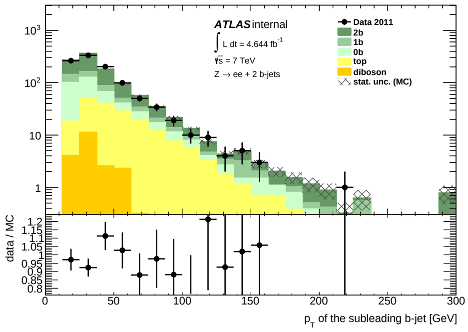

(c)

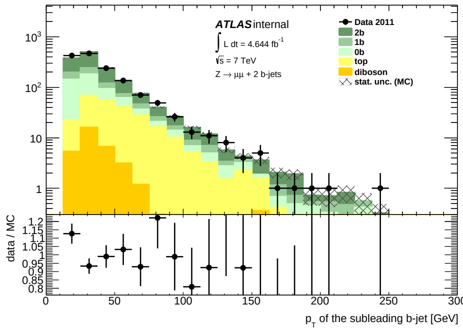

(d)

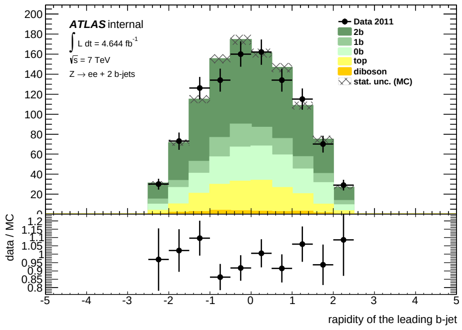

(e)

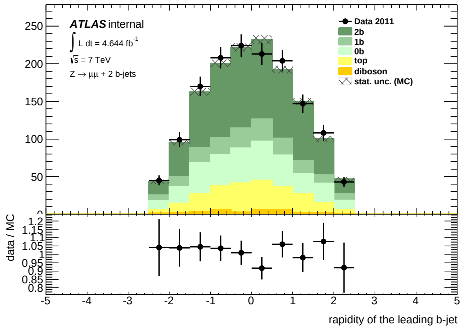

(f)

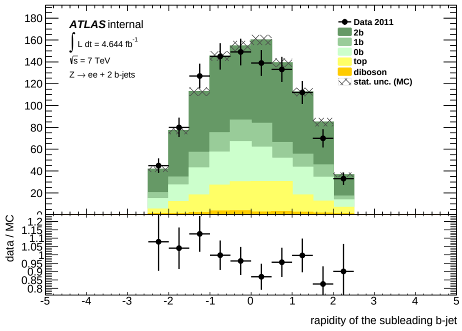

(g)

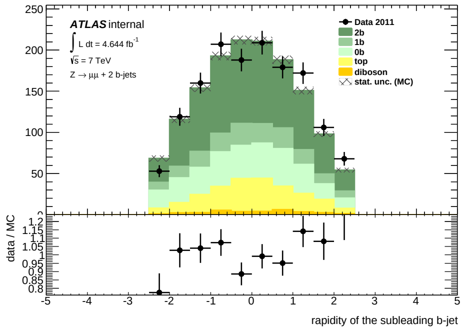

(h)

Figure 60: Transverse momentum leading and subleading tagged jet (a-d) and rapidity for the leading and subleading jets (e-h) for the sample with at least two tagged jets, shown in the electron and muon channels.

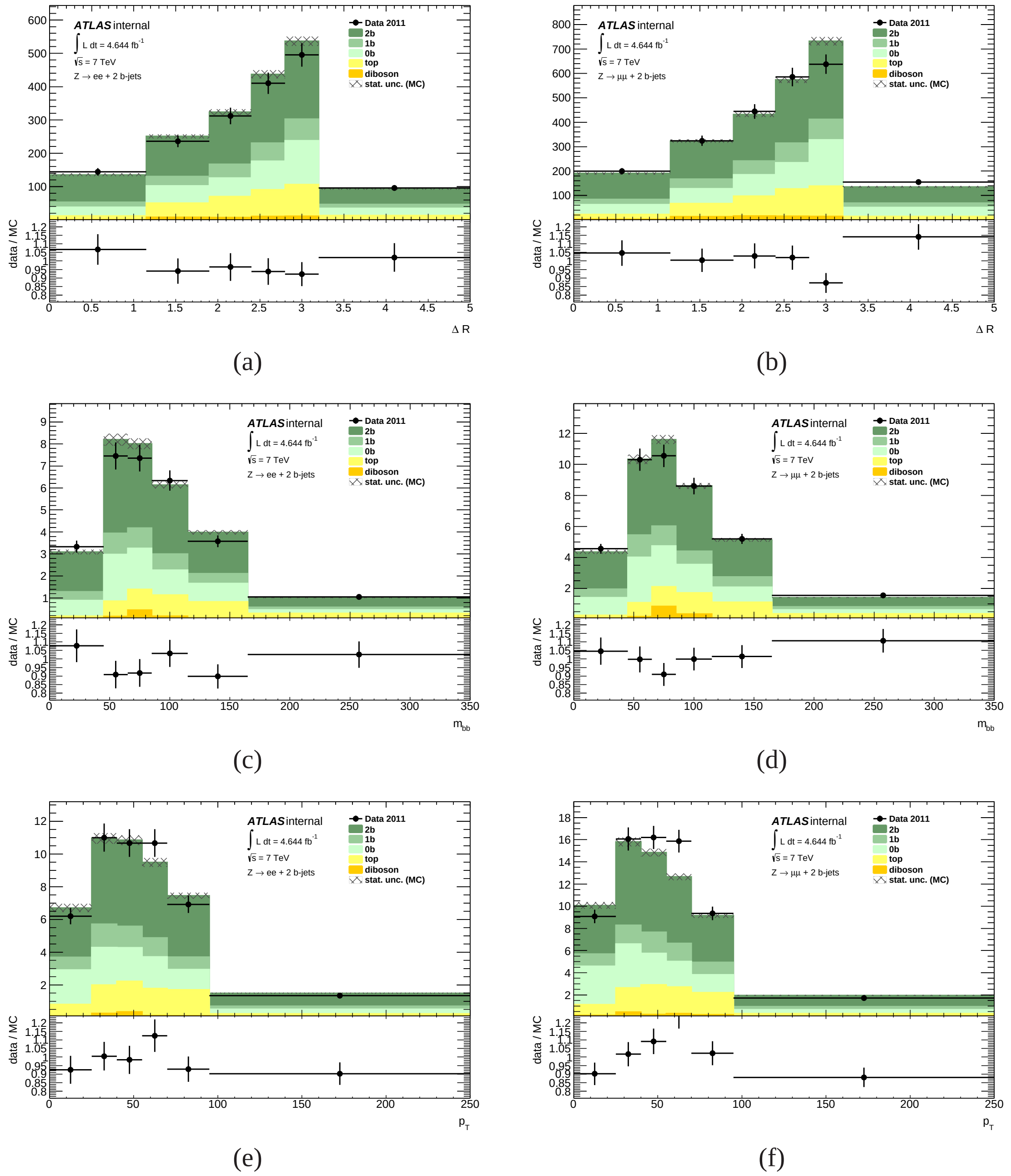

Figure 61: Distributions of the variables in which the differential $Z + bb$ measurement is performed.

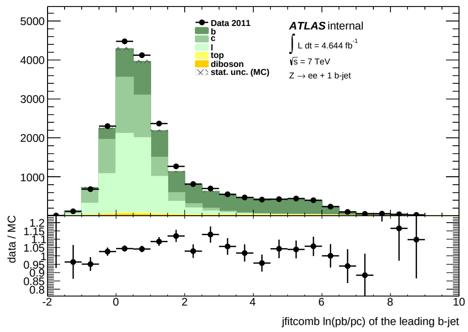

(a)

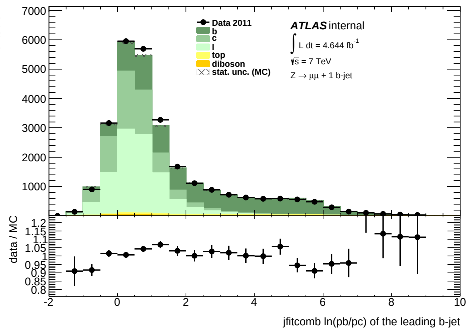

(b)

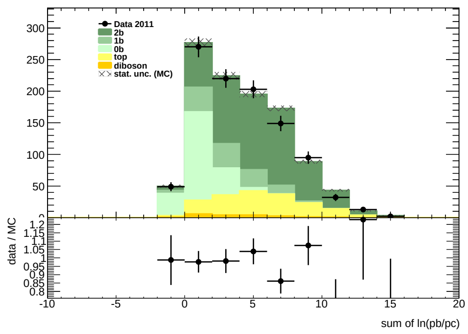

(c)

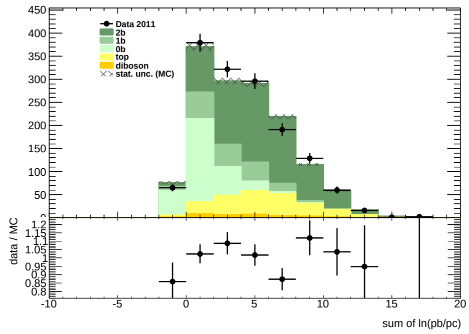

(d)

Figure 62: Variables used in determining the flavour composition. (a,b) show $\ln(pb/pc)$ of b-tagged jets in the subsample with at least 1 b tag required. (c,d) show the sum of the $\ln(pb/pc)$ values for the subsample selected by requiring 2 b tags. The various jet flavour templates are individually shown using the normlisation from the Monte Carlo, before the fit is performed.

12 Differential $Z + bb$ fits

For the differential $Z + bb$ cross-section measurement, the same discriminating variable is used, namely:

$$\ln \frac{p_{b,1}}{p_{c,1}} + \ln \frac{p_{b,2}}{p_{c,2}} \equiv \sum \ln \frac{p_b}{p_c}.$$

The fits to this variable are now performed in bins of 3 kinematic distributions: Zp_T, M_{bb}, $\Delta R(b, b)$. To reduce sensitivity to statistical fluctuations in the limited Monte Carlo samples, a template convolution method is used, described in Section 12.1. The fit results are then given in Section 12.2.

12.1 Template construction

The shape of the distribution for different flavour jet pairs is obtained from Monte Carlo simulation. Two methods to extract the templates can be used. The simplest method is to take the value of $\sum \ln(p_b/p_c)$ for each jet pair in MC. However, the finite size of the simulated event sample causes statistical fluctuations in these templates. To avoid this issue, a second method is introduced that creates a $\sum \ln(p_b/p_c)$ template from the $\ln(p_b/p_c)$ shape of individual jets. This so-called convolution method utilises the fact that the b-hadron decay is a process inside the jet, which can only depend on the properties of the containing jet. Moreover, it is found that the shape of $\ln(p_b/p_c)$ depends strongly on the p_{T} of the jet and very little on other jet variables. The convolution method exploits this relation by replacing the value of $\ln(p_b/p_c)$ for a jet of $p_{\mathrm{T}} = X$ by the distribution of $\ln(p_b/p_c)$ found for any jet of $p_{\mathrm{T}} = X$.

The convolution algorithm works as follows: in a sample of dijet pairs, the leading- versus sub-leading jet p_{T} is binned in a two-dimensional histogram. For each individual jet in this sample, the $\ln(p_b/p_c)$ value is binned as a function of jet p_{T}. To generate a dijet template of $\sum \ln(p_b/p_c)$, the algorithm loops over all bins in the p_{T} histogram with a non-zero number of entries. Via the p_{T} of the two jets, each of these bins corresponds to two single-jet templates. A partial dijet template is then generated by multiplying every bin in the first template with every bin in the second template, adding the result to the bin that corresponds to the sum of the bin values of the individual templates. The number of entries in bin n_k of this partial dijet template is therefore given by:

$$n_k(p_{\mathrm{T}1}, p_{\mathrm{T}2}) = \frac{1}{2} \sum_i \sum_{j=k-i}^{k-i+1} n_i(p_{\mathrm{T}1}) \times n_j(p_{\mathrm{T}2}).$$

Here the ambiguity that arises due to the granularity of the bins is resolved by splitting each contribution between two bins in the dijet template. To prevent this from smearing the distribution, the convolution is performed in a finer binning and the dijet template is rebinned afterwards. In this way each p_{T} combination from the two-dimensional dijet histogram results in a partial dijet template. By adding the dijet templates for all these combinations, scaled by the number of times a combination occurs, a smooth dijet template is obtained.

A comparison between the templates extracted directly from Monte Carlo and those generated using the convolution method is show in Fig. 63. The two methods show good agreement.

12.2 Fit method and results

The true number of bb pairs is fitted differentially in bins of the p_{T} of the Z boson, the invariant mass of the bb pair and the distance between the two b-jets. For each of these bins, three templates of $\sum \ln(p_b/p_c)$ are constructed from Monte Carlo. The double-b template contains $Z+bb$ events for which both b-tagged jets are true b-jets. The flavour combinations uu, cu, cc, bu and bc are added together and will be referred to in the figures as “other”. In this template the single-b contributions (bu and bc) are scaled by a factor

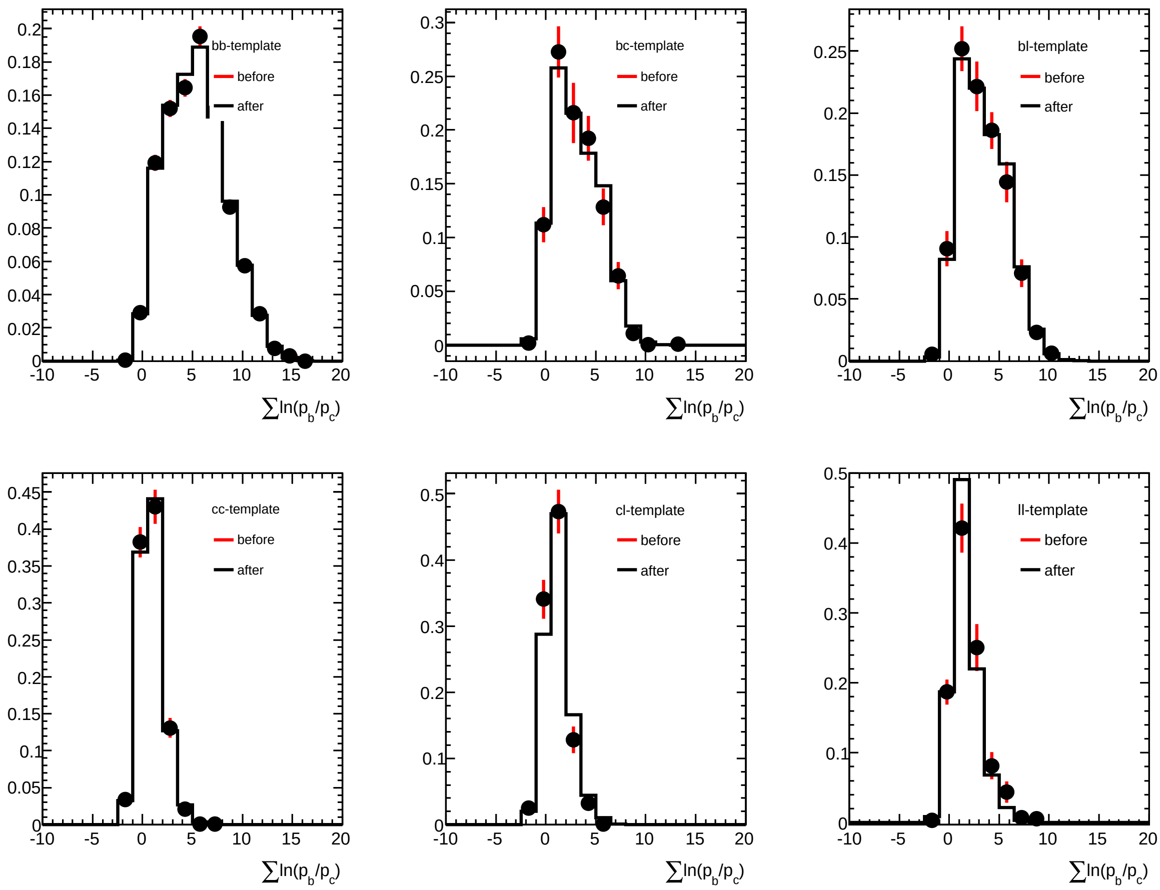

Figure 63: Comparison of the templates extracted directly from Monte Carlo (before) and when applying the convolution method (after). The six figures show the distribution of $\sum \ln(p_b/p_c)$ for the flavour combinations *bb*, *bc*, *bu*, *cc*, *cu* and *uu* respectively.

of 1.37 as determined from the $Z+b$ fits. Finally, a background template is used, representing the background events that pass the $Z+bb$ signal selection. The normalisation of the background template is fixed to the expected number of background events, leaving only the normalisation of the bb and non-bb templates as free floating parameters. The fit results are shown in Figs. 64, 65 and 66.

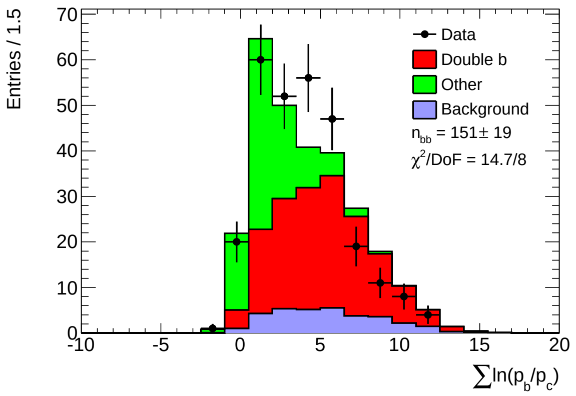

(a) $p_{T,Z} < 25\,\mathrm{GeV}$

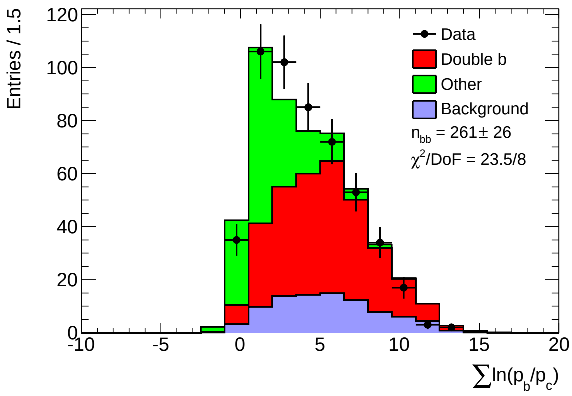

(b) $25 < p_{T,Z} < 40\,\mathrm{GeV}$

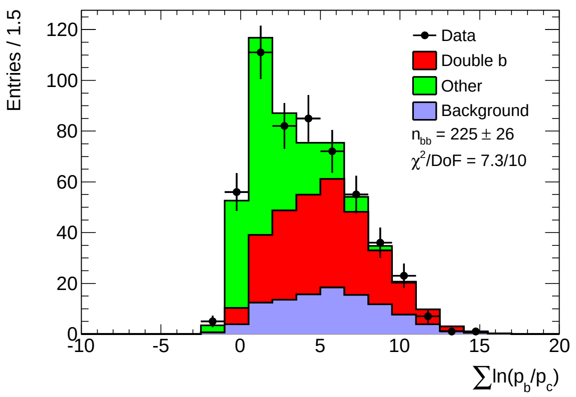

(c) $40 < p_{T,Z} < 55\,\mathrm{GeV}$

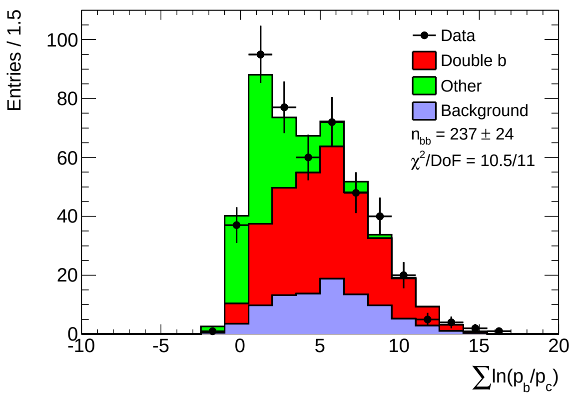

(d) $55 < p_{T,Z} < 70\,\mathrm{GeV}$

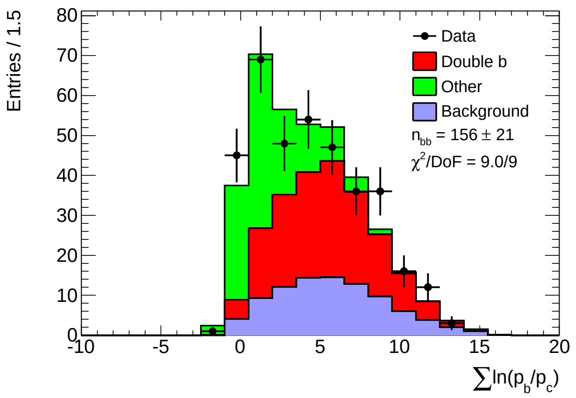

(e) $70 < p_{T,Z} < 95\,\mathrm{GeV}$

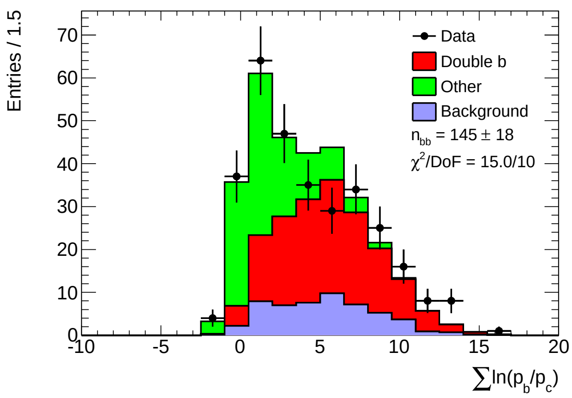

(f) $95 < p_{T,Z} < 250\,\mathrm{GeV}$

Figure 64: Result of fitting the number of true bb pairs, n_{bb}, in bins of Z transverse momentum.

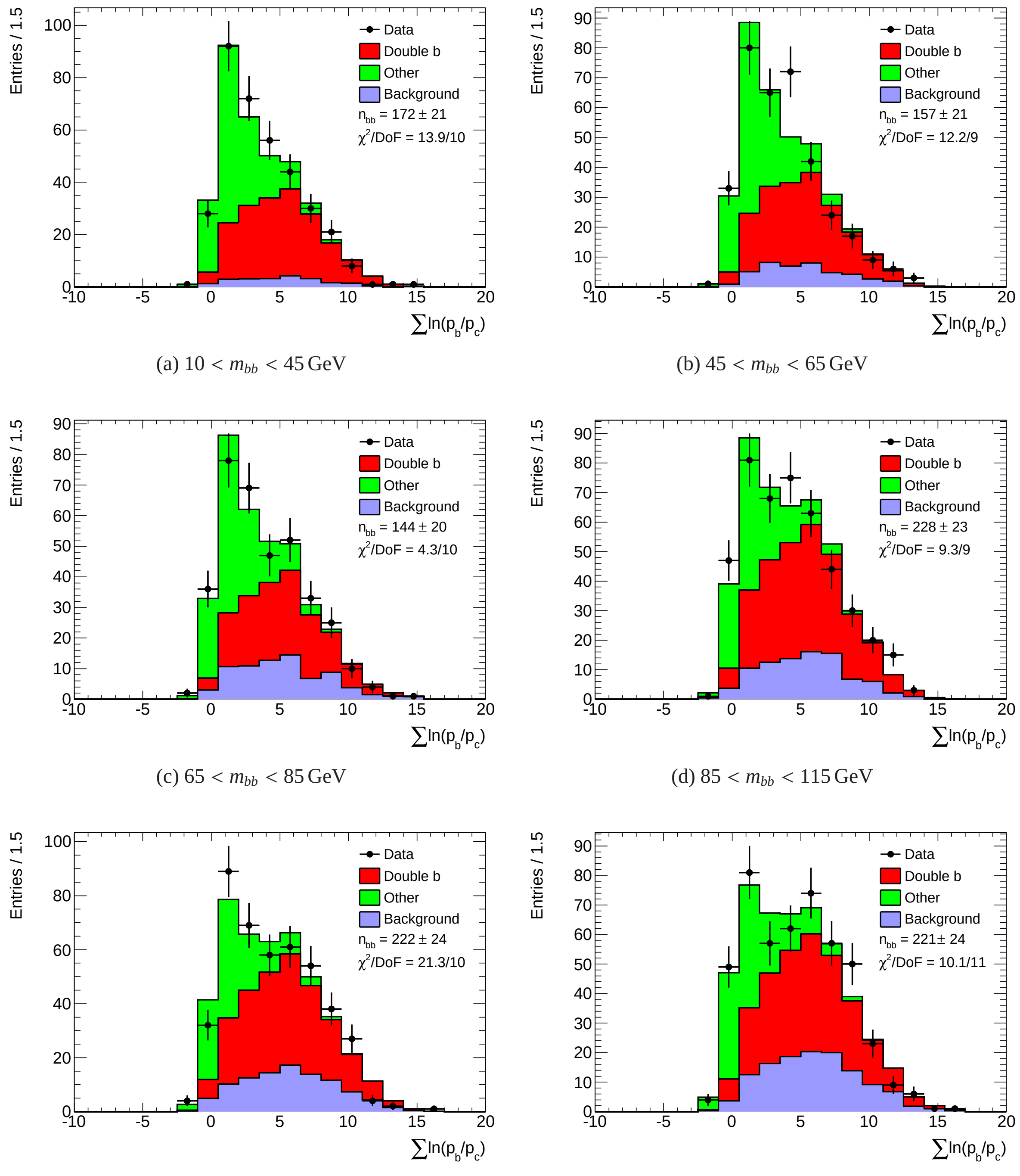

(a) $10 < m_{bb} < 45$ GeV

(b) $45 < m_{bb} < 65$ GeV

(c) $65 < m_{bb} < 85$ GeV

(d) $85 < m_{bb} < 115$ GeV

(e) $115 < m_{bb} < 165$ GeV

(f) $165 < m_{bb} < 350$ GeV

Figure 65: Result of fitting the number of true bb pairs, n_{bb}, in bins of the invariant mass of the b-jet pair.

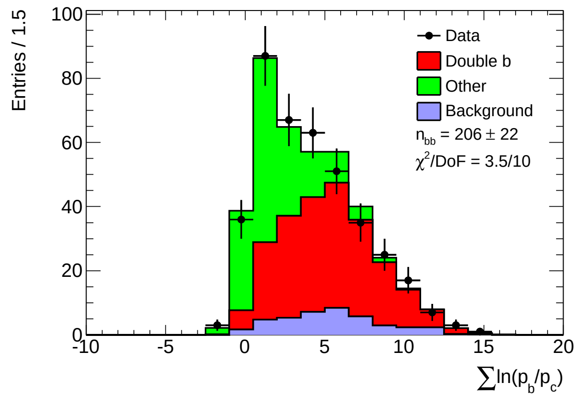

(a) $0.4 < \Delta R_{bb} < 1.15$

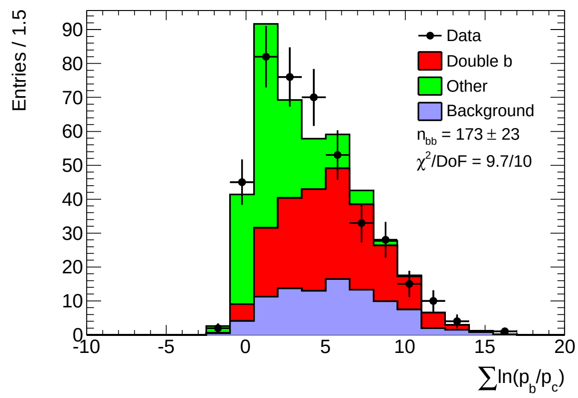

(b) $1.15 < \Delta R_{bb} < 1.9$

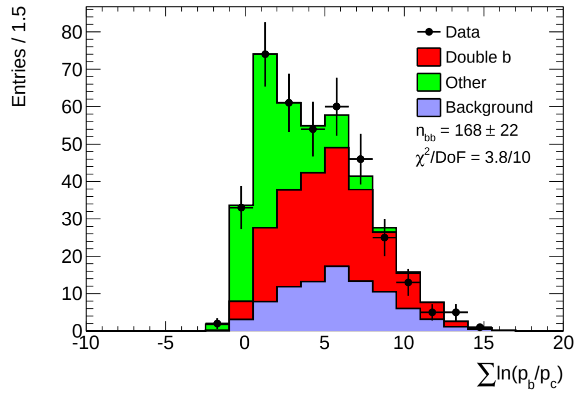

(c) $1.9 < \Delta R_{bb} < 2.4$

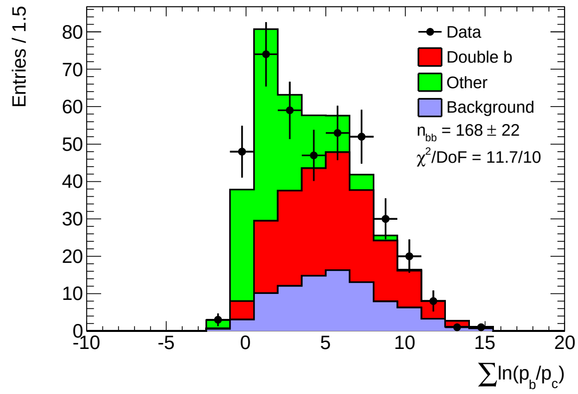

(d) $2.4 < \Delta R_{bb} < 2.8$

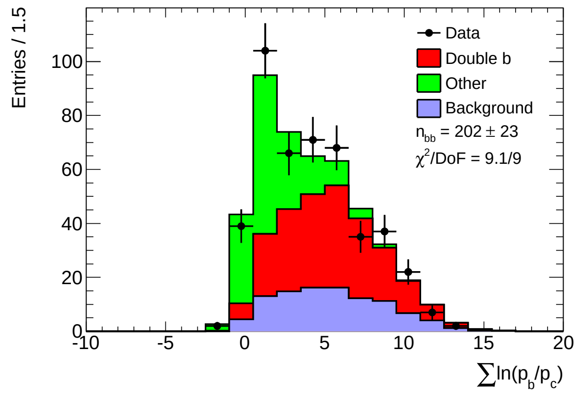

(e) $2.8 < \Delta R_{bb} < 3.2$

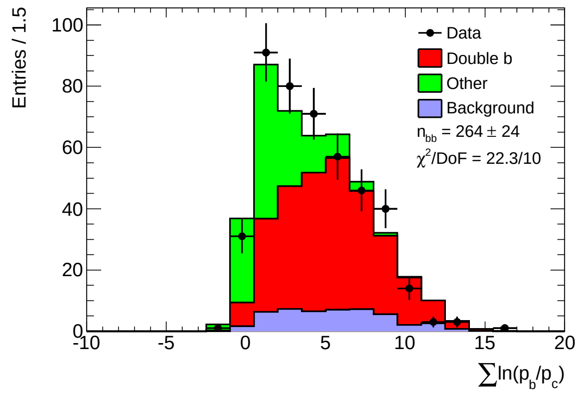

(f) $3.2 < \Delta R_{bb} < 5$

Figure 66: Result of fitting the number of true bb pairs, n_{bb}, in bins of the distance ΔR between the two b-jets.

13 Unfolding the Z+bb Distributions

The next step is to correct the fitted b-jet yields for resolution and efficiency effects. The method proceeds as follows:

- the fits to $\Sigma \ln(pb/pu)$ yield the number of reconstructed Z+ jet events where at least two jets b-tagged and contain b-hadrons. This is either the total number, or in bins of a distribution.
- this number is corrected for the b-tagging efficiency, using a correction derived in Monte Carlo
- a bin-by-bin correction (or C-factor) is then applied, to correct for detector resolution effects and other reconstruction inefficiencies, such as the trigger, lepton efficiencies and jet reconstruction, as well as the cut on Missing transverse energy, which is not applied at particle level. For the differential distributions, this result is cross-checked using the Bayesian unfolding method, as implemented in RooUnfold.
- the result is then divided by the luminosity, to obtain a cross section, and a factor of 2 to convert the $ee + mumu$ result to a per-lepton result.

More details on these steps are provided in this Section.

13.1 b-Tagging Efficiency Correction

Before unfolding, the fitted Z+bb yields are corrected for the b-tagging efficiency. This is done based on detector level quantities, as the efficiencies were determined based on detector-level jets. It is calculated from Monte Carlo of all events with a reconstructed Z and at least two jets, where at least two of these jets contain b-hadrons, divided by the number of the same events where both b-jets are also b-tagged.

Figure 67 shows this correction factor as a function of the three differential variables being studied.

13.2 Unfolding

To perform the unfolding, the resolution and efficiency 2D matrix is filled in Monte Carlo for each distribution as follows:

1. all events passing the reconstruction level selection are put in the underflow of the y axis, applying all reconstruction level scale factors and generator level weights.
2. all events passing the particle level selection are put in the underflow of the x axis, applying only the generator level weights.
3. event which pass both reco and particle level, and in which the the leading reco b-jets match the leading particle b-jets (based on a simple $\Delta R < 0.4$ matching) are also put into the body of the matrix, plotting the particle quantity against the reconstructed, applying all reconstruction level scale factors and generator level weights.

For this matrix, simple bin-by-bin corrections (C-factors) can be calculated from the ratio of 2/1. A C-factor for the inclusive sample is simply the integral of 2 divided by the integral of 1. When cross-checking the full unfolding using the Bayesian method, the matrix (3) is also used.

13.2.1 Fiducial $Z + b\bar{b}$ inclusive cross section

All parts are now in place to extract the total fiducial Z+bb cross section. Table 20 details the fitted yields, b-tagging efficiency and C-factor for each lepton channel, and the combined. Using the recorded luminosity, the cross section times $Z \to ll$ branching fraction is also given in the Table.

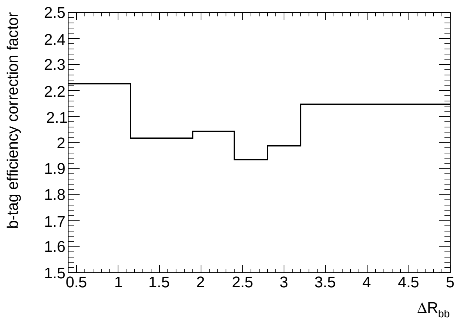

(a)

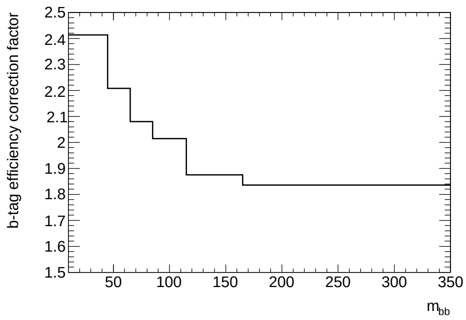

(b)

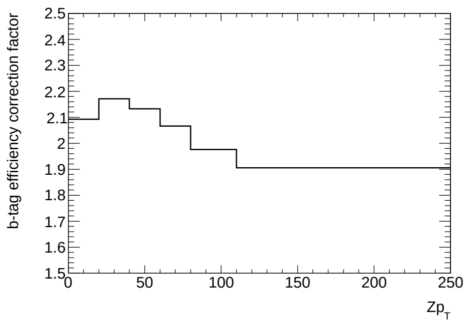

(c)

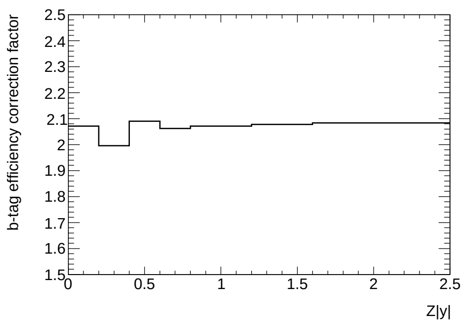

(d)

Figure 67: Correction factor for the b-tagging efficiency in the Z+bb analysis. Shown as a function of (a) $\Delta R(b,b)$, (b) M_{bb}, (c) Zp_T and (d) $Z|y|$.

term	electron channel	muon channel	combined
$n_{2b,fit,\ell}$	483.8	727.3	1207.5
$N_{mt,rec}$	380.5	500.4	880.4
$N_{m,rec}$	767.4	1027.8	1794.4
$N_{m,true}$	1804.7	1802.9	3607.8
$\epsilon_{2b,\ell}$	0.50	0.49	0.49
C_ℓ	0.43	0.57	0.50
$\mathcal{L}_\ell$	4579.9	4579.9	4579.9
$\sigma(Z + b\bar{b}) \cdot BR$	0.501	0.572	0.540

Table 20: Terms contributing to the cross section, separately for electron and muon channel and for the combined measurement.

13.3 $Z + b\bar{b}$ differential cross sections

For the differential $Z + bb$ measurements, bin-by-bin unfolding is used by default, with Bayesian unfolding used as a cross check. Unfolding matrices with some additional informational plots are shown in Figures 68 - 71. The additional plots show:

- *Matching correction* shows the fraction of reconstructed events that also pass the particle level selection. This "fake" correction therefore removes events from the reco sample that fail the particle level selection (generally due to migration effects). It is handled either as a separate step in the Bayesian unfolding, or is simply folded into the bin-by-bin correction.
- *Efficiency correction* shows the factor to correct for events that are not reconstructed. This is the number of particle level events in a given bin, divided by the number that are also reconstructed.
- *Efficiency*, is calculated from all particle level events that are also reconstructed, and is the fraction in a given bin that are also reconstructed in the same bin. Low efficiencies implies a non-diagonal resolution matrix.
- *Purity*, defined as the fraction of reconstruction level events in a given bin that originate in the same bin at particle level. Purity contains similar information to the efficiency, convoluted with the shape of the distribution in question.

It can be seen that the efficiencies are all very high, hence the matrix is highly diagonal and the simpler approach of bin-by-bin unfolding is justified.

Statistical uncertainties on the unfolded distribution are determined using ensemble testing.

- 5000 pseudo-datasets are derived from the fitted b-jet yield in real data. For each pseudo-dataset, the bin contents are fluctuated randomly within a Gaussian distribution with a width given by the fit uncertainty.
- all pseudo-datasets are then unfolded and compared the the nominal data result. In the case of bin-by-bin unfolding, the RMS if the spread in each bin is assigned as the statistical uncertainty.
- For the Bayesian unfolding, The full covariance and correlation matrix is calculated. The number of iterations for the unfolding is chosen based on the behaviour of the correlation matrix, stopping at 4 iterations gives bin-to-bin correlations which reasonably mimic the correlations expected from the form of the migration matrix, with no large off-diagonal elements. Too few iterations underestimates the correlations; too many results in large off-diagonals as the method converges on the full matrix inversion solution.

To perform a closure test and to estimate the unfolding bias, the unfolded data are folded back through the migration matrix (including the effects of the efficiency correction and matching correction) and compared to the input data distribution. The results of this “folding test” are shown in Figures 72 to 75. It can be seen that the two unfolding methods agree well, and any unfolding biases are generally small.

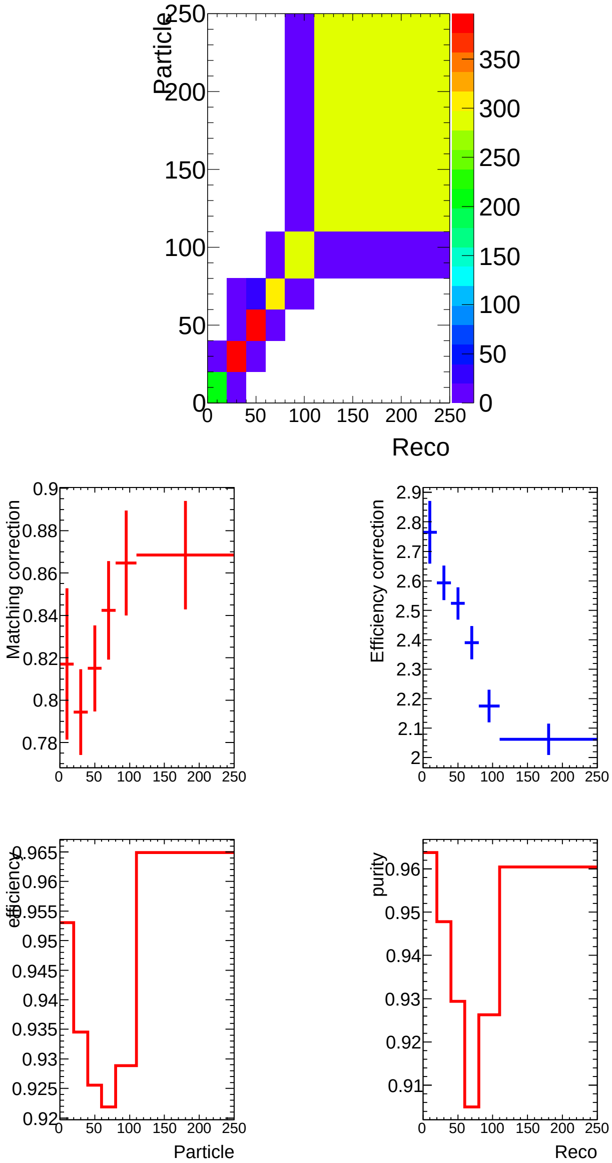

Figure 68: Top: the migration matrix for Z boson p_{T} ($Z + bb$ differential measurement). Middle left: the matrix efficiency; middle right: the matrix purity. Bottom left: the matching correction, bottom right: the efficiency correction. All defined in the text.

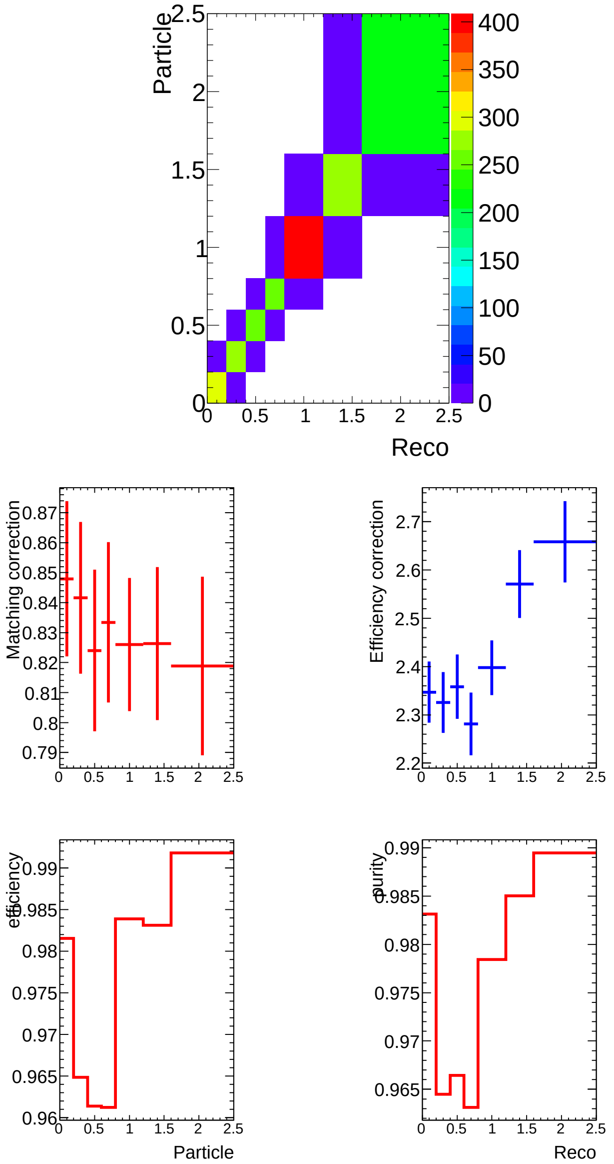

Figure 69: Top: the migration matrix for Z boson y ($Z + bb$ differential measurement). Middle left: the matrix efficiency; middle right: the matrix purity. Bottom left: the matching correction, bottom right: the efficiency correction. All defined in the text.

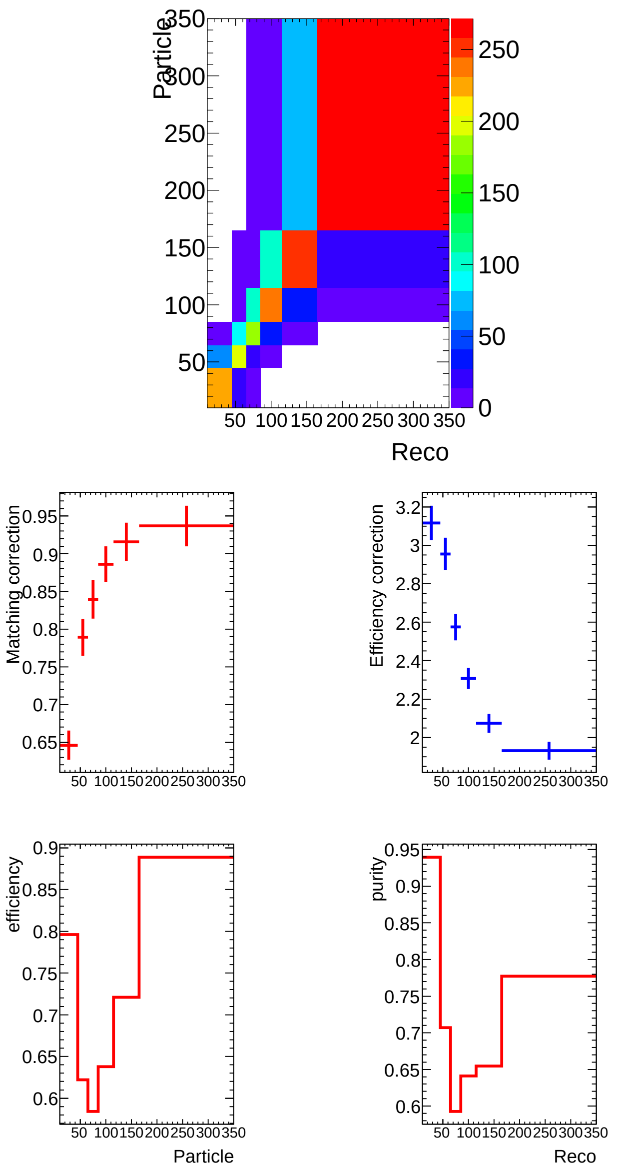

Figure 70: Top: the migration matrix for *bb* mass (*Z* + *bb* differential measurement). Middle left: the matrix efficiency; middle right: the matrix purity. Bottom left: the matching correction, bottom right: the efficiency correction. All defined in the text.

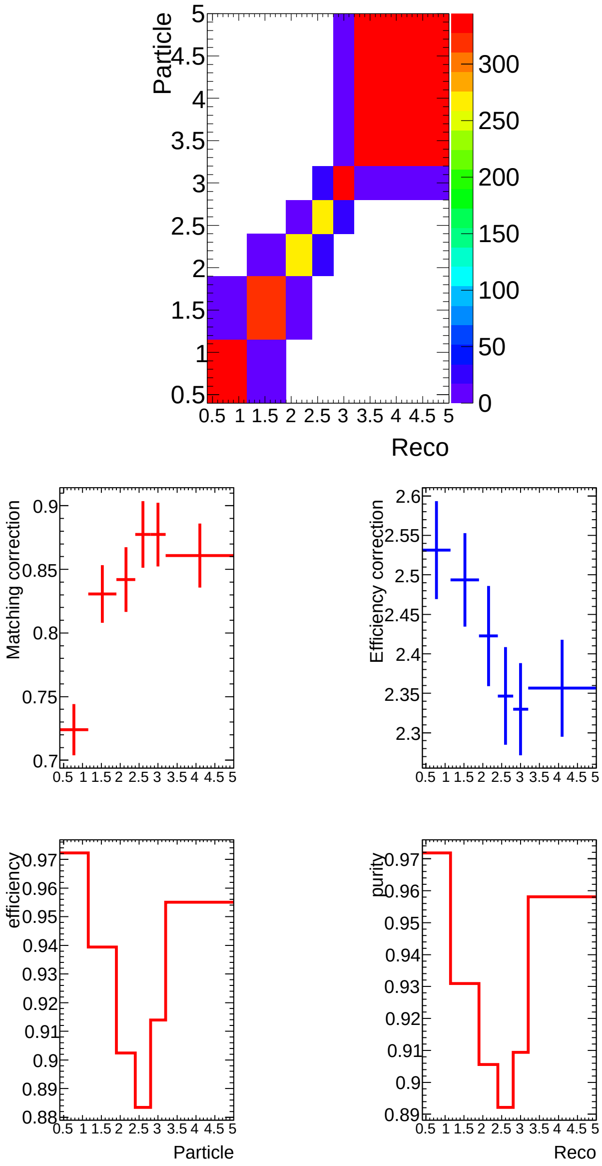

Figure 71: Top: the migration matrix for $\Delta R(bb)$ ($Z + bb$ differential measurement). Middle left: the matrix efficiency; middle right: the matrix purity. Bottom left: the matching correction, bottom right: the efficiency correction. All defined in the text.

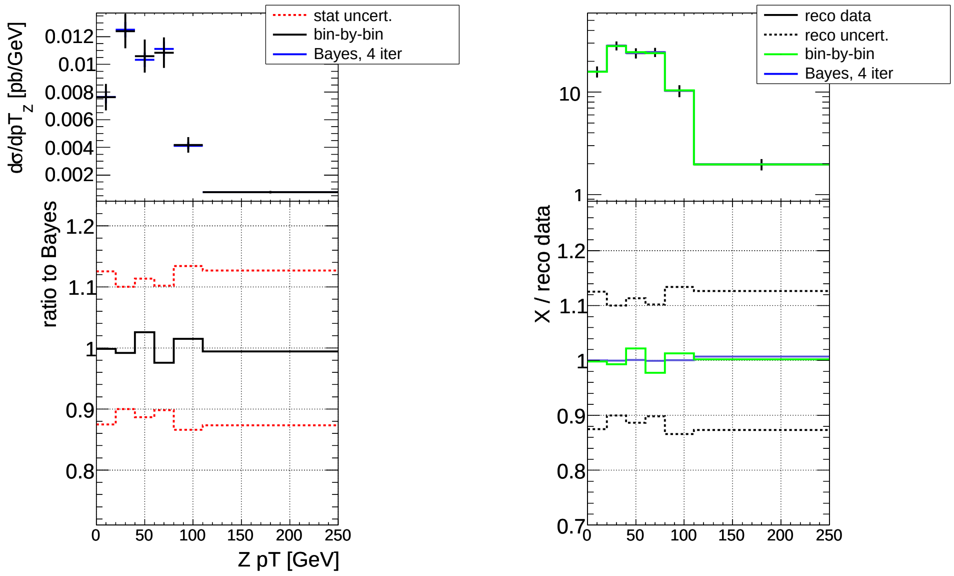

Figure 72: Left: comparison between different unfolding methods at particle level for Z boson p_{T} ($Z+bb$ differential measurement). Right: closure test result. The unfolded data (obtained using either Bayesian or bin-by-bin unfolding) is folded back through the matrix and compared to the detector level data. The ALPGEN+HERWIG distributions are shown for comparison.

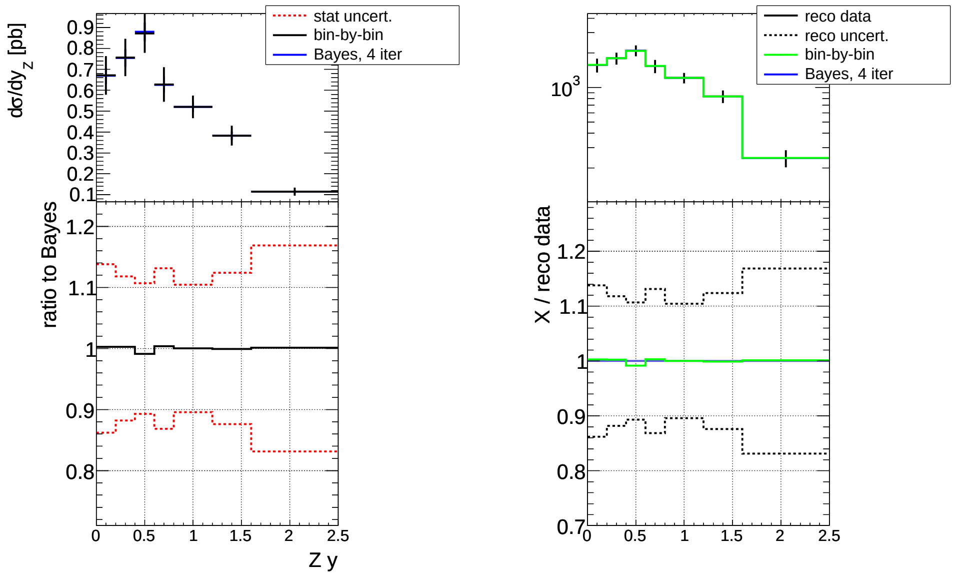

Figure 73: Left: comparison between different unfolding methods at particle level for Z boson y ($Z+bb$ differential measurement). Right: closure test result. The unfolded data (obtained using either Bayesian or bin-by-bin unfolding) is folded back through the matrix and compared to the detector level data. The ALPGEN+HERWIG distributions are shown for comparison.

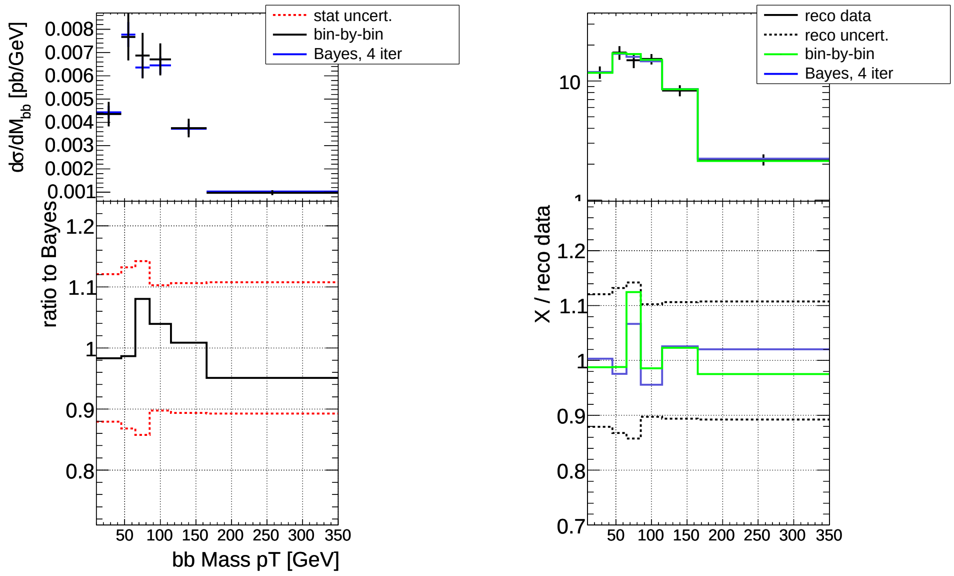

Figure 74: Left: comparison between different unfolding methods at particle level for bb mass ($Z + bb$ differential measurement)). Right: closure test result. The unfolded data (obtained using either Bayesian or bin-by-bin unfolding) is folded back through the matrix and compared to the detector level data. The ALPGEN+HERWIG distributions are shown for comparison.

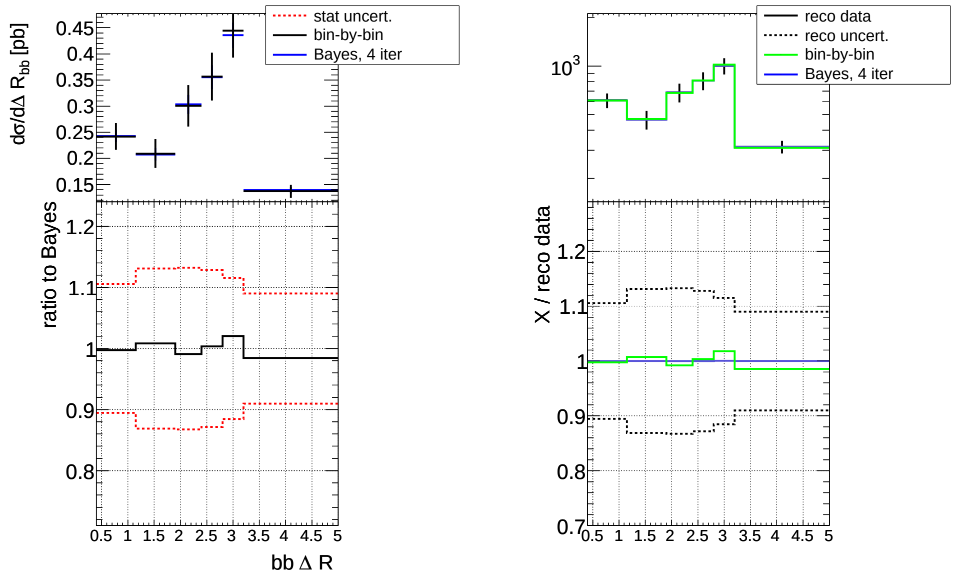

Figure 75: Left: comparison between different unfolding methods at particle level for $\Delta R(bb)$ ($Z + bb$ differential measurement). Right: closure test result. The unfolded data (obtained using either Bayesian or bin-by-bin unfolding) is folded back through the matrix and compared to the detector level data. The ALPGEN+HERWIG distributions are shown for comparison.

14 Systematic Uncertainties

In this following section we list the systematic uncertainties considered. All systematic shifts are applied to Monte Carlo predictions only. They are taken into account for the fit of the signal yield and also applied to the unfolding and corrections.

14.1 CP Group uncertainties

The software packages that are used for this evaluation are listed in Table 5.

14.1.1 b-Tagging efficiency

The dominant systematic for this analsis is the uncertainty on the b-tagging efficiency. We break down this efficiency uncertainty into the 10 eigenvectors for b-jets, but do not decompose the charm and light jet uncertainties as these are significantly smaller in the final result. To estimate this uncertainty the scale factors that are applied to the MC (see Section 4) are shifted up and down within the uncertainties (provided by the BTagging Calibration Interface, [22]). Since the efficiency and the inefficiency are anti-correlated one has to shift one up when the other is shifted down and vice-versa. This is done separately for b-jet, c-jet and mistag efficiency scale factors. Default scale factors are used for b-jets with p_T¿300GeV, no addition extrapolation factor is applied.

14.1.2 Jet Energy Scale

The uncertainty on the jet energy has been derived using the MultijetJESUncertaintyProvider tool that is provided by the Jet/Etmiss group ([23]). In this analysis, the breakdown into 16 individual nuisance parameters is used.

14.1.3 Jet Energy Resolution (JER)

To account for a possible underestimate of the jet energy resolution in simulation an additional p_T smearing is added to the jets [24]. The resulting change in the cross section is symmeterised to obtain an estimate of the downward shift in resolution.

14.1.4 Lepton identification efficiency, energy scale and resolution

The lepton identification efficiencies are applied as recommended by the Egamma and muon performance groups. Both for the electron and for the muon case the efficiency scale factors (see Section 4) are varied upwards and downwards according to the given uncertainty. This is derived as a function of the kinematic properties of the leptons. The electron and muon momentum scale and resolution are also varied within their uncertainties as determined by the relevant CP groups.

14.2 Luminosity uncertainty

An uncertainty of 1.8 % on the delivered luminosity is assumed [25].

14.3 $t\bar{t}$ cross-section prediction

The overall normalisation for the template that corresponds to the non-Z+jets contribution is fixed in the fit of the signal yield. The theoretical prediction for the inclusive $t\bar{t}$ production cross section is $\sigma_{t\bar{t}} = 166.8^{+16.5}_{-17.8}\ pb$ ([26] [27] [28] [29]). To estimate the impact of this uncertainty on the normalisation the fit is applied with $\sigma_{tt} + \Delta\sigma_{tt}$ and $\sigma_{tt} - \Delta\sigma_{tt}$.

14.4 Estimate of systematic uncertainty due to gluon splitting and MPI effects

Using the *MPI* and gluon splitting flags obtained for events with a b parton from the HFOR procedure, the systematic uncertainty resulting from these components is estimated by doubling their contribution to the light jet sample and symmetrizing the resulting difference with respect to the nominal result.

14.5 b-Jet Template Shape Uncertainty

As described in section 5 the $\ln(pb/pc)$ distribution for b-jets is observed to be mis-modelled in a top pair control region. To correct for this in signal selected events, weights are applied to HERWIG showered MCs with significant b-jet contributions to correct charge particle multiplicities from b hadron decays to emulate those expected from EvtGen. These weights intentionally modify the b template shapes for both signal and real b-jet background aiming to bring them closer to that expected for b-jets in data. However, corrections to decay tables do not account for additional mis-modellings which may come from hadronisation or b hadron decay daughter reconstruction efficiency. Section 5.4 describes an alternative data-driven weighting scheme based on the top pair control region which can be directly applied to the signal region. The derived functional form of the data/MC ratio from that study provides a per b-jet weight as a function of $\ln(pb/pc)$ for the range (2.0,9.0), jets outside of this range are assigned weights of unity. b-jet templates are then derived from the Alpgen MC replacing the event level EvtGen weight with this alternative jet level weight. The fits are then repeated and the difference between the EvtGen weighted fits and alternative weighted fits are taken as a measure of template shape uncertainty. Although this method yields an inherently one sided measurement the result is symmeterised when assigned as a systematic uncertainty.

14.6 Non-b Template Shape Uncertainty

Fit results are less sensitive to mis-modelling of the light and charm jet templates, whose shapes are almost degenerate in $\ln(pb/pc)$, as their distributions are narrow and well separated from the b-jet dominated region. However, mis-modelling of jet fragmentation or charm hadron decay charge particle multiplicities are among the physics effects which could bias these shapes if the MC provides a poor model of such processes. In order to evaluate the size such distortions might have on the fit result the Alpgen template shapes are re-weighted to emulate those expected from an alternative simulation provided by Sherpa with identical event selection requirements. Fits are then repeated with the non-b template components re-weighted and the difference taken as a symmeterised systematic uncertainty.

14.6.1 Charm Jets

Charm jet templates from Sherpa simulation of Z+jet events are derived from samples generated with massive b and c quarks and then filtered for heavy flavour hadrons. For charm the filter requires no weakly decaying b hadron of any p_T with $|\eta| < 4.0$, and then requires at least one weakly decaying c hadron of any p_T with $|\eta| < 4.0$. The sample thus provides a pure truth level selection of events containing a Z boson and at least one charm hadron coming from the matrix element or shower but not from b hadron decays. Figure 76 shows the inclusive comparison of charm jets from Sherpa to the default selection from Alpgen. The ratio is found to be well fitted with a 2nd order polynomial with χ^2/DoF=6.48/5, the fitted parameters are given in table 21. The fit is restricted to the range (−1.0,3.0), jets outside of this range are assigned weights of unity. The function provides per jet weights as a function of $\ln(pb/pc)$ which are applied when forming the Alpgen charm template to emulate the response of $\ln(pb/pc)$ for charm in Sherpa.

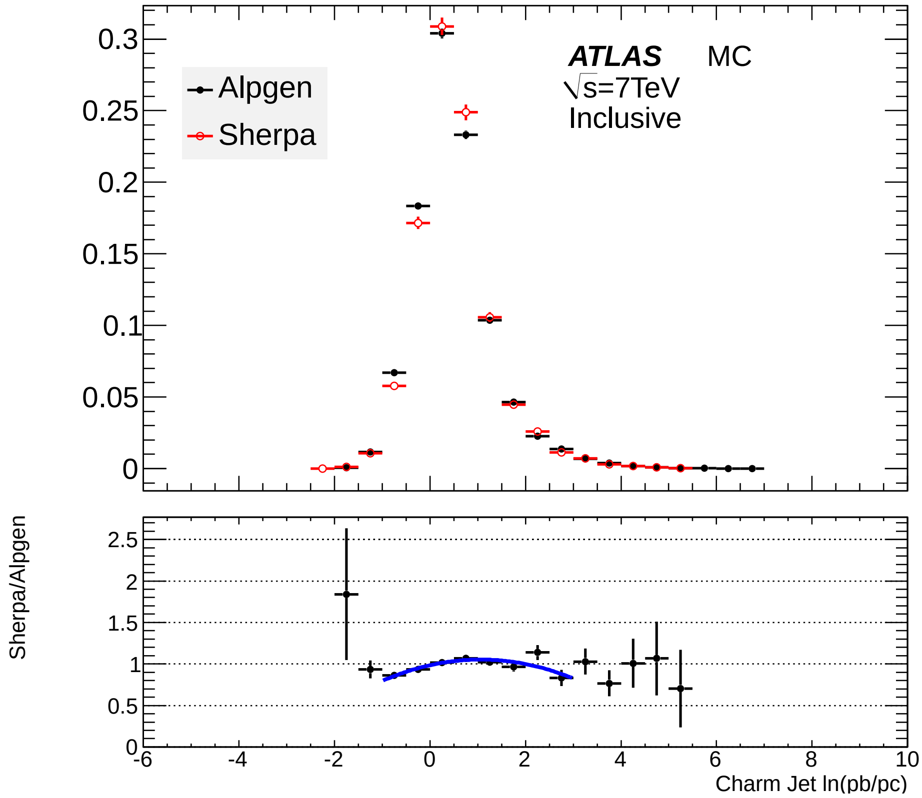

Figure 76: Distribution of $\ln(pb/pc)$ for charm jets comparing Sherpa and Alpgen MC with identical selection. The ratio is fitted with a second order polynomial which is used to re-weight templates containing charm jets as a systematic uncertainty.

14.6.2 Light Jets

The method for obtaining a re-weighted Alpgen distribution for light jets is analogous to that for charm jets described above. However, the light filtered samples generated with massive b and c quarks provide too few statistics to derive a usable weight function. Instead higher statistics MEnloPS Z+jets Sherpa samples are used; however, these samples are generated with massless b quarks which causes the soft $b\bar{b}$ contribution from gluon splitting in the final state to be significantly enhanced. Consequently there is an unphysical contribution to the light templates from jets containing soft b hadrons (i.e., with $p_T < 5$ GeV). Therefore, before forming a light jet template from this sample any event with a b hadron in the truth record is vetoed. Figure 77 shows the inclusive comparison of selected light jets from Sherpa compared to the default selection from Alpgen. The ratio is again found to be well fitted with a 2nd order polynomial with χ^2/DoF=6.46/5, the fitted parameters are given in table 22. The fit is restricted to the range $(-1.0, 3.0)$, jets outside this range are assigned weights of unity. As for charm, the function provides per jet weights as a function of $\ln(pb/pc)$ which are applied when forming the Alpgen templates so they emulate the $\ln(pb/pc)$ light jet shapes from Sherpa.

14.7 Single-b template normalisation uncertainty for Z+bb

When combining the bc and bl with cc, cl and ll templates to make the non-bb template, the single-b contribution was scaled up from the Monte Carlo prediction, based on a fit to data. This scaling is varied within the systematics obtained in Section 10.2:

Parameter	Fitted Value
p0	0.985±0.015
p1	0.129±0.027
p2	−0.061±0.016

Table 21: Fitted polynomial parameters for charm jets used to derive weights used for template systematic uncertainties.

Parameter	Fitted Value
p0	0.983±0.014
p1	-0.017±0.028
p2	−0.034±0.017

Table 22: Fitted polynomial parameters for light jets used to derive weights used for template systematic uncertainties.

- the single-b component (bu and bc) of the non-bb template is scaled up and down by 15%;
- the c-component is scaled up and down by 15%;

14.8 Monte Carlo Statistics

The Monte Carlo statistical error directly enters the bin-by-bin unfolding correction, as well as the b-tagging efficiency correction. This statistical uncertainty is propagated to the final cross section results.

14.8.1 Statistical correlation in unfolding

For the Zb analysis by default the impact of MC statistics on the unfolding is evaluated by simultaneously smearing all bins in the migration matrix using a random Gaussian fluctuation with the relative statistical uncertainty of that bin as the standard deviation. This is repeated 5000 times and the σ of those 5000 unfolded values for a given bin taken as the relative uncertainty. To first order this gives an uncertainty $\sim \sqrt{N}$ of the diagonal element in a given analysis bin. However this is conservative as events in the migration matrix are statistically correlated with the fiducial truth histogram also used in RooUnfold. A full treatment using binomial formalism will be made before approval.

14.9 Cross section systematics for $Z + b$ measurement

The fractional systematic uncertainties on the differential cross sections for all of the observables studied in the $Z + b$ phase space are presented in Figure 78. The b-Tagging efficiency uncertainty dominates, along with the Jet energy scale uncertainty.

Both of these systematic uncertainty have been evaluated using the technique of the decomposition of the total error, as shown in Fig.78, into optimized combinations of the various error sources. In Fig. 79 and 80 the breakdown into error components is shown for the b-tagging efficiency and the jet energy scale uncertainty respectively.

14.10 Cross section systematics for $Z + bb$ measurement

Systematic uncertainties on the $Z + bb$ differential cross section measurements are presented in Figures 81 - 84.

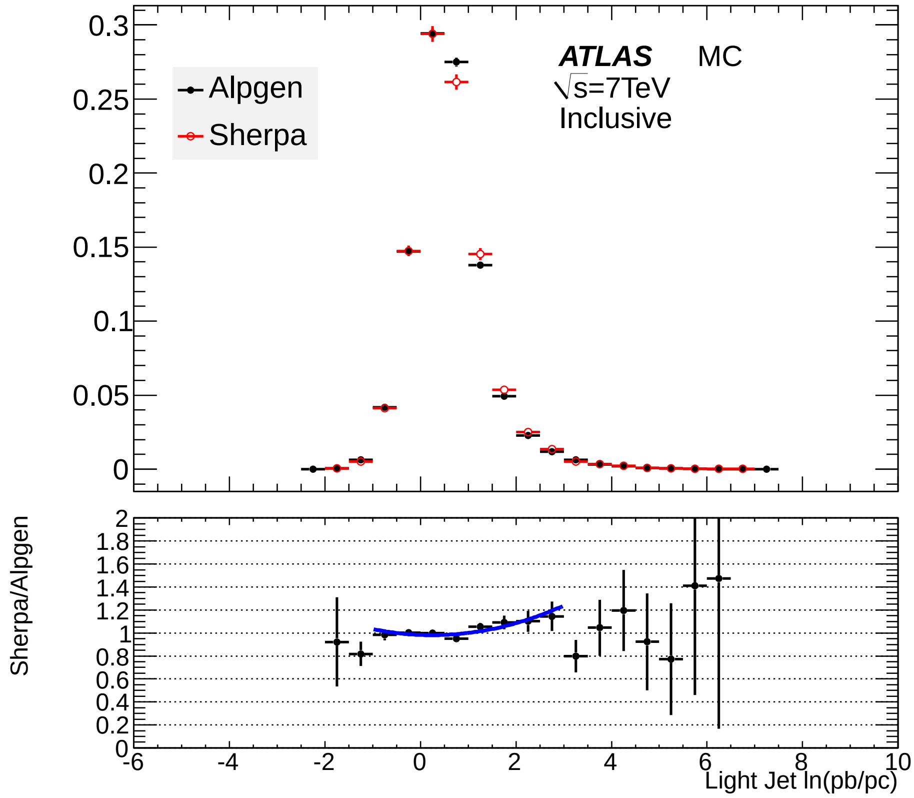

Figure 77: Distribution of $\ln(pb/pc)$ for light jets comparing Sherpa and Alpgen MC with identical selection. The ratio is fitted with a second order polynomial which is used to re-weight templates containing light jets as a systematic uncertainty.

14.11 Systematic Tables

Uncertainties of fit signal yield, C factor and inclusive $Z + bb$ cross section are summarised in Table 23 and 24. The detailed results for each eigenvector variation are given in Tables 25 and 26.

Tables 27 - 30 list the uncertainties obtained for the differential $Z + bb$ measurement.

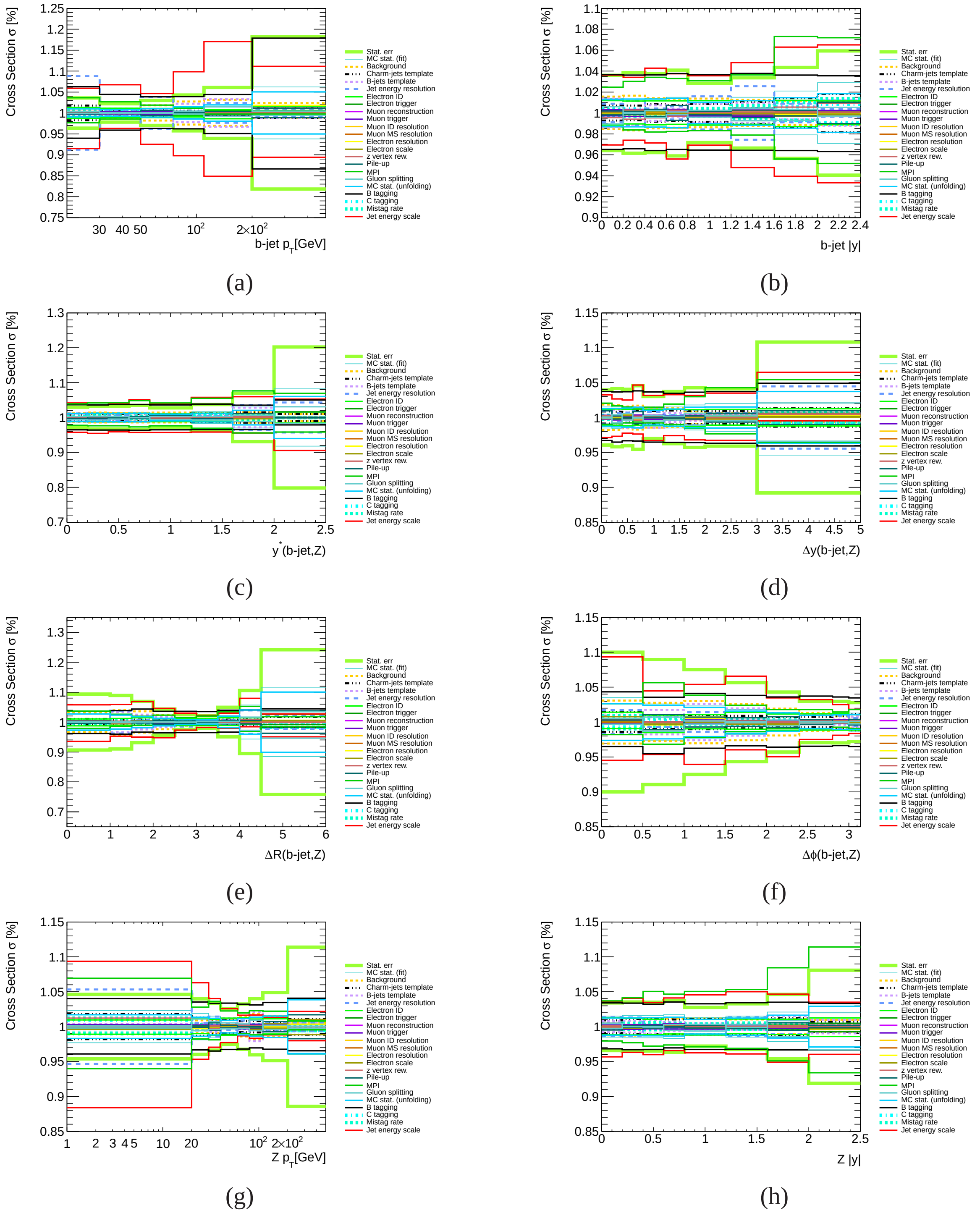

(a) (b) (c) (d) (e) (f) (g) (h)

Figure 78: The fractional systematic uncertainties broken down by source for the $Z + b$ cross sections: differentially in b-jet p_{T}(a), b-jet rapididty (b), $\mathrm{Y}^{\star}(\mathrm{Z}, \mathrm{b}-\mathrm{jet})$ (c), $|\Delta\mathrm{Y}(\mathrm{Z}, \mathrm{b}-\mathrm{jet})|$ (d), $\Delta R(Z, b-jet)$ (e), $\Delta\phi(Z, b-jet)$ (f), $Z\,p_{\mathrm{T}}$(g) and Z rapidity (h).

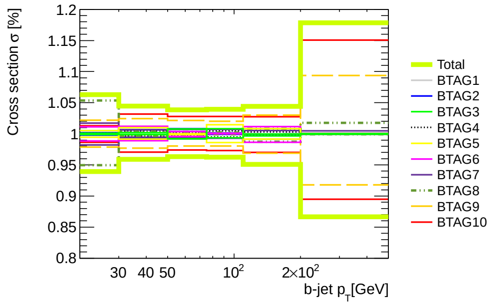

(a)

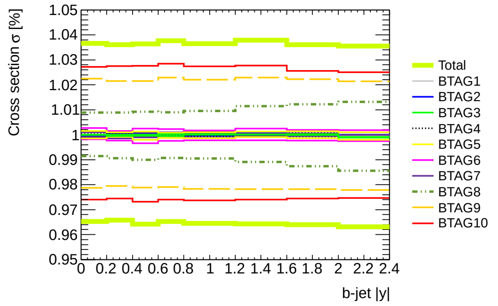

(b)

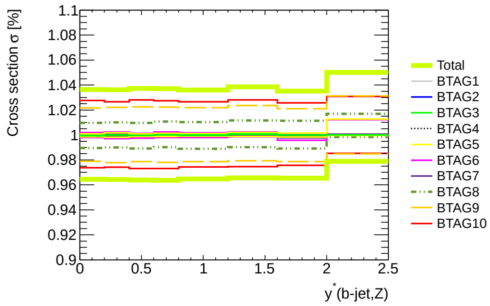

(c)

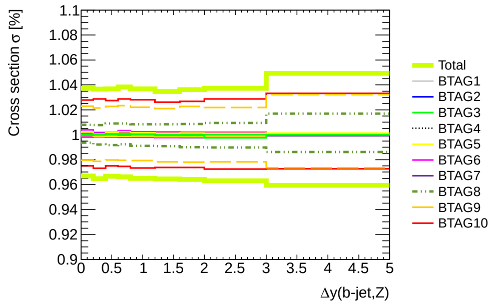

(d)

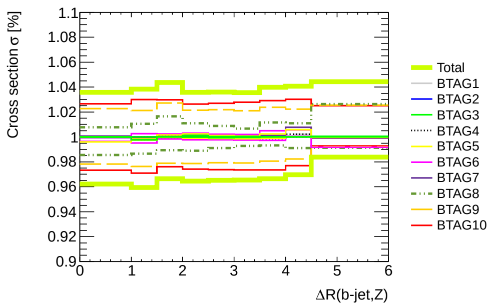

(e)

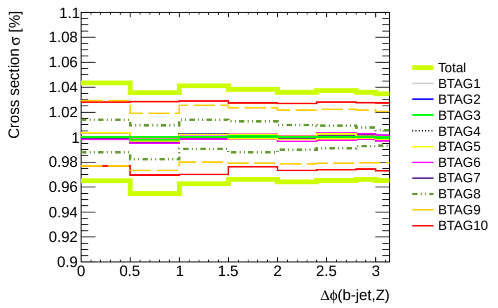

(f)

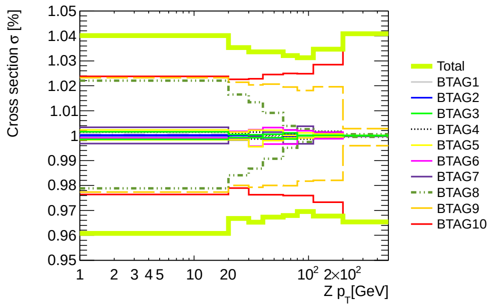

(g)

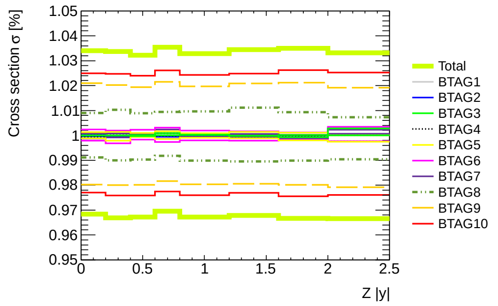

(h)

Figure 79: The fractional b-tagging efficiency error decomposed into sub-components; b-jet p_{T}(a), b-jet rapididty (b), $\mathrm{Y}^{\star}(\mathrm{Z}, \mathrm{b}-\mathrm{jet})$ (c), $|\Delta\mathrm{Y}(\mathrm{Z}, \mathrm{b}-\mathrm{jet})|$ (d), $\Delta R(Z, b-jet)$ (e), $\Delta\phi(Z, b-jet)$ (f), $Z p_{\mathrm{T}}$(g) and Z rapidity (h).

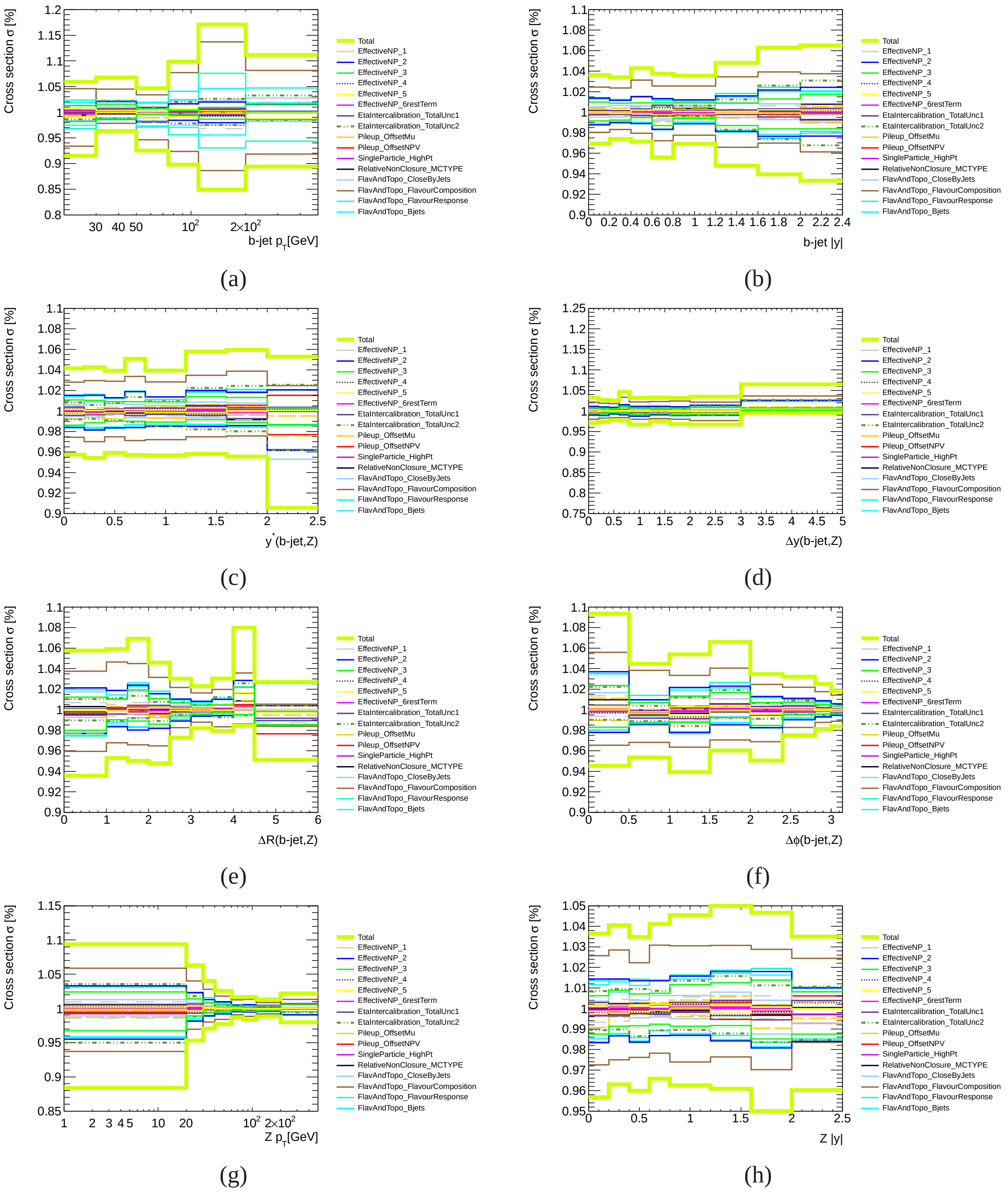

Figure 80: The fractional jet-energy error decomposed into sub-components; b-jet p_{T}(a), b-jet rapididty (b), $\mathrm{Y}^{\star}(\mathrm{Z}, \mathrm{b}-\mathrm{jet})$ (c), $|\Delta\mathrm{Y}(\mathrm{Z}, \mathrm{b}-\mathrm{jet})|$ (d), $\Delta R(Z, b-jet)$ (e), $\Delta\phi(Z, b-jet)$ (f), $Z\,p_{\mathrm{T}}$(g) and Z rapidity (h).

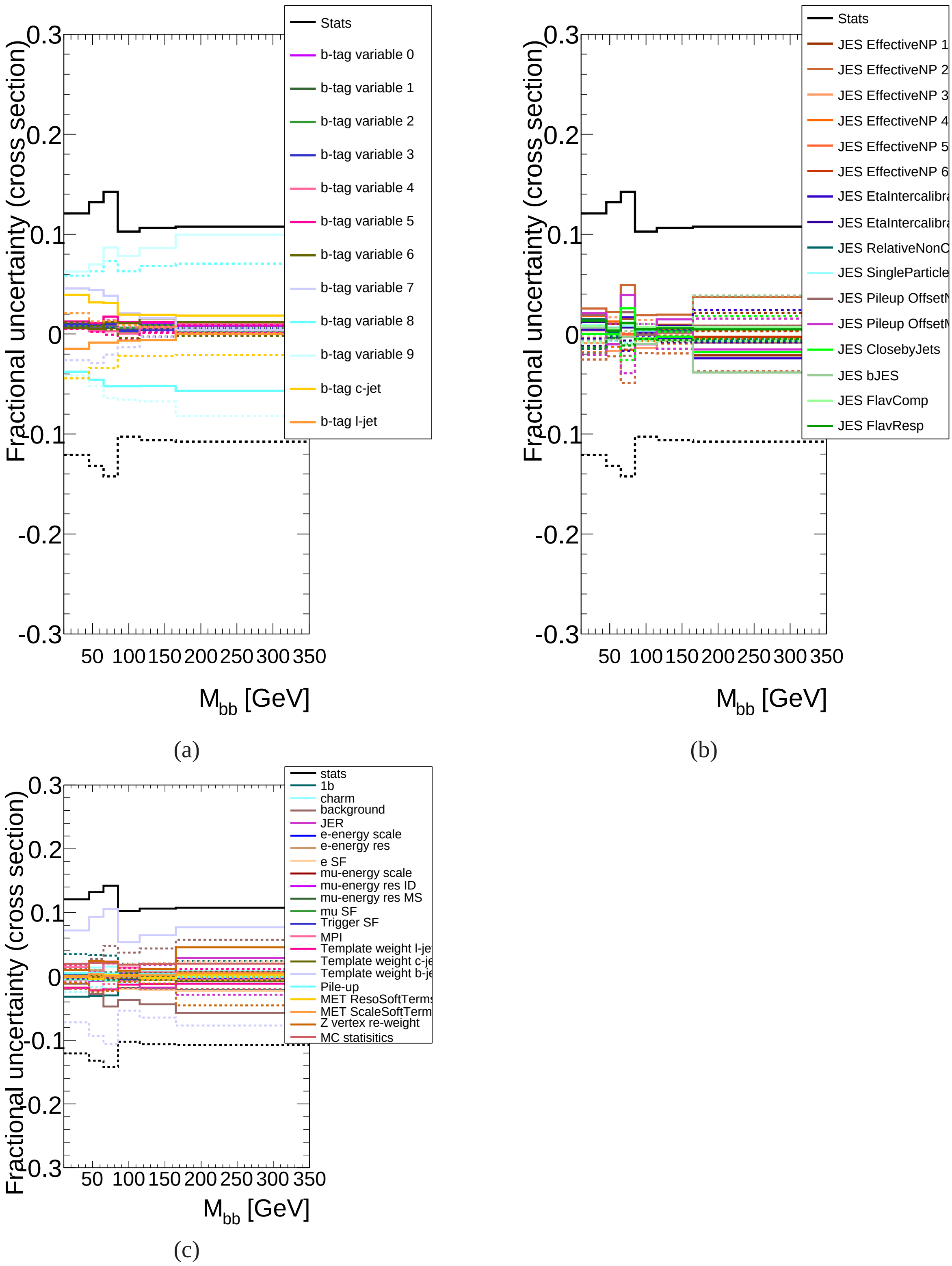

Figure 81: Fractional uncertainties of systematics for the differential $Z + bb$ cross sections measured as function of M_{bb}. Systematics are broken into three categories (a) b-tagging systematics, (b) JES systematics and (c) all other systematics. The statistical unctertainy is also included. M_{bb} (b) ΔR_{bb} and (c) Z boson p_{T}.

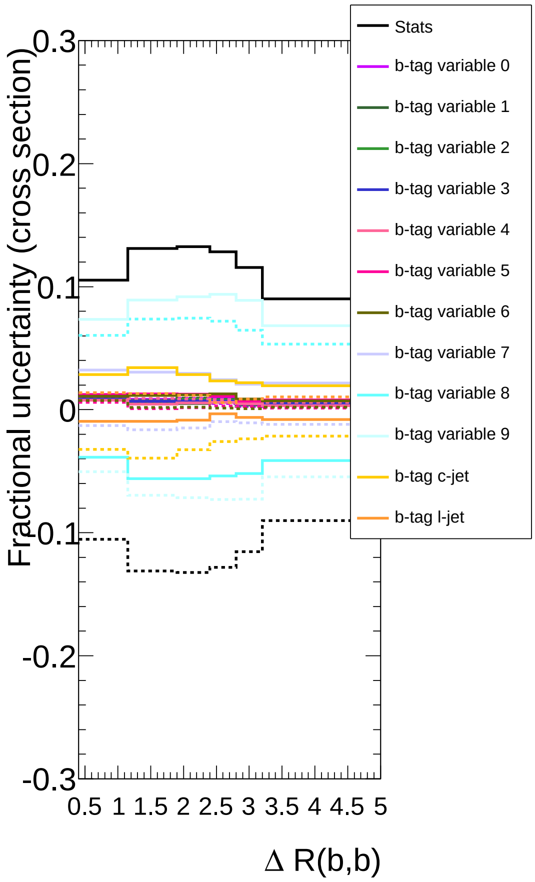

(a)

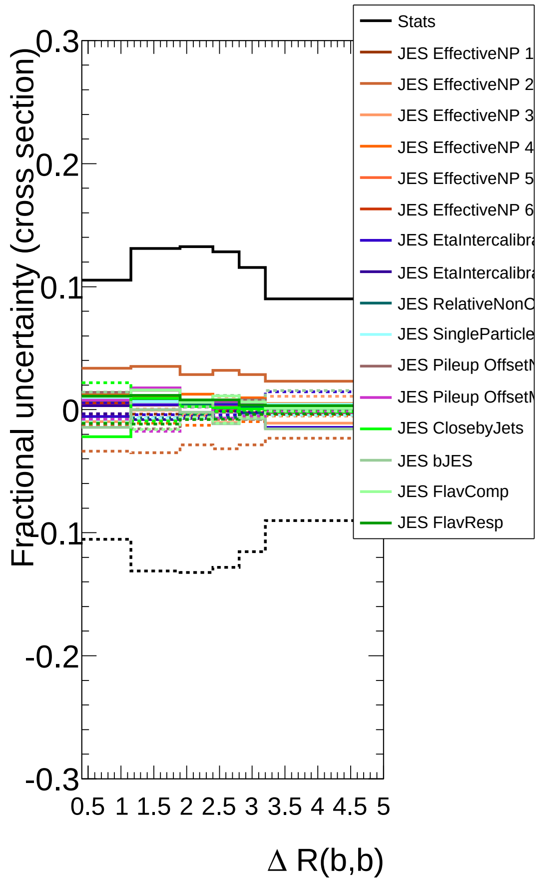

(b)

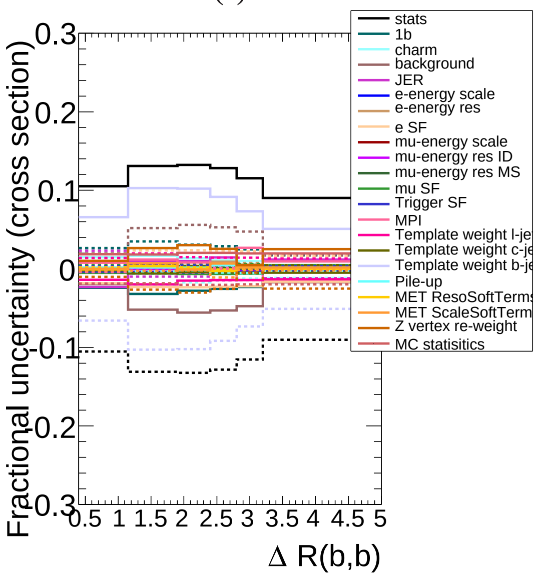

(c)

Figure 82: Fractional uncertainties of systematics for the differential $Z + bb$ cross sections measured as function of ΔR_{bb}. Systematics are broken into three categories (a) b-tagging systematics, (b) JES systematics and (c) all other systematics. The statistical unctertainy is also included.

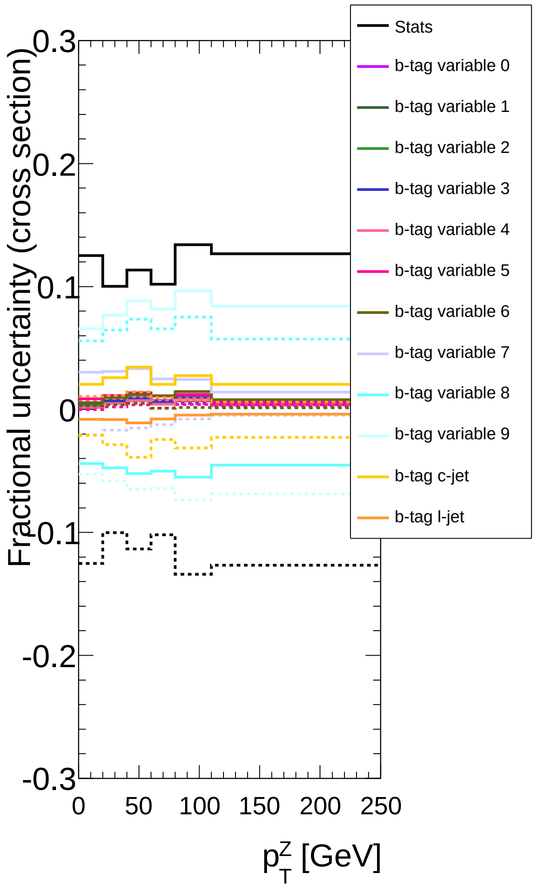

(a)

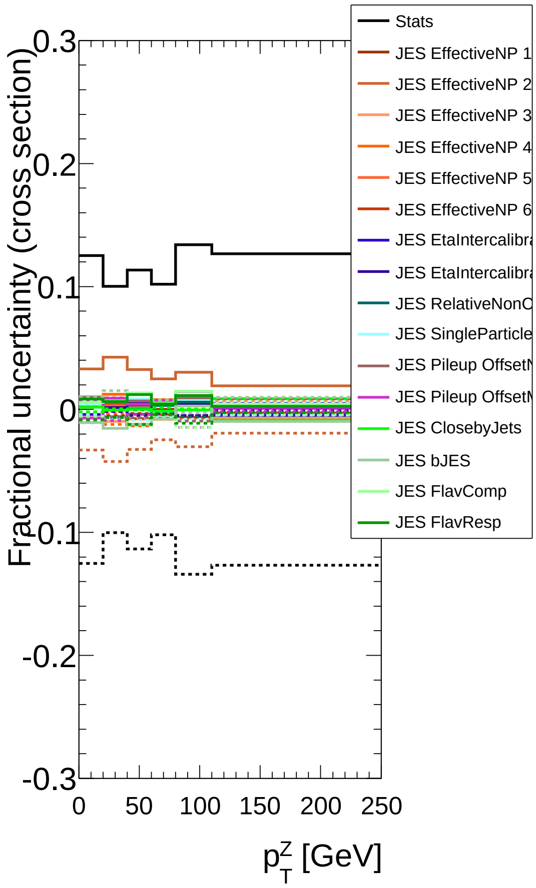

(b)

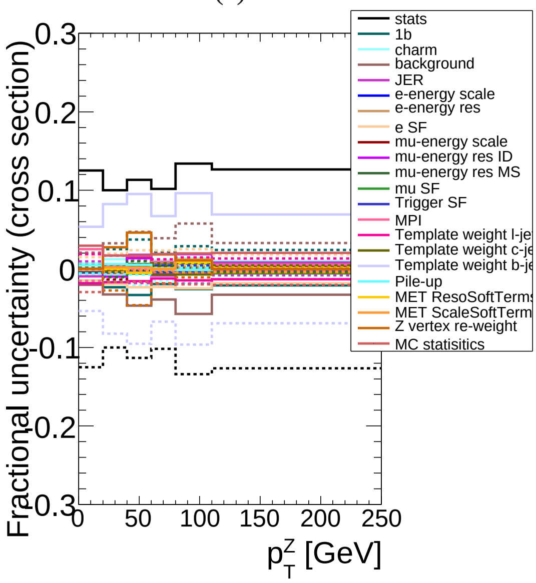

(c)

Figure 83: Fractional uncertainties of systematics for the differential $Z + bb$ cross sections measured as function of Z boson p_T. Systematics are broken into three categories (a) b-tagging systematics, (b) JES systematics and (c) all other systematics. The statistical unctertainy is also included.

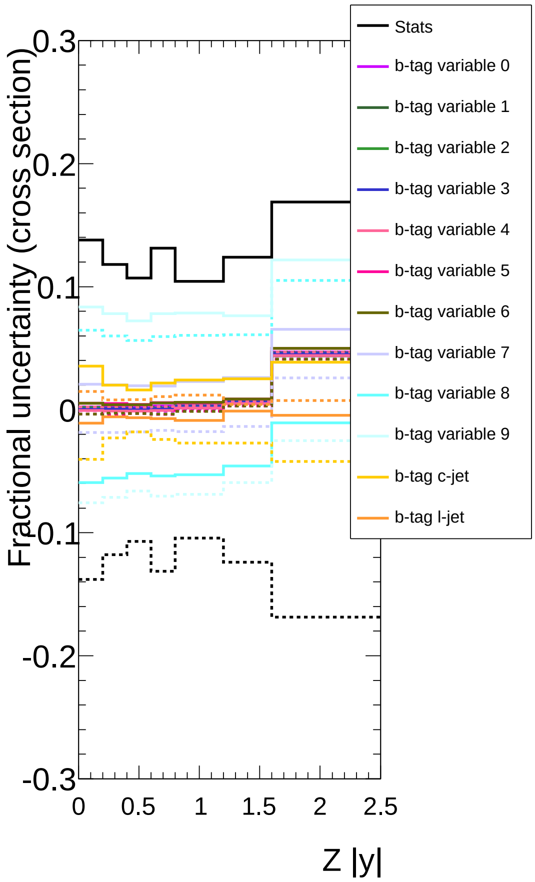

(a)

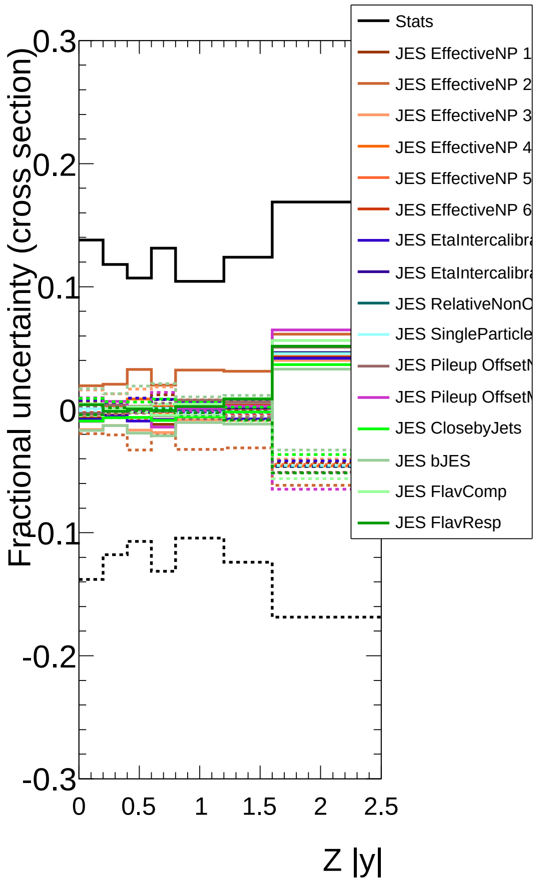

(b)

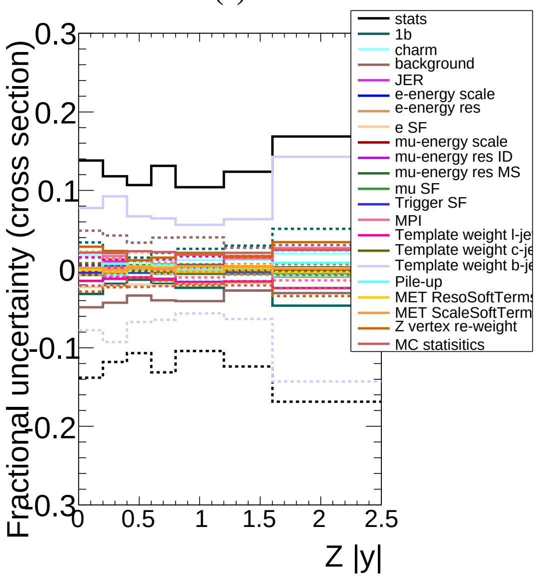

(c)

Figure 84: Fractional uncertainties of systematics for the differential $Z + bb$ cross sections measured as function of $Z|y|$. Systematics are broken into three categories (a) b-tagging systematics, (b) JES systematics and (c) all other systematics. The statistical unctertainy is also included.

	electron channel				muon channel			
systematic	$n_{2b,fit,e}$	$\epsilon_{2b,e}$	C_e	σ_e	$n_{2b,fit,\mu}$	$\epsilon_{2b,\mu}$	C_μ	σ_μ
MC templ. stat.	2.1	-	-	2.1	1.9	-	-	1.9
JES↑	+0.04	-2.26	+8.66	-5.81	+0.55	-2.81	+9.60	-5.60
JES↓	-1.08	+2.62	-9.01	+5.94	-0.56	+2.59	-8.69	+6.16
JER	-1.04	-0.61	+0.57	-0.99	+1.15	-1.35	+0.71	+1.82
b jet *b* tag eff. (EV)↑	+1.88	+1.29	+5.65	+6.41	+1.73	+1.40	+5.75	+6.25
b jet *b* tag eff. (EV)↓	-1.91	-1.25	-5.76	-6.08	-1.77	-1.34	-5.87	-5.95
c jet *b* tag eff.↑	+2.21	-0.05	+0.01	+2.25	+2.20	+0.01	+0.03	+2.15
c jet *b* tag eff.↓	-2.47	+0.05	-0.01	-2.51	-2.42	-0.01	-0.03	-2.38
u jet *b* tag eff.↑	-	-	-	-	-	-	-	-
u jet *b* tag eff.↓	-	-	-	-	-	-	-	-
TemplateW↑	+6.06	+0.20	+0.67	+5.15	+6.69	+0.41	+0.77	+5.44
TemplateW↓	-6.07	-0.20	-0.67	-5.25	-6.66	-0.42	-0.77	-5.54
TemplateSingleB↑	-2.11	-	-	-2.11	-1.55	-	-	-1.55
TemplateSingleB↓	+2.28	-	-	+2.28	+1.66	-	-	+1.66
TemplateC↑	+1.06	-	-	+1.06	+1.16	-	-	+1.16
TemplateC↓	-1.24	-	-	-1.24	-1.30	-	-	-1.30
ElEff↑	-1.79	-0.03	+0.76	-1.01	-	-	-	-
ElEff↓	+1.72	+0.03	-0.58	+1.12	-	-	-	-
ElTrig↑	-0.18	+0.02	+0.54	-0.74	-	-	-	-
ElTrig↓	+0.18	-0.02	-0.54	+0.74	-	-	-	-
MuEff↑	-	-	-	-	-0.24	-	+0.69	-0.93
MuEff↓	-	-	-	-	+0.24	-	-0.69	+0.94
MuTrig↑	-	-	-	-	-0.18	-	+0.49	-0.67
MuTrig↓	-	-	-	-	+0.18	-	-0.49	+0.68
EES↑	+0.15	-	-	+0.15	-	-	-	-
EES↓	+0.15	-	-	+0.15	-	-	-	-
EER↑	-0.14	-0.03	+0.01	-0.12	-	-	-	-
EER↓	+0.71	+0.03	+0.05	+0.63	-	-	-	-
MES↑	-	-	-	-	-0.01	-0.01	+0.01	-0.01
MES↓	-	-	-	-	-0.07	+0.03	-0.04	-0.06
MERMS↑	-	-	-	-	+0.02	-0.05	-0.03	+0.09
MERMS↓	-	-	-	-	+0.05	-0.04	+0.03	+0.06
MERID↑	-	-	-	-	-0.08	+0.01	-	-0.10
MERID↓	-	-	-	-	-	+0.01	+0.01	-0.01
MetResoSoft↑	-0.10	+0.01	-0.04	-0.07	-0.17	-0.03	-0.01	-0.13
MetResoSoft↓	+0.27	+0.06	+0.02	+0.18	-0.02	-0.02	+0.01	-0.01
MetScaleSoft↑	+0.42	-0.01	-0.12	+0.55	+0.21	-0.03	-0.05	+0.29
MetScaleSoft↓	-0.34	+0.04	+0.09	-0.47	-0.24	+0.01	+0.04	-0.29

Table 23: Systematic uncertainties for the inclusive Zbb measurement (in %). Uncertainties are given for the fit result, 2 *b*-tag efficiency, correction factor and the cross section.

systematic	combination of electron and muon channel $n_{2b,fit}$	ϵ_{2b}	C	σ
MC templ. stat.	1.4	-	-	1.4
JES↑	+0.34	+6.39	+9.20	-5.69
JES↓	-0.75	-6.46	-8.83	+6.10
JER	+0.33	-0.39	+0.65	+0.73
b jet *b* tag eff. (EV)↑	+1.81	+4.41	+5.71	+6.33
b jet *b* tag eff. (EV)↓	-1.84	-4.48	-5.82	-6.01
c jet *b* tag eff.↑	+2.21	+0.01	+0.02	+2.20
c jet *b* tag eff.↓	-2.48	-0.01	-0.03	-2.47
u jet *b* tag eff.↑	-0.00	-	-	-0.00
u jet *b* tag eff.↓	-0.00	-	-	-0.00
TemplateW↑	+6.45	+1.05	+0.73	+5.35
TemplateW↓	-6.44	-1.05	-0.73	-5.45
TemplateSingleB↑	-1.78	-	-	-1.78
TemplateSingleB↓	+1.91	-	-	+1.91
TemplateC↑	+1.10	-	-	+1.10
TemplateC↓	-1.31	-	-	-1.31
ElEff↑	-0.73	+0.05	+0.14	-0.93
ElEff↓	+0.70	-0.08	-0.17	+0.93
ElTrig↑	-0.07	+0.24	+0.23	-0.32
ElTrig↓	+0.07	-0.24	-0.23	+0.32
MuEff↑	-0.14	+0.39	+0.40	-0.53
MuEff↓	+0.14	-0.39	-0.39	+0.54
MuTrig↑	-0.11	+0.28	+0.28	-0.39
MuTrig↓	+0.11	-0.28	-0.28	+0.39
EES↑	+0.15	-	-	+0.15
EES↓	+0.15	-	-	+0.15
EER↑	-0.14	-0.03	+0.01	-0.12
EER↓	+0.71	+0.03	+0.05	+0.63
MES↑	-0.01	-0.01	+0.01	-0.01
MES↓	-0.07	+0.03	-0.04	-0.06
MERMS↑	+0.02	-0.05	-0.03	+0.09
MERMS↓	+0.05	-0.04	+0.03	+0.06
MERID↑	-0.08	+0.01	-	-0.10
MERID↓	-	+0.01	+0.01	-0.01
MetResoSoft↑	-0.14	-0.04	-0.02	-0.10
MetResoSoft↓	+0.10	+0.03	+0.01	+0.08
MetScaleSoft↑	+0.28	-0.10	-0.08	+0.39
MetScaleSoft↓	-0.28	+0.09	+0.06	-0.36

Table 24: Systematic uncertainties for the inclusive Zbb measurement (in %). Uncertainties are given for the fit result, 2 *b*-tag efficiency, correction factor and the cross section.

	electron channel				muon channel			
systematic	$n_{\text{2b,fit,e}}$	$\epsilon_{\text{2b,e}}$	C_{e}	σ_e	$n_{\text{2b,fit},\mu}$	$\epsilon_{\text{2b},\mu}$	C_μ	σ_μ
b jet *b* tag eff. (EV)↑	+1.88	+1.29	+5.65	+6.41	+1.73	+1.40	+5.75	+6.25
b jet *b* tag eff. (EV)↓	-1.91	-1.25	-5.76	-6.08	-1.77	-1.34	-5.87	-5.95
b jet *b* tag EV 0↑	-0.11	-0.04	+0.10	-0.17	-0.09	-0.01	+0.08	-0.16
b jet *b* tag EV 0↓	+0.11	+0.04	-0.10	+0.17	+0.09	+0.01	-0.08	+0.16
b jet *b* tag EV 0↑	-0.11	-0.04	+0.10	-0.17	-0.09	-0.01	+0.08	-0.16
b jet *b* tag EV 0↓	+0.11	+0.04	-0.10	+0.17	+0.09	+0.01	-0.08	+0.16
b jet *b* tag EV 1↑	+0.08	+0.03	-0.08	+0.14	+0.03	+0.01	-0.09	+0.11
b jet *b* tag EV 1↓	-0.08	-0.03	+0.08	-0.14	-0.03	-0.01	+0.09	-0.11
b jet *b* tag EV 2↑	-0.03	+0.01	-0.01	-0.04	-0.01	+0.02	+0.01	-0.03
b jet *b* tag EV 2↓	+0.03	-0.01	+0.01	+0.04	+0.01	-0.02	-0.01	+0.03
b jet *b* tag EV 3↑	+0.07	-0.03	+0.10	-	+0.06	-0.01	+0.09	-0.02
b jet *b* tag EV 3↓	-0.07	+0.03	-0.10	-	-0.06	+0.01	-0.09	+0.02
b jet *b* tag EV 4↑	-0.05	+0.06	-0.23	+0.12	-0.06	+0.07	-0.26	+0.13
b jet *b* tag EV 4↓	+0.05	-0.06	+0.23	-0.12	+0.06	-0.07	+0.26	-0.13
b jet *b* tag EV 5↑	-0.06	-0.07	+0.40	-0.38	-0.11	-0.08	+0.40	-0.42
b jet *b* tag EV 5↓	+0.06	+0.07	-0.39	+0.38	+0.11	+0.08	-0.40	+0.42
b jet *b* tag EV 6↑	-0.24	-0.02	+0.14	-0.36	-0.26	-0.02	+0.15	-0.39
b jet *b* tag EV 6↓	+0.24	+0.02	-0.14	+0.36	+0.26	+0.02	-0.15	+0.39
b jet *b* tag EV 7↑	-0.14	-0.61	+2.49	-1.96	-0.11	-0.61	+2.49	-1.94
b jet *b* tag EV 7↓	+0.13	+0.63	-2.45	+2.01	+0.11	+0.63	-2.46	+1.99
b jet *b* tag EV 8↑	+1.85	+1.13	-5.05	+6.07	+1.70	+1.25	-5.16	+5.91
b jet *b* tag EV 8↓	-1.88	-1.07	+5.19	-5.71	-1.74	-1.18	+5.30	-5.57

Table 25: Eigenvector decomposition contributions to the systematic uncertainty. Systematic uncertainties for the inclusive Zbb measurement (in %). Uncertainties are given for the fit result, 2 *b*-tag efficiency, correction factor and the cross section.

systematic	combination of electron and muon channel $n_{2b,fit}$	ϵ_{2b}	C	σ
b jet *b* tag eff. (EV)↑	+1.81	+4.41	+5.71	+6.33
b jet *b* tag eff. (EV)↓	-1.84	-4.48	-5.82	-6.01
b jet *b* tag EV 0↑	-0.10	+0.07	+0.09	-0.17
b jet *b* tag EV 0↓	+0.10	-0.07	-0.09	+0.17
b jet *b* tag EV 1↑	+0.05	-0.07	-0.09	+0.12
b jet *b* tag EV 1↓	-0.05	+0.07	+0.09	-0.12
b jet *b* tag EV 2↑	-0.02	+0.01	-0.00	-0.04
b jet *b* tag EV 2↓	+0.02	-0.01	-	+0.04
b jet *b* tag EV 3↑	+0.06	+0.07	+0.10	-0.01
b jet *b* tag EV 3↓	-0.06	-0.07	-0.10	+0.01
b jet *b* tag EV 4↑	-0.06	-0.18	-0.25	+0.13
b jet *b* tag EV 4↓	+0.06	+0.18	+0.25	-0.13
b jet *b* tag EV 5↑	-0.09	+0.32	+0.40	-0.40
b jet *b* tag EV 5↓	+0.09	-0.32	-0.40	+0.40
b jet *b* tag EV 6↑	-0.25	+0.12	+0.14	-0.38
b jet *b* tag EV 6↓	+0.25	-0.12	-0.14	+0.38
b jet *b* tag EV 7↑	-0.12	+1.86	+2.49	-1.95
b jet *b* tag EV 7↓	+0.12	-1.84	-2.46	+2.00
b jet *b* tag EV 8↑	+1.78	-3.98	-5.11	+5.99
b jet *b* tag EV 8↓	-1.81	+4.06	+5.25	-5.64

Table 26: Eigenvector decomposition contributions to the systematic uncertainty. Systematic uncertainties for the inclusive Zbb measurement (in %). Uncertainties are given for the fit result, 2 *b*-tag efficiency, correction factor and the cross section.

Combined Channel						
ΔR_{bb}	(0.4, 1.15)	(1.15, 1.9)	(1.9, 2.4)	(2.4, 2.8)	(2.8, 3.2)	(3.2, 5.0)
1b ↑	-1.80	-2.82	-2.80	-2.88	-1.83	-1.92
1b ↓	1.97	3.08	3.11	3.28	1.99	2.12
charm ↑	1.12	1.45	1.18	1.44	1.47	1.74
charm ↓	-1.41	-1.86	-1.48	-1.80	-1.77	-2.15
background ↑	-1.83	-4.68	-5.47	-5.24	-4.77	-1.87
background ↓	1.84	4.70	5.51	5.24	4.79	1.88
JER ↑	-1.58	2.24	3.86	-0.01	-1.44	0.35
JER ↓	1.58	-2.24	-3.86	0.01	1.44	-0.35
e-energy scale ↑	-0.01	0.02	-0.19	-0.19	-0.25	-0.08
e-energy scale ↓	0.15	0.32	0.09	0.58	0.34	0.03
e-energy res ↑	0.22	-0.24	-0.08	1.21	0.04	-0.15
e-energy res ↓	0.28	0.02	0.18	0.77	0.75	0.51
e SF ↑	-1.70	-2.20	-2.38	-2.28	-2.15	-1.63
e SF ↓	1.73	2.24	2.41	2.32	2.17	1.65
mu-energy scale ↑	-0.06	-0.01	-0.02	-0.05	0.04	-0.13
mu-energy scale ↓	0.00	0.07	0.12	0.09	-0.06	-0.08
mu-energy res ID ↑	-0.04	-0.02	0.05	-0.04	-0.06	-0.12
mu-energy res ID ↓	0.05	-0.06	-0.06	0.10	0.00	0.03
mu-energy res MS ↑	0.13	0.26	0.01	0.10	0.06	-0.10
mu-energy res MS ↓	-0.09	0.18	-0.03	0.19	0.12	-0.03
mu SF ↑	-0.51	-0.60	-0.63	-0.64	-0.60	-0.49
mu SF ↓	0.51	0.60	0.63	0.64	0.61	0.50
Trigger SF ↑	-0.32	-0.40	-0.44	-0.44	-0.43	-0.34
Trigger SF ↓	0.33	0.40	0.44	0.45	0.44	0.35
MPI ↑	1.26	0.72	0.19	-0.26	5.27	-0.49
MPI ↓	-0.63	-0.32	-0.09	0.14	-2.81	0.31
Template weight l-jets ↑	-1.32	-1.57	-1.41	-1.10	-1.19	-1.24
Template weight l-jets ↓	1.32	1.57	1.41	1.10	1.19	1.24
Template weight c-jets ↑	-0.39	-0.26	-0.40	-0.37	-0.78	-0.64
Template weight c-jets ↓	0.39	0.26	0.40	0.37	0.78	0.64
Template weight b-jets ↑	6.22	7.39	10.23	10.18	8.09	5.43
Template weight b-jets ↓	-6.22	-7.39	-10.23	-10.18	-8.09	-5.43
Pile-up ↑	0.08	-0.43	-0.34	0.36	0.10	1.27
Pile-up ↓	0.01	0.21	0.26	-0.37	-0.17	-1.08
MET ResoSoftTerms ↑	-0.11	0.14	0.11	-0.29	0.33	0.06
MET ResoSoftTerms ↓	0.12	0.43	0.15	-0.04	-0.03	0.03
MET ScaleSoftTerms ↑	0.09	0.55	-0.16	0.71	0.20	-0.01
MET ScaleSoftTerms ↓	-0.31	-0.17	-0.24	-1.07	-0.13	-0.25
Z vertex re-weight ↑	-0.05	-0.42	3.32	2.88	1.07	3.91
Z vertex re-weight ↓	0.05	0.42	-3.32	-2.88	-1.07	-3.91
MC stat ↑	3.78	3.73	4.15	4.12	3.95	3.99
MC stat ↓	-3.71	-3.66	-4.06	-4.03	-3.87	-3.91
JES EffectiveNP 1 ↑	-0.45	0.86	0.29	0.38	0.11	-0.55
JES EffectiveNP 1 ↓	0.45	-0.86	-0.29	-0.38	-0.11	0.55
JES EffectiveNP 2 ↑	1.90	3.97	4.14	3.56	3.37	2.57
JES EffectiveNP 2 ↓	-1.90	-3.97	-4.14	-3.56	-3.37	-2.57
JES EffectiveNP 3 ↑	-1.23	0.21	-1.69	-0.39	-0.68	-1.09
JES EffectiveNP 3 ↓	1.23	-0.21	1.69	0.39	0.68	1.09
JES EffectiveNP 4 ↑	0.85	1.12	0.96	0.89	1.13	0.47
JES EffectiveNP 4 ↓	-0.85	-1.12	-0.96	-0.89	-1.13	-0.47
JES EffectiveNP 5 ↑	0.11	0.97	0.26	0.77	-0.03	0.04
JES EffectiveNP 5 ↓	-0.11	-0.97	-0.26	-0.77	0.03	-0.04
JES EffectiveNP 6restTerm ↑	0.13	1.02	0.58	0.79	-0.00	0.25
JES EffectiveNP 6restTerm ↓	-0.13	-1.02	-0.58	-0.79	0.00	-0.25
JES EtaIntercalibration Modelling ↑	-0.38	0.45	-0.41	0.45	-0.20	-1.26
JES EtaIntercalibration Modelling ↓	0.38	-0.45	0.41	-0.45	0.20	1.26
JES EtaIntercalibration TotalStat ↑	-0.29	1.19	0.28	0.42	0.17	-0.28
JES EtaIntercalibration TotalStat ↓	0.29	-1.19	-0.28	-0.42	-0.17	0.28
JES RelativeNonClosure MC11c ↑	0.39	0.62	0.44	0.51	0.21	-0.16
JES RelativeNonClosure MC11c ↓	-0.39	-0.62	-0.44	-0.51	-0.21	0.16
JES SingleParticle HighPt ↑	0.67	0.61	0.61	0.87	0.33	0.28
JES SingleParticle HighPt ↓	-0.67	-0.61	-0.61	-0.87	-0.33	-0.28
JES Pileup OffsetNPV ↑	0.97	0.96	0.06	1.18	0.91	-0.10
JES Pileup OffsetNPV ↓	-0.97	-0.96	-0.06	-1.18	-0.91	0.10
JES Pileup OffsetMu ↑	-1.20	1.78	-0.92	1.26	0.66	0.64
JES Pileup OffsetMu ↓	1.20	-1.78	0.92	-1.26	-0.66	-0.64
JES ClosebyJets ↑	-2.49	1.15	0.05	0.03	-0.24	-0.22
JES ClosebyJets ↓	2.49	-1.15	-0.05	-0.03	0.24	0.22
JES bJES ↑	-1.60	-0.02	-1.01	-0.39	-1.09	-1.58
JES bJES ↓	1.60	0.02	1.01	0.39	1.09	1.58
JES FlavComp ↑	-0.09	0.71	0.62	0.61	1.19	-0.02
JES FlavComp ↓	0.09	-0.71	-0.62	-0.61	-1.19	0.02
JES FlavResp ↑	0.25	0.23	0.26	0.96	0.44	0.46
JES FlavResp ↓	-0.25	-0.23	-0.26	-0.96	-0.44	-0.46
b-tag variable 0 ↑	0.57	0.77	0.59	0.98	0.67	0.22
b-tag variable 0 ↓	0.54	0.56	0.28	0.61	0.42	0.15
b-tag variable 1 ↑	0.52	0.63	0.26	0.75	0.52	0.11
b-tag variable 1 ↓	0.59	0.70	0.61	0.84	0.57	0.26
b-tag variable 2 ↑	0.53	0.79	0.56	0.80	0.59	0.20
b-tag variable 2 ↓	0.58	0.54	0.31	0.79	0.50	0.17
b-tag variable 3 ↑	0.57	0.58	0.36	0.71	0.47	0.19
b-tag variable 3 ↓	0.55	0.75	0.50	0.88	0.62	0.18
b-tag variable 4 ↑	0.54	0.68	0.47	0.88	0.64	0.20
b-tag variable 4 ↓	0.57	0.64	0.40	0.71	0.45	0.16
b-tag variable 5 ↑	0.74	0.96	0.66	0.80	0.58	0.24
b-tag variable 5 ↓	0.37	0.37	0.21	0.78	0.52	0.13
b-tag variable 6 ↑	0.69	1.07	0.87	1.16	0.83	0.29
b-tag variable 6 ↓	0.42	0.25	0.00	0.43	0.28	0.07
b-tag variable 7 ↑	0.68	1.17	0.88	1.07	0.68	0.38
b-tag variable 7 ↓	0.43	0.16	-0.02	0.52	0.41	-0.02
b-tag variable 8 ↑	-0.28	-1.97	-2.33	-2.16	-2.00	-1.21
b-tag variable 8 ↓	1.39	3.31	3.19	3.74	3.09	1.56
b-tag variable 9 ↑	1.72	4.00	3.98	4.59	3.91	1.88
b-tag variable 9 ↓	-0.62	-2.68	-3.15	-3.02	-2.84	-1.52
b-tag c-jet ↑	1.47	2.52	2.20	2.59	2.34	2.81
b-tag c-jet ↓	-1.74	-2.91	-2.45	-2.87	-2.51	-3.14
b-tag l-jet ↑	0.14	-0.17	-0.06	0.03	-1.14	-0.94

Table 27: Systematic uncertainties for the differential Zbb measurement (in ΔR_{bb}).

Combined Channel						
m_{bb}	(10, 45)	(45, 65)	(65, 85)	(85, 115)	(115, 165)	(165, 350)
1b ↑	-2.15	-3.28	-2.45	-1.97	-1.82	-2.36
1b ↓	2.37	3.59	2.69	2.15	1.99	2.63
charm ↑	1.99	2.21	1.39	1.18	1.27	0.99
charm ↓	-2.48	-2.65	-1.73	-1.46	-1.60	-1.32
background ↑	-1.07	-2.90	-4.52	-3.68	-4.40	-5.88
background ↓	1.08	2.92	4.55	3.68	4.38	5.86
JER ↑	-1.93	-2.85	7.01	-1.38	-2.13	2.68
JER ↓	1.93	2.85	-7.01	1.38	2.13	-2.68
e-energy scale ↑	-0.01	-0.08	-0.13	0.01	-0.17	-0.34
e-energy scale ↓	-0.07	0.60	0.08	0.14	0.40	0.39
e-energy res ↑	-0.21	0.98	-0.62	-0.46	0.43	0.70
e-energy res ↓	0.07	1.01	-0.55	0.33	0.66	0.78
e SF ↑	-1.51	-2.02	-2.02	-2.06	-2.12	-2.38
e SF ↓	1.53	2.06	2.07	2.09	2.14	2.38
mu-energy scale ↑	-0.03	0.02	-0.07	0.07	-0.01	-0.11
mu-energy scale ↓	0.09	0.01	0.00	0.07	0.09	-0.12
mu-energy res ID ↑	-0.00	-0.02	-0.07	0.03	0.00	-0.06
mu-energy res ID ↓	0.07	-0.02	-0.03	-0.03	0.03	0.03
mu-energy res MS ↑	0.13	0.08	-0.02	0.18	0.08	0.02
mu-energy res MS ↓	-0.11	0.58	0.20	0.06	0.17	-0.08
mu SF ↑	-0.47	-0.54	-0.65	-0.55	-0.59	-0.66
mu SF ↓	0.48	0.54	0.65	0.55	0.60	0.66
Trigger SF ↑	-0.31	-0.36	-0.45	-0.40	-0.41	-0.46
Trigger SF ↓	0.31	0.36	0.45	0.40	0.41	0.46
MPI ↑	1.99	0.44	-0.39	1.26	0.12	0.34
MPI ↓	-1.03	-0.30	0.25	-0.64	-0.06	-0.19
Template weight l-jets ↑	-2.15	-1.83	-1.67	-1.19	-0.97	-1.30
Template weight l-jets ↓	2.15	1.83	1.67	1.19	0.97	1.30
Template weight c-jets ↑	-0.35	-0.05	0.04	-0.59	-0.66	-0.95
Template weight c-jets ↓	0.35	0.05	-0.04	0.59	0.66	0.95
Template weight b-jets ↑	6.45	10.94	5.82	7.00	8.34	7.70
Template weight b-jets ↓	-6.45	-10.94	-5.82	-7.00	-8.34	-7.70
Pile-up ↑	0.15	-0.70	0.25	0.38	0.01	0.10
Pile-up ↓	-0.11	0.51	-0.46	-0.39	0.02	-0.02
MET ResoSoftTerms ↑	-0.01	-0.50	0.25	0.01	-0.25	0.36
MET ResoSoftTerms ↓	-0.07	0.05	0.14	0.03	0.06	-0.11
MET ScaleSoftTerms ↑	0.19	0.64	0.04	-0.04	0.23	0.48
MET ScaleSoftTerms ↓	-0.27	-0.23	-0.25	-0.04	-0.64	-0.65
Z vertex re-weight ↑	0.68	3.91	1.57	1.29	0.43	4.93
Z vertex re-weight ↓	-0.68	-3.91	-1.57	-1.29	-0.43	-4.93
MC stat ↑	3.94	4.20	4.10	3.70	3.89	4.06
MC stat ↓	-3.87	-4.11	-4.02	-3.64	-3.81	-3.98
JES EffectiveNP 1 ↑	0.21	0.95	1.79	0.34	0.41	-2.04
JES EffectiveNP 1 ↓	-0.21	-0.95	-1.79	-0.34	-0.41	2.04
JES EffectiveNP 2 ↑	1.53	4.81	4.55	1.39	2.66	3.61
JES EffectiveNP 2 ↓	-1.53	-4.81	-4.55	-1.39	-2.66	-3.61
JES EffectiveNP 3 ↑	-1.17	-3.63	0.27	-1.26	-0.38	0.10
JES EffectiveNP 3 ↓	1.17	3.63	-0.27	1.26	0.38	-0.10
JES EffectiveNP 4 ↑	1.55	1.67	0.71	1.20	1.36	-0.84
JES EffectiveNP 4 ↓	-1.55	-1.67	-0.71	-1.20	-1.36	0.84
JES EffectiveNP 5 ↑	0.27	0.18	0.10	0.17	0.46	0.89
JES EffectiveNP 5 ↓	-0.27	-0.18	-0.10	-0.17	-0.46	-0.89
JES EffectiveNP 6restTerm ↑	0.51	0.72	0.88	0.56	0.82	-0.68
JES EffectiveNP 6restTerm ↓	-0.51	-0.72	-0.88	-0.56	-0.82	0.68
JES EtaIntercalibration Modelling ↑	1.15	-0.44	1.78	1.81	-2.59	-2.12
JES EtaIntercalibration Modelling ↓	-1.15	0.44	-1.78	-1.81	2.59	2.12
JES EtaIntercalibration TotalStat ↑	0.40	1.51	0.22	0.11	0.85	-0.91
JES EtaIntercalibration TotalStat ↓	-0.40	-1.51	-0.22	-0.11	-0.85	0.91
JES RelativeNonClosure MC11c ↑	0.75	-0.26	2.02	0.37	0.13	-0.59
JES RelativeNonClosure MC11c ↓	-0.75	0.26	-2.02	-0.37	-0.13	0.59
JES SingleParticle HighPt ↑	0.46	0.86	0.79	0.35	0.56	0.48
JES SingleParticle HighPt ↓	-0.46	-0.86	-0.79	-0.35	-0.56	-0.48
JES Pileup OffsetNPV ↑	1.25	-0.46	2.80	0.90	-1.12	0.64
JES Pileup OffsetNPV ↓	-1.25	0.46	-2.80	-0.90	1.12	-0.64
JES Pileup OffsetMu ↑	0.58	-2.26	6.22	-0.48	1.00	-1.64
JES Pileup OffsetMu ↓	-0.58	2.26	-6.22	0.48	-1.00	1.64
JES ClosebyJets ↑	0.77	-1.61	4.28	1.24	-3.50	-1.57
JES ClosebyJets ↓	-0.77	1.61	-4.28	-1.24	3.50	1.57
JES bJES ↑	0.18	0.93	-1.24	-0.72	-0.94	-3.57
JES bJES ↓	-0.18	-0.93	1.24	0.72	0.94	3.57
JES FlavComp ↑	-1.61	1.54	-0.26	2.64	-1.29	0.85
JES FlavComp ↓	1.61	-1.54	0.26	-2.64	1.29	-0.85
JES FlavResp ↑	-0.68	0.39	-0.05	2.44	-1.18	0.37
JES FlavResp ↓	0.68	-0.39	0.05	-2.44	1.18	-0.37
b-tag variable 0 ↑	0.30	0.88	0.74	0.48	0.79	0.68
b-tag variable 0 ↓	0.38	0.83	0.56	0.29	0.32	0.43
b-tag variable 1 ↑	0.27	0.87	0.49	0.35	0.47	0.49
b-tag variable 1 ↓	0.41	0.83	0.82	0.41	0.64	0.62
b-tag variable 2 ↑	0.35	0.80	0.75	0.54	0.72	0.46
b-tag variable 2 ↓	0.33	0.92	0.56	0.22	0.39	0.65
b-tag variable 3 ↑	0.35	0.91	0.70	0.28	0.33	0.55
b-tag variable 3 ↓	0.33	0.80	0.61	0.48	0.78	0.56
b-tag variable 4 ↑	0.30	0.68	0.47	0.36	0.70	0.92
b-tag variable 4 ↓	0.38	1.03	0.84	0.41	0.41	0.19
b-tag variable 5 ↑	0.52	1.08	1.07	0.69	0.74	0.25
b-tag variable 5 ↓	0.16	0.63	0.23	0.08	0.37	0.86
b-tag variable 6 ↑	0.42	0.90	0.94	0.73	1.02	0.92
b-tag variable 6 ↓	0.26	0.81	0.36	0.03	0.09	0.19
b-tag variable 7 ↑	0.59	1.88	1.47	0.80	0.70	0.31
b-tag variable 7 ↓	0.08	-0.17	-0.18	-0.03	0.42	0.80
b-tag variable 8 ↑	-0.33	-0.88	-1.82	-1.70	-1.88	-2.55
b-tag variable 8 ↓	1.01	2.57	3.10	2.46	2.97	3.62
b-tag variable 9 ↑	1.18	2.77	3.72	3.16	3.52	4.74
b-tag variable 9 ↓	-0.49	-1.09	-2.45	-2.40	-2.45	-3.68
b-tag c-jet ↑	2.80	3.62	2.35	2.10	2.02	1.97
b-tag c-jet ↓	-3.25	-3.78	-2.66	-2.33	-2.29	-2.30
b-tag l-jet ↑	-0.96	-0.79	-0.62	-0.45	-0.79	0.08

Table 28: Systematic uncertainties for the differential Zbb measurement (in m_{bb}).

Combined Channel						
Zp_T	(0, 20)	(20, 40)	(40, 60)	(60, 80)	(80, 110)	(110, 250)
1b ↑	-1.85	-2.19	-4.08	-1.81	-2.07	-2.19
1b ↓	1.97	2.38	4.49	1.98	2.35	2.47
charm ↑	2.43	1.49	1.70	0.93	1.01	1.11
charm ↓	-2.84	-1.82	-2.19	-1.23	-1.29	-1.39
background ↑	-2.44	-3.31	-4.57	-3.70	-5.49	-3.21
background ↓	2.44	3.31	4.58	3.72	5.49	3.22
JER ↑	-5.82	2.92	1.00	-0.85	2.07	0.73
JER ↓	5.82	-2.92	-1.00	0.85	-2.07	-0.73
e-energy scale ↑	0.02	-0.03	-0.15	0.25	0.21	-0.69
e-energy scale ↓	-0.06	-0.10	0.27	0.12	0.94	0.42
e-energy res ↑	-0.07	-0.82	0.99	0.94	0.83	-1.17
e-energy res ↓	-0.60	0.89	1.56	0.55	0.54	0.03
e SF ↑	-1.24	-1.96	-2.36	-2.19	-2.39	-1.77
e SF ↓	1.24	1.98	2.40	2.23	2.41	1.80
mu-energy scale ↑	-0.21	0.07	-0.01	0.13	-0.37	0.05
mu-energy scale ↓	-0.01	-1.44	1.08	-0.00	-0.28	0.34
mu-energy res ID ↑	-0.31	-1.18	0.90	0.06	-0.19	-0.10
mu-energy res ID ↓	-0.02	0.11	-0.10	0.33	-0.54	0.21
mu-energy res MS ↑	-0.27	-0.11	0.35	0.65	-0.59	0.13
mu-energy res MS ↓	0.10	-1.13	0.43	0.62	-0.04	0.58
mu SF ↑	-0.57	-0.54	-0.58	-0.56	-0.63	-0.58
mu SF ↓	0.58	0.54	0.59	0.57	0.63	0.58
Trigger SF ↑	-0.44	-0.38	-0.40	-0.39	-0.43	-0.37
Trigger SF ↓	0.44	0.38	0.41	0.39	0.43	0.37
MPI ↑	7.42	-0.26	-2.24	0.22	1.91	0.36
MPI ↓	-5.15	0.13	1.26	-0.07	-1.05	-0.17
Template weight l-jets ↑	-3.40	-1.47	-1.14	-0.96	-1.13	-1.30
Template weight l-jets ↓	3.40	1.47	1.14	0.96	1.13	1.30
Template weight c-jets ↑	-0.40	-0.10	-0.37	-0.95	-0.77	-0.34
Template weight c-jets ↓	0.40	0.10	0.37	0.95	0.77	0.34
Template weight b-jets ↑	4.52	8.28	8.64	7.58	9.11	7.27
Template weight b-jets ↓	-4.52	-8.28	-8.64	-7.58	-9.11	-7.27
Pile-up ↑	-0.44	0.38	1.26	-0.53	-0.20	-0.38
Pile-up ↓	0.13	-0.47	-1.26	0.50	0.29	0.37
MET ResoSoftTerms ↑	-0.15	0.04	-0.45	0.11	0.84	0.06
MET ResoSoftTerms ↓	0.09	0.00	0.18	-0.05	0.70	0.03
MET ScaleSoftTerms ↑	0.06	0.31	0.23	-0.01	1.04	-0.01
MET ScaleSoftTerms ↓	-0.14	-0.44	-0.30	-0.18	-0.45	-0.48
Z vertex re-weight ↑	1.60	2.18	4.78	0.98	0.08	-0.67
Z vertex re-weight ↓	-1.60	-2.18	-4.78	-0.98	-0.08	0.67
MC stat ↑	6.01	3.42	3.38	3.83	3.95	4.14
MC stat ↓	-5.83	-3.37	-3.32	-3.76	-3.88	-4.06
JES EffectiveNP 1 ↑	0.34	0.29	0.06	-0.37	0.35	-0.27
JES EffectiveNP 1 ↓	-0.34	-0.29	-0.06	0.37	-0.35	0.27
JES EffectiveNP 2 ↑	4.13	3.51	3.55	2.07	2.83	2.10
JES EffectiveNP 2 ↓	-4.13	-3.51	-3.55	-2.07	-2.83	-2.10
JES EffectiveNP 3 ↑	-1.45	-0.95	-1.23	-0.92	-0.11	-0.77
JES EffectiveNP 3 ↓	1.45	0.95	1.23	0.92	0.11	0.77
JES EffectiveNP 4 ↑	0.45	0.96	1.32	0.15	0.55	1.36
JES EffectiveNP 4 ↓	-0.45	-0.96	-1.32	-0.15	-0.55	-1.36
JES EffectiveNP 5 ↑	-0.28	0.17	0.62	-0.01	0.50	0.25
JES EffectiveNP 5 ↓	0.28	-0.17	-0.62	0.01	-0.50	-0.25
JES EffectiveNP 6restTerm ↑	0.09	0.30	0.76	0.02	0.41	0.33
JES EffectiveNP 6restTerm ↓	-0.09	-0.30	-0.76	-0.02	-0.41	-0.33
JES EtaIntercalibration Modelling ↑	-0.53	-1.13	0.02	-0.37	0.69	-0.60
JES EtaIntercalibration Modelling ↓	0.53	1.13	-0.02	0.37	-0.69	0.60
JES EtaIntercalibration TotalStat ↑	0.47	0.26	0.35	-0.08	0.14	-0.01
JES EtaIntercalibration TotalStat ↓	-0.47	-0.26	-0.35	0.08	-0.14	0.01
JES RelativeNonClosure MC11c ↑	-0.41	0.45	0.09	0.02	0.40	0.27
JES RelativeNonClosure MC11c ↓	0.41	-0.45	-0.09	-0.02	-0.40	-0.27
JES SingleParticle HighPt ↑	0.20	0.45	0.75	0.29	0.67	0.48
JES SingleParticle HighPt ↓	-0.20	-0.45	-0.75	-0.29	-0.67	-0.48
JES Pileup OffsetNPV ↑	0.62	1.06	0.66	0.52	1.05	1.00
JES Pileup OffsetNPV ↓	-0.62	-1.06	-0.66	-0.52	-1.05	-1.00
JES Pileup OffsetMu ↑	2.97	0.11	1.00	0.12	1.04	0.17
JES Pileup OffsetMu ↓	-2.97	-0.11	-1.00	-0.12	-1.04	-0.17
JES ClosebyJets ↑	2.14	-0.53	-0.20	-0.16	-0.10	-1.03
JES ClosebyJets ↓	-2.14	0.53	0.20	0.16	0.10	1.03
JES bJES ↑	-1.77	-1.52	-1.68	-1.10	0.19	-0.46
JES bJES ↓	1.77	1.52	1.68	1.10	-0.19	0.46
JES FlavComp ↑	2.42	0.14	1.71	0.44	1.54	-0.01
JES FlavComp ↓	-2.42	-0.14	-1.71	-0.44	-1.54	0.01
JES FlavResp ↑	1.89	0.43	1.17	0.39	1.08	-0.05
JES FlavResp ↓	-1.89	-0.43	-1.17	-0.39	-1.08	0.05
b-tag variable 0 ↑	0.31	0.46	0.72	0.22	0.95	0.74
b-tag variable 0 ↓	0.16	0.27	0.52	0.17	0.49	0.53
b-tag variable 1 ↑	0.14	0.33	0.54	0.10	0.68	0.62
b-tag variable 1 ↓	0.32	0.40	0.70	0.28	0.76	0.64
b-tag variable 2 ↑	0.21	0.49	0.69	0.22	0.76	0.62
b-tag variable 2 ↓	0.25	0.24	0.55	0.17	0.69	0.65
b-tag variable 3 ↑	0.20	0.30	0.62	0.14	0.67	0.59
b-tag variable 3 ↓	0.26	0.44	0.62	0.25	0.78	0.68
b-tag variable 4 ↑	0.16	0.43	0.63	0.21	0.77	0.70
b-tag variable 4 ↓	0.32	0.30	0.61	0.18	0.67	0.57
b-tag variable 5 ↑	0.44	0.47	0.79	0.31	0.86	0.79
b-tag variable 5 ↓	0.04	0.26	0.45	0.08	0.59	0.48
b-tag variable 6 ↑	0.52	0.66	0.94	0.46	1.05	0.79
b-tag variable 6 ↓	-0.06	0.07	0.30	-0.07	0.40	0.48
b-tag variable 7 ↑	0.36	0.53	1.16	0.45	0.99	0.82
b-tag variable 7 ↓	0.10	0.19	0.07	-0.07	0.44	0.45
b-tag variable 8 ↑	-1.61	-1.49	-1.96	-1.79	-2.01	-1.14
b-tag variable 8 ↓	2.10	2.21	3.18	2.16	3.41	2.39
b-tag variable 9 ↑	2.31	2.82	3.92	2.79	4.24	2.90
b-tag variable 9 ↓	-1.84	-2.13	-2.69	-2.43	-2.88	-1.67
b-tag c-jet ↑	3.92	2.61	3.24	1.29	1.75	2.02
b-tag c-jet ↓	-4.04	-2.88	-3.75	-1.57	-1.98	-2.22
b-tag l-jet ↑	-2.48	-0.43	-0.17	0.07	0.26	-0.01

Table 29: Systematic uncertainties for the differential Zbb measurement (in Zp_T).

Combined Channel							
$Z_{\|y\|}$	(0, 0.2)	(0.2, 0.4)	(0.4, 0.6)	(0.6, 0.8)	(0.8, 1.2)	(1.2, 1.6)	(1.6, 2.5)
1b ↑	-3.64	-1.90	-1.29	-1.59	-2.05	-2.89	-4.92
1b ↓	3.93	2.12	1.45	1.73	2.25	3.22	5.63
charm ↑	1.55	0.87	0.70	1.20	1.92	1.34	2.86
charm ↓	-1.99	-1.11	-0.83	-1.52	-2.44	-1.62	-3.42
background ↑	-4.75	-4.10	-3.43	-4.04	-4.18	-2.78	-3.55
background ↓	4.77	4.10	3.44	4.03	4.15	2.80	3.56
JER ↑	-2.35	2.01	-1.23	1.68	0.68	2.31	-1.08
JER ↓	2.35	-2.01	1.23	-1.68	-0.68	-2.31	1.08
e-energy scale ↑	-0.79	-0.22	0.09	0.34	-0.22	-0.22	0.48
e-energy scale ↓	0.25	0.42	-0.22	1.21	-1.08	0.29	0.17
e-energy res ↑	-0.15	1.23	0.02	0.37	0.29	0.58	-2.73
e-energy res ↓	-0.04	1.64	-0.30	1.56	-0.03	0.03	-0.22
e SF ↑	-2.32	-2.01	-1.96	-2.25	-2.01	-1.65	-2.18
e SF ↓	2.36	2.04	2.02	2.26	2.01	1.67	2.21
mu-energy scale ↑	-0.17	0.02	0.01	-0.10	-0.08	-0.17	0.47
mu-energy scale ↓	0.10	0.02	-0.04	0.18	-0.04	-0.08	-0.05
mu-energy res ID ↑	-0.11	0.09	-0.04	0.07	0.03	-0.17	-0.25
mu-energy res ID ↓	0.03	-0.25	0.32	0.02	0.04	-0.12	0.10
mu-energy res MS ↑	-0.08	-0.11	0.10	-0.23	0.36	0.24	-0.13
mu-energy res MS ↓	-0.02	-0.11	-0.05	0.52	0.05	-0.00	0.20
mu SF ↑	-0.53	-0.52	-0.50	-0.53	-0.61	-0.63	-0.72
mu SF ↓	0.53	0.52	0.50	0.53	0.62	0.64	0.73
Trigger SF ↑	-0.44	-0.45	-0.40	-0.44	-0.43	-0.32	-0.20
Trigger SF ↓	0.44	0.45	0.40	0.44	0.43	0.32	0.21
MPI ↑	-0.37	3.19	-0.68	-1.45	2.08	0.64	2.63
MPI ↓	0.17	-1.63	0.37	0.81	-1.08	-0.37	-1.31
Template weight l-jets ↑	-1.49	-1.19	-1.11	-1.23	-1.54	-1.30	-2.06
Template weight l-jets ↓	1.49	1.19	1.11	1.23	1.54	1.30	2.06
Template weight c-jets ↑	-0.59	-0.50	-0.21	-0.63	-0.52	-0.20	-0.57
Template weight c-jets ↓	0.59	0.50	0.21	0.63	0.52	0.20	0.57
Template weight b-jets ↑	8.87	9.54	7.86	5.22	4.23	7.59	20.27
Template weight b-jets ↓	-8.87	-9.54	-7.86	-5.22	-4.23	-7.59	-20.27
Pile-up ↑	-0.14	0.52	-0.53	0.36	0.48	-0.49	0.59
Pile-up ↓	0.11	-0.62	0.48	-0.53	-0.44	0.54	-0.33
MET ResoSoftTerms ↑	-0.04	-0.33	0.11	0.30	-0.33	0.29	0.20
MET ResoSoftTerms ↓	0.01	0.08	-0.06	-0.07	0.13	0.61	-0.17
MET ScaleSoftTerms ↑	0.11	-0.09	0.23	0.24	0.39	0.35	0.40
MET ScaleSoftTerms ↓	-0.70	-0.42	0.05	-0.58	-0.36	-0.19	-0.44
Z vertex re-weight ↑	1.71	1.54	-0.10	0.98	1.32	1.86	7.67
Z vertex re-weight ↓	-1.71	-1.54	0.10	-0.98	-1.32	-1.86	-7.67
MC stat ↑	4.23	4.12	4.57	4.41	3.68	4.20	
4.98							
MC stat ↓	-4.14	-4.04	-4.47	-4.31	-3.61	-4.12	
-4.85							
JES EffectiveNP 1 ↑	-0.92	-0.93	-0.26	-0.81	-0.05	0.00	3.88
JES EffectiveNP 1 ↓	0.92	0.93	0.26	0.81	0.05	-0.00	-3.88
JES EffectiveNP 2 ↑	1.03	1.83	3.59	2.58	4.52	3.98	3.97
JES EffectiveNP 2 ↓	-1.03	-1.83	-3.59	-2.58	-4.52	-3.98	-3.97
JES EffectiveNP 3 ↑	-2.18	-1.45	-2.17	-1.91	-0.62	-0.68	1.64
JES EffectiveNP 3 ↓	2.18	1.45	2.17	1.91	0.62	0.68	-1.64
JES EffectiveNP 4 ↑	0.50	0.34	0.89	0.14	0.31	1.14	3.87
JES EffectiveNP 4 ↓	-0.50	-0.34	-0.89	-0.14	-0.31	-1.14	-3.87
JES EffectiveNP 5 ↑	-0.77	-0.17	-0.02	-0.51	-0.10	0.49	4.08
JES EffectiveNP 5 ↓	0.77	0.17	0.02	0.51	0.10	-0.49	-4.08
JES EffectiveNP 6restTerm ↑	-0.58	0.04	0.05	-0.35	-0.06	0.65	3.90
JES EffectiveNP 6restTerm ↓	0.58	-0.04	-0.05	0.35	0.06	-0.65	-3.90
JES EtaIntercalibration Modelling ↑	-1.20	-0.59	-1.17	-1.56	-0.41	-0.19	2.66
JES EtaIntercalibration Modelling ↓	1.20	0.59	1.17	1.56	0.41	0.19	-2.66
JES EtaIntercalibration TotalStat ↑	-0.74	-0.63	0.07	-0.48	-0.20	-0.14	4.05
JES EtaIntercalibration TotalStat ↓	0.74	0.63	-0.07	0.48	0.20	0.14	-4.05
JES RelativeNonClosure MC11c ↑	-0.75	-0.08	0.17	-0.20	-0.40	0.13	3.51
JES RelativeNonClosure MC11c ↓	0.75	0.08	-0.17	0.20	0.40	-0.13	-3.51
JES SingleParticle HighPt ↑	0.00	-0.00	0.00	-0.00	0.07	0.89	3.72
JES SingleParticle HighPt ↓	0.00	0.00	0.00	0.00	-0.07	-0.89	-3.72
JES Pileup OffsetNPV ↑	-0.51	0.93	-0.23	0.45	1.35	0.54	2.18
JES Pileup OffsetNPV ↓	0.51	-0.93	0.23	-0.45	-1.35	-0.54	-2.18
JES Pileup OffsetMu ↑	-2.27	0.31	-0.44	0.48	-0.68	0.98	4.27
JES Pileup OffsetMu ↓	2.27	-0.31	0.44	-0.48	0.68	-0.98	-4.27
JES ClosebyJets ↑	-1.39	-1.03	-0.78	-0.86	-0.57	-0.16	4.55
JES ClosebyJets ↓	1.39	1.03	0.78	0.86	0.57	0.16	-4.55
JES bJES ↑	-1.79	-1.68	-2.37	-1.28	-1.27	-0.68	2.96
JES bJES ↓	1.79	1.68	2.37	1.28	1.27	0.68	-2.96
JES FlavComp ↑	-0.43	-0.07	0.47	-1.71	0.95	0.94	4.82
JES FlavComp ↓	0.43	0.07	-0.47	1.71	-0.95	-0.94	-4.82
JES FlavResp ↑	0.05	-0.21	0.14	-0.50	0.63	0.44	2.65
JES FlavResp ↓	-0.05	0.21	-0.14	0.50	-0.63	-0.44	-2.65
b-tag variable 0 ↑	0.09	0.06	0.03	0.12	0.24	1.03	3.49
b-tag variable 0 ↓	-0.09	-0.06	-0.03	-0.12	-0.07	0.82	3.26
b-tag variable 1 ↑	-0.02	-0.04	-0.05	-0.09	-0.01	0.85	3.33
b-tag variable 1 ↓	0.02	0.03	0.05	0.09	0.17	1.00	3.41
b-tag variable 2 ↑	0.13	0.07	0.07	0.03	0.02	0.90	3.51
b-tag variable 2 ↓	-0.13	-0.08	-0.07	-0.04	0.14	0.95	3.23
b-tag variable 3 ↑	-0.13	-0.05	-0.06	-0.06	0.07	0.90	3.36
b-tag variable 3 ↓	0.13	0.04	0.06	0.06	0.09	0.95	3.39
b-tag variable 4 ↑	0.02	-0.02	0.09	-0.05	0.11	0.99	3.51
b-tag variable 4 ↓	-0.02	0.01	-0.09	0.05	0.05	0.86	3.24
b-tag variable 5 ↑	0.15	0.18	0.12	0.24	0.19	0.97	3.53
b-tag variable 5 ↓	-0.15	-0.19	-0.12	-0.24	-0.02	0.88	3.26
b-tag variable 6 ↑	0.29	0.17	0.17	0.44	0.38	1.15	3.81
b-tag variable 6 ↓	-0.29	-0.18	-0.17	-0.44	-0.22	0.70	2.97
b-tag variable 7 ↑	0.35	0.37	0.16	0.20	0.38	1.14	3.59
b-tag variable 7 ↓	-0.35	-0.38	-0.16	-0.21	-0.22	0.71	3.18
b-tag variable 8 ↑	-2.55	-2.16	-1.54	-2.16	-2.22	-0.93	0.96
b-tag variable 8 ↓	2.53	2.15	1.50	2.14	2.34	2.79	5.83
b-tag variable 9 ↑	3.37	2.84	2.26	2.76	2.75	3.37	6.47
b-tag variable 9 ↓	-3.38	-2.86	-2.30	-2.81	-2.67	-1.52	0.32
b-tag c-jet ↑	3.16	1.77	1.23	1.60	3.04	2.32	4.74
b-tag c-jet ↓	-3.60	-2.03	-1.32	-1.81	-3.50	-2.53	-4.90
b-tag l-jet ↑	-0.08	-0.28	-0.03	-0.30	-1.97	0.69	-0.46

Table 30: Systematic uncertainties for the differential Zbb measurement (in $Z_{|y|}$).

15 Theoretical Predictions

A next-to-leading order prediction is obtained from MCFM using the five-flavor MSTW2008 PDFs. MCFM is a parton level pQCD calculation, with partons clustered into jets in the final state, which allows event generation for a flexible implementation of the kinematic requirements defining a fiducial signal. In this case, leptons and jets are required to have $p_{\mathrm{T}} > 20$ GeV and to be produced at $|\eta| < 2.5$ and $|y| < 2.4$, respectively. In addition the di-lepton invariant mass has to be in the range 76 – 106 GeV. Lepton-jet overlap removal criteria are applied consistently with the particle level selection described in section 4.2 and the jets are accepted as b-tagged if they match a b-parton according to the same criteria applied to B hadrons in section 4.2. The MCFM Monte Carlo capability is exploited to obtain a breakdown of the predicted cross section, passing the acceptance requirements, into the various intervals of the differential distributions measured in data.

In general, to obtain a full prediction, results from several sub-processes, implemented in the calculation, must be combined. In particular, for the $Z+b$ prediction at NLO the various sub-processes involved will describe final states with only one b-jet, events with two b-jets one of them not in the acceptance or merged to the other one in the jet-finding algorithm and events with b-jets in the acceptance. The renormalisation and factorisation scales in the calculation are set to the sum in quadrature of the Z boson mass and p_{T} on an event by event basis.

The uncertainty on the prediction has three main sources: the choice of the scales used in the calculation, the uncertainty on α_s and the experimental errors on the measurements used as input for the PDF set. The dependency of the results on the choice of the renormalisation and factorisation scales is assessed by independently shifting up then down the two scales by a factor of 2. The calculation is repeated by changing the value of the strong coupling constant of plus and minus one standard deviation consistently in the matrix element and in the PDF set applied. The remaining uncertainty arising from the experimental contraints on the PDF set adopted is also assessed, by applying the recommended procedures. In addition to estimate these sources of uncertainties, the spread on the predictions arising from the the choice of different PDF sets has been accessed and will be presented as an indication of extra theory uncertainty.

The data measurements are defined based on a particle-level signal definition quite close to the experimentally accessible observable and, therefore, cannot be directly compared to the parton level MCFM prediction. In order to allow the data-theory comparison, the parton level MCFM prediction must be corrected for the effects of QED FSR from the leptons and for the “non-perturbative corrections” induced by hadronisation, underlying event overlapping with the hard scattering and multiparton interactions.

The QED correction is derived from the Alpgen samples by comparing the results of the nominal particle level selection, based on ”dressed” leptons, with those obtained using Born leptons, i.e. leptons from the Born level multi-parton Alpgen matrix element, before the radiation is applied through the interface with the Herwig parton-shower. Fig. 114 and 115, in appendix D, show the multiplicative corrective factors to be applied to the MCFM prediction in all bins of the differential Zb distributions. The QED FSR correction appears to be rather stable within the phase-space of interest for the measurements described here; therefore, the average value of 0.97 ± 0.01 has been estimated and applied in all bins both for the Zb and Zbb selection. The error on the correction arises from the MC statistics of the Alpgen sample.

Non-perturbative corrections are derived using SHERPA 1.4.1, using the CT10 PDF set. In the SHERPA multi-parton Monte Carlo both matrix element and parton shower can lead to b-jet production in the final state and all overlaps are internally removed. The processes contributing to the signal definition can be separated into two categories: processes with at least one hard jet from a single heavy flavour parton and processes where a gluon splits into a pair of b-partons close in phase space which are not resolved by the jet-finding procedure. The contributions from the two categories are estimated separately and then summed up. Multi-parton interactions and fragmentation are, typically, emulated, but this features can be disabled thus allowing to compare parton-level and hadron-level predictions. The non-perturbative corrections are estimated as the ratio of the yield of signal b-jet or $Z + bb$ events predicted in each analysis bin with and without the emulation of hadronisation and multi-partin interactions. In one case, b-jets are defined by a match to a b quark (equivalent to MCFM) , in the other case, b-jets match a B hadron as in section 4.2. High statistics samples of events with two oppositely charged muons and up to four partons in the final state have been produced. The same procedure is applied using the PYTHIA Monte Carlo, version 6.427 with PDF set CTEQ 5L from the internal PYTHIA library and with the Perugia 2011 tune, in order to assess the systematic uncertainly on the correction as the absolute difference between the results obtained with the two simulations.

The distributions predicted by SHERPA and PYTHIA and the corresponding estimate of the non-perturbative corrections are shown in Fig. 85 to 87 and they are reported in tables in appendix D.

The correction factors on the inclusive $Z + b$ jet-cross section are: 0.916 ± 0.005 (SHERPA) and 0.902 ± 0.004 (PYTHIA). Larger corrections are obtained for the $Z+bb$ inclusive cross section: 0.818 ± 0.014 (SHERPA) and 0.822 ± 0.010 (PYTHIA). The average of the corrections derived with SHERPA and PYTHIA is applied to the MCFM predictions in each bin to bring the parton level prediction to the particle level. A bin-dependent source of systematic uncertainty on the prediction is assigned, to account for the difference between the two estimates of the non perturbative effects, as half of the difference between them.

Another theory prediction with a NLO accuracy of the matrix element but based on the four-flavor calculation scheme has been considered for comparison to the data: the AMC@NLO[30] MC with PDF set MSTW2008(N)LO_nf4 . A set of 10^6 parton-level simulated events representing Zbb production at LHC is available from the authors for further processing. No kinematic cuts are applied at generator level to the b-partons, which are treated as massive. As a consequence the sample is, in principle, suitable to describe the $Z + b$ inclusive data sample, as well as the Zbb sample. Events from AMC@NLO need to be showered (for these specific events, by the HERWIG 6 Monte Carlo) in order to predict physical observables. The showering brings, as extra benefit, the resummation to all orders of many classes of large logarithms that appear in the cross section. On top of the showers, the HERWIG 6 run included the fragmentation, hadronization and hadron decays phases. The events obtained in this way were finally corrected for the contribution of multi-parton interactions, as predicted by ALPGEN interfaces to HERWIG , in order to include all relevant non-perturbative effects. *This prediction is in the process of being updated with a similar one obtained with the same setting of the renormalization and factorization scales used for the MCFM predition*.

The AMC@NLO generator has been used also to produce a sample of events with lepton pairs and at least one b-jet, using a five-flavor calculation scheme in the mass-less approximation for the b-quark. The choice of the PDF set and the setting of the dynamic scales have been done in such a way to ensure coherence with the fixed order MCFM prediction. A sample of 250,000 events (*the MC statistics is currently increasing*) has been generated and showered with Herwig++. The contribution to the cross section from events with an hard parton scattering in the pp collision producing a Z and another parton interaction producing b-jets is obtained from ALPGEN as in the case of the Zbb sample.

A comparison of the total cross sections predicted for the two selections, inclusive cross section of b-jet produced in association with Z (per b-jet and per event) and Zbb cross section (per event), are summarized in table 31. The theory systematic uncertainties are assumed fully correlated in all bins of the distributions.

Cross section (fb)	MCFM(mstw2008)xNPcorr.	aMC@NLO Zbb (4f)	aMC@NLO Zbb (5f)
$\sigma(Zb)$	$5210 \pm 33(stat) - 766 + 788(syst)$	3546 ± 17	4923 ± 38
$\sigma(Zb) \times N_{b-jet}$	$5441 \pm 36(stat) - 829 + 829(syst)$	4027 ± 19	5224 ± 40
$\sigma^{\star}(Zb) \times N_{b-jet}$	$4314 \pm 33(stat) - 456 + 535(syst)$	3238 ± 16	4232 ± 37
$\sigma(Zbb)$	$411 \pm 8(stat) - 72 + 71(syst)$	462 ± 6	288 ± 10

Cross section (fb)	PDF	MCFM	σ_{stat}	$\sigma(\alpha_s)$		$\sigma(scales)$		$\sigma(pdf)$		σ_{NP+FSR}
$\sigma(Zb)$	MSTW2008	5210	33	+147	-125	+766	-743	+110	-135	76
$\sigma(Zb) \times N_{b-jet}$	MSTW2008	5441	36	+104	-130	+816	-808	+110	-131	79
$\sigma^{\star}(Zb) \times N_{b-jet}$	MSTW2008	4314	33	+141	-121	+509	-427	+88	-104	76
$\sigma(Zbb)$	MSTW2008	411	8	+28	-20	+67	-70	+7	-9	7
$\sigma(Zb)$	CT10	4835	26	+121	-67	+726	-614	+164	-158	70
$\sigma(Zb) \times N_{b-jet}$	CT10	5053	30	+91	-71	+772	-693	+153	-148	73
$\sigma^{\star}(Zb) \times N_{b-jet}$	CT10	4012	31	+79	-59	+480	-365	+121	-119	70
$\sigma(Zbb)$	CT10	384	4	+11	-18	+56	-62	+19	-18	7
$\sigma(Zb)$	NNPDF23	5402	19	+100	-76	+771	-721	+423	-404	78
$\sigma(Zb) \times N_{b-jet}$	NNPDF23	5642	32	+87	-84	+820	-791	+371	-370	82
$\sigma^{\star}(Zb) \times N_{b-jet}$	NNPDF23	4473	26	+73	-67	+503	-409	+292	-295	78
$\sigma(Zbb)$	NNPDF23	421	9	+18	-14	+61	-80	+29	-30	7

Cross section (fb)	SHERPA	ALPGEN	PYTHIA
$\sigma(Zb)$	3770.0 ± 7.7	3226.3 ± 8.5	3331.5 ± 2.6
$\sigma(Zb) \times N_{b-jet}$	4208.4 ± 8.0	3655.0 ± 9.0	3696.1 ± 2.8
$\sigma^{\star}(Zb) \times N_{b-jet}$	3642.9 ± 7.3	2971.2 ± 7.3	3197.9 ± 2.6
$\sigma(Zbb)$	421.6 ± 2.3	–	356.1 ± 1.4

Table 31: Theory predictions for the total fiducial cross sections in comparison. All predictions are at particle level, hence MCFM is corrected for non-perturbative QCD effects (fragmentation and multi-parton interactions) and QED radiation effects. Errors from the MC statistics are quoted for all generators. For MCFM the sum in quadrature of all systematic theory uncertainty discussed in the text is also reported in the top table, while the breakdown into the various components is shown in the middle table for a few choices of the PDF set. The notation $\sigma(Zbb)$, $\sigma(Zb)$, $\sigma(Zb) \times N_{b-jet}$ and $\sigma^{\star}(Zb) \times N_{b-jet}$ are used to refer to the Zbb and Zb inclusive cross section, to the b-jet cross section in events with at least one b-jet and to the b-jet cross section in events with at least one b-jet and Z transverse momentum greated than 20 GeV.

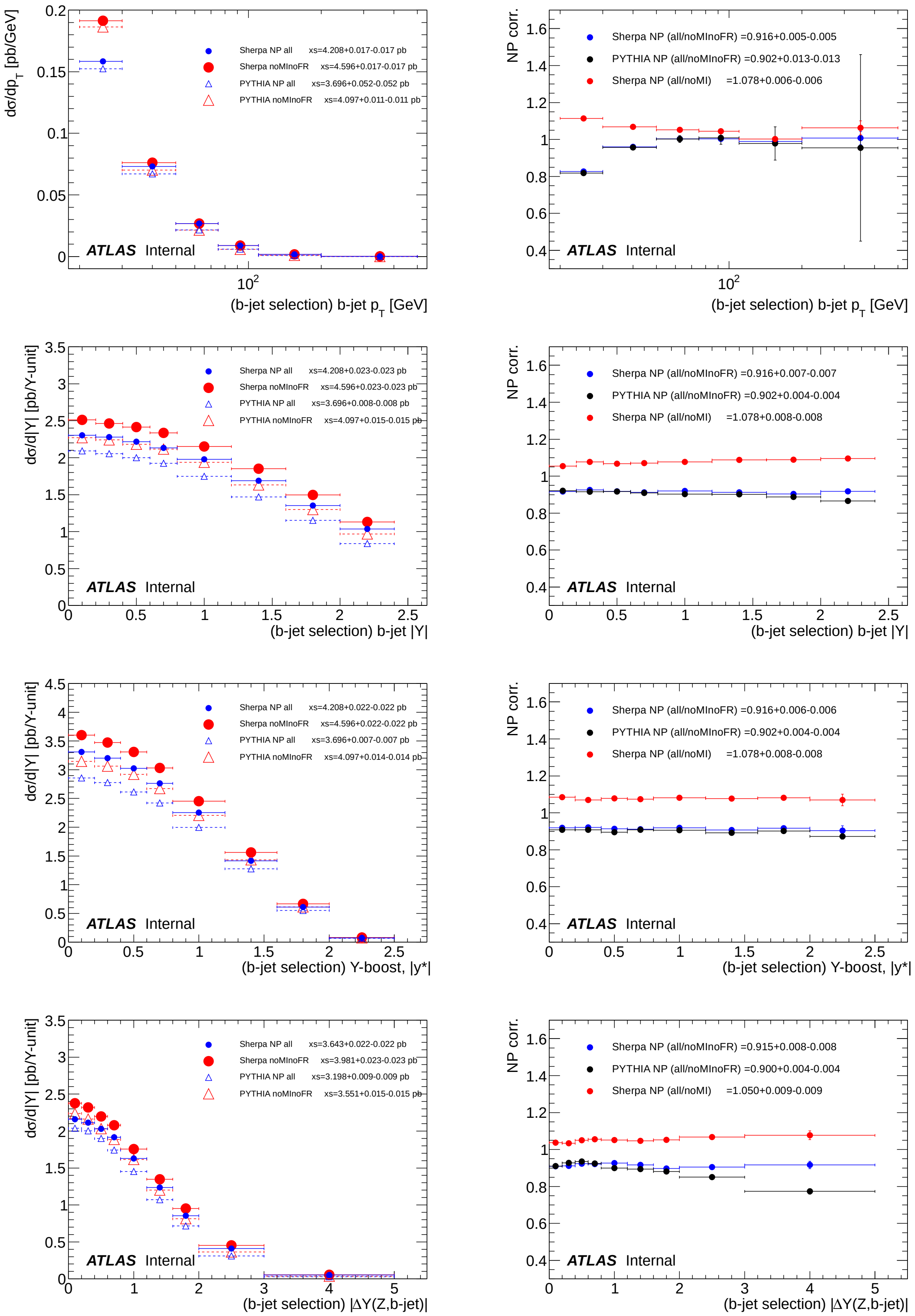

Figure 85: QCD non-perturbative corrections (NP) for the differential distributions of b-jet $p_{\mathrm{T}}$and rapidity, $y^{\star}$ of the system formed by the b-jet and the Z and $|\Delta y|$ between b-jet and Z in $Z + b$ selection. The effects are evaluated with SHERPA and PYTHIA as the ratio of the predictions for the differential cross-sections, shown to the left, with all NP effects enabled to the predictions obtained when disabling all effects. In red the ratio of the SHERPA prediction with all non-perturbative corrections included to the prediction with multi-parton interaction disables is shown.

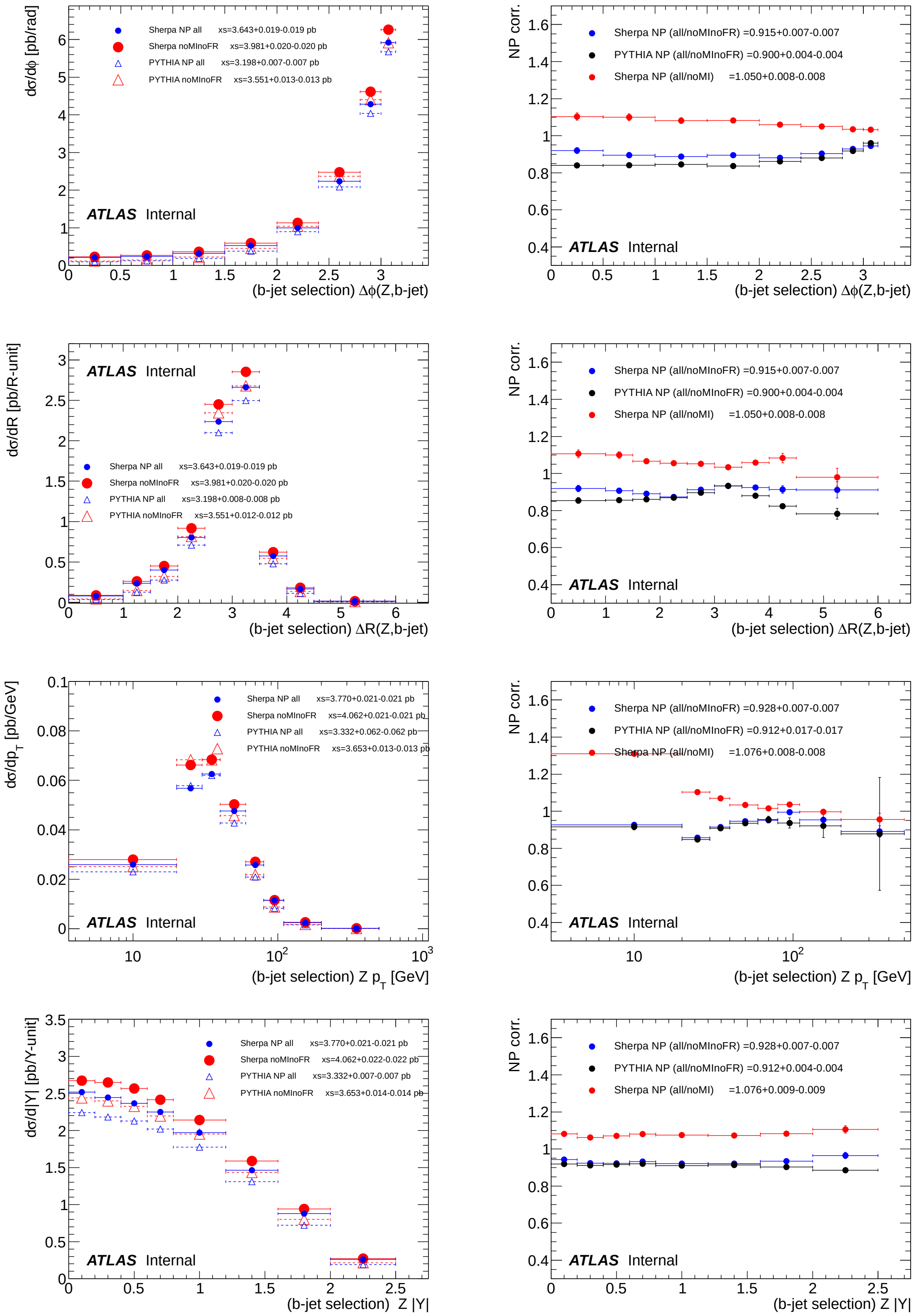

Figure 86: QCD non-perturbative corrections (NP) for the differential distributions $\Delta\phi$ and ΔR between b-jet and Z, Z p_T and rapidity, in the $Z+b$ selection. The effects are evaluated with SHERPA and PYTHIA as the ratio of the predictions for the differential cross-sections, shown to the left, with all NP effects enabled to the predictions obtained when disabling all effects. In red the ratio of the SHERPA prediction with all non-perturbative corrections included to the prediction with multi-parton interaction disables is shown.

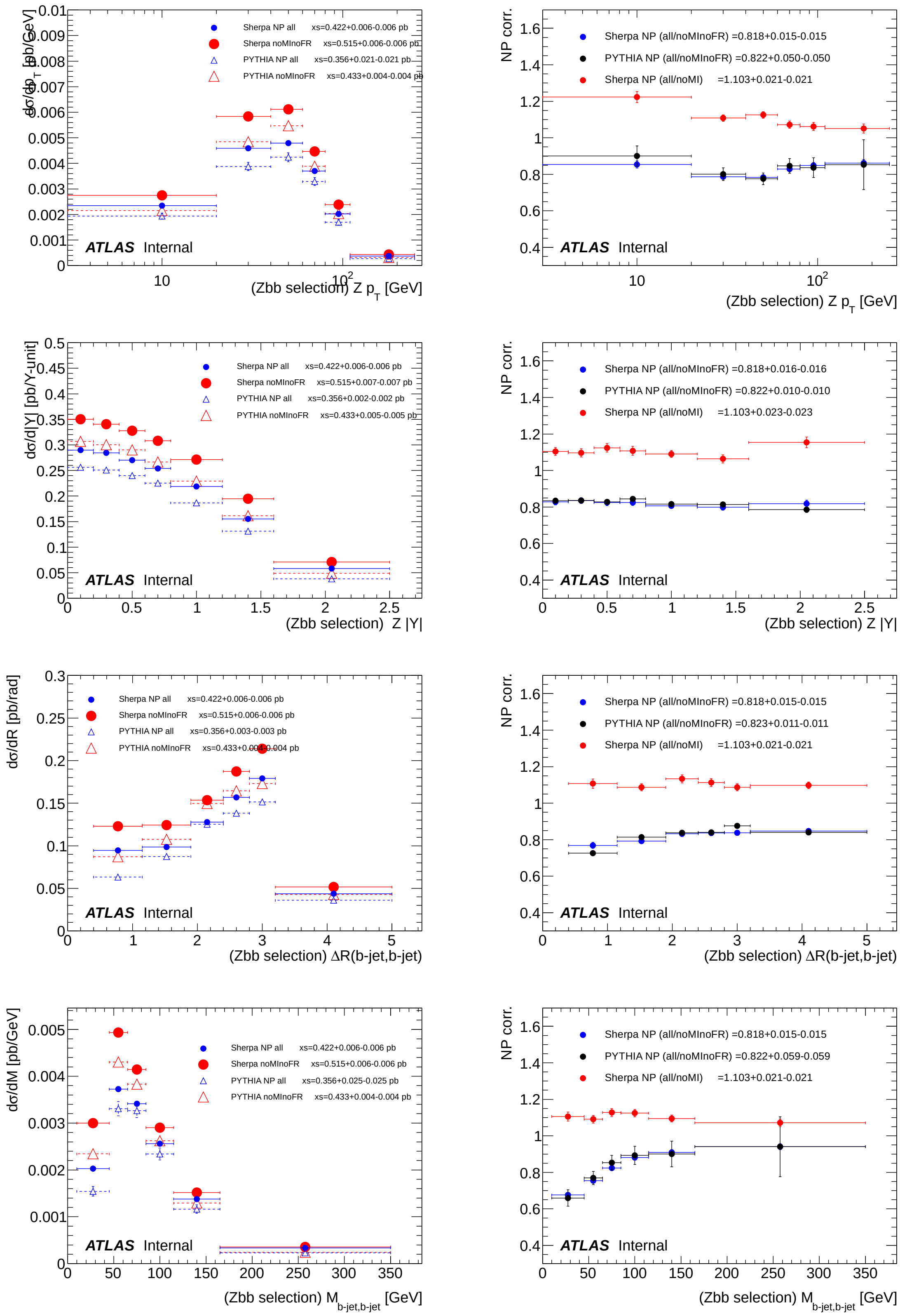

Figure 87: QCD non-perturbative corrections (NP) for the differential distributions of p_T and rapidity of the Z boson, distance in R between the two b-jets and invarinat mass of the two b-jets in the $Z + bb$ selection. The effects are evaluated with SHERPA and PYTHIA as the ratio of the predictions for the differential cross-sections, shown to the left, with all NP effects enabled to the predictions obtained when disabling all effects. In red the ratio of the SHERPA prediction with all non-perturbative corrections included to the prediction with multi-parton interaction disables is shown.

16 Results

16.1 Results for the $Z + b$ final state

The jet-level differential cross sections for $Z + b$ observables are shown in figure 88. MCFM and SHERPA are seen to describe the jet p_T dependence of the cross section well. MCFM also describes the normalisation, while Sherpa has a 20% normalisation deficit. The p_T dependence predicted by aMC@NLO meanwhile is seen to be significantly different. The rapidity dependence predicted by all three models is good. The angular variables ΔR and $\Delta\phi$ are shown in the same figure. Here, SHERPA gives a remarkably good description of the data up to a normalisation factor, while the prediction from MCFM is strongly disfavoured. aMC@NLO produces a reasonable description of $\Delta\phi$ and ΔR up to values of around 3.5.

The event-level differential cross sections for $Z + b$ observables are shown in figure 89 (c) and (d). None of the models give a satisfactory description of the $Z p_T$ dependence of the cross section, while the shape of Z rapidity is generally well reproduced.

The PDF dependence of the theoretical predictions together with a breakdown of the systematic uncertainties on the theory are shown in Figures 90 and 91.

16.2 Results for the $Z + bb$ final state

The resulting cross section for the $Z + bb$ inclusive measurement, calculated as described in Section 13 is

$$\sigma(Z + b\bar{b}) \cdot BR(Z \to ee, \mu\mu) = 0.54 \pm 0.02(\text{stat.})^{+0.06}_{-0.06}(\text{syst.}) \pm 0.01(\text{lumi.})pb$$

For comparison, cross sections were also calculated separately in the electron and muon decay channel, yielding

$$\sigma(Z + b\bar{b}) \cdot BR(Z \to ee) = 0.50 \pm 0.04(\text{stat.})^{+0.05}_{-0.06}(\text{syst.}) \pm 0.01(\text{lumi.})pb$$

and

$$\sigma(Z + b\bar{b}) \cdot BR(Z \to \mu\mu) = 0.57 \pm 0.03(\text{stat.})^{+0.06}_{-0.06}(\text{syst.}) \pm 0.01(\text{lumi.})pb$$

This result is in good agreement with the theoretical predictions summarised in Table 32. The PYTHIA prediction is low, as can be expected for a LO parton shower.

Theory	Cross section (pb)
MCFM +CT10	$0.403^{+0.082}_{-0.066}$
MCFM +MSTW08	$0.426^{+0.086}_{-0.070}$
AMC@NLO	0.471 ± 0.015
SHERPA	0.423 ± 0.005
PYTHIA	0.358 ± 0.025

Table 32: Theory predictions for the total fiducial Z+bb cross sections. All predictions are at particle level. The MCFM uncertainty includes the scale, PDF, α_s and npc effects. All other predictions are quoted with statistical uncertainties only.

The results of the differential $Z + bb$ cross section measurements as are shown in Fig. 92. Within uncertainties, all four measurements agree well with predictions, with some tension between data and MCFM being visible in the low $\Delta R(bb)$ region.

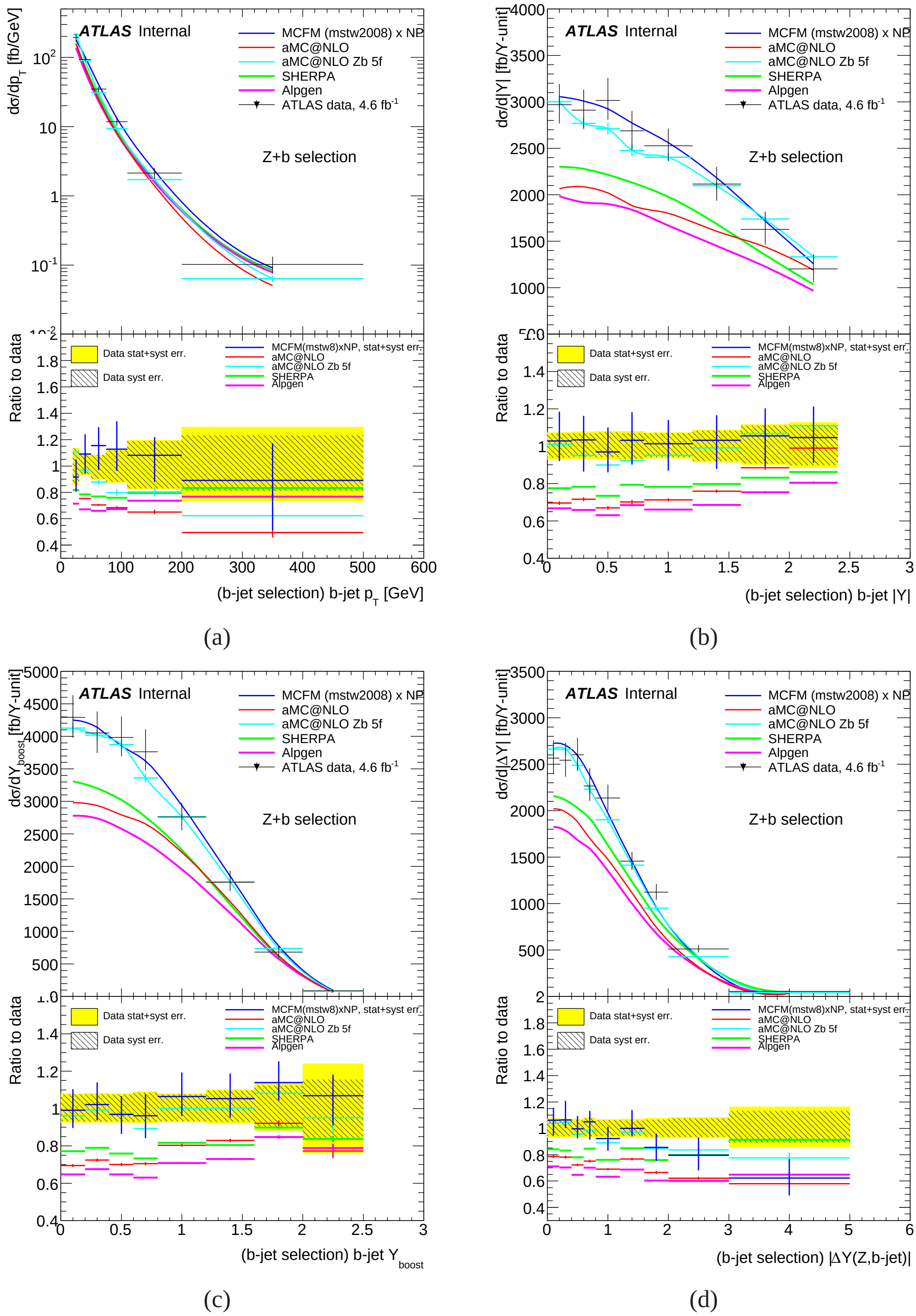

Figure 88: Comparison of SHERPA ALPGEN MCFM and aMC@NLO, in the 4-flavor and 5-flavor schemas, to data for b-jet distributions in the *Zb* inclusive selection: (a) b-jet p_{T}, (b) b-jet $|y|$, (c) $y^{\star}$ of the b-jet and Z system and (d) $|\Delta y(Z, b{-}\mathrm{jet})|$ between the b-jet and the Z in events with $p_{\mathrm{T}}(Z) > 20$ GeV. The MCFM prediction has been calculated using the NP corrections derived from SHERPA and PYTHIA . The ALPGEN prediction is scaled by a k-factor to correct it to NLO.

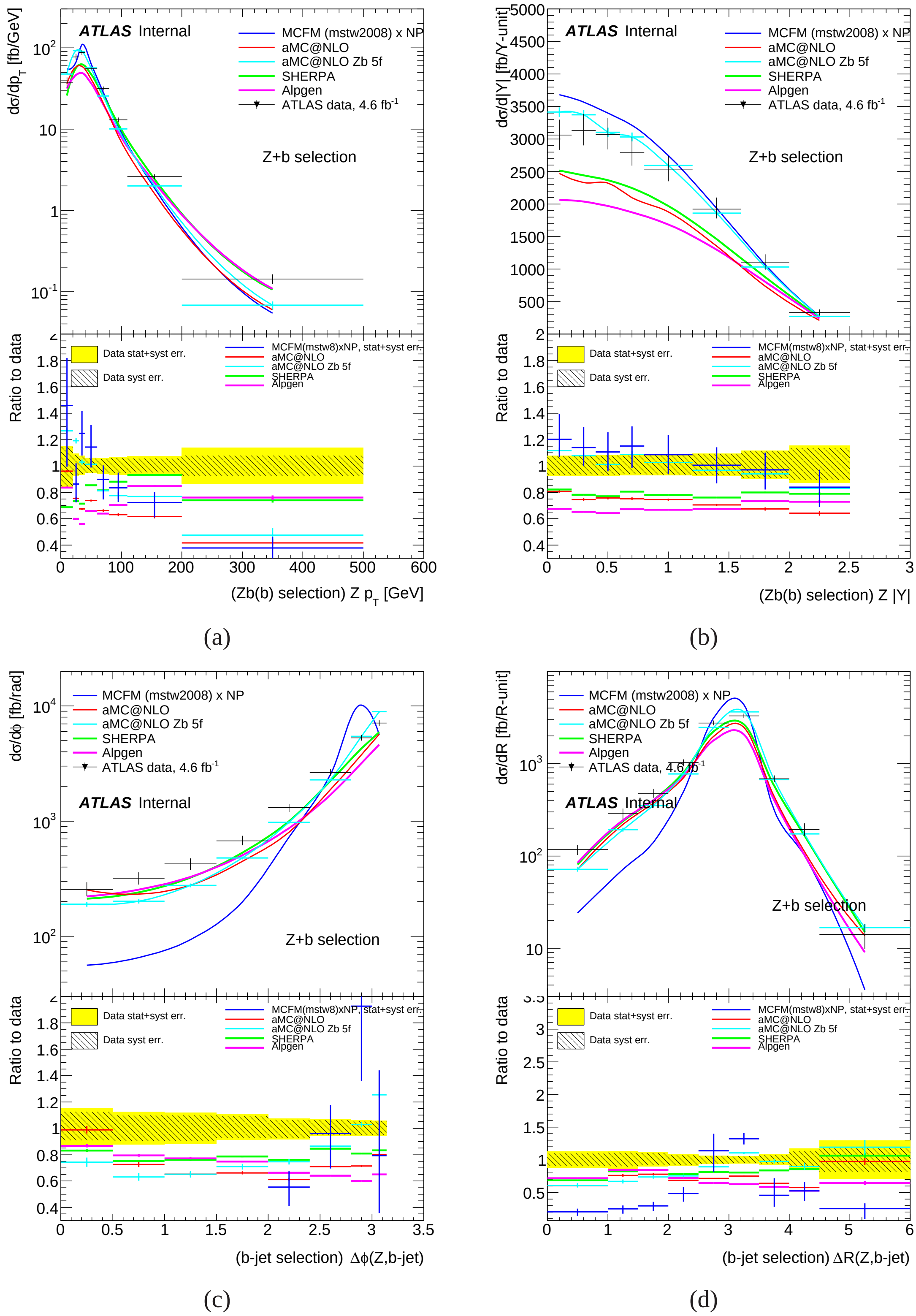

Figure 89: Comparison of SHERPA ALPGEN MCFM and aMC@NLO, in the 4-flavor and 5-flavor schemas, to data for event-based distributions in the *Zb* inclusive selection: separation in ϕ and R between b-jet and the Z for events with $p_T(Z) > 20$ GeV (a-b), Z transverse momentum and absolute rapidity (c-d). The MCFM prediction has been calculated using the NP corrections derived from SHERPA and PYTHIA . The ALPGEN prediction is scaled by a k-factor to correct it to NLO.

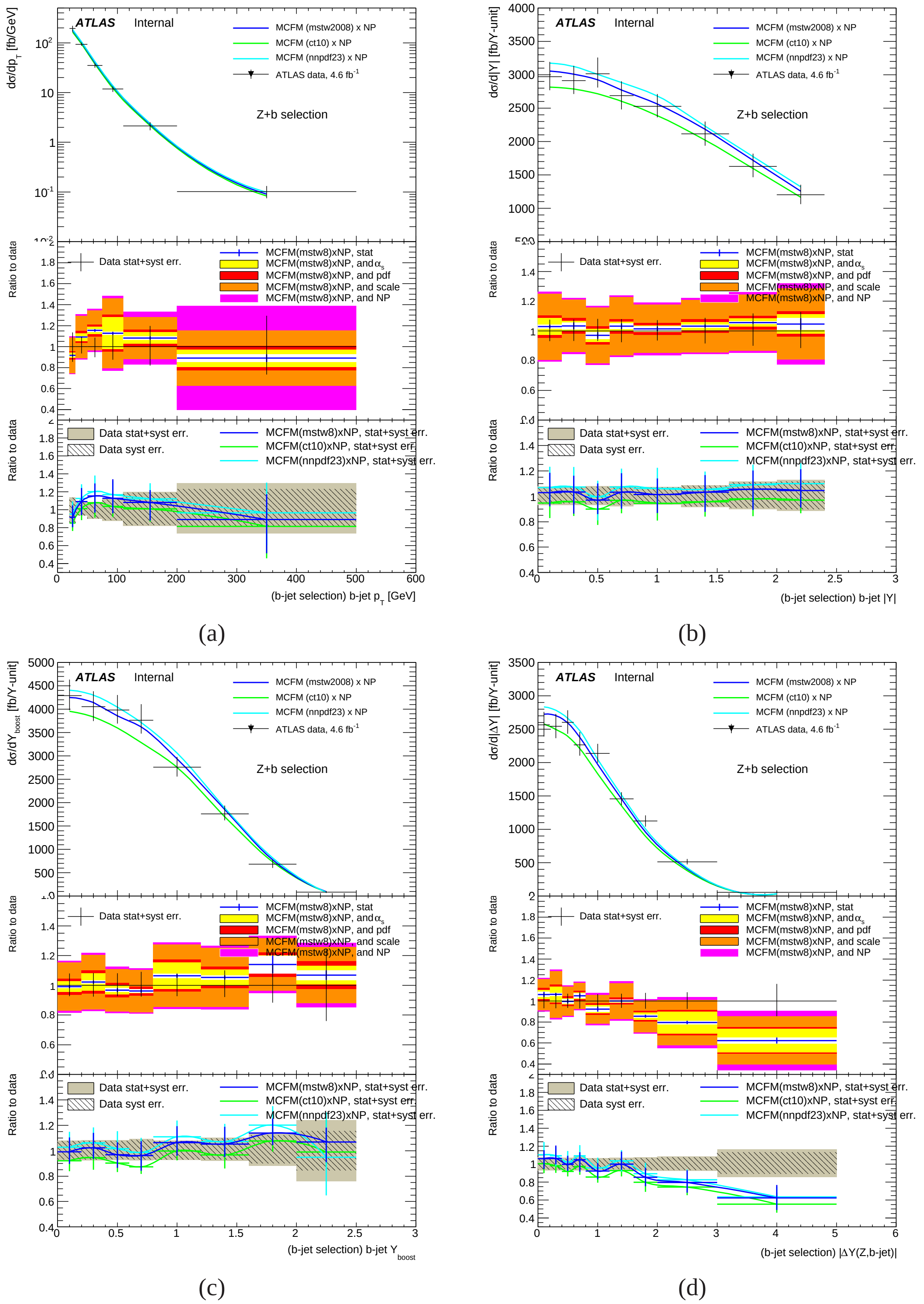

Figure 90: *Zb* inclusive selection. Comparison between data and the MCFM predictions with various PDF sets and breakdown of the theory incertainty into the various sources when MSTW2008 is used. (a) b-jet p_{T}, (b) b-jet $|y|$, (c-d) $y^{\star}$ of the b-jet and Z system and separation in rapidity between teh Z and the b-jet in events with $\Delta\phi(Z, b\text{–jet})$ and $\Delta R(Z, b\text{–jet})$ between the b-jets and the Z in events with $p_{\mathrm{T}}(Z) > 20$ GeV. The MCFM prediction has been calculated using the NP corrections derived from SHERPA and PYTHIA . In the middle inset of each plot the sources of systematic uncertainty on the MCFM prediction are added linearly in order to appreciate the relative size.

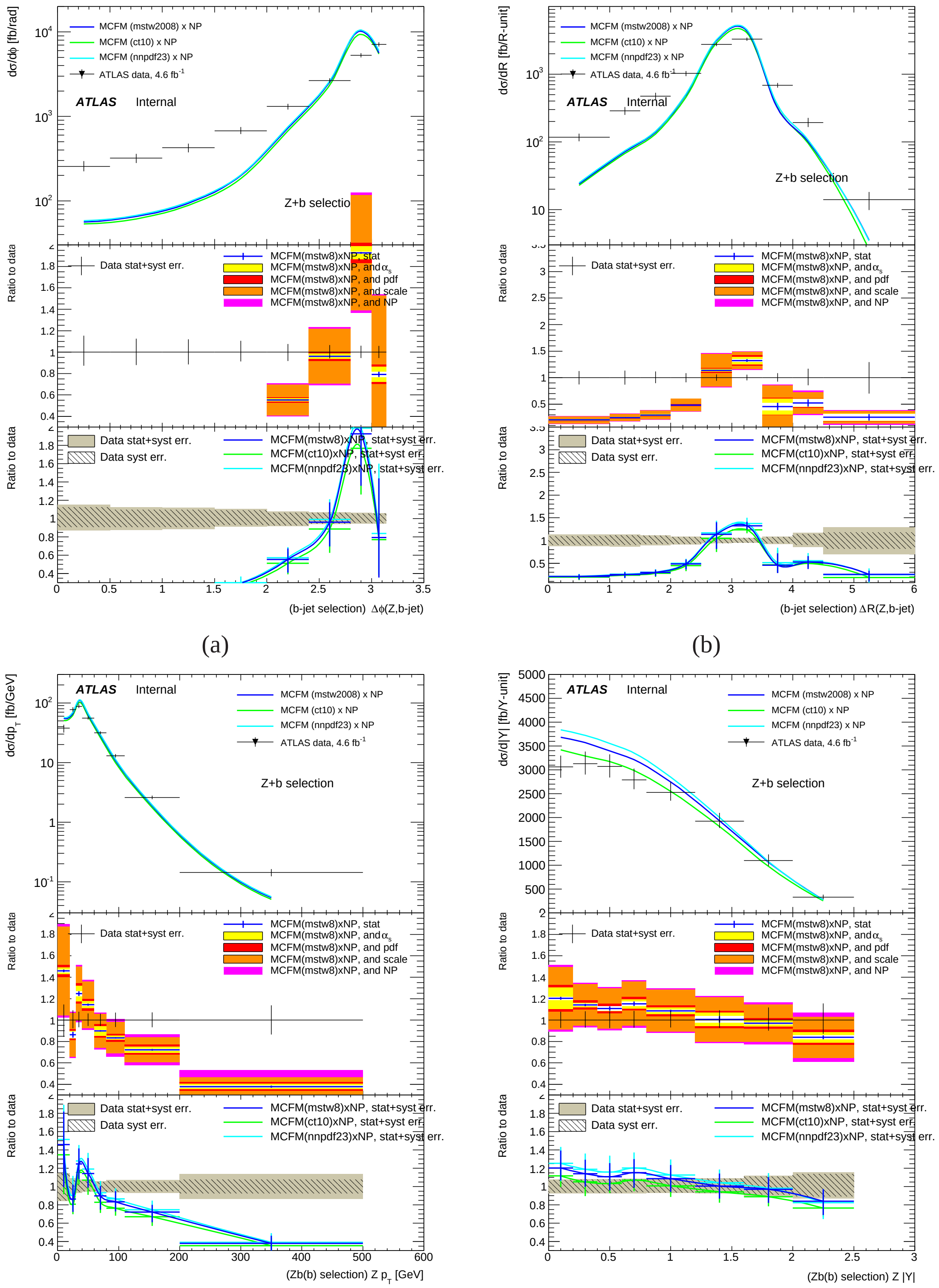

(a) (b)

(c) (d)

Figure 91: *Zb* inclusive selection. Comparison between data and the MCFM predictions with various PDF sets and breakdown of the theory incertainty into the various sources when MSTW2008 is used. $\Delta\phi(Z, b-\text{jet})$ and $\Delta R(Z, b-\text{jet})$ between the b-jets and the Z in events with $p_T(Z) > 20$ GeV (a-b), Z transverse momentum and absolute rapidity (c-d). The MCFM prediction has been calculated using the NP corrections derived from SHERPA and PYTHIA . In the middle inset of each plot the sources of systematic uncertainty on the MCFM prediction are added linearly in order to appreciate the relative size.

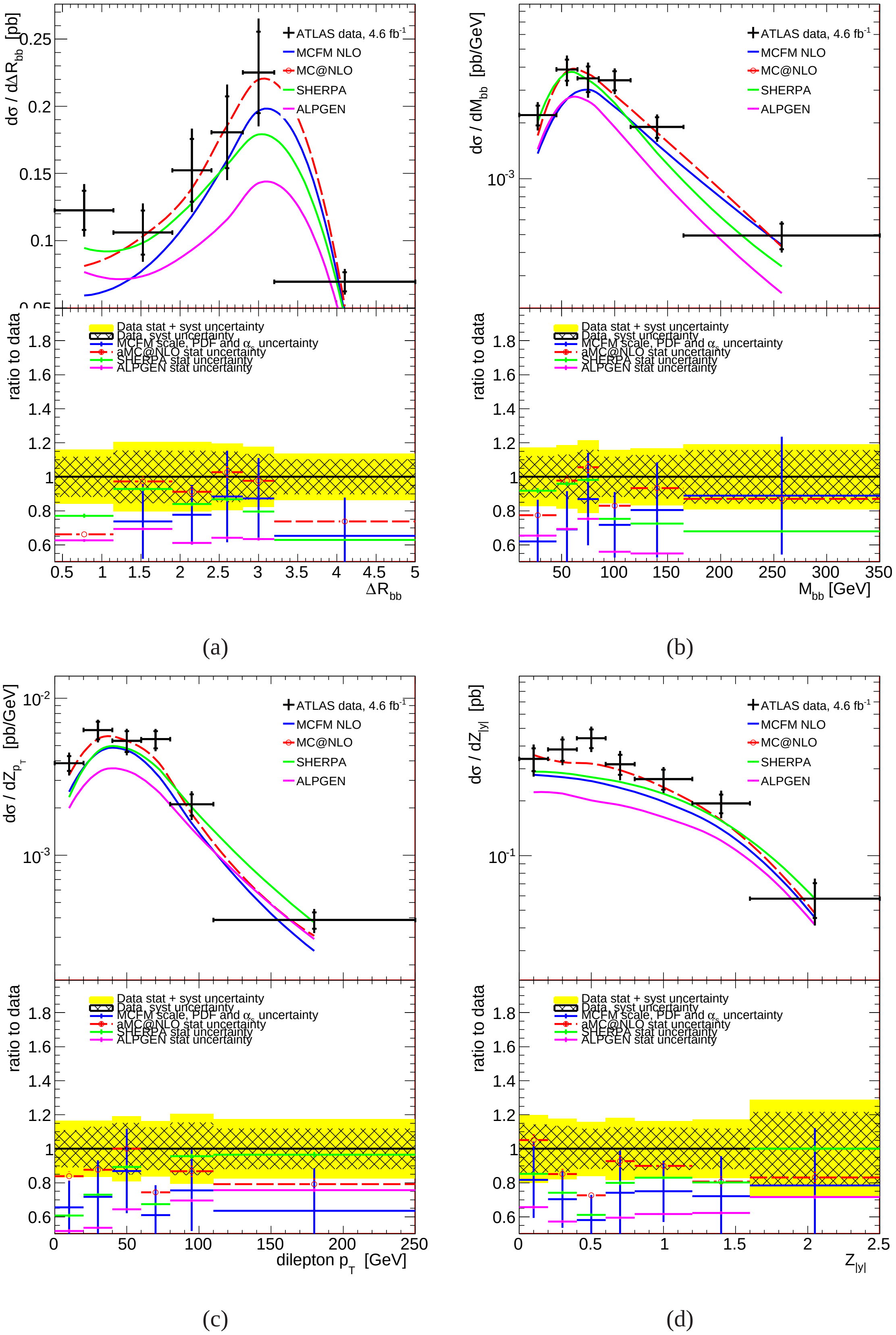

Figure 92: Comparison of Sherpa, MCFM and aMC@NLO to data for (a) ΔR_{bb}, (b) m_{bb}, (c) $Z p_T$ and (d) $Z|y|$. The MCFM prediction has been calculated using the sherpa NP corrections and the MSTW2008 PDFs. TO DO update for systematic effects on MCFM.

17 Conclusion

PENDING FINAL RESULTS!

References

[1] J. M. Campbell and R. Ellis, *MCFM for the Tevatron and the LHC*, Nucl.Phys.Proc.Suppl. **205-206** (2010) 10–15, `arXiv:1007.3492 [hep-ph]`.

[2] T. Sjostrand, S. Mrenna, and P. Z. Skands, *PYTHIA 6.4 Physics and Manual*, JHEP **0605** (2006) 026, `arXiv:hep-ph/0603175 [hep-ph]`.

[3] G. Corcella, I. Knowles, G. Marchesini, S. Moretti, K. Odagiri, et al., *HERWIG 6: An Event generator for hadron emission reactions with interfering gluons (including supersymmetric processes)*, JHEP **0101** (2001) 010, `arXiv:hep-ph/0011363 [hep-ph]`.

[4] S. Frixione and B. Webber, *Matching NLO QCD computations and parton shower simulations*, JHEP **0206** (2002) 029, `arXiv:hep-ph/0204244 [hep-ph]`.

[5] M. L. Mangano, M. Moretti, F. Piccinini, R. Pittau, and A. D. Polosa, *ALPGEN, a generator for hard multiparton processes in hadronic collisions*, JHEP **0307** (2003) 001, `arXiv:hep-ph/0206293 [hep-ph]`.

[6] T. Gleisberg, S. Hoeche, F. Krauss, M. Schonherr, S. Schumann, et al., *Event generation with SHERPA 1.1*, JHEP **0902** (2009) 007, `arXiv:0811.4622 [hep-ph]`.

[7] D0 Collaboration, V. M. Abazov et al., *Measurement of the Ratio of Inclusive Cross Sections* $\sigma(p\overline{p} \to Z + bjet)/\sigma(p\overline{p} \to Z + jet)$ *at* $\sqrt{s} = 1.96\,\text{TeV}$, Phys. Rev. Lett. **94** (2005) 161801. `http://link.aps.org/doi/10.1103/PhysRevLett.94.161801`.

[8] CDF collaboration Collaboration, T. Aaltonen et al., *Measurement of Cross Sections for b Jet Production in Events with a Z Boson in* p^- *anti-p Collisions at* $\sqrt{s}$ *= 1.96-TeV*, Phys.Rev. **D79** (2009) 052008, `arXiv:0812.4458 [hep-ex]`.

[9] CMS Collaboration Collaboration, S. Chatrchyan et al., *Measurement of the Z/gamma*+b-jet cross section in pp collisions at 7 TeV*, JHEP **1206** (2012) 126, `arXiv:1204.1643 [hep-ex]`.

[10] ATLAS Collaboration Collaboration, G. Aad et al., *Measurement of the cross-section for* b^- *jets produced in association with a Z boson at* $\sqrt{s} = 7$ *TeV with the ATLAS detector*, Phys.Lett. **B706** (2012) 295–313, `arXiv:1109.1403 [hep-ex]`.

[11] The ATLAS Collaboration, *Proposal and Motivations for 2011 Trigger Menu*, ATL-COM-DAQ-2011-007, January, 2011.

[12] J. Alwall, S. Hoche, F. Krauss, N. Lavesson, L. Lonnblad, et al., *Comparative study of various algorithms for the merging of parton showers and matrix elements in hadronic collisions*, Eur.Phys.J. **C53** (2008) 473–500, `arXiv:0706.2569 [hep-ph]`.

[13] The ATLAS Collaboration, *New ATLAS event generator tunes to 2010 data*, ATL-PHYS-PUB-2011-008, May, 2011.

[14] D. Stump, J. Huston, J. Pumplin, W.-K. Tung, H.-L. Lai, S. Kuhlmann, and J. F. Owens, *Inclusive jet production, parton distributions, and the search for new physics*, Journal of High Energy Physics **2003** (2003) no. 10, 046. `http://stacks.iop.org/1126-6708/2003/i=10/a=046`.

[15] H.-L. Lai, M. Guzzi, J. Huston, Z. Li, P. M. Nadolsky, et al., *New parton distributions for collider physics*, Phys.Rev. **D82** (2010) 074024, `arXiv:1007.2241 [hep-ph]`.

[16] P. M. Nadolsky, H.-L. Lai, Q.-H. Cao, J. Huston, J. Pumplin, et al., *Implications of CTEQ global analysis for collider observables*, Phys.Rev. **D78** (2008) 013004, arXiv:0802.0007 [hep-ph].

[17] The ATLAS Collaboration, *Measurement of the Mistag Rate with 5 fb-1 of Data Collected by the ATLAS Detector*, ATLAS-CONF-2012-040, March, 2012.

[18] The ATLAS Collaboration, *Measurement of the cross section for the production of a W boson in association with b-jets in 4.64 fb-1 of pp collisions at* $\sqrt{s} = 7$ *TeV*, ATL-COM-PHYS-2012-828, June, 2012.

[19] The ATLAS Collaboration, *Measuring the b-tag efficiency in a ttbar sample with* $4.7 fb^{-1}$ *of data from the ATLAS detector*, ATLAS-CONF-2012-097, June, 2012.

[20] W. Verkerke and D. Kirkby, *RooFit Users Manual*, v2.91, October, 2008.

[21] R. Brun and F. Rademakers, *ROOT - An Object Oriented Data Analysis Framework*, Nucl. Inst. and Meth. in Phys. Res. A **389** (1997) 81–86. http://root.cern.ch/.

[22] *Calibrating the b-Tag Efficiency and Mistag Rate in 35* pb^{-1} *of Data with the ATLAS Detector*, Tech. Rep. ATLAS-CONF-2011-089, CERN, Geneva, Jun, 2011.

[23] *Update on the jet energy scale systematic uncertainty for jets produced in proton-proton collisions at* $\sqrt{s} = 7$ *TeV measured with the ATLAS detector*, Tech. Rep. ATLAS-CONF-2011-007, CERN, Geneva, Feb, 2011.

[24] *Jet energy resolution and selection efficiency relative to track jets from in-situ techniques with the ATLAS Detector Using Proton-Proton Collisions at a Center of Mass Energy* $sqrts = 7$ *TeV*, Tech. Rep. ATLAS-CONF-2010-054, CERN, Geneva, Jul, 2010.

[25] *Improved Luminosity Determination in* **pp** *Collisions at* $\sqrt{s} = \mathbf{7}$ *TeV using the ATLAS Detector at the LHC*, Tech. Rep. ATLAS-CONF-2012-080, CERN, Geneva, Jul, 2012.

[26] M. Aliev, H. Lacker, U. Langenfeld, S. Moch, P. Uwer, et al., *HATHOR: HAdronic Top and Heavy quarks crOss section calculatoR*, Comput.Phys.Commun. **182** (2011) 1034–1046, arXiv:1007.1327 [hep-ph].

[27] A. Martin, W. Stirling, R. Thorne, and G. Watt, *Parton distributions for the LHC*, Eur.Phys.J. **C63** (2009) 189–285, arXiv:0901.0002 [hep-ph].

[28] A. Martin, W. Stirling, R. Thorne, and G. Watt, *Uncertainties on alpha(S) in global PDF analyses and implications for predicted hadronic cross sections*, Eur.Phys.J. **C64** (2009) 653–680, arXiv:0905.3531 [hep-ph].

[29] M. Cacciari, M. Czakon, M. Mangano, A. Mitov, and P. Nason, *Top-pair production at hadron colliders with next-to-next-to-leading logarithmic soft-gluon resummation*, Phys.Lett. **B710** (2012) 612–622, arXiv:1111.5869 [hep-ph].

[30] J. Alwall, M. Herquet, F. Maltoni, O. Mattelaer, and T. Stelzer, *MadGraph 5 : Going Beyond*, JHEP **1106** (2011) 128, arXiv:1106.0522 [hep-ph].

A Further details on the HFOR overlap removal

The quark classification for the HFOR overlap removal is technically done as follows, using Monte Carlo samples at AOD or EVNT level: As a first step, b-quarks are searched for in the event. The b-quarks that do not have a b-quark descendant are kept as "final state" b-quark (i.e. after parton showering). Bottom quarks that originate from a bottom-hadron decay are ignored and will not be kept as final state b-quarks. The second step consists of determining the origin of each final state b-quark (ME, GS, MPI). If the status code of the final state b-quark is 141 or 142, it is considered a quark originating directly from one of the incoming protons through the parton distribution functions, and it is ignored. Note that at the AOD level, descendants of these quarks may have been filtered out because of their low transverse momentum or their large pseudo-rapidity. If the final state b-quark is not a PDF quark, all ancestors of the b-quark are looked at. If any of the ancestors is a b- or $\bar{b}$-quark with status code 141 or 142, the HF quark is considered a PDF quark and is ignored. If any of the ancestors is a b-quark and has status code 123 or 124, the b-quark is given a preliminary "ME" label. If any of the ancestors has identification code 0 and status code 120, the b-quark is given a preliminary "MPI" label. If any of the ancestors is not a b-quark and has status code 121 or 122, the b-quark is given a preliminary "GS" label. If at this stage the final state b-quark is not ignored, it can have multiple preliminary origin labels: a b-quark may originate from a gluon splitting where the gluon was created in an MPI vertex, or if the b-quark originates directly from an MPI vertex, it will have status code 123 or 124 as for the ME origin. The final classification label of a final state b-quark is then determined in the following order. If the b-quark has a preliminary MPI label, the final origin label is set to MPI. If the b-quark has no preliminary MPI label but a preliminary ME label, it is given the final label ME. If the b-quark has a preliminary GS label but no preliminary MPI label nor a preliminary ME label, the final origin label is set to GS. This results in the overlap removal described in the main text.

In what follows the effects of the procedure are presented in more detail. Distributions of ΔR of b-quark-pairs and b-hadron-pairs is shown in Figure 93, for both the Z+light-parton and $Z + b\bar{b}$ samples. Also shown are the classifications according to the HFOR procedure. For small ΔR, the contribution from the parton shower dominates, as expected. For b-quarks with $p_{\mathrm{T}} > 20$ GeV, the transition between the GS-region ($\Delta R < 0.4$) and the ME-region ($\Delta R > 0.4$) is smooth, after applying HFOR. It has to be noted that the parton shower predicts almost a factor two more b-quark pairs than the full matrix-element calculation for the small ΔR region. The distribution of the separation ΔR between b-hadrons (i.e. those b-hadrons that subsequently decay to other b-hadrons or light-flavour hadrons) shows similar features; for $p_{\mathrm{T}} > 20$ GeV there is a smooth transition and the parton shower predicts significantly more b-hadron pairs at small separation than the full matrix-element calculation. The distributions for b-hadrons include the MPI component because their ME or GS origin cannot be found in the event record.

In Figure 94, ΔR distributions of b-quark pairs are shown for specific initial states (defined by the incoming partons of the hard process that ALPGEN simulated). The qg initial state can be simulated also by a qq initial state with an initial state parton shower. However, the gg initial state that ALPGEN simulates has no equivalent in a parton shower approach, and the HFOR procedure would thus remove too many events in the $\Delta R < 0.4$ range. This can clearly be seen in Figure 94(b). However, the number of events that gets incorrectly removed is rather small.

To see the effect of HFOR on actual b-hadron jets (i.e. the objects that we are trying to identify), jets are reconstructed with the anti-kT algorithm (see Section 4) using generated stable particles as input to the clustering algortihm, excluding neutrinos and muons. These jets are then matched to b-hadrons ("initial state" b-hadrons, or b-hadrons that originate from a non-b-hadron and that subsequently decay directly to a b- or non-b-hadron), to identify the b-jets (ΔR(jet-b-hadron < 0.4). In Figure 95, distributions of the transverse momentum of these b-jets are shown. The left column shows the transverse momentum distribution for jets which are uniquely matched to exactly one b-hadron. The right column shows the distribution for jets that are matched to more than one b-hadron. The bottom row shows the ratio of the combined Z+light-parton / $Z+b\bar{b}$ sample after applying HFOR and the original $Z+b\bar{b}$ sample without applying HFOR. For the uniquely-matched jets, the contribution from the Z+light-parton sample is below the 1% level after HFOR and has no significant impact on the distribution itself, compared to the full $Z+b\bar{b}$ sample (without HFOR applied). For the jets that encompass more than one b-hadron, the contribution from the Z+light-parton samples is dominant and there is a significant difference between the original $Z+b\bar{b}$ sample (without HFOR applied) and the $Z+b\bar{b}$ sample as defined by HFOR.

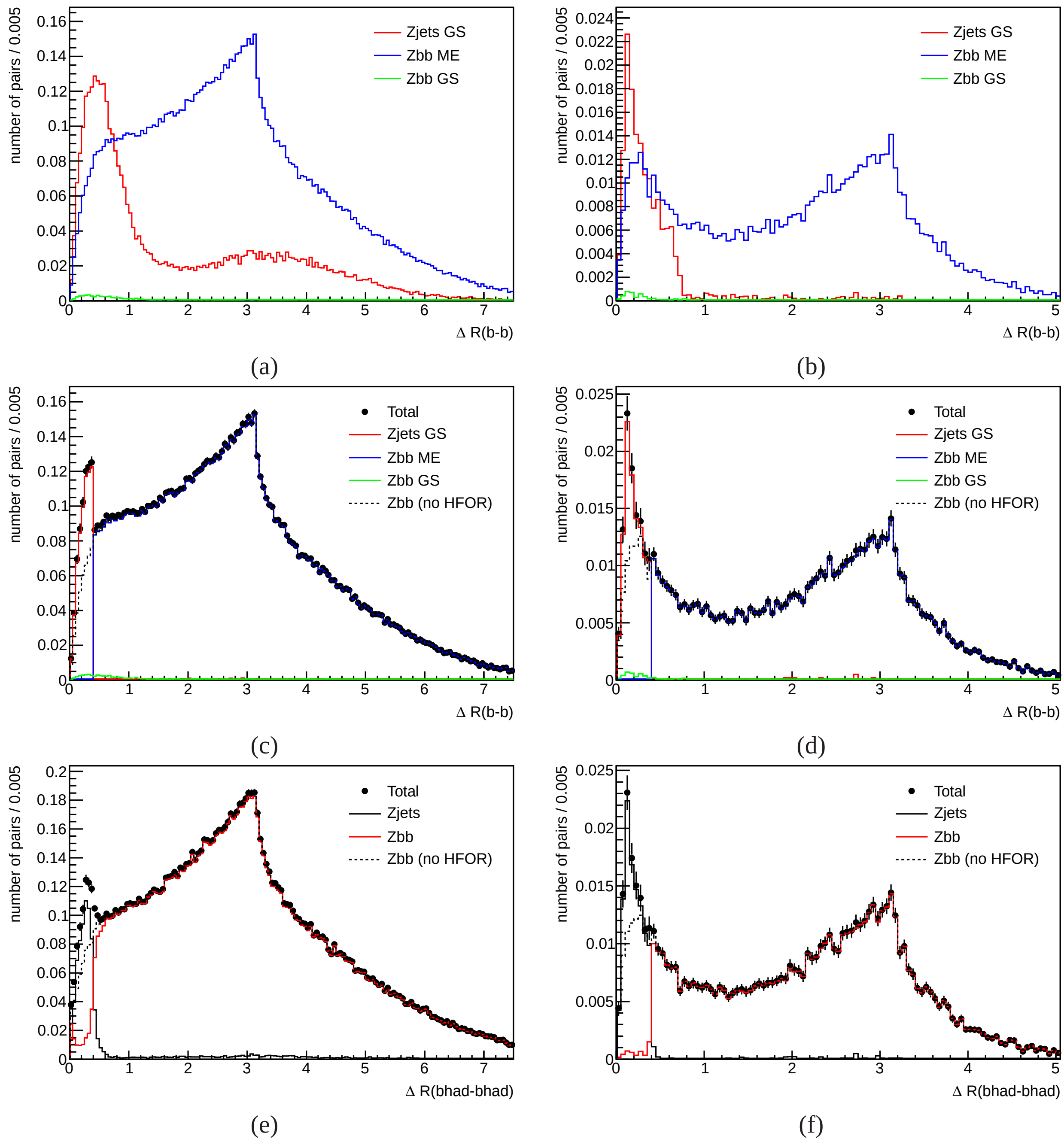

Figure 93: Separation ΔR between final state (see text for definition) b-quarks (a-d) and b-hadrons (e,f). No cut on the transverse momentum of the particles is applied for the distributions in the left-column (a,c,e), whereas a $p_{\mathrm{T}} > 20$ GeV cut has been applied to the quarks / hadrons for the distributions in the right column (b,d,f). Figures (a) and (b) show the ΔR distribution for b-quarks from the various sources (GS, ME) before overlap removal, for the Z+light-parton samples (labeled as “Zjets”) and the $Z + b\bar{b}$ samples (labeled as “Zbb”). The same distributions after overlap removal are shown in Figures (c) and (d), including the distribution from the $Z+b\bar{b}$-sample by itself before overlap removal. Figures (e) and (f) are ΔR distributions for b-hadrons after overlap removal. Note that in figures (e) and (f), the contribution from MPI is also included. All samples are normalised to an integrated luminosity of one.

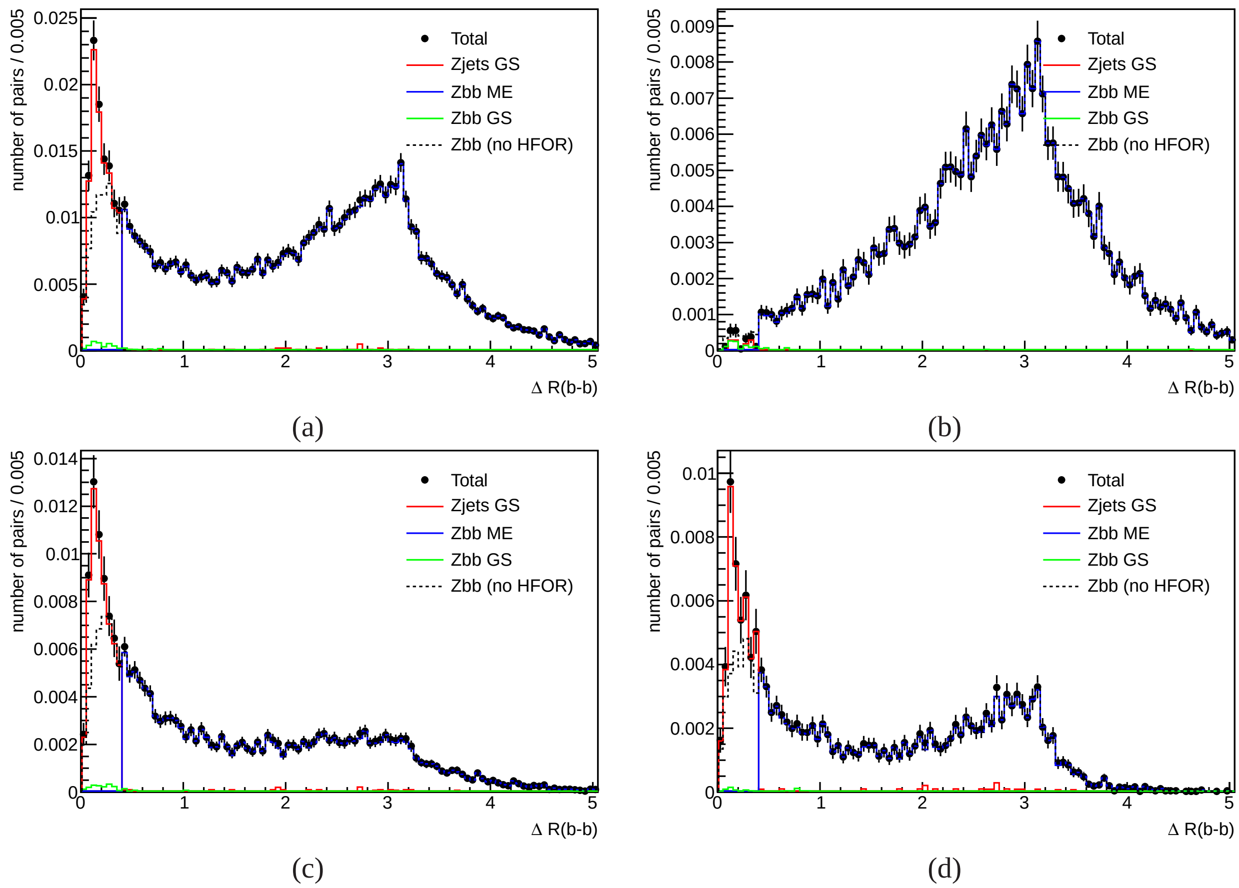

Figure 94: Separation ΔR between final state b-quarks (see text for definition) with $p_{\mathrm{T}} > 20$ GeV after overlap removal for the various sources of b-quark pairs (GS, ME) and input samples (Z+light-parton, $Z + b\bar{b}$). The distributions in Figure (a) are for all events, whereas (b), (c) and (d) are for gg, qg, qq initial states, respectively. The initial states are defined by the incoming partons in the ALPGEN matrix-element calculation. All samples are normalised to an integrated luminosity of one.

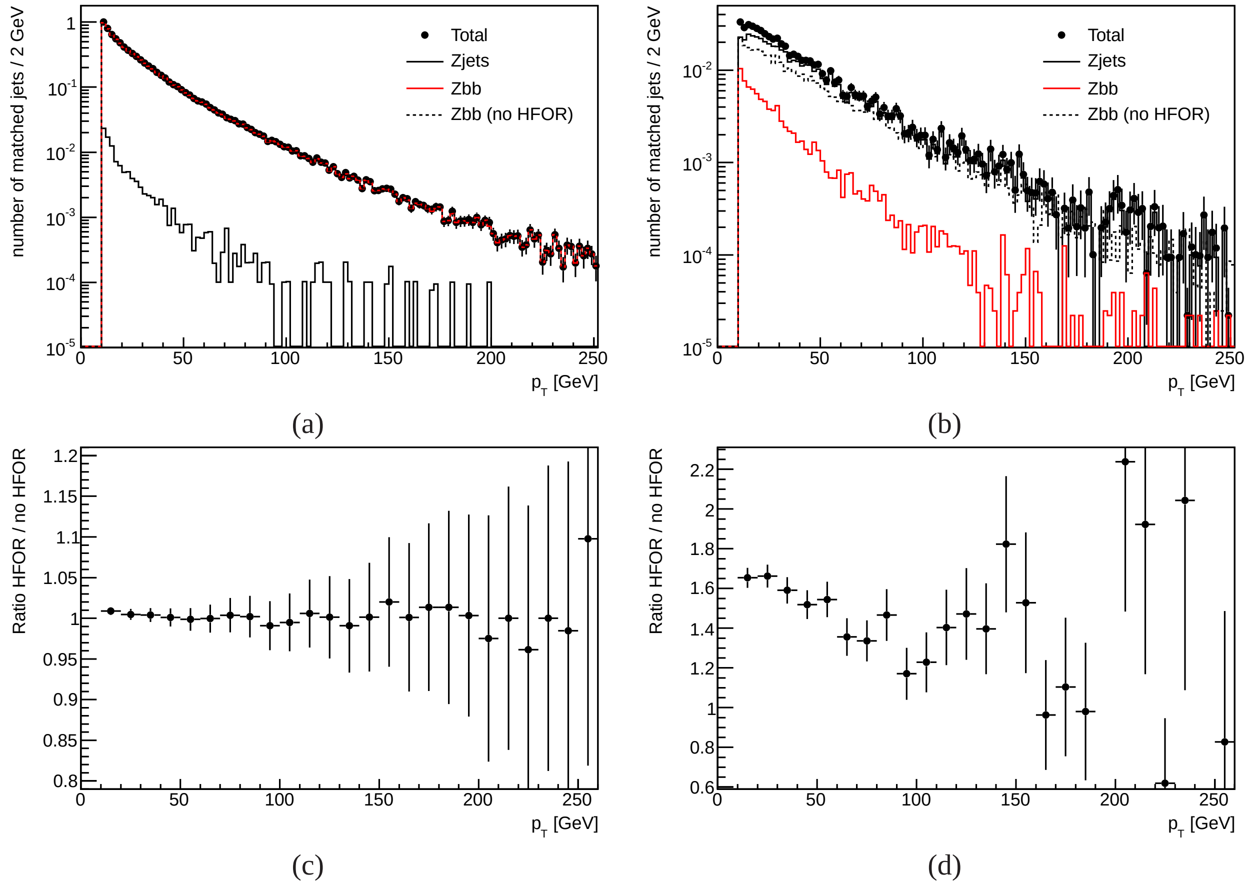

Figure 95: Transverse momentum of particle-level jets matched to b-hadrons, after applying HFOR. In Figure (a) and (c), only jets matched to exactly one b-hadron are plotted, in Figure (b) and (d), the jet is matched to more than one b-hadron. The bottom row shows the ratio of the Z+light-parton and $Z + b\bar{b}$ samples combined with HFOR and the original $Z + b\bar{b}$ sample, i.e. the ratio of the "Total" and the "Zbb (no HFOR)" distributions in the top row. All samples are normalised to an integrated luminosity of one.

B Electron vs Muon Channel in the double tagged sample

In the following appendix a detailed summary of the studies made on the electron-muon channel discrepancy will be presented. Note that in all figures in this Appendix, the Monte Carlo is presented "out-of-the-box", with just the standard 1.25 k-factor applied to all Z events. No additional scaling of the heavy flavour component is applied (for example to represent the known results of the flavour fits). We therefor expect some normalisation differences between data and Monte Carlo, due to the known underestimate of Z+b events by Alpgen.

B.1 Event Selection Stages

B.1.1 Z + at least one *b*-jet

At the stage of requiring at least one *b*-tagged jet in the event, it is seen that Alpgen Monte Carlo underestimates the data by approximately 14% level in both lepton channels. This is expected, due to a known underestimate of heavy flavour production in Alpgen, and shows no sign of an inconsistency between electron and muon channels. Only after requiring the second b-tagged jet do signs of disagreement appear.

To begin the investigation, Figure 96 shows the MV1 distribution for all other jets, after requiring 1 b-tagged jet in the event, tagged with MV1 at 75%. The MV1 75% operating point corresponds to a cut of 0.404219. An excess is particularly at the highest MV1 values in the muon channel, consistent with the cause being genuine b-jets. There is also evidence of some excess in the range 0.4-0.7 in the muon channel, which can hint at a possible tagging point dependence, which is presented in the summary Table 35.

B.1.2 Z + at least two *b*-jets

After the selection of a second *b*-tagged jet, the data excess in the electron channel decreases to 3.1% while the excess in the muon channel grows to 17%. Figure 97 shows the p_{T} distributions for the leading and sub-leading tagged jet in the Z+2-tag sample, and Figure 98 shows the rapidity. These plots are split into the flavour of the jet being plotted. Figure 99 shows the dilepton invariant mass and the missing Et. These plots are split into the flavour combinations of the two tagged jets in the event.

In general, the electron channel has good agreement between data and Monte Carlo, while in the muon channel there is an excess in data. This excess appears to be evenly distributed across all distributions, except possibly being concentrated at low jet p_{T}.

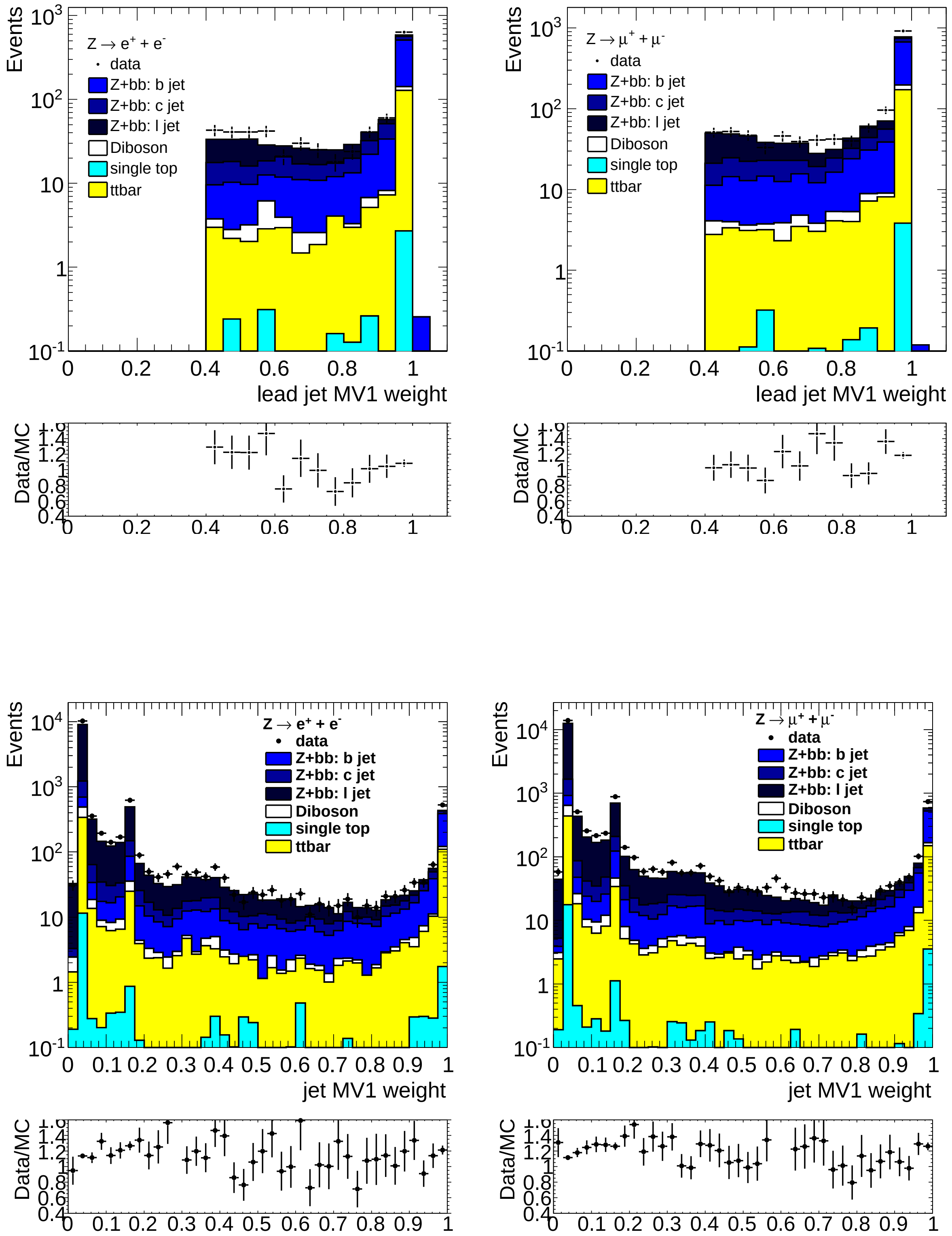

Figure 96: MV1 distributions in the Z + >= 1 tagged jet sample. Top: the MV1 distribution for the tagged jet. Bottom: MV1 for all other jets in the event (no tagging required). Left: electron channel, right: muon channel.

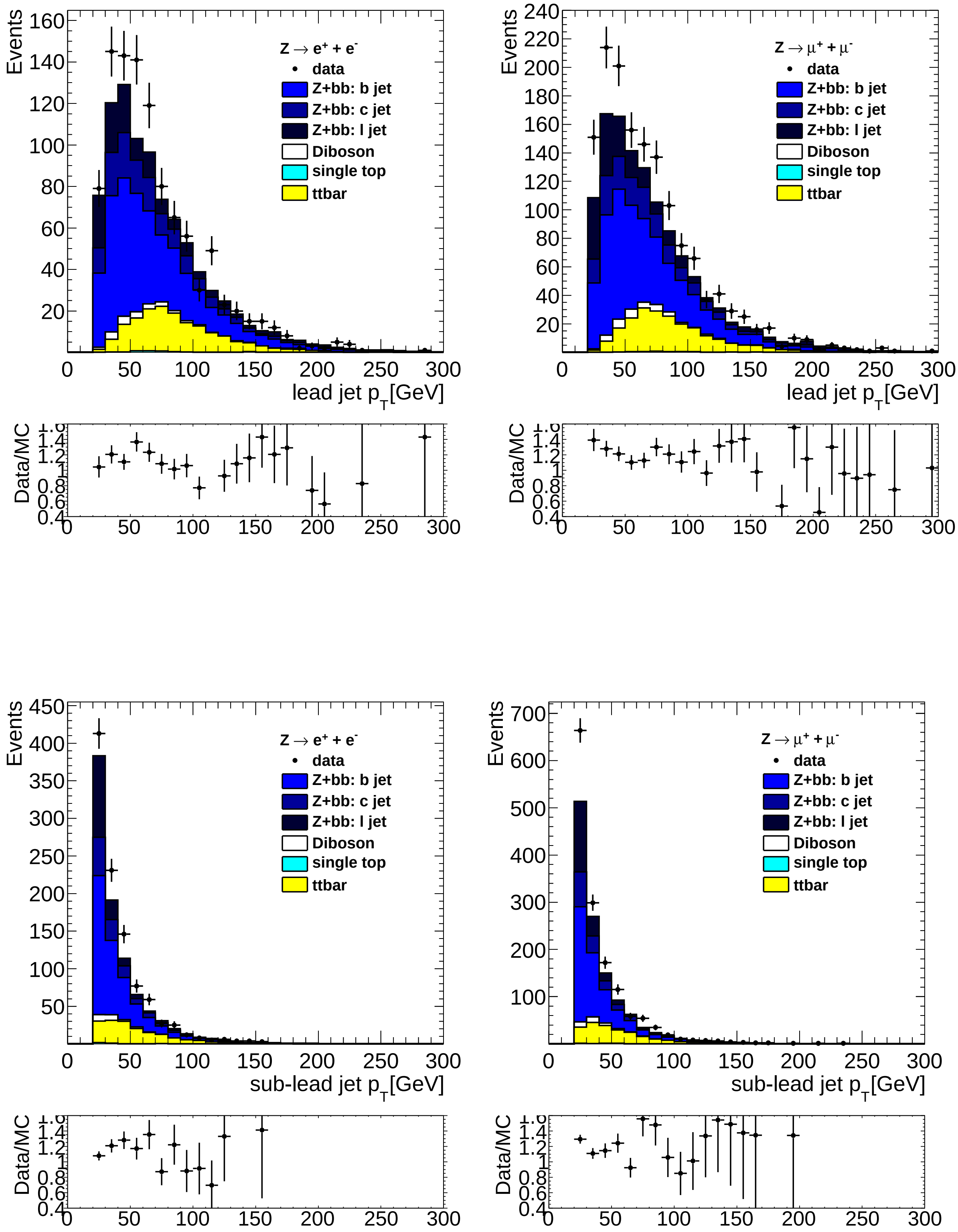

Figure 97: Leading (top) and sub-leading (bottom) *b*-tagged jets pT distribution in the electron (left) and muon (right) channels for an event selection with a Z boson candidate and at least two *b*-tagged jets.

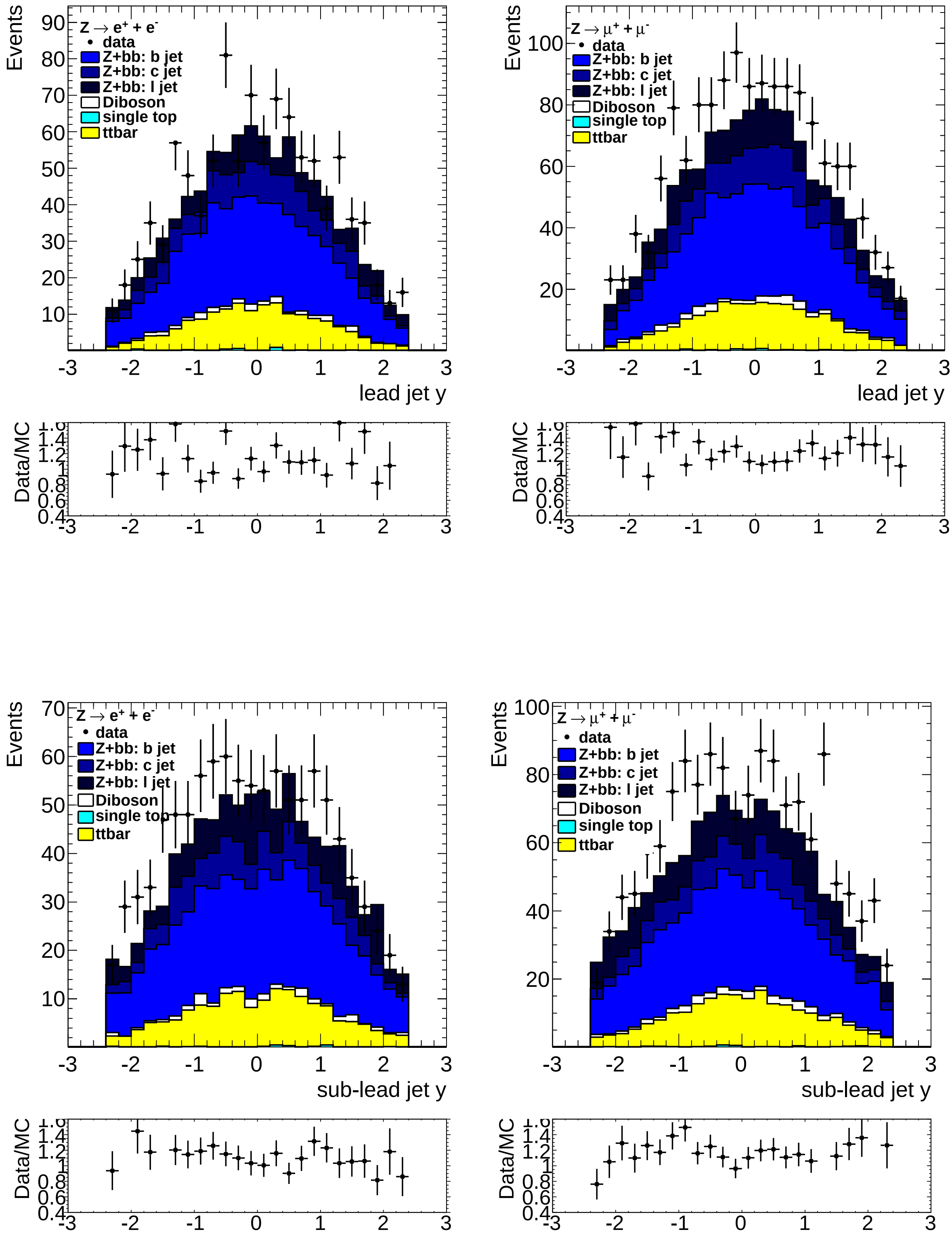

Figure 98: Leading (top) and sub-leading (bottom) b-tagged jets pT distribution in the electron (left) and muon (right) channels for an event selection with a Z boson candidate and at least two b-tagged jets.

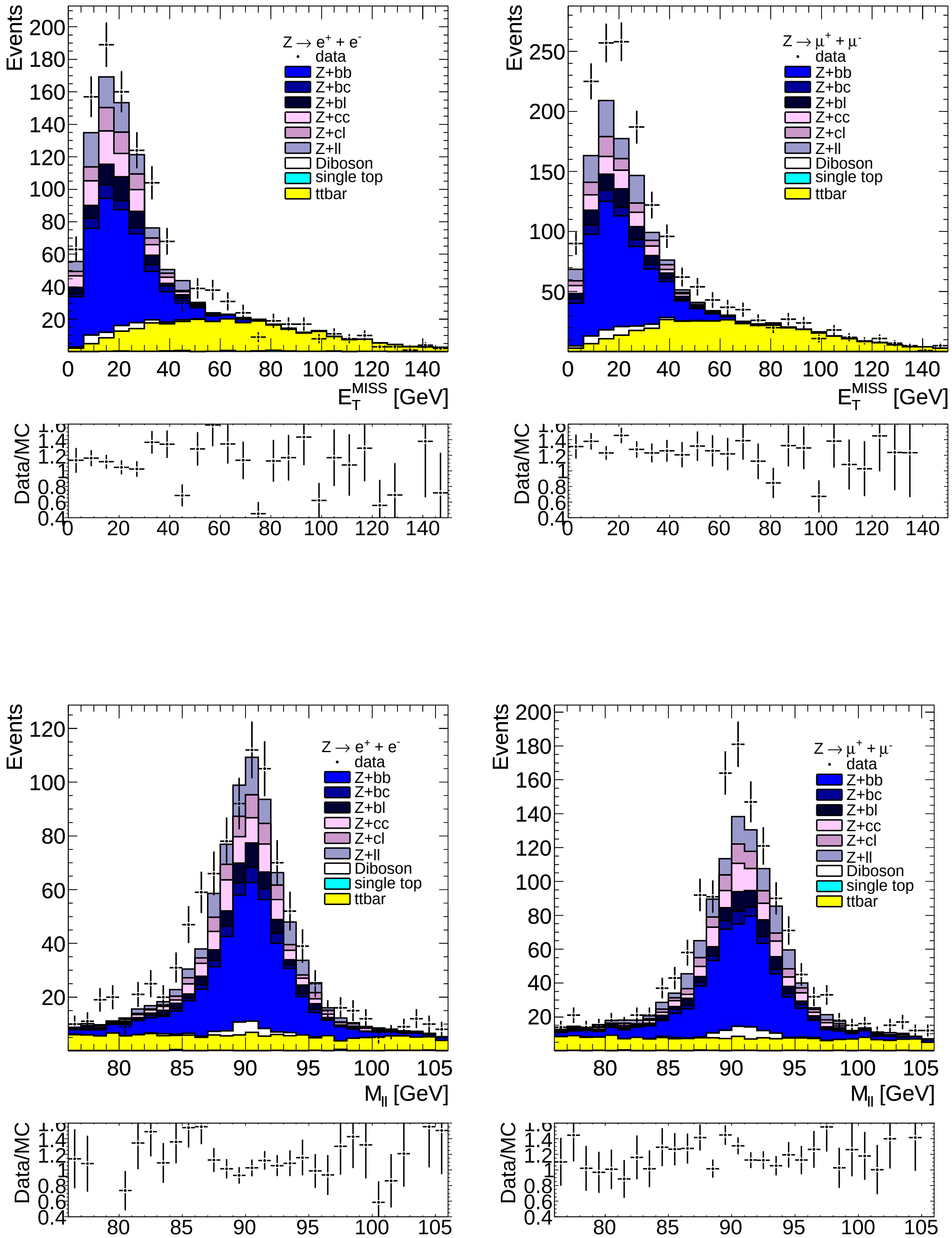

Figure 99: Missing Et (top) and dilepton mass (bottom) in the electron (left) and muon (right) channels for an event selection with a Z boson candidate and at least two *b*-tagged jets.

B.1.3 Top Normalisation

To check if the normalisation issue is really isolated to Z+bb sample or is also a problem for the top pair background, the following check is performed. The dilepton mass cut (76-106 GeV) is removed, allowing significantly more top into the final sample. The data missing Et distribution then fitted using a 2-template fit, consisting of the Z+jets template (not broken down into flavours) and the top pair template. All other contributions (single top, diboson) are fixed at their MC predictions. Multijet is assumed to be negligible. The fit is then repeated with the dilepton mass constraint re-applied, to check for consistency. Results for the Z+1-tag sample are shown in Fig. 100, and for the 2-tag sample in Fig. 101. Fit results in terms of the scale factor applied to the nominal MC prediction are displayed on the Figures.

It can be seen that there is a hint of a slight underestimate of the top contribution across all channels, though generally consistent with 1.0 within the fit uncertainty, and certainly within the 10% systematic uncertainty applied to the top normalisation.

Comparing the Z+jets fitted scale factor fitted in the Z+2-tag sample in electron and muon channels, the values agree to within 0.6σ before applying the dilepton mass constraint, rising to 1.6σ after this constraint. These uncertainties are purely the statistical uncertainties on this simple 2-template fit. The behaviour in the Z+1-tag sample is comparable, with the electron channel moving after applying the dilepton mass constraint. However in this case, the electron and muon channel Z+jets scale factors disagree without the constraint, but agree very well with the constraint. This picture is consistent with the results of the full cross section analysis based on template fits to pb/pc.

As this study indicates some dependence on the dilepton mass distribution, the process is repeated fitting that instead of the MEt. In this case, the missing Et cut is removed to increase the top contribution. Results are shown in Figures 102 and 103 for the 1- and 2-tag samples respectively.

In general the fitted results in the 2-tag sample from either the MEt or the dileptons mass are consistent (comparing Figures 101 and 103). The outlier is the Z+jets scale factor in the electron channel, without the dilepton mass or MEt constraints applied. This is fitted as 1.16 ± 0.05 on the MEt distribution and 1.04 ± 0.04 on the dilepton mass distribution - a difference of 1.8σ assuming no correlations between these fits.

In all fits, the correlation between the Z+jets and top template is ≈ -0.3. This allows the reader to gauge the impact of fixing one of the scale factors. For example, fixing the Z+jets scale factor at a value or 1.16, 3σ above the fitted value in the electron channel dilepton mass of 1.04 ± 0.04, pushes up the the top scale factor down by $0.3 \times 3\sigma$, or to a value of 1.05 - perfectly consistent with all other fitted values for the top scale factor. This is verified by performing the fit (not shown here), which has a lower p-value of 0.09 compared to 0.192 when floating both templates.

Of the many variations possible on these fits, Figure 104 shows the fits to MEt (with dilepton constraint applied) and dilepton mass (with MEt constraint applied) in the Z+2-tag sample, after fixing the top scale factor to 1.00. This is now just a simple 1-parameter fit (the Z+jets normalisation). The now familiar electron-muon difference is apparent, while the fits look reasonable, albeit of a slightly lower quality in the electron channel. Again, this test reveals no sign of a cause for the electron and muon differences.

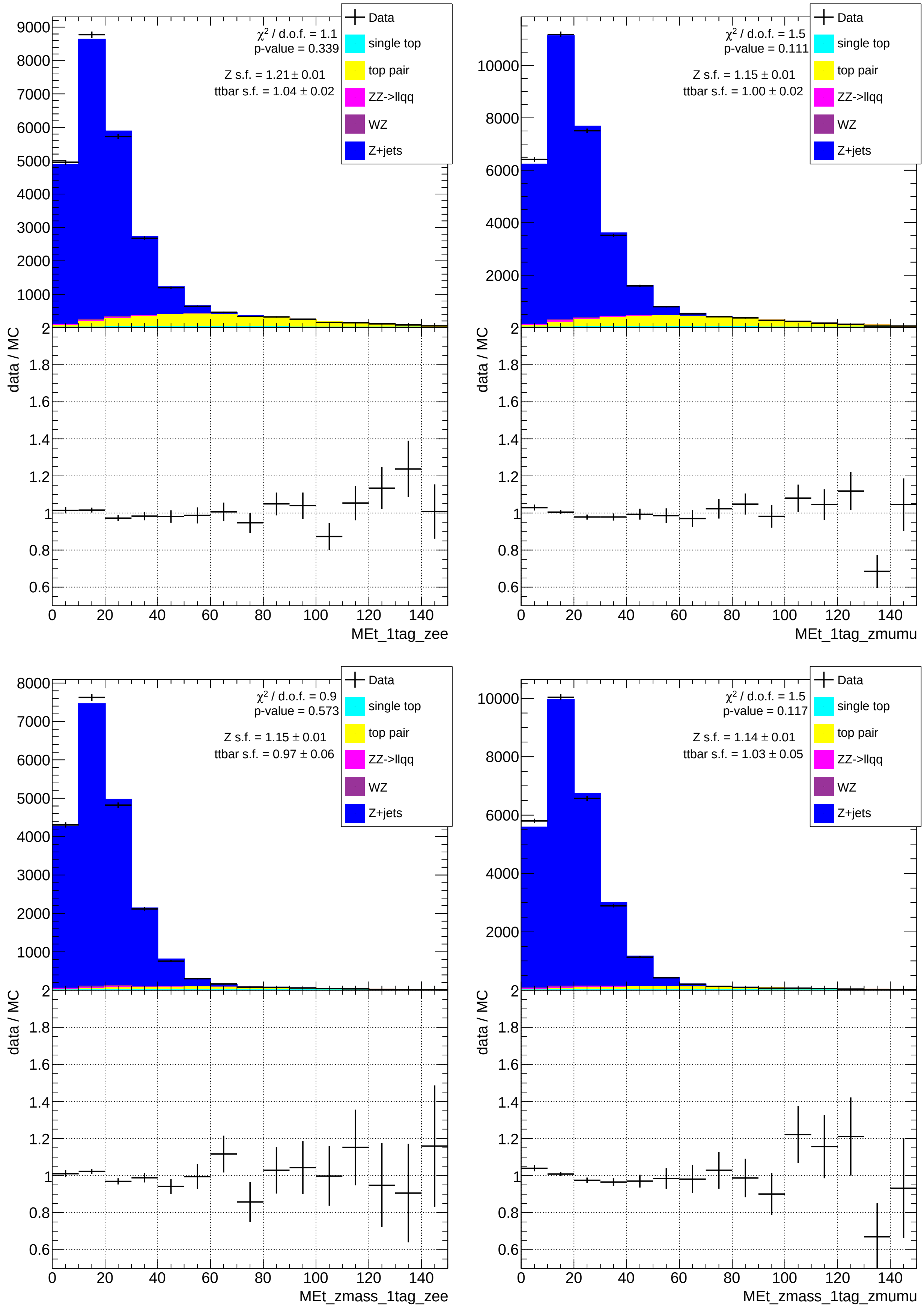

Figure 100: Fitting the Missing Et distribution in Z+single tag sample, shown by electron channel (left) and muon channel (right). The fit is performed without the dilepton mass constraint applied (top), and with (bottom).

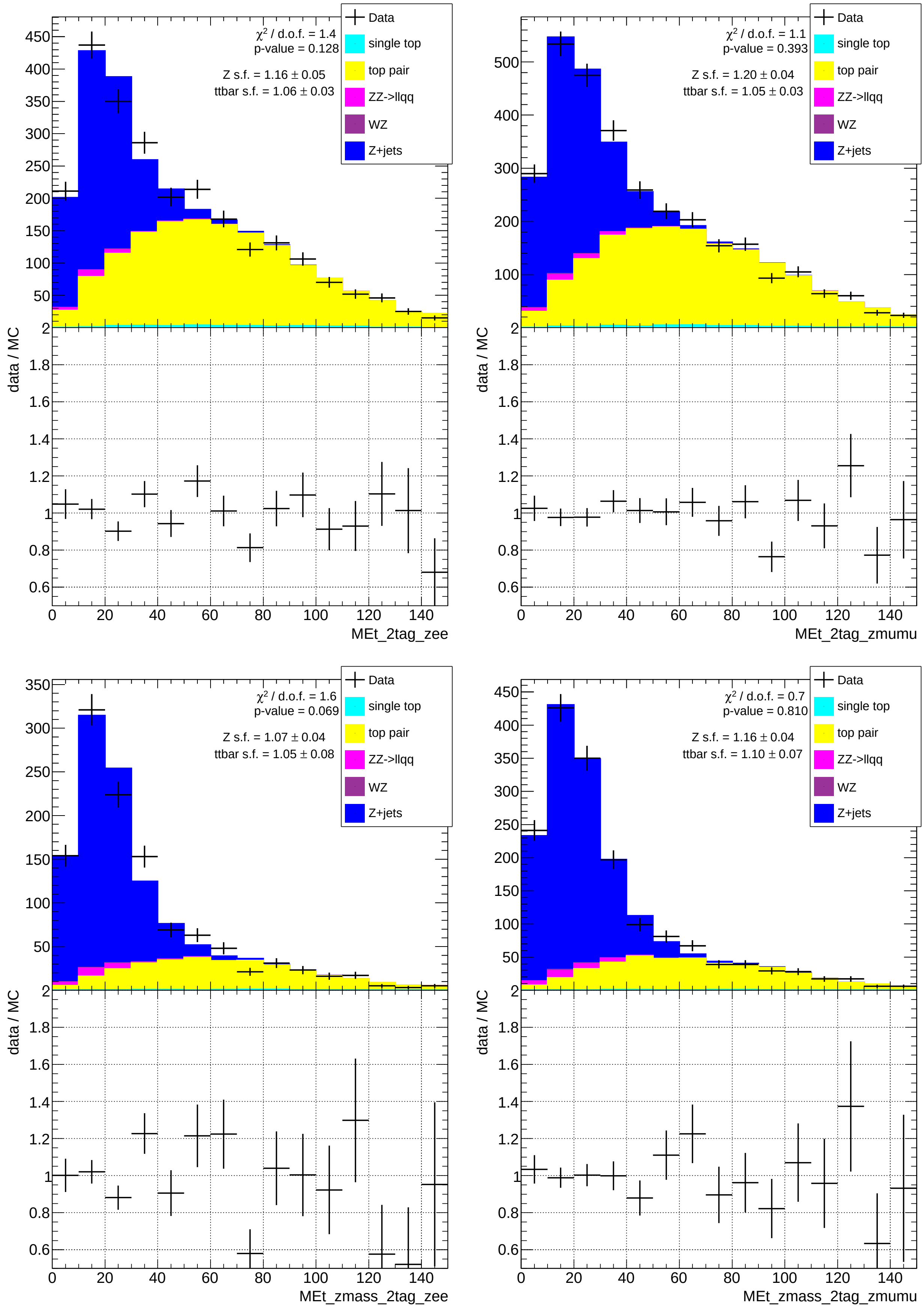

Figure 101: Fitting the Missing Et distribution in Z+single tag sample, shown by electron channel (left) and muon channel (right). The fit is performed without the dilepton mass constraint applied (top), and with (bottom). The bottom plots are completely equivalent to the top plots of Fig. 99, but with different binning.

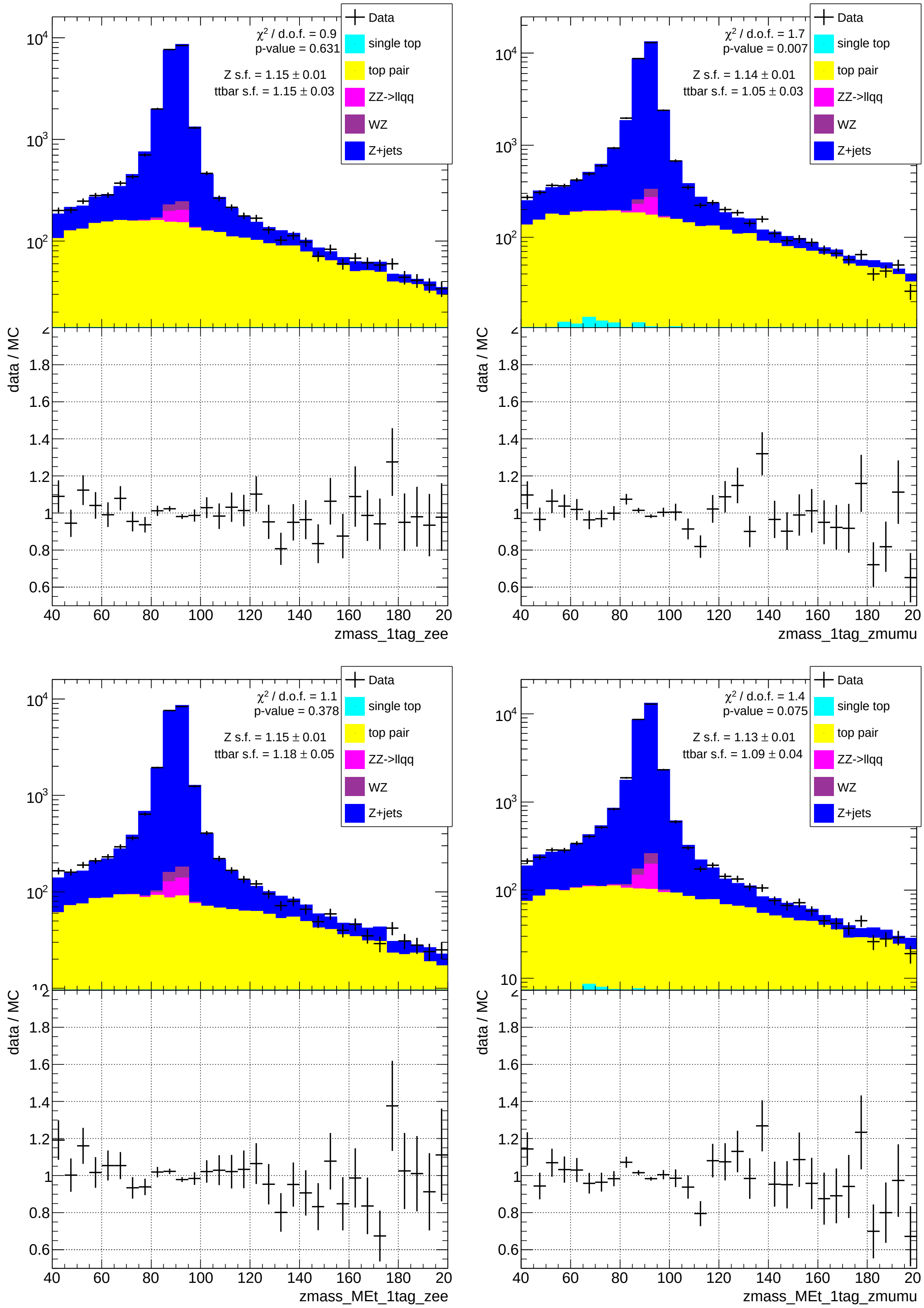

Figure 102: Fitting the dilepton mass distribution in Z+single tag sample, shown by electron channel (left) and muon channel (right). The fit is performed without the MEt constraint applied (top), and with (bottom).

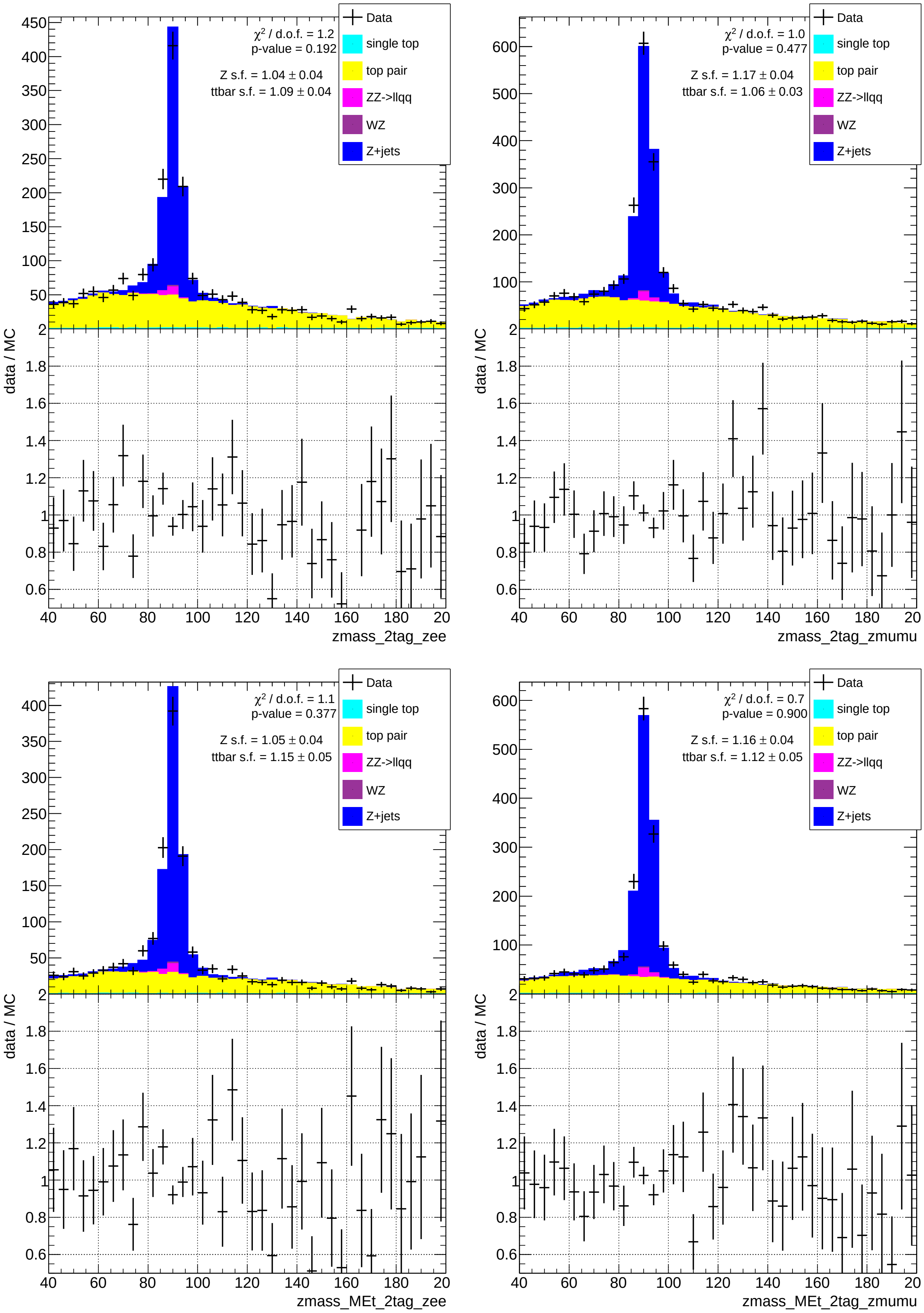

Figure 103: Fitting the dilepton mass distribution in Z+2-tag sample, shown by electron channel (left) and muon channel (right). The fit is performed without the MEt constraint applied (top), and with (bottom).

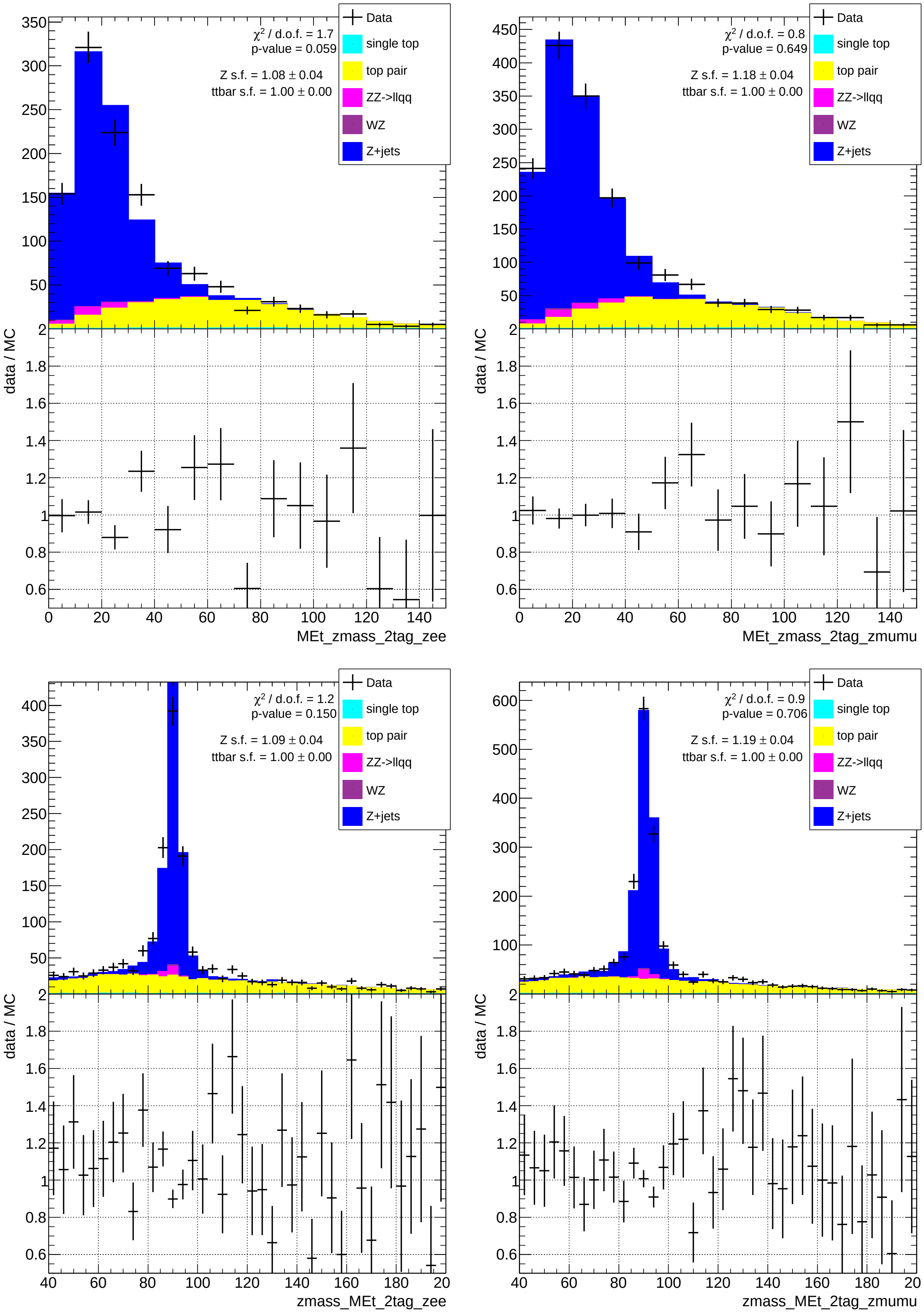

Figure 104: Fitting the Z+2-tag sample after fixing the top scale factor. Shown by electron channel (left) and muon channel (right).

B.1.4 Jets in the range 20-30 GeV

To identify any possible source of disagreement at low jet p_T, events are selected where both tagged jets have a p_T in the range 20-30 GeV. The rapidities of these jets are shown in Fig 105, and the MV1 distributions are shown in Fig 106. No problem is obvious within the available statistics.

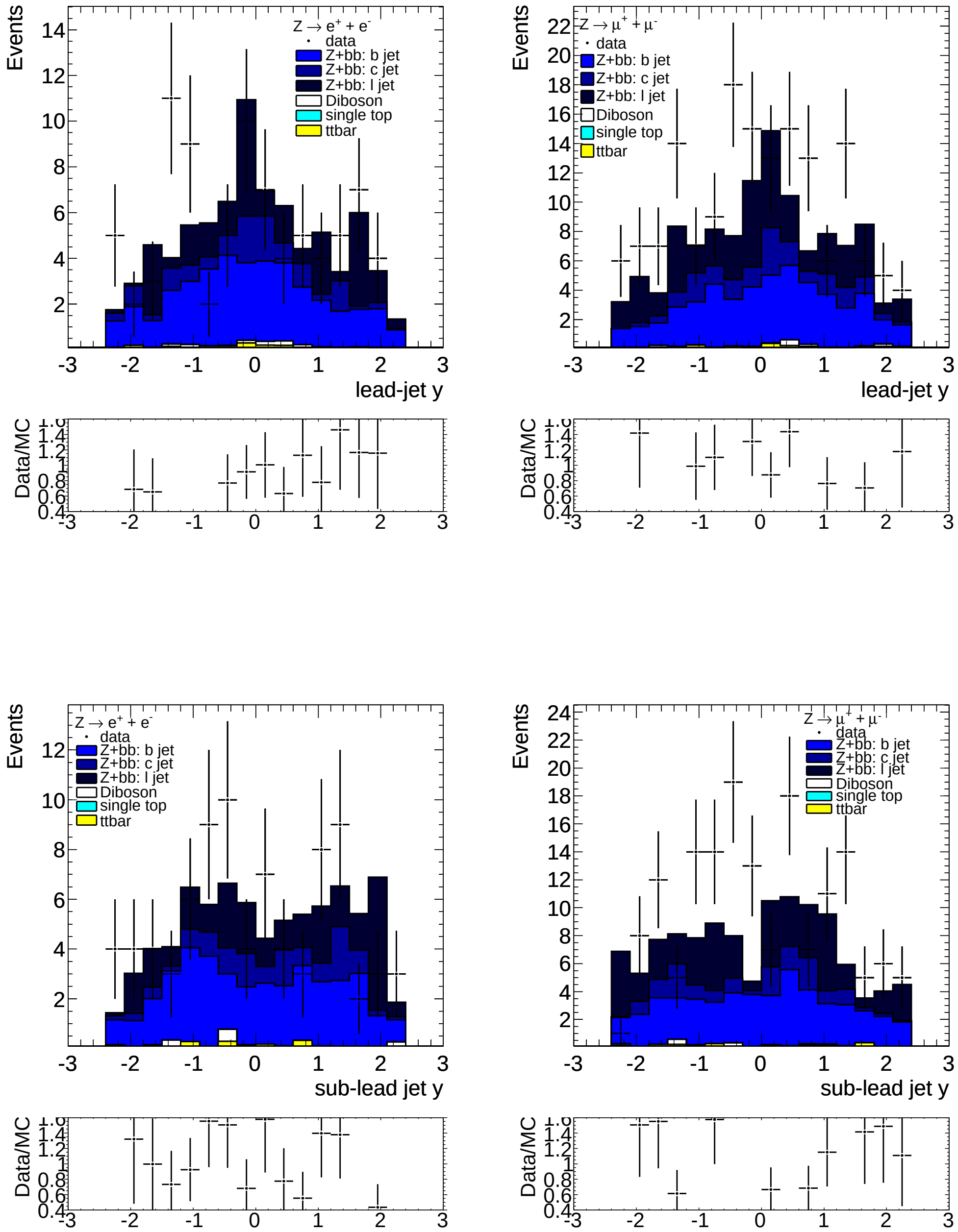

Figure 105: Rapidities of leading (top) and subleading (bottom) jets in the cases where both jets have pT in the range 20-30 GeV. Shown by electron channel (left) and muon channel (right).

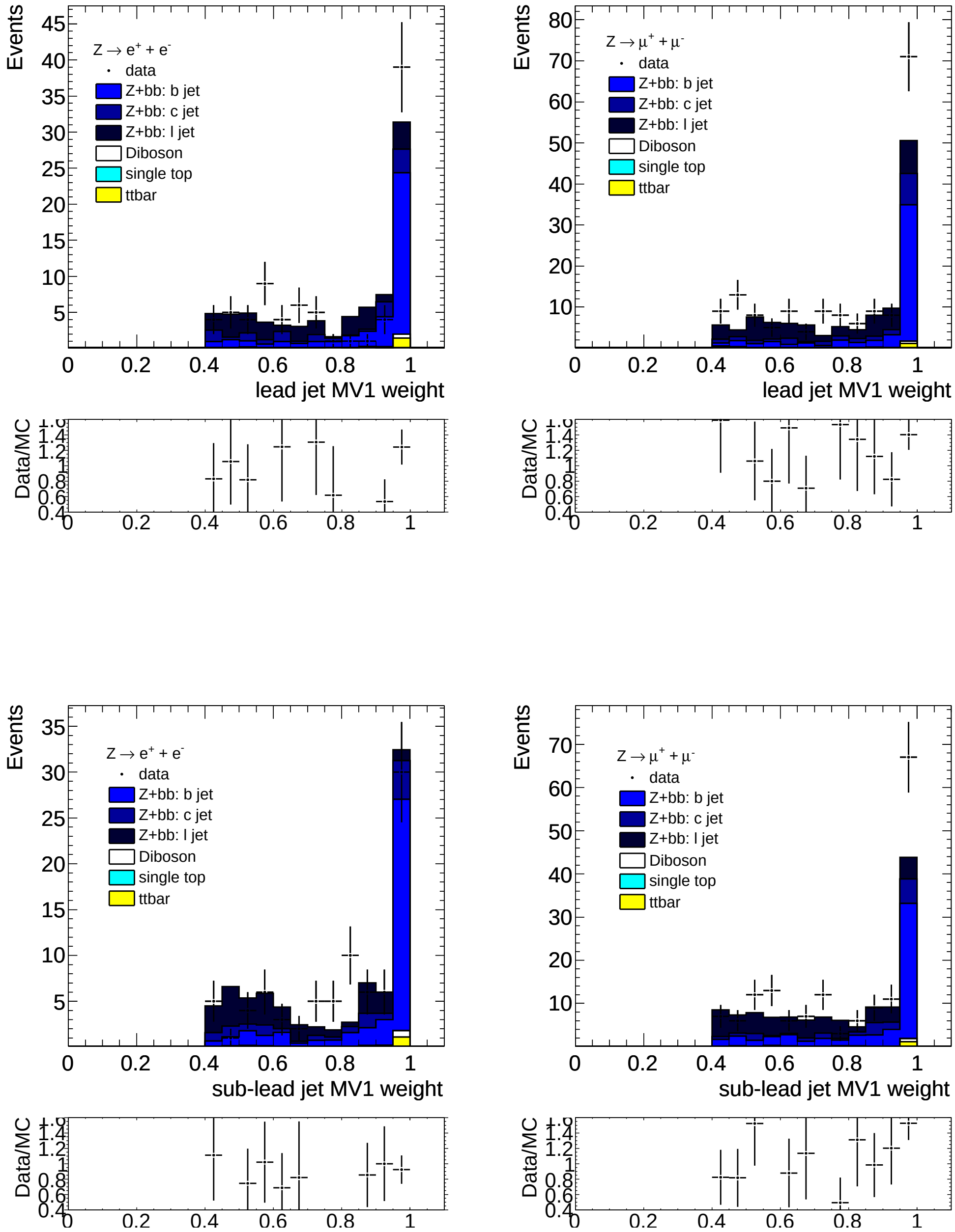

Figure 106: MV1 distributions of leading (top) and subleading (bottom) jets in the cases where both jets have pT in the range 20-30 GeV. Shown by electron channel (left) and muon channel (right).

B.2 ΔR(jet, lepton)

To check for any effects relating to leptons close by jets (isolation, semi-leptonic b-decays, etc), the distributions of ΔR(jet, leptons) are shown here. The sample is split into events passing MV1 60%, and the rest of the MV1 75% events in Fig. 107, and into events with jets in the pT range 20-30 and all others in Fig. 108.

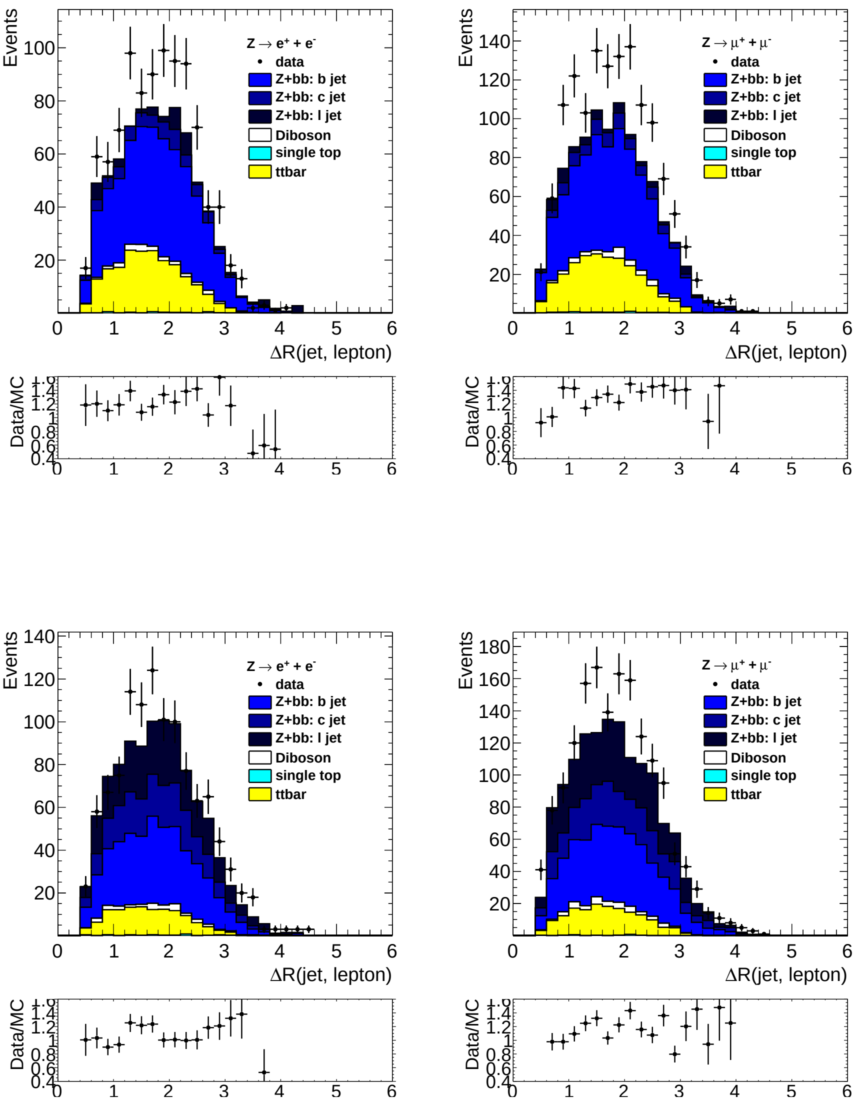

Figure 107: Distributions of ΔR(leptons, jets) for events with two jet passing MV1 60% (top) and the rest of the MV1 75% events (bottom). Shown by electron channel (left) and muon channel (right).

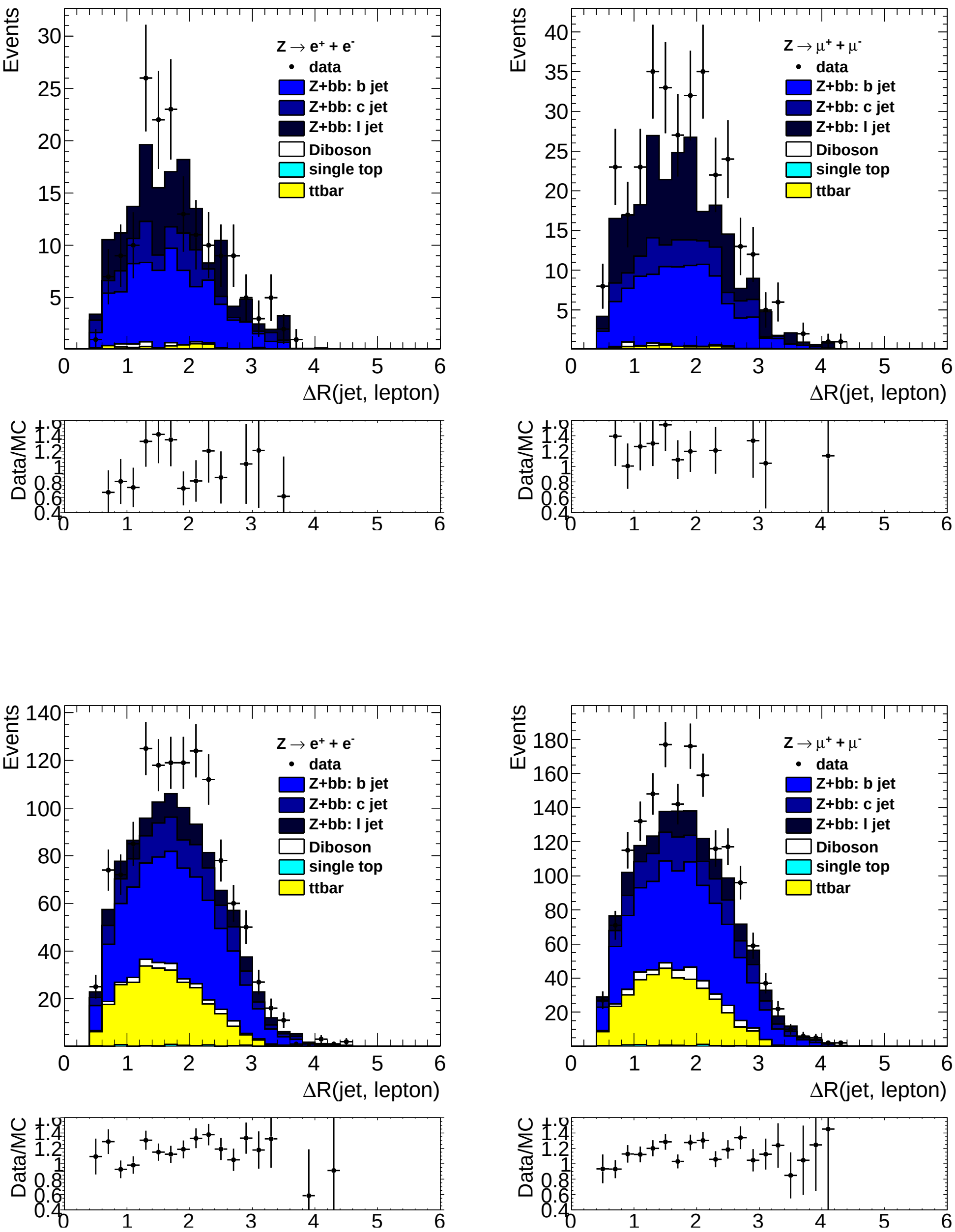

Figure 108: Distributions of ΔR(leptons, jets) for events with two jets with pT 20-30 GeV (top) and the rest of the events (bottom). Shown by electron channel (left) and muon channel (right).

B.3 Trigger Period Dependence

The data excess in both the electron and muon channels has been examined as a function of the 2011 trigger-periods. The top three (bottom two) row distributions from Figure 109 show the data excess (data minus simulation) as a function of the signal electrons (muons) invariant mass. Table 33 gives the event yields for data and simulation, the various triggers and the corresponding trigger integrated luminosity. A fair agreement between the data and simulation in the three periods split by trigger in the electron channel is observed while the muon channel presents a consistent data excess centered around the Z boson mass in both trigger periods.

Trigger	Period	$\int \mathcal{L}(t)\,\mathrm{d}t$	MC yield	Data yield	Excess
EF_2e12_medium	D to J	1659 pb^{-1}	251 ± 7.3	242 ± 15.6	-3.6% ± 6.8%
EF_2e12T_medium	K	583 pb^{-1}	88.5 ± 3.8	103 ± 10.1	16.4% ± 12.5%
EF_2e12Tvh_medium	L to M	2401 pb^{-1}	331.4 ± 7.9	347 ± 18.6	4.7% ± 6.1%
EF_mu18_MG	D to I	1430 pb^{-1}	282 ± 7.4	336 ± 18.3	19.1% ± 7.2%
EF_mu18_MG_medium	J to M	3213 pb^{-1}	581.7 ± 10.8	675 ± 25.9	16.0% ± 4.9%

Table 33: Data (fifth column) and Monte Carlo (fourth column) event yields in the electron (third an fourth rows) and muon (fifth and sixth rows) channels for the triggers used in 2011. The electron and muon channel triggers are shown in the first column as well as the data period interval (second column) and the corresponding integrated luminosity (third column).

B.4 Pileup Period Dependence

A similar pileup distribution was simulated in each 2011 MC11c sample for an equivalent fraction of events as in data. The data excess has been investigated as a function of the pileup conditions in the electron (Figure 110, top three distributions) and muon channels (Figure 110, bottom three distributions) via the leading two leptons invariant mass distributions. Due to the relative small integrated luminosity, the first two pileup periods have been merged. The data and simulation event yields corresponding to the investigated pileup periods as well their corresponding integrated luminosity and the relative excess are given in table 34. A consistent excess of events is observed systematically in all pileup-split periods in muon channel around the Z boson mass while the electron channel data is well modeled by simulation.

Period	$\int \mathcal{L}(t)\,\mathrm{d}t$	MC yield	Data yield	Relative excess
e-channel, D to H	1102pb^{-1}	169.3 ± 6.2	166 ± 12.9	-1.9% ± 8.4%
e-channel, I to K	1140pb^{-1}	170.2 ± 5.5	179 ± 13.4	5.2% ± 8.6%
e-channel, L to M	2402pb^{-1}	331.4 ± 7.9	347 ± 18.6	4.7% ± 6.1%
μ-channel, D to H	1102pb^{-1}	214.3 ± 6.4	251 ± 15.8	17.1% ± 8.2%
μ-channel, I to K	1140pb^{-1}	231.5 ± 6.8	275 ± 16.6	18.8% ± 8%
μ-channel, L to M	2402pb^{-1}	418 ± 9.2	485 ± 22	16% ± 5.9%

Table 34: Data (fourth column) and Monte Carlo (third column) event yields in the electron (second, third an fourth rows) and muon (fifth, sixth and seventh rows) channels corresponding to the 2011 pileup conditions. The first column gives the data period intervals in which the pileup conditions were similar; the second column gives the integrated luminosity for each pileup period interval.

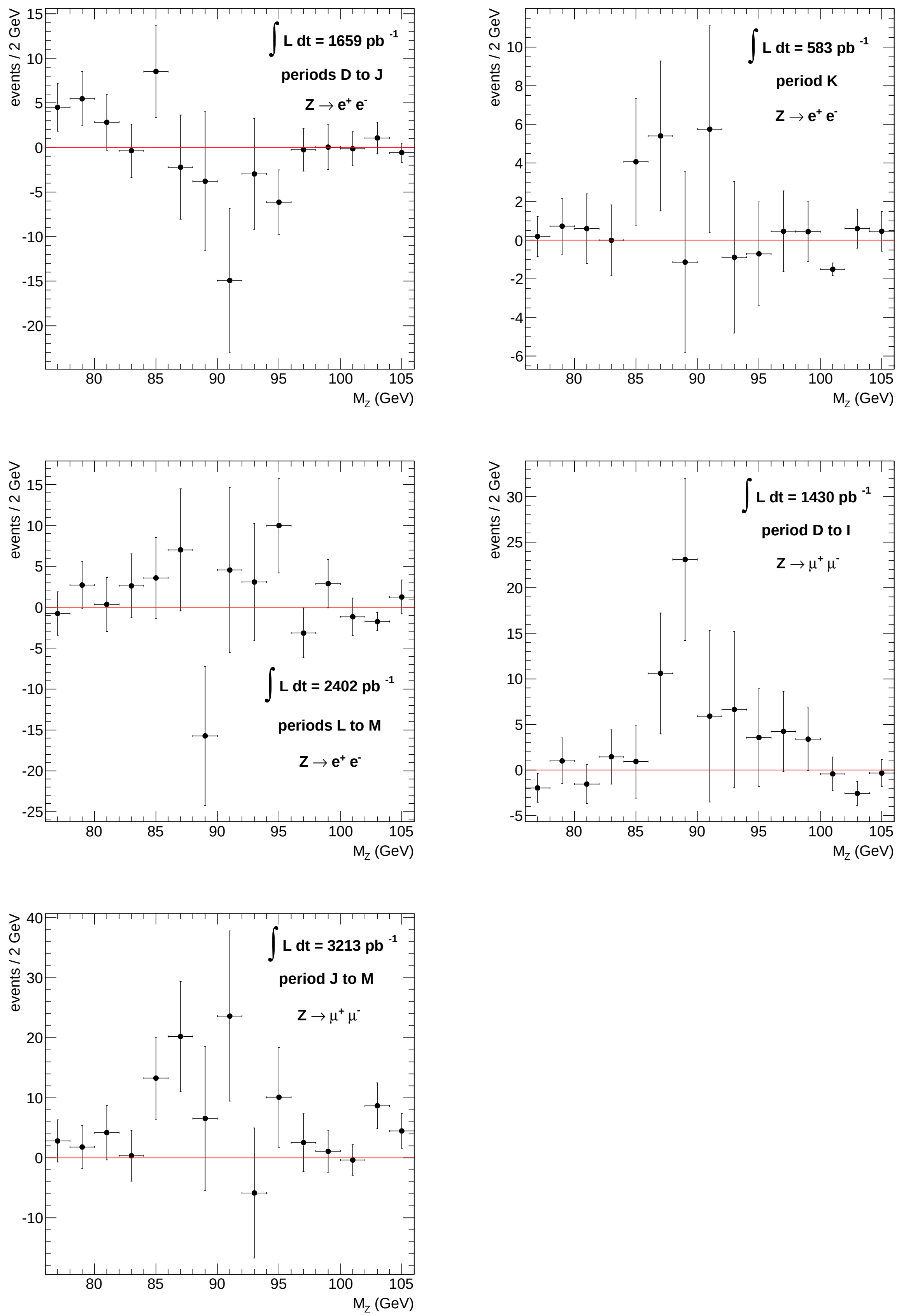

Figure 109: Signal leptons invariant mass distributions of the data excess in the electron (first row rows) and muon (bottom row) channels split according to the 2011 data trigger dependence. All distributions correspond to an event selection with a Z boson candidate and at least two *b*-tagged jets.

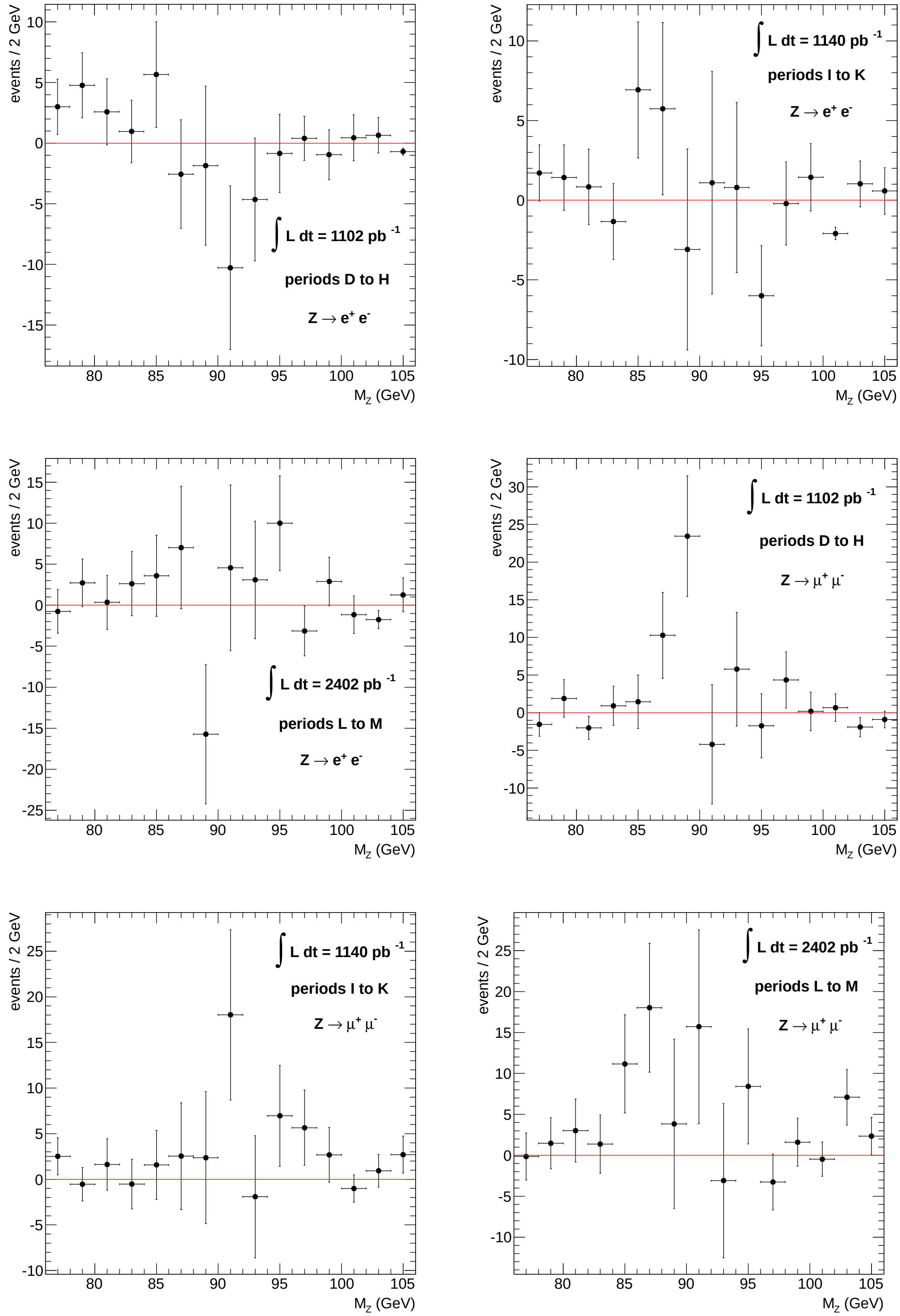

Figure 110: Signal leptons data excess invariant distributions in the electron (first two rows) and muon (bottom two rows) channels split according to the 2011 data pileup dependence. All distributions correspond to an event selection with a Z boson candidate and at least two *b*-tagged jets.

B.5 Cross-check Summary

Table 35 summarises all the cross checks. In the table, n_{bb} is the fitted number of $Z+bb$ events and bb s.f. is the factor by which the Monte Carlo prediction was scaled up or down in the fit. ϵ_{bb} and C represent the b-tagging efficiency correction and the remaining C-factor used in a simple unfolding to obtain the cross section (σ). The ratio ($\mu\mu/ee$) and difference ($\Delta\sigma$) between the muon and electron results are given for each scenario, as well as the significance of this difference (pull). All uncertainties quoted are just statistical, and this significance is calculated only with this statistical uncertainty.

In addition to the checks described above, the analysis is repeated limiting the jet and lepton acceptances, to check for any unexpected behaviour at higher values of η. The cross-section in the regions low low jet pT and in slices of b tagging point are also shown.

It can be seen that the electron and muon channels are most consistent when using the tighter tagging point (MV1 60%) or raising the jet pT. However, the cross section results when using MV1 60% increase by 10-15% compared to MV1 75%, which is at the limit of what would be covered by the b-tagging systematics. Ongoing studies suggest this is a feature of the MV1 6-% scale factors, driven by inconsistencies in the dijet scale factor measurement. Overall, the investigations have turned up no indicator of a specific problem in the electron vs muon channel, so we conclude the difference observed in the nominal selection is due to a 1.8σ fluctuation.

ee	nominal	jet $\|y\|$ <1.2	no MET cut	lepton $\|\eta\|$ <1.32	Jet pT> 30 GeV	20 <Jet pT< 30 GeV	MV1 60%	MV1 70%	MV1 75-60%
n_{bb}	471±35	186±22	480±38	318±28	272±27	35±11	325±26	419±33	156±31
bb s.f.	1.14	0.99	1.14	1.17	1.15	1.05	1.34	1.15	1.00
ϵ_{bb}	0.490	0.537	0.491	0.491	0.568	0.359	0.279	0.424	0.276
C	0.427	0.178	0.430	0.276	0.208	0.048	0.424	0.427	0.341
σ (pb)	0.485±0.036	0.419±0.050	0.490±0.039	0.506±0.045	0.498±0.049	0.437±0.137	0.592±0.047	0.498±0.039	0.358±0.071
$\mu^+\mu^-$									
n_{bb}	719±44	296±28	702±48	416±32	384±32	60±16	455±32	620±44	304±41
bb s.f.	1.31	1.17	1.28	1.43	1.24	1.29	1.42	1.3	1.5
ϵ_{bb}	0.480	0.528	0.482	0.488	0.553	0.350	0.275	0.416	0.266
C	0.570	0.240	0.573	0.300	0.280	0.066	0.567	0.570	0.483
σ (pb)	0.566±0.035	0.504±0.048	0.548±0.037	0.612±0.047	0.536±0.045	0.562±0.150	0.629±0.044	0.564±0.040	0.511±0.069
$\mu\mu/ee$	1.166	1.202	1.118	1.209	1.077	1.287	1.062	1.132	1.427
$\Delta\sigma$ (pb)	0.081	0.085	0.058	0.106	0.038	0.125	0.037	0.066	0.153
pull	1.615	1.229	1.075	1.631	0.573	0.616	0.565	1.170	1.545

Table 35: Summary of electron vs muon channel cross checks. See text for definition.

C QCD Background Cross Check

This appendix describes an alternative method for obtaining the multijet background in the Z+bb analysis The same comclusion is reached: the QCD background is negligible and does not further have to be taken into account in the fit procedures. The method for estimating QCD background that is used for the muon decay channel is described in detail and the modifications to the approach required in the electron channel are outlined.

QCD background is estimated via a two-step approach. In the first step, a control region defined by a wider Z mass window of 51 GeV - 131 GeV is considered. In the second step, the result is used to obtain the corresponding number of events in the signal region (76 GeV $< m_Z <$ 106 GeV).

The first step of the procedure is based on the assumption that the ratio of the number of QCD events with isolated muons to those with non-isolated muons is independent of whether or not one applies the jet selection:

$$\left.\frac{N^{\mathrm{QCD}}_{\mathrm{isolated}}}{N^{\mathrm{QCD}}_{\mathrm{non-isolated}}}\right|_{\mathrm{before\ jet\ selection}} = \left.\frac{N^{\mathrm{QCD}}_{\mathrm{isolated}}}{N^{\mathrm{QCD}}_{\mathrm{non-isolated}}}\right|_{\mathrm{final\ jet\ selection}} .$$

This equation is solved for the number $N^{\mathrm{QCD}}_{\mathrm{isolated}}$ of QCD events with isolated muons after the final event selection (numerator on the right hand side). The other three terms in the equation are obtained by subtracting the number of Monte Carlo events from known non-QCD sources from the number of data events. These Monte Carlo contributions are scaled by a factor $f_{\mathrm{bdg},\mu} = N_{\mathrm{data}}/N_{\mathrm{MC}}$ determined from the sample before the jet selection but within the signal Z mass window.

Channel	CR ee	SR ee	CR $\mu\mu$	SR $\mu\mu$
$Z + b\bar{b}$ + light partons	419	397	554	501
Z + light partons	251	235	319	297
$t\bar{t}$	103	41	122	48
di-boson	20	19	25	24
other backgrounds	2	1.5	3	2
QCD estimate	22	13.3 ± 10 (stat.) ± 9 (syst.)	11	6.5 ± 1.4(stat.) ± 3.5 (syst.)
signal + background	817	720	1034	900
data	834	713	1179	1022

Table 36: QCD background estimate: overview of results. CR: Control Region, SR: Signal Region.

In the second step the QCD distribution, equal to the Data minus the scaled MonteCarlo, in the isolated channel and before the jets selection, outside the Z mass peak, is used as template (see figure 111). Results from this region were further used in the QCD assessment for Z + 2 b-tagged jets signal region.

The QCD estimation inside the Z peak for the template distribution is done via averaging the number of events from the left sideband - $\mathrm{QCD_L}$ (51 GeV $< M_{\mu\mu} <$ 75 GeV) and the right sideband - $\mathrm{QCD_R}$ (107 GeV $< M_{\mu\mu} <$ 131 GeV). The average was then rescaled inside the Z window:

$$\mathrm{QCD_Z} = \frac{30\ \mathrm{GeV}}{25\ \mathrm{GeV}} \cdot \frac{\mathrm{QCD_L} + \mathrm{QCD_R}}{2} \tag{3}$$

since each of the sidebands correspond a 25 GeV window while the Z region corresponds to a 30 GeV window. The ratio of inside-to-outside multijet events with respect to the Z window ($\mathrm{QCD_Z}/\mathrm{QCD_L} + \mathrm{QCD_R}$) is used as a multiplication parameter, λ, for the QCD estimate after the final event selection outside the Z peak. The multiplication paramater takes a value of $\lambda = 3/5$ given the previous definitions.

Finally the QCD background inside the Z peak for signal Z + 2 b-tagged jet events is estimated to be approximately 6.5 events.

Statistical uncertainty assessment
The statistical uncertainty of the QCD background was performed using the error propagation formula. The number of events for Data (MonteCarlo) inside the Z window and inside the Control Region were taked as fully correlated. The statistical uncertainty was estimated to be ±1.5 events.

Systematical uncertainty assessment
The "up" variation with respect to the nominal estimation, has been evaluated by taking the left sideband and rescaling it to the Z peak, resulting in $\mathrm{QCD_L} \cdot 6/5$ events at the Z peak. The ratio of the QCD estimation inside the Z peak to the QCD estimation outside the Z peak has been taken in this case as the λ parameter.
The "down" variation with respect to the nominal estimation, has been evaluated by taking the right sideband and rescaling it to the Z peak, resulting in $\mathrm{QCD_R} \cdot 6/5$ events at the Z peak. The ratio of the QCD estimation inside the Z peak to the QCD estimation outside the Z peak has been taken in this case as the λ parameter.
The systematic uncertainty of the multijets background after the final event selection inside the Z peak was estimated to be approximately ±3.6 events.

Results obtained via the data-driven method presented in this section in the assessment of the QCD background have confirmed the apriori assumption, namely that multijets background plays a negligible role for the Z + 2 b-tagged jets analysis. The contribution in the muon channel was estimated to be 6.5 ± 1.5 (stat) ± 3.6 (sys) multijet events while the estimation in the electron channel is 13.3 ± 10 (stat) ± 9 (sys) events.

The input distributions used in step 1 of the approach are shown in Figure 112, parts (a), (b) and (d).

For the electron channel, a similar method is applied, but rather than using isolated and non-isolated leptons, the electrons are required to have the same sign charge and opposite sign charge, respectively. The corresponding distributions are shown in Figure 113.

The results for control and signal region for both Z boson decay channels are summarised in Table 36.

Note that a cross-check using the method described previously for the Zb analysis gives consistent results, giving 0 ± 19 and 30 ± 23 events in the muon and electron channels, respectively.

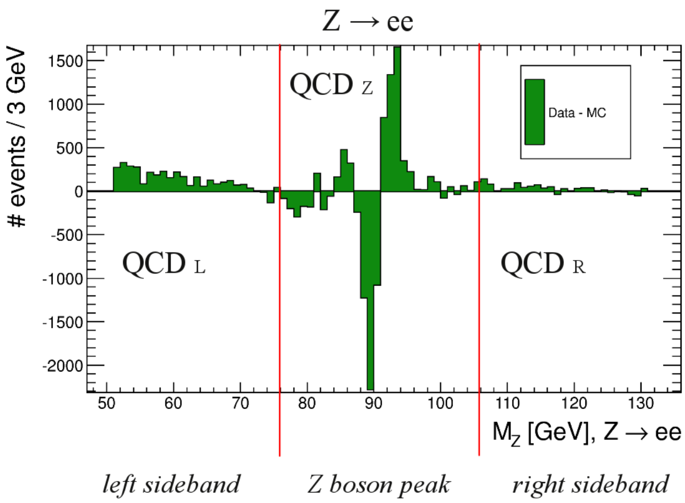

Figure 111: QCD distribution after the scaled MC subtraction from the Data for the isolated channel, before jets selection.

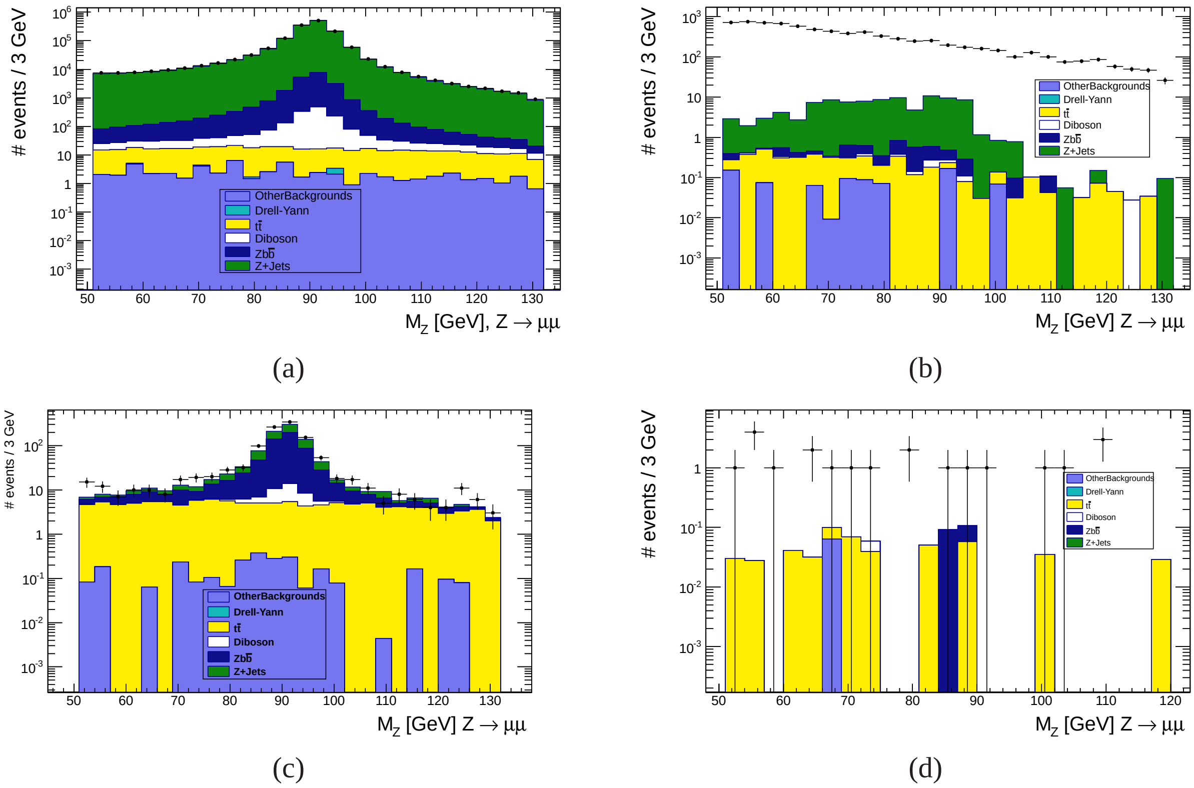

Figure 112: Data and non-QCD sources as described by Monte Carlo in the control region, for the muon channel. Parts (a) and (b) show distributions before the jet selection, parts (c) and (d) distributions with the final event selection applied. Parts (a) and (c) show events with isolated muons, parts (b) and (d) events with non-isolated muons. The inputs to step 1 of the background determination procedure are determined from parts (a), (b) and (d) of the figure.

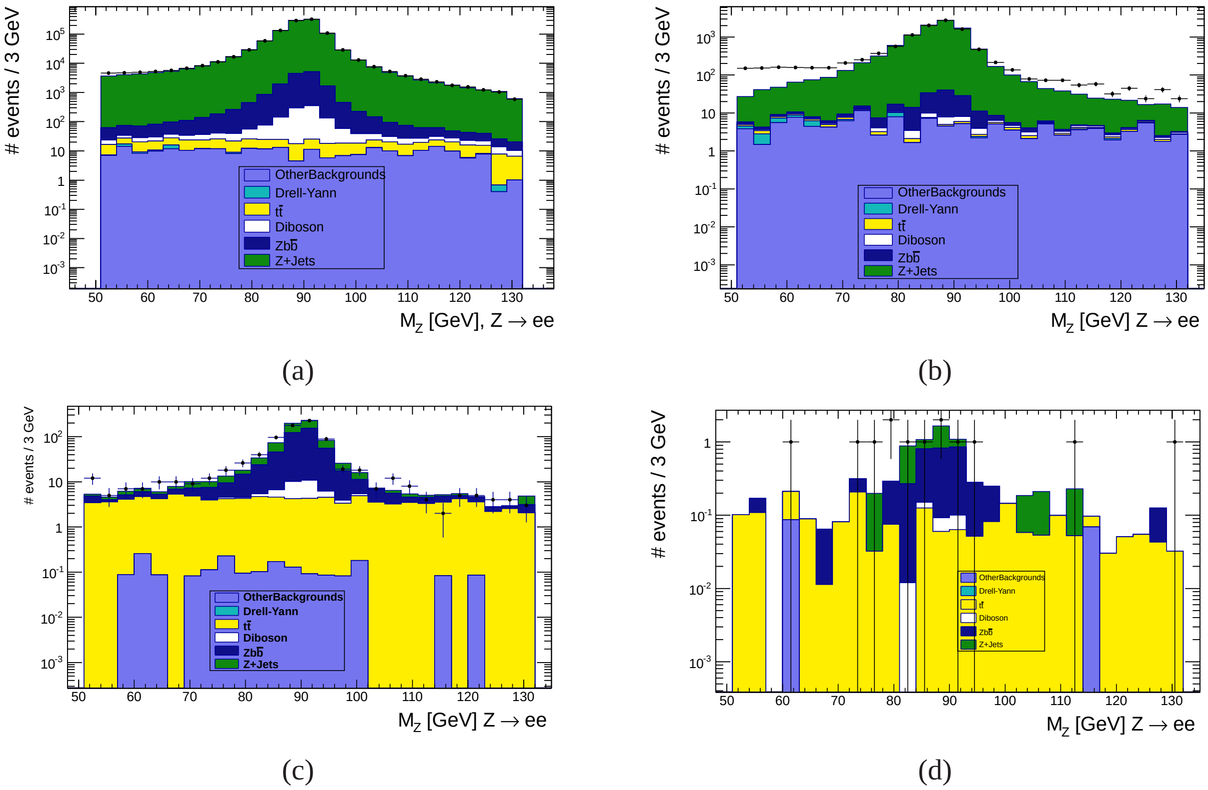

Figure 113: Data and non-QCD sources as described by Monte Carlo in the control region, for the electron channel. Parts (a) and (b) show distributions before the jet selection, parts (c) and (d) distributions with the final event selection applied. Parts (a) and (c) show events with opposite sign electrons, parts (b) and (d) events with same sign electrons. The inputs to step 1 of the background determination procedure are determined from parts (a), (b) and (d) of the figure.

D Corrections to NLO predictions from MCFM and comparison of theory predictions

D.1 QED radiation from the leptons

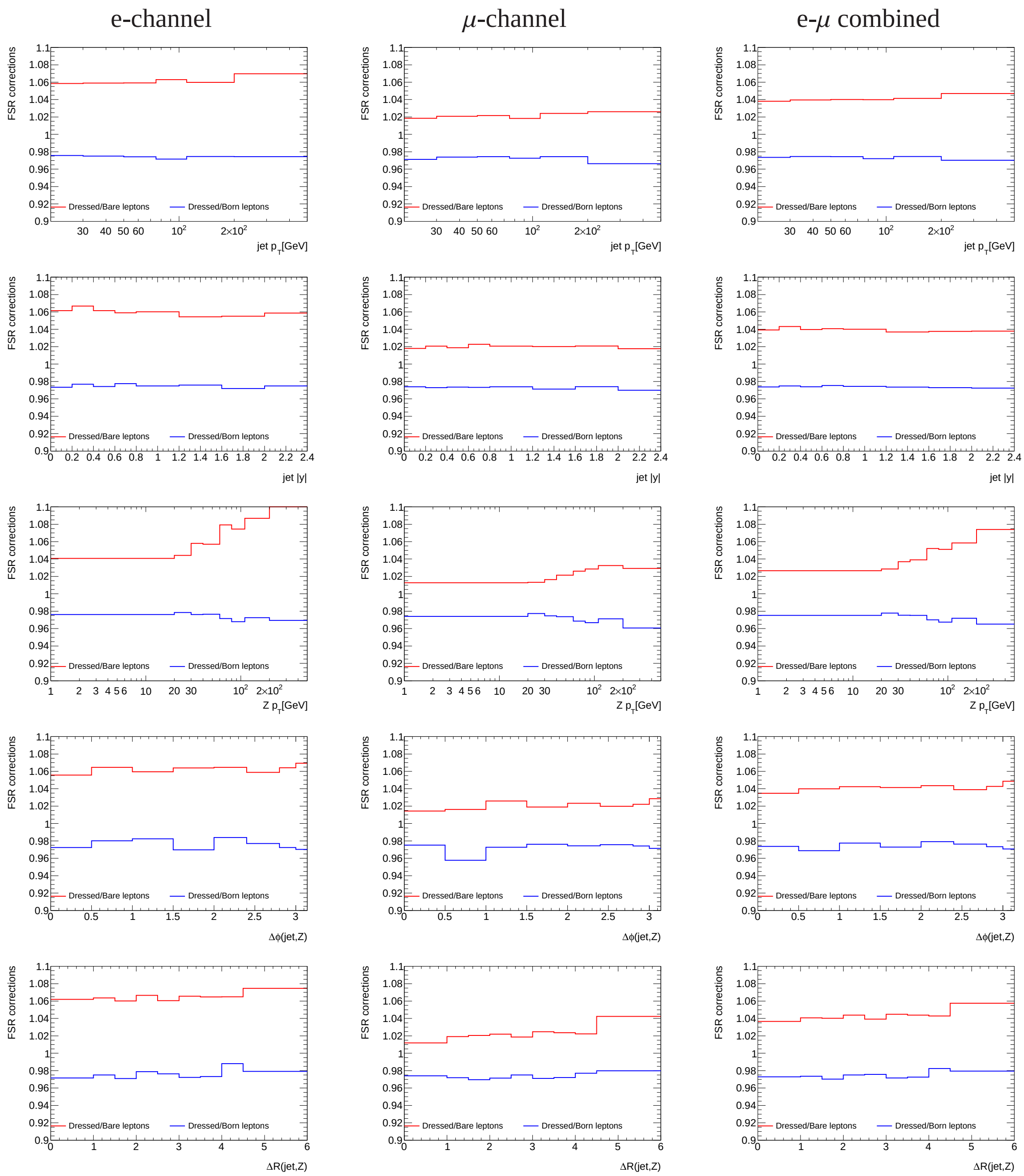

Figure 114: QED FSR corrections for the $Z + b$ selection in the various differential distributions as predicted by Alpgen. In all plots the blue lire represents the correction to be applied to the MCFM prediction, defined as the ratio of the yield obtained when dressed leptons are used to the yield obtained when the selection is applied to Born leptons. For comparison, the ratio of prediction for dressed leptons to the prediction for bare leptons (after photon radiation) is shown in red.

(μ-channel) (e-channel)

Figure 115: QED FSR corrections for the $Z + bb$ selection in the various differential distributions as predicted by Alpgen. In all plots the blue lire represents the correction to be applied to the MCFM prediction, defined as the ratio of the yield obtained when dressed leptons are used to the yield obtained when the selection is applied to Born leptons. For comparison, the ratio of prediction for dressed leptons to the prediction for bare leptons (after photon radiation) is shown in red.

Bins	e-channel		μ-channel		e-μ combined	
b-jet p_T [GeV]	Dressed/Bare	Dressed/Born	Dressed/Bare	Dressed/Born	Dressed/Bare	Dressed/Born
(20,30)	1.059 ± 0.006	0.976 ± 0.006	1.018 ± 0.006	0.971 ± 0.006	1.038 ± 0.004	0.974 ± 0.004
(30,50)	1.059 ± 0.005	0.975 ± 0.005	1.021 ± 0.005	0.974 ± 0.006	1.040 ± 0.004	0.974 ± 0.004
(50,75)	1.059 ± 0.007	0.974 ± 0.007	1.022 ± 0.007	0.974 ± 0.008	1.040 ± 0.005	0.974 ± 0.005
(75,110)	1.063 ± 0.010	0.972 ± 0.011	1.018 ± 0.011	0.973 ± 0.012	1.040 ± 0.008	0.972 ± 0.008
(110,200)	1.060 ± 0.015	0.975 ± 0.016	1.024 ± 0.017	0.974 ± 0.018	1.041 ± 0.011	0.975 ± 0.012
(200,500)	1.070 ± 0.041	0.974 ± 0.043	1.026 ± 0.050	0.966 ± 0.052	1.047 ± 0.032	0.970 ± 0.033
b-jet $\|y\|$	Dressed/Bare	Dressed/Born	Dressed/Bare	Dressed/Born	Dressed/Bare	Dressed/Born
(0,0.2)	1.062 ± 0.009	0.973 ± 0.009	1.018 ± 0.010	0.974 ± 0.010	1.039 ± 0.006	0.974 ± 0.007
(0.2,0.4)	1.067 ± 0.009	0.977 ± 0.009	1.021 ± 0.010	0.973 ± 0.010	1.043 ± 0.007	0.975 ± 0.007
(0.4,0.6)	1.061 ± 0.009	0.974 ± 0.010	1.019 ± 0.010	0.973 ± 0.010	1.040 ± 0.007	0.974 ± 0.007
(0.6,0.8)	1.059 ± 0.009	0.978 ± 0.010	1.023 ± 0.010	0.973 ± 0.010	1.041 ± 0.007	0.975 ± 0.007
(0.8,1.2)	1.060 ± 0.007	0.975 ± 0.007	1.021 ± 0.008	0.974 ± 0.008	1.040 ± 0.005	0.974 ± 0.005
(1.2,1.6)	1.054 ± 0.008	0.976 ± 0.008	1.020 ± 0.009	0.971 ± 0.009	1.037 ± 0.006	0.974 ± 0.006
(1.6,2)	1.055 ± 0.010	0.972 ± 0.010	1.021 ± 0.010	0.974 ± 0.010	1.038 ± 0.007	0.973 ± 0.007
(2,2.4)	1.059 ± 0.012	0.975 ± 0.012	1.018 ± 0.012	0.970 ± 0.013	1.038 ± 0.008	0.972 ± 0.009
Z p_T [GeV]	Dressed/Bare	Dressed/Born	Dressed/Bare	Dressed/Born	Dressed/Bare	Dressed/Born
(0,20)	1.041 ± 0.010	0.976 ± 0.010	1.013 ± 0.010	0.974 ± 0.011	1.027 ± 0.007	0.975 ± 0.007
(20,30)	1.044 ± 0.008	0.978 ± 0.008	1.013 ± 0.009	0.977 ± 0.009	1.029 ± 0.006	0.978 ± 0.006
(30,40)	1.058 ± 0.007	0.976 ± 0.008	1.016 ± 0.008	0.975 ± 0.008	1.037 ± 0.005	0.975 ± 0.006
(40,60)	1.057 ± 0.006	0.977 ± 0.006	1.021 ± 0.006	0.974 ± 0.006	1.039 ± 0.004	0.975 ± 0.004
(60,80)	1.079 ± 0.008	0.972 ± 0.008	1.026 ± 0.008	0.969 ± 0.009	1.052 ± 0.006	0.970 ± 0.006
(80,110)	1.075 ± 0.009	0.968 ± 0.010	1.029 ± 0.010	0.967 ± 0.011	1.051 ± 0.007	0.967 ± 0.007
(110,200)	1.087 ± 0.011	0.973 ± 0.011	1.033 ± 0.013	0.971 ± 0.013	1.059 ± 0.008	0.972 ± 0.009
(200,500)	1.121 ± 0.027	0.969 ± 0.030	1.029 ± 0.033	0.961 ± 0.035	1.074 ± 0.021	0.965 ± 0.022
$\Delta\phi(Z, b\text{-}jet)$	Dressed/Bare	Dressed/Born	Dressed/Bare	Dressed/Born	Dressed/Bare	Dressed/Born
(0,0.5)	1.056 ± 0.027	0.972 ± 0.028	1.014 ± 0.030	0.975 ± 0.030	1.035 ± 0.020	0.974 ± 0.020
(0.5,1)	1.065 ± 0.024	0.980 ± 0.026	1.016 ± 0.027	0.958 ± 0.029	1.040 ± 0.018	0.969 ± 0.019
(1,1.5)	1.060 ± 0.020	0.982 ± 0.021	1.026 ± 0.023	0.973 ± 0.023	1.042 ± 0.015	0.978 ± 0.015
(1.5,2)	1.064 ± 0.016	0.970 ± 0.017	1.019 ± 0.018	0.976 ± 0.018	1.041 ± 0.012	0.973 ± 0.012
(2,2.4)	1.065 ± 0.013	0.984 ± 0.013	1.023 ± 0.014	0.974 ± 0.015	1.043 ± 0.009	0.979 ± 0.010
(2.4,2.8)	1.059 ± 0.009	0.977 ± 0.009	1.020 ± 0.010	0.976 ± 0.010	1.039 ± 0.007	0.976 ± 0.007
(2.8,3)	1.064 ± 0.009	0.972 ± 0.010	1.022 ± 0.010	0.974 ± 0.010	1.043 ± 0.007	0.973 ± 0.007
(3,π)	1.069 ± 0.010	0.970 ± 0.011	1.028 ± 0.011	0.971 ± 0.011	1.049 ± 0.007	0.971 ± 0.008
$\Delta R(Z, b\text{-}jet)$	Dressed/Bare	Dressed/Born	Dressed/Bare	Dressed/Born	Dressed/Bare	Dressed/Born
(0,1)	1.062 ± 0.020	0.972 ± 0.021	1.012 ± 0.023	0.974 ± 0.023	1.037 ± 0.015	0.973 ± 0.015
(1,1.5)	1.064 ± 0.016	0.975 ± 0.017	1.019 ± 0.018	0.972 ± 0.019	1.041 ± 0.012	0.974 ± 0.012
(1.5,2)	1.060 ± 0.012	0.971 ± 0.013	1.020 ± 0.014	0.970 ± 0.014	1.040 ± 0.009	0.970 ± 0.009
(2,2.5)	1.067 ± 0.009	0.979 ± 0.009	1.022 ± 0.010	0.971 ± 0.010	1.044 ± 0.006	0.975 ± 0.007
(2.5,3)	1.060 ± 0.005	0.976 ± 0.006	1.019 ± 0.006	0.975 ± 0.006	1.039 ± 0.004	0.976 ± 0.004
(3,3.5)	1.066 ± 0.005	0.972 ± 0.006	1.025 ± 0.006	0.971 ± 0.006	1.045 ± 0.004	0.972 ± 0.004
(3.5,4)	1.065 ± 0.013	0.973 ± 0.014	1.024 ± 0.014	0.972 ± 0.015	1.044 ± 0.010	0.973 ± 0.010
(4,4.5)	1.065 ± 0.029	0.988 ± 0.030	1.022 ± 0.033	0.977 ± 0.033	1.043 ± 0.021	0.982 ± 0.022
(4.5,6)	1.075 ± 0.066	0.979 ± 0.070	1.042 ± 0.074	0.980 ± 0.077	1.057 ± 0.049	0.980 ± 0.051

Table 37: QED FSR corrections for the $Z+b$ selection in the various differential distributions as predicted by Alpgen.

E Top Enriched Control Region

The studies documented in section 5 make use of an analysis control region of top enriched events in the lepton plus jets channel. The event selection criteria and additional corrections applied to these data are documented in this appendix.

E.1 Event Selection

For the most part the event and physics object selection, scale corrections and efficiency scale factors are identical to those documented for the signal region in section 4. Modifications to the baseline selection to obtain the control region are given below. Due to requirements on number of selected leptons and E_T^{miss} there is no overlap between the control region and signal region.

E.1.1 Electrons

- Single electron triggers: `EF_e20_medium` for periods D-J; `EF_e22_medium` for period K; `EF_e22vh_medium1` for periods L-M. Efficiency correction factors for these triggers are applied in MC.
- $E_T \geq 25\,\mathrm{GeV}$.
- Pass the *egammaPID::ElectronTightPP* criteria. Corresponding efficiency scale factors are applied in MC.
- Pileup corrected calorimeter isolation for cone 0.3 with $\sum p_T(\mathrm{cal})/\mathrm{E_T} < 0.14$.
- Track isolation for cone 0.3 with $\sum p_T(\mathrm{ID})/\mathrm{E_T} < 0.13$.

E.1.2 Muons

- $p_T \geq 25\,\mathrm{GeV}$.
- Pileup corrected calorimeter isolation for cone 0.3 with $\sum p_T(\mathrm{cal})/\mathrm{p_T} < 0.14$.
- Track isolation for cone 0.3 with $\sum p_T(\mathrm{ID})/\mathrm{p_T} < 0.15$.

E.1.3 Leptonic W Reconstruction

Events are required to have exactly one selected lepton of either flavour, provided the trigger for that flavour lepton fired. The recontructed transverse mass defined as,

$$m_T = \sqrt{2p_T^{\mathrm{lepton}} E_T^{\mathrm{miss}}(1 - \cos\Delta\phi(\mathrm{lepton}, \mathrm{E_T^{Miss}}))}, \tag{4}$$

is required to satisfy $m_T \geq 60\,\mathrm{GeV}$.

E.1.4 Additional Criteria

- $E_T^{\mathrm{Miss}} \geq 30\,\mathrm{GeV}$.
- At least four selected jets.

MC	Scale Factor
W+bb	1.091
W+cc	1.091
W+c	1.082
W+light	0.955
Inclusive (μ-channel)	0.84
Inclusive (e-channel)	0.90

Table 38: Scale factors applied to W+jets MC derived by the top group. The relative flavour contributions are reweighted keeping the total normalisation constant, the overall W+jets intergral is then scaled by the inclusive factor.

E.2 Data to MC Comparison

In comparing data to MC five electroweak processes are considered: $t\bar{t}$ (MC@NLO+Jimmy); W+jets (Alpgen+Jimmy); single top (MC@NLO+Jimmy except t-channel AcerMC+pythia); Z+jets (Alpgen+Jimmy); Diboson (HERWIG). For the Alpgen+Jimmy samples HFOR is applied in their combination. Correction factors derived by the top group are applied to both the W+jets flavour fractions and overall scale; these corrections are applied globally rather than on an event by event basis and listed in table 38. Figures 116 and 117 show various event level variables for the muon and electron channels respectively; table 39 summarises the predicted contribution from each electroweak process and compares their sum to the yield observed in data. Uncertainties are not currently derived in the control region; however it can be seen that in the electron channel the MC does a good job of reproducing the data normalisation, whereas the muon channel suffers from a deficit of ~13% in the MC prediction with respect to data. It is not *a priori* clear whether the normalisation discrepancy in the muon channel is due to uncertainties in the muon selection or the result of a residual multijet background.

	Muon Channel			Electron Channel		
Process	All	2 Tag Bin	3 Tag Bin	All	2 Tag Bin	3 Tag Bin
Data	56023	11449	1918	50347	10416	1747
$t\bar{t}$	19846	8588	1505	18414	7958	1421
W+jets	26015	678	81	27604	700	43
Single Top	1830	586	76	1678	527	69
Z+jets	1527	55	4	2079	74	6
Diboson	379	14	1	349	14	1
Total MC	49596	9921	1667	50125	9298	1540
Data/MC	1.130	1.154	1.151	1.004	1.120	1.134

Table 39: Comparison of data yield and MC prediction for the muon and electron channels in the top enriched control region.

Studies of the properties of b-jets are made using control region events with exactly two b-tagged jets. It can be seen from Figures 116 (b) and 117 (b) that both channels suffer a 12-15% deficit in the MC with respect to data in the bin corresponding to this selection. Given that the electron channel shows no evidence for multijet background it is likely this discrepancy is dominated by MC normalisation rather than the consequence of an additional background. This is supported twofold. First the MC@NLO+Jimmy $t\bar{t}$ MC is substituted for Powheg+pythia or Alpgen+Jimmy and the change in discrepancy for the alternative MCs is given in Table 40. It can be seen that, although the muon channel discrepancy always exceeds the electron channel, there is a significant range with worse agreement between MC and data for Powheg+pythia and better agreement for Alpgen+Jimmy. Secondly comparison is made of the selected m_T distribution and the full m_T distribution with no E_T^{miss} cut applied, as shown in Figures 118 and 119 for the muon and electron channels respectively. Despite the looser selection designed to enhance any potential multijet background the Data/MC ratio for $m_T \geq 60$ GeV is found to be 1.153 and 1.128 for the muon and electron channels respectively, which does not differ significantly from the same ratio with the tighter default selection (particularly for the muon channel). Given that a large range of normalisation is observed with different $t\bar{t}$ MCs and that no significant enhancement of any multijet contribution is observed with a looser selection, for all subsequent study of the control region two tag bin the Data/MC ratio is forced equal to unity by scaling up the MC@NLO+Jimmy top MC normalisation. In principle these scaling factors should be universal but this is found not to be the case due to the impact of b-tagging scale factors in MC. Typically the normalisation correction for the MC@NLO+Jimmy $t\bar{t}$ MC is found to be ~10-15%.

	Muon Channel		Electron Channel	
Process	Yield	Data/MC	Yield	Data/MC
Data	11449	–	10416	–
MC@NLO+Jimmy + Other EW	9921	1.154	9298	1.120
Powheg+pythia + Other EW	9555	1.198	8930	1.166
Alpgen+Jimmy + Other EW	10655	1.075	10107	1.031

Table 40: Comparison of data yield discrepencies in the 2 tag bin of the control region for different $t\bar{t}$ MCs.

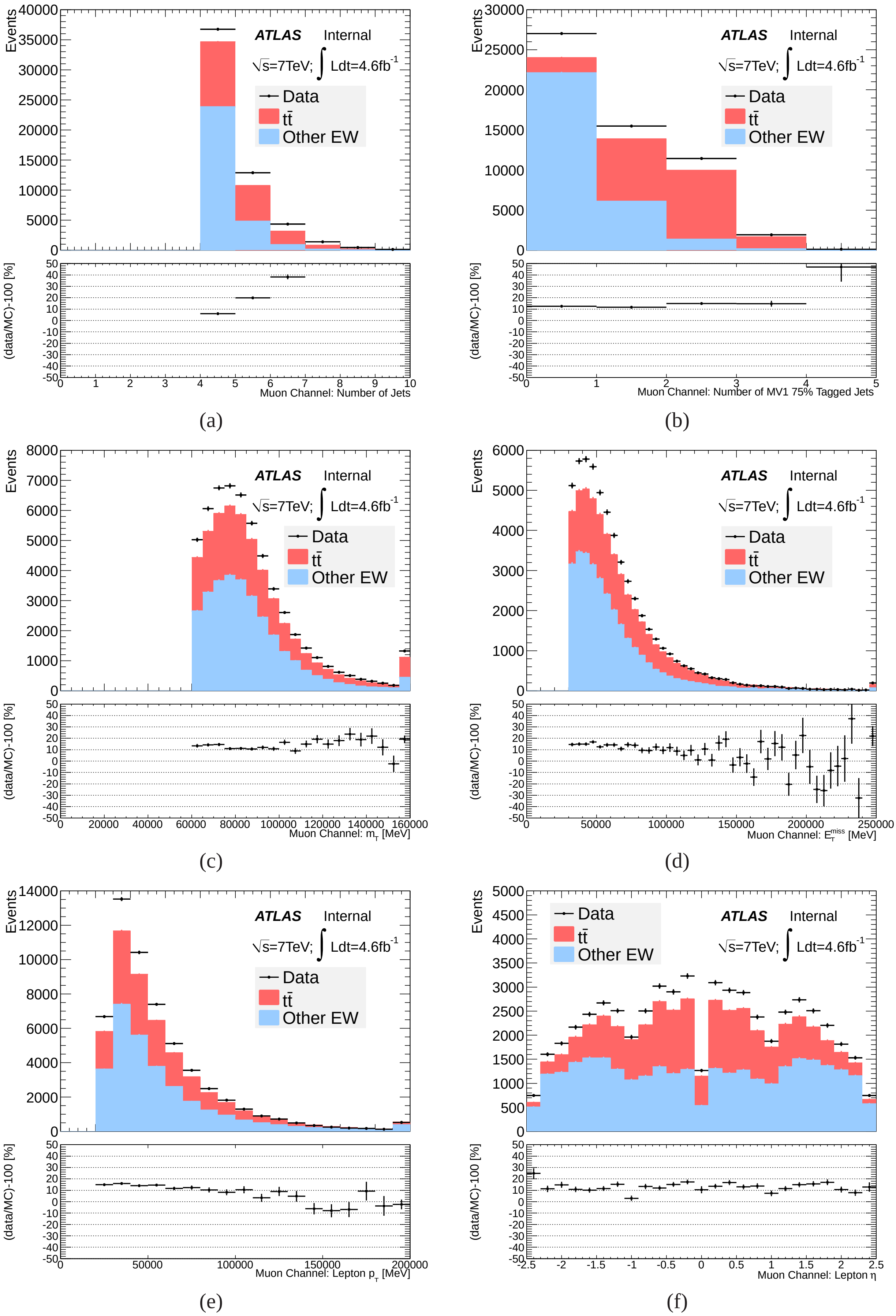

Figure 116: Control region muon channel event level plots: (a) Number of jets; (b) number of tagged jets; (c) m_T; (d) E_T^{miss}; (e) muon p_T; (f) muon η.

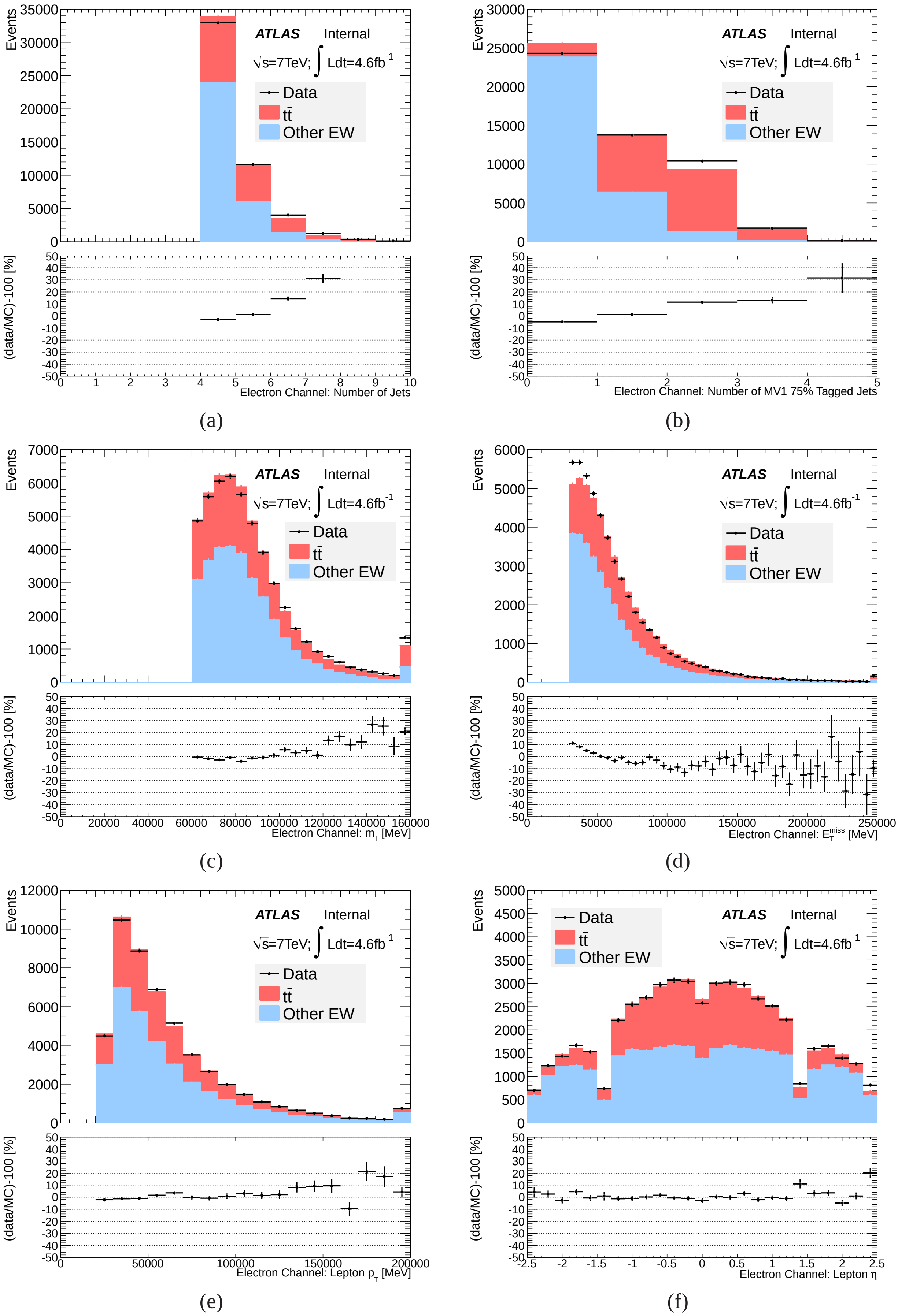

Figure 117: Control region electron channel event level plots: (a) Number of jets; (b) number of tagged jets; (c) m_T; (d) E_T^{miss}; (e) electron p_T; (f) electron η.

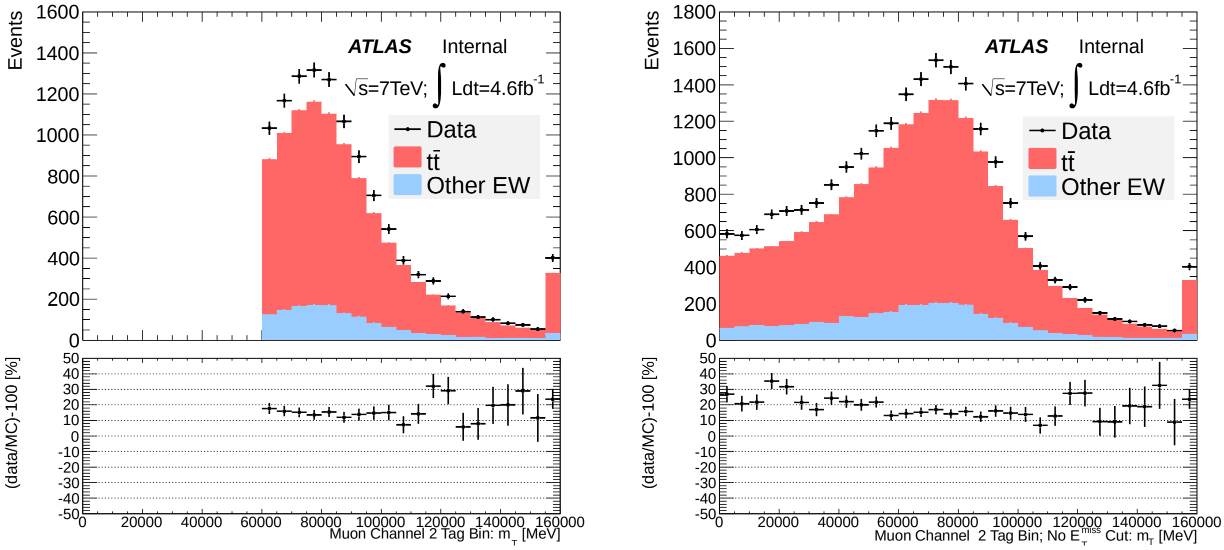

(a) (b)

Figure 118: Comparison of m_T in the muon channel 2 tag bin, (a) with default selection and (b) with no E_t^{miss} cut.

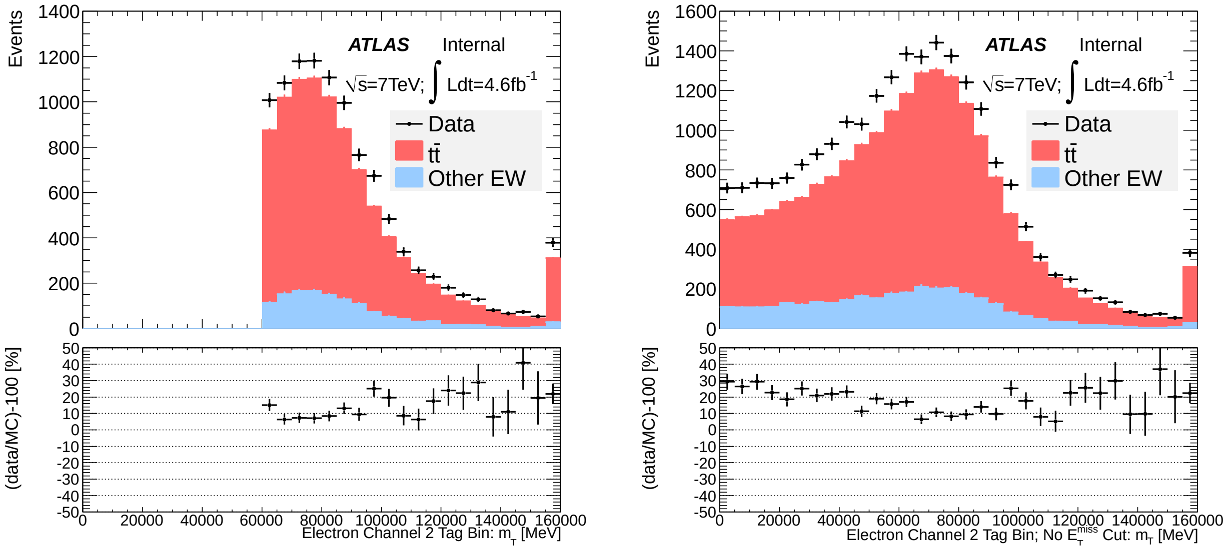

(a) (b)

Figure 119: Comparison of m_T in the electron channel 2 tag bin, (a) with default selection and (b) with no E_t^{miss} cut.

F Goodness of fit tests for Zbb analysis

To test the valididity of the fit procedure and check for any fit bias several fit tests have been performed.

F.1 Linearity Test

For each bin in the Zbb differential observables, the three templates (bb, non-bb and background) are taken with the fit scale factors applied. The bb template is further scaled by a factor X, (X=0.5, 0.75, 1.0, 1.5, 2.0). The scaled bb template is then combined with the other and background template to form a parent sample. From this parent sample 500 pseudo-datasets are formed by varying each bin by a poisson centred on the parent sample bin value. Each of the pseudo data-sets are then fitted with the pre-fit templates, which have only had the single-b proportion scale factor applied. The fitted value of X is then calculated. The Linearity Distributions for each variable are shown in Figs. 120, 121, 122 and 123.

F.2 Fit quality

To test the quality of the fitting the differentail $Z+bb$ variables several tests have been performed. Firstly Templates scaled by the fit scale factors are combined into a parent dataset. The number of fitted $Z+bb$ events N_{bb} is taken from the fit. 1000 pseudo datasets are drawn from the parent by fluctuating each bin in the parent sample around the bin value. The pseuso datasets are then fitted with the pre-fit templates and the number of Z+bb events from the fit, N^P_{bb} is derived along with the error on the fit σ^P_{bb}. The pull is defined as $(N^P_{bb} - N_{bb})/\sigma^P_{bb}$, it should centre on zero and have a width of 1. The pull distributions with a fiited guassian function are shown in Figs. 124, 125, 126 and 127. The χ^2 per degree of freedom is also calculated for each fit to the pseudo datasets. These are shown in Figs. 128, 129, 130 and 131. Finally the p-value corresponding to the χ^2 fit results are shown in Figs. 132, 133, 134 and 135.

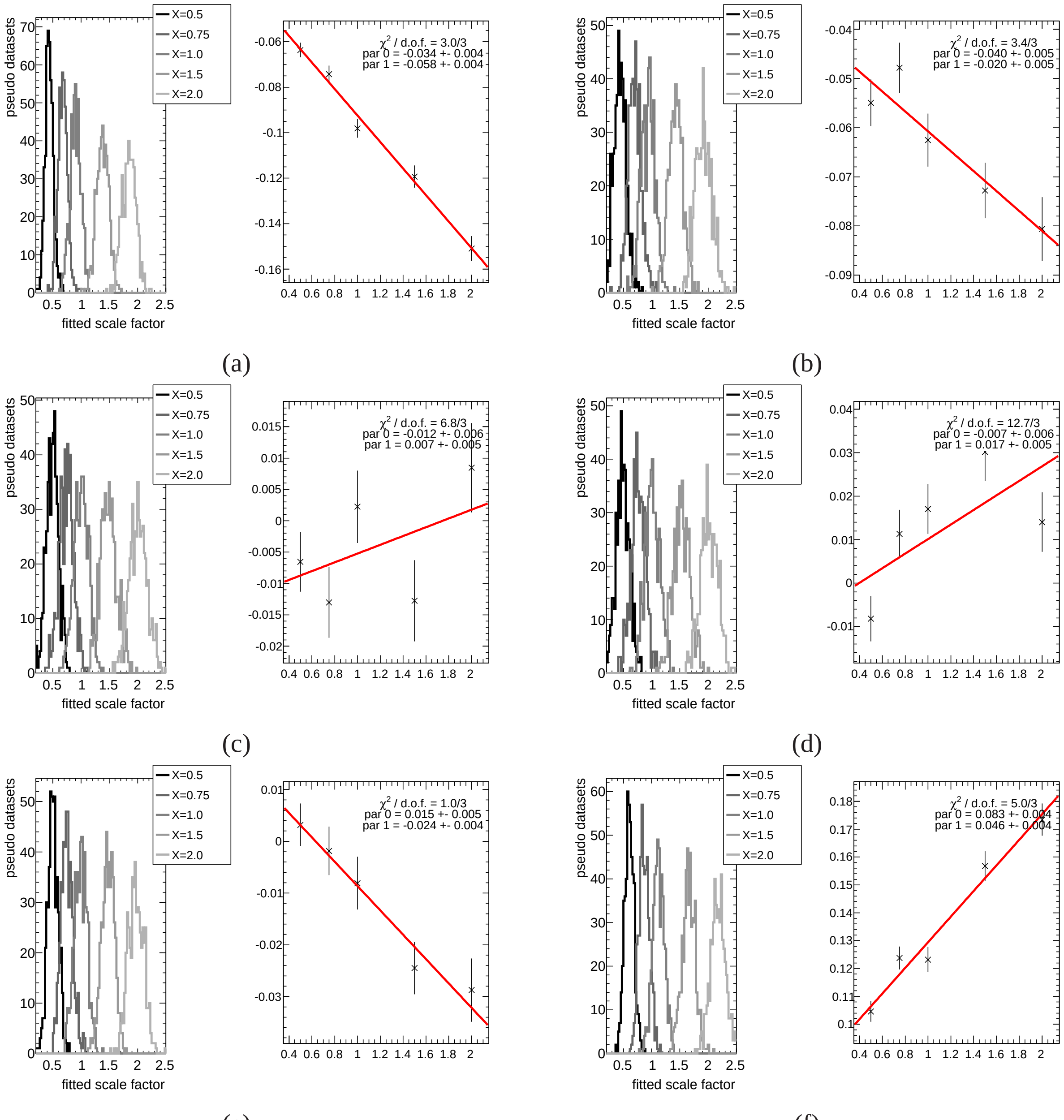

Figure 120: Linearity tests for the differential $Z+bb$ fits. In all fitted bins of ΔR_{bb}, (a) $0.4 < \Delta R_{bb} < 1.15$, (b) $1.15 < \Delta R_{bb} < 1.9$, (c) $1.9 < \Delta R_{bb} < 2.4$, (d) $2.4 < \Delta R_{bb} < 2.8$, (e) $2.8 < \Delta R_{bb} < 3.2$ and (f) $3.2 < \Delta R_{bb} < 5$

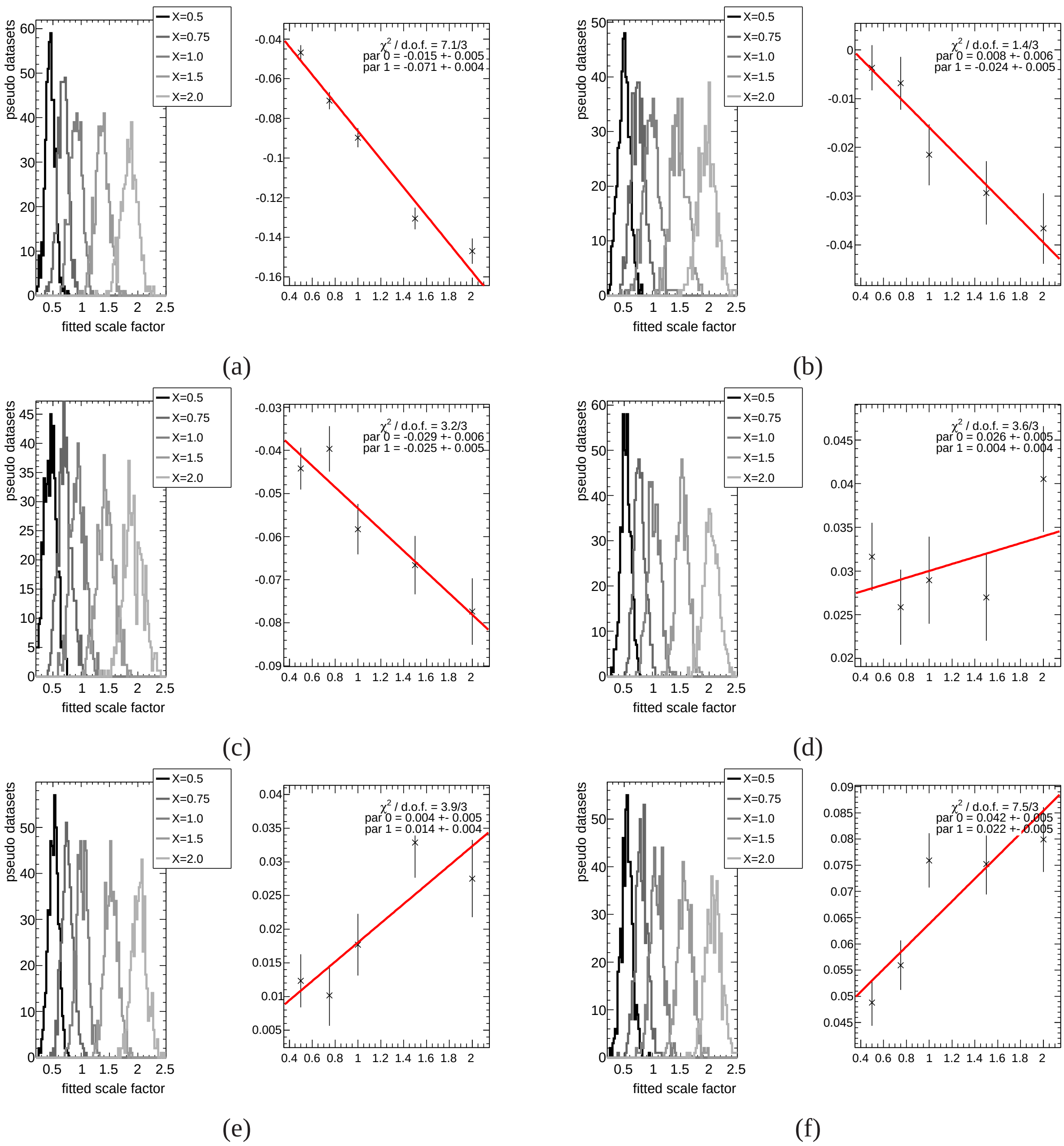

Figure 121: Linearity tests for the differential $Z+bb$ fits. In all fitted bins of m_{bb}, (a) $10 < m_{bb} < 45 GeV$, (b) $45 < m_{bb} < 65 GeV$, (c) $65 < m_{bb} < 85 GeV$, (d) $85 < m_{bb} < 115 GeV$, (e) $115 < m_{bb} < 165 GeV$ and (f) $165 < m_{bb} < 350 GeV$

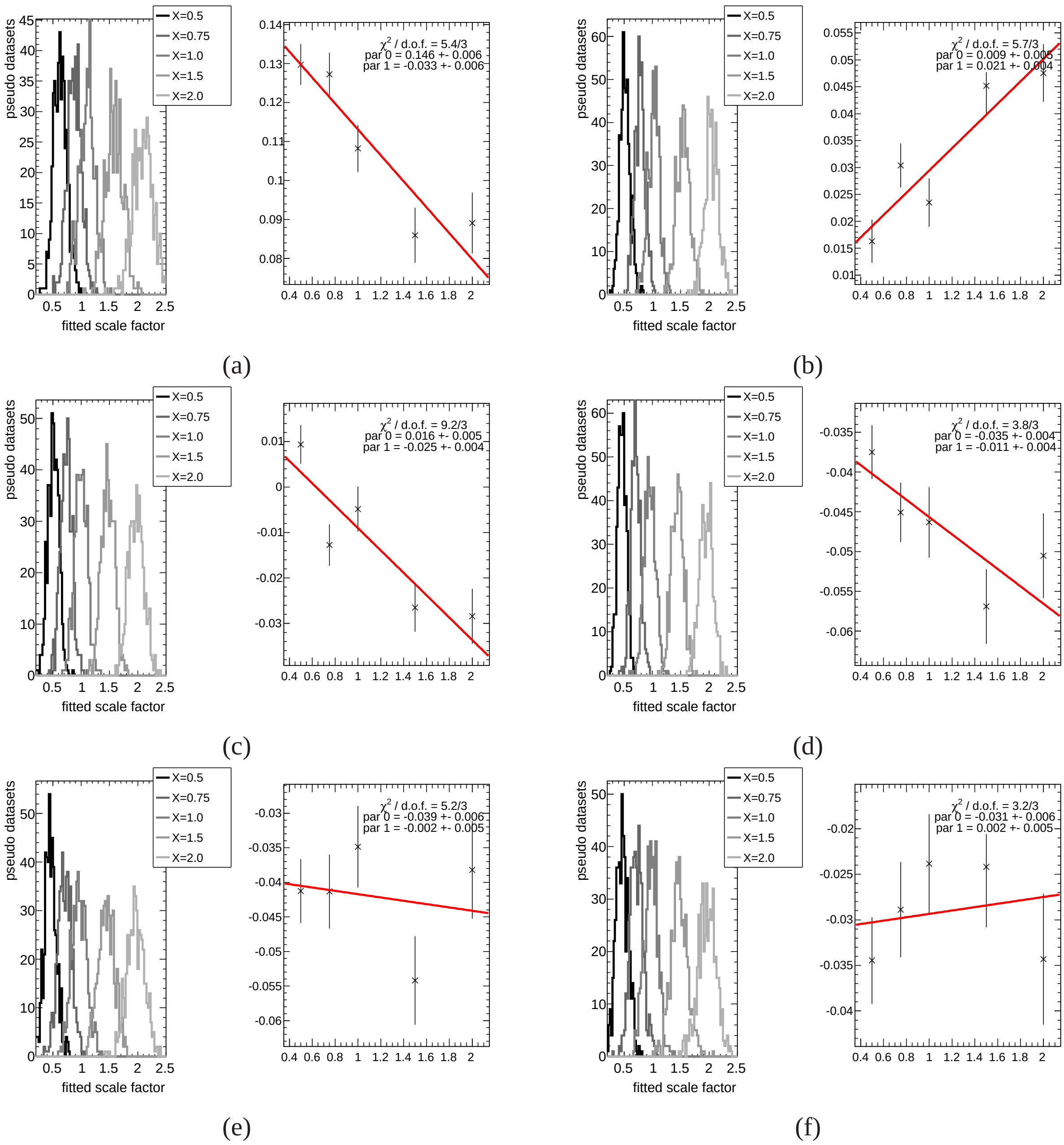

Figure 122: Linearity tests for the differential $Z + bb$ fits. In all fitted bins of $p_{T,Z}$, (a) $p_{T,Z} < 20 GeV$, (b) $20 < p_{T,Z} < 40 GeV$, (c) $40 < p_{T,Z} < 60 GeV$, (d) $60 < p_{T,Z} < 80 GeV$, (e) $80 < p_{T,Z} < 110 GeV$ and (f) $110 < p_{T,Z} < 250 GeV$

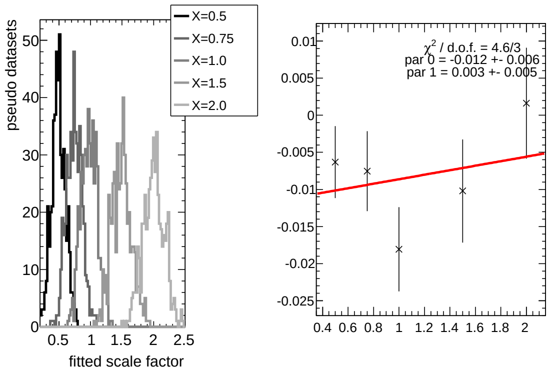

(a)

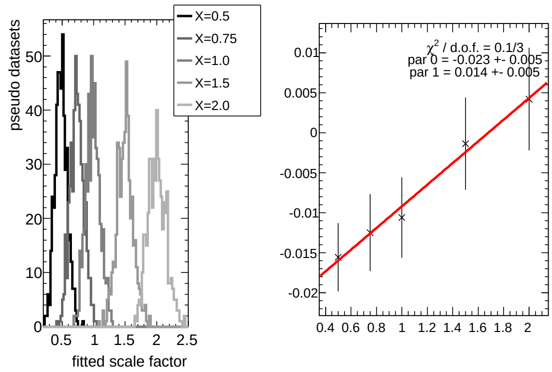

(b)

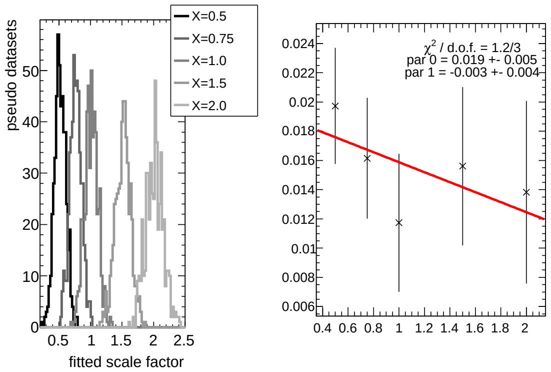

(c)

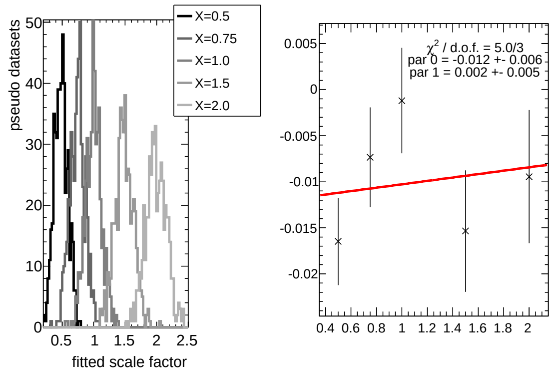

(d)

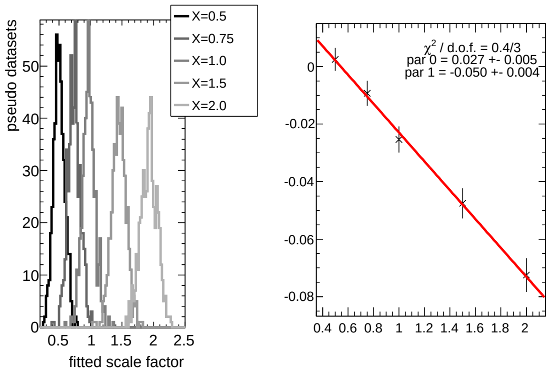

(e)

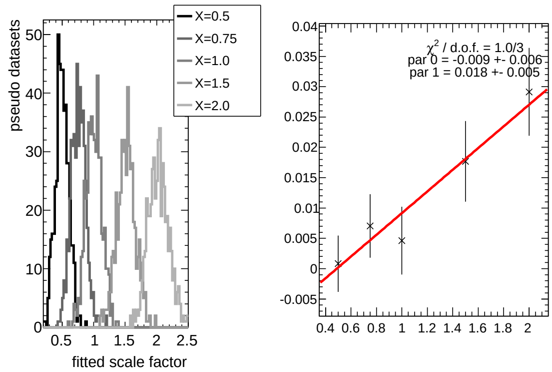

(f)

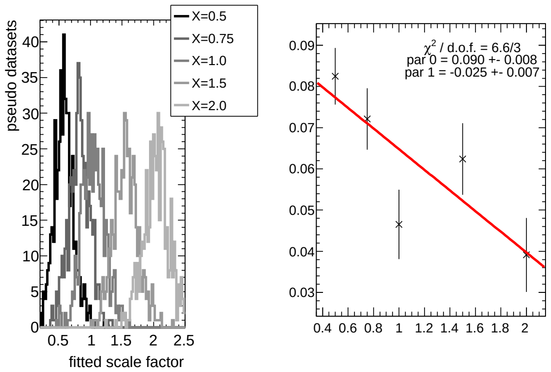

(g)

Figure 123: Linearity tests for the differential $Z + bb$ fits. In all fitted bins of $Z|y|$, (a) $0 < Z|y| < 0.2$, (b) $0.2 < Z|y| < 0.4$, (c) $0.4 < Z|y| < 0.6$, (d) $0.6 < Z|y| < 0.8$, (e) $0.8 < Z|y| < 1.2$, (f) $1.2 < Z|y| < 1.6$ and (g) $1.6 < Z|y| < 2.5$

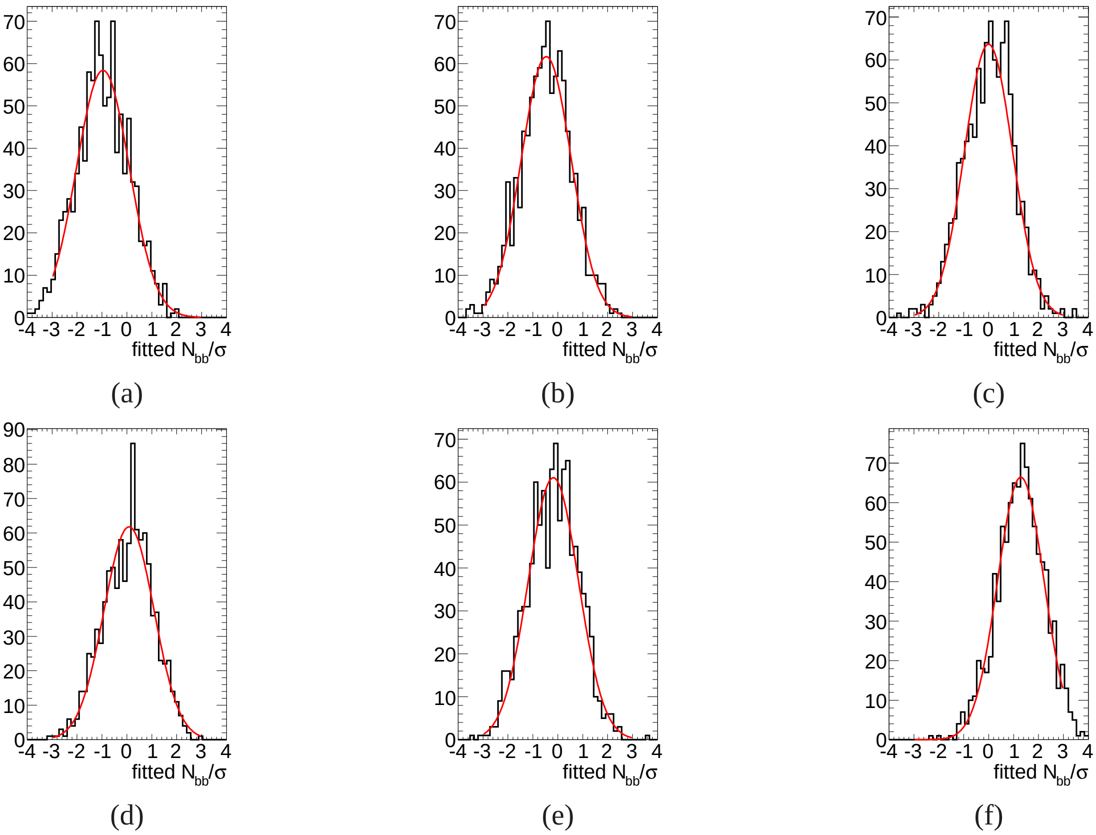

Figure 124: Pull tests for the differential $Z + bb$ fits. In all fitted bins of ΔR_{bb}, (a) $0.4 < \Delta R_{bb} < 1.15$, (b) $1.15 < \Delta R_{bb} < 1.9$, (c) $1.9 < \Delta R_{bb} < 2.4$, (d) $2.4 < \Delta R_{bb} < 2.8$, (e) $2.8 < \Delta R_{bb} < 3.2$ and (f) $3.2 < \Delta R_{bb} < 5$

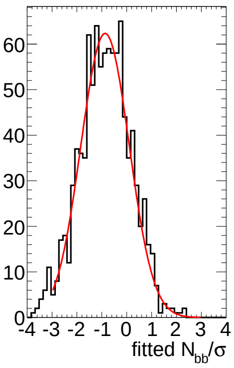

(a)

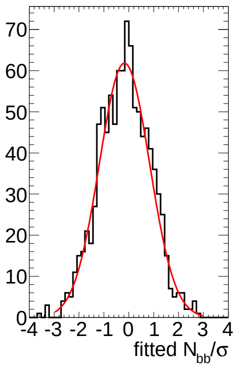

(b)

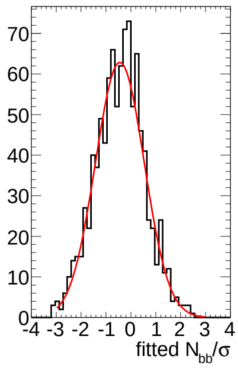

(c)

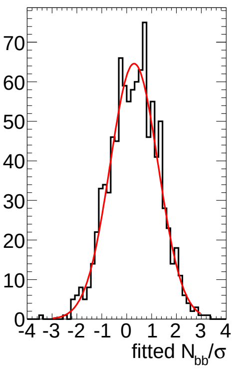

(d)

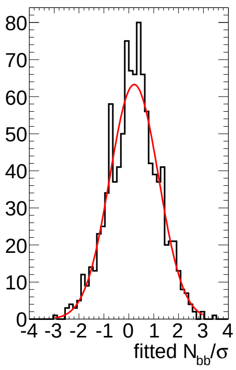

(e)

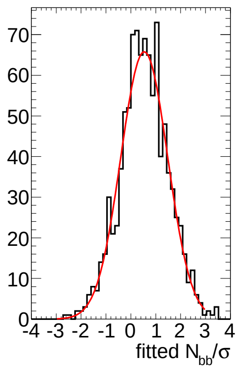

(f)

Figure 125: Pull tests for the differential $Z + bb$ fits. In all fitted bins of m_{bb}, (a) $10 < m_{bb} < 45 GeV$, (b) $45 < m_{bb} < 65 GeV$, (c) $65 < m_{bb} < 85 GeV$, (d) $85 < m_{bb} < 115 GeV$, (e) $115 < m_{bb} < 165 GeV$ and (f) $165 < m_{bb} < 350 GeV$

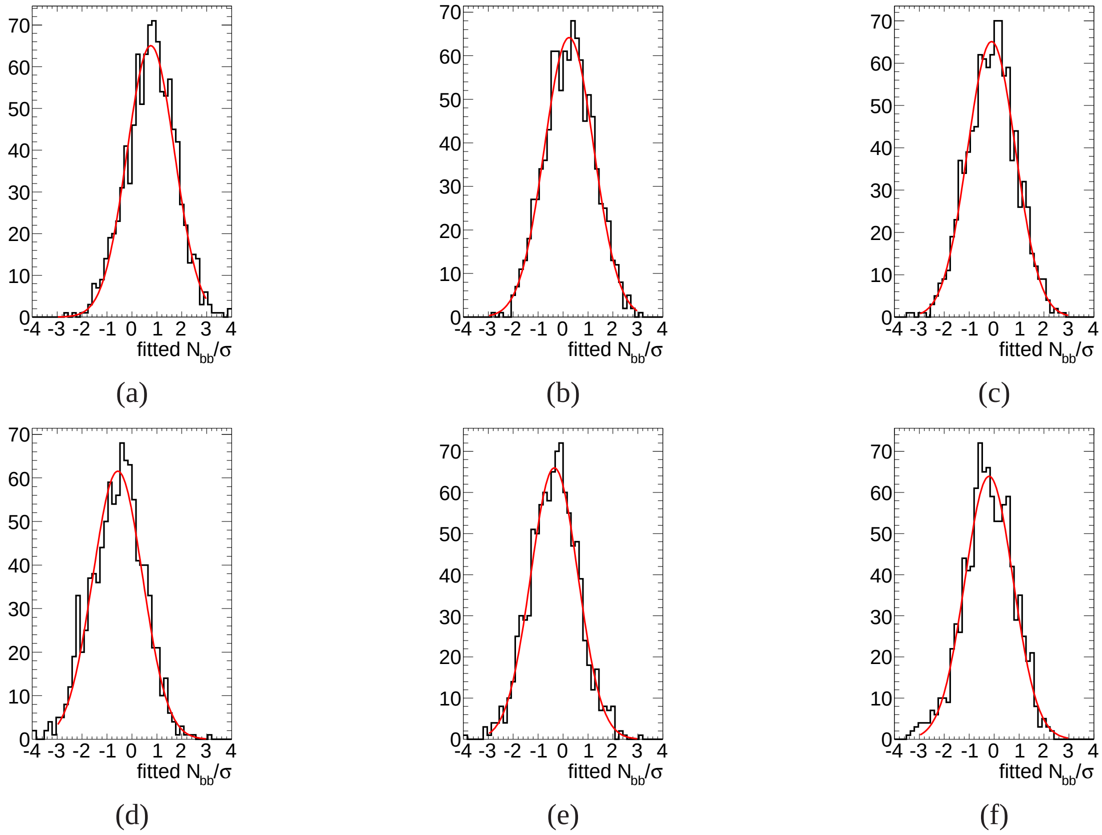

Figure 126: Pull tests for the differential $Z + bb$ fits. In all fitted bins of $p_{\mathrm{T},Z}$, (a) $p_{\mathrm{T},Z} < 20 GeV$, (b) $20 < p_{\mathrm{T},Z} < 40 GeV$, (c) $40 < p_{\mathrm{T},Z} < 60 GeV$, (d) $60 < p_{\mathrm{T},Z} < 80 GeV$, (e) $80 < p_{\mathrm{T},Z} < 110 GeV$ and (f) $110 < p_{\mathrm{T},Z} < 250 GeV$

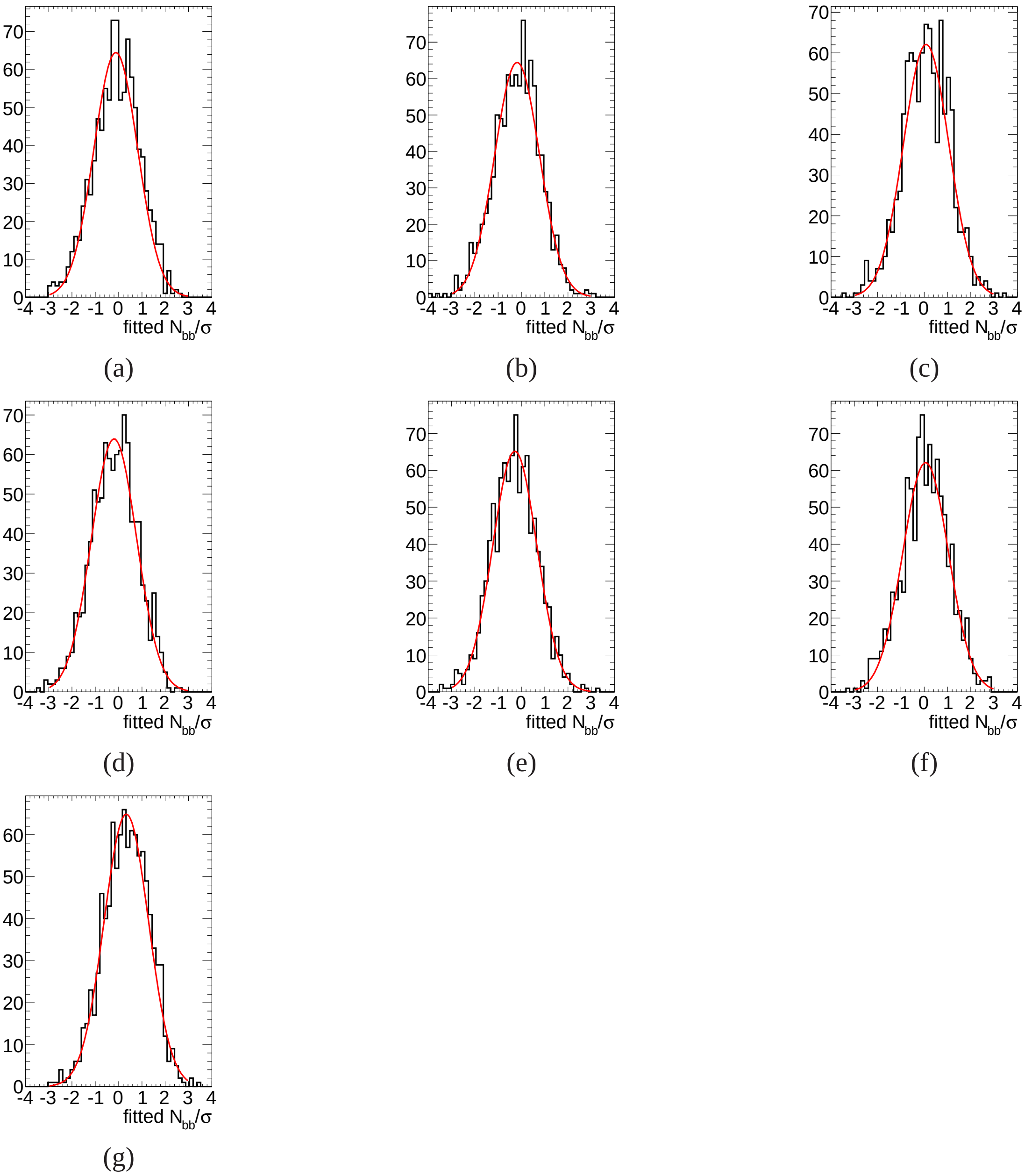

Figure 127: Pull tests for the differential $Z + bb$ fits. In all fitted bins of $Z|y|$, (a) $0 < Z|y| < 0.2$, (b) $0.2 < Z|y| < 0.4$, (c) $0.4 < Z|y| < 0.6$, (d) $0.6 < Z|y| < 0.8$, (e) $0.8 < Z|y| < 1.2$, (f) $1.2 < Z|y| < 1.6$ and (g) $1.6 < Z|y| < 2.5$

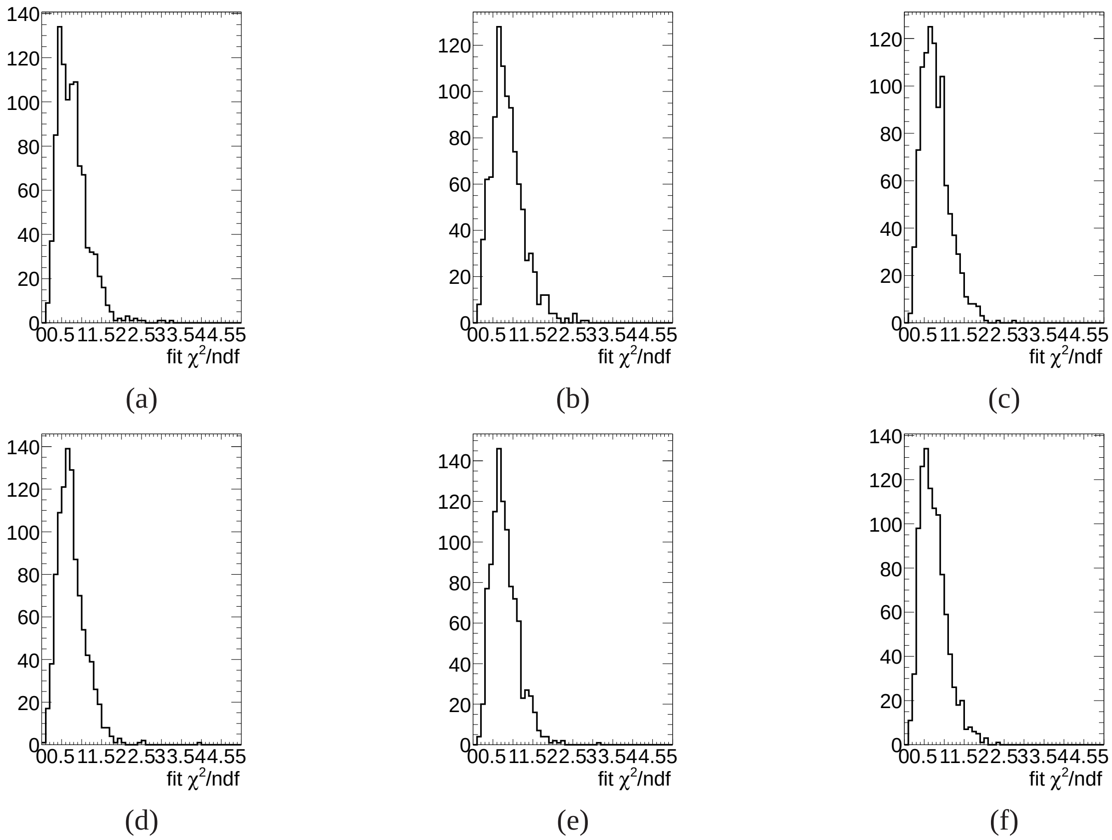

Figure 128: χ^2 tests for the differential $Z + bb$ fits. In all fitted bins of ΔR_{bb}, (a) $0.4 < \Delta R_{bb} < 1.15$, (b) $1.15 < \Delta R_{bb} < 1.9$, (c) $1.9 < \Delta R_{bb} < 2.4$, (d) $2.4 < \Delta R_{bb} < 2.8$, (e) $2.8 < \Delta R_{bb} < 3.2$ and (f) $3.2 < \Delta R_{bb} < 5$

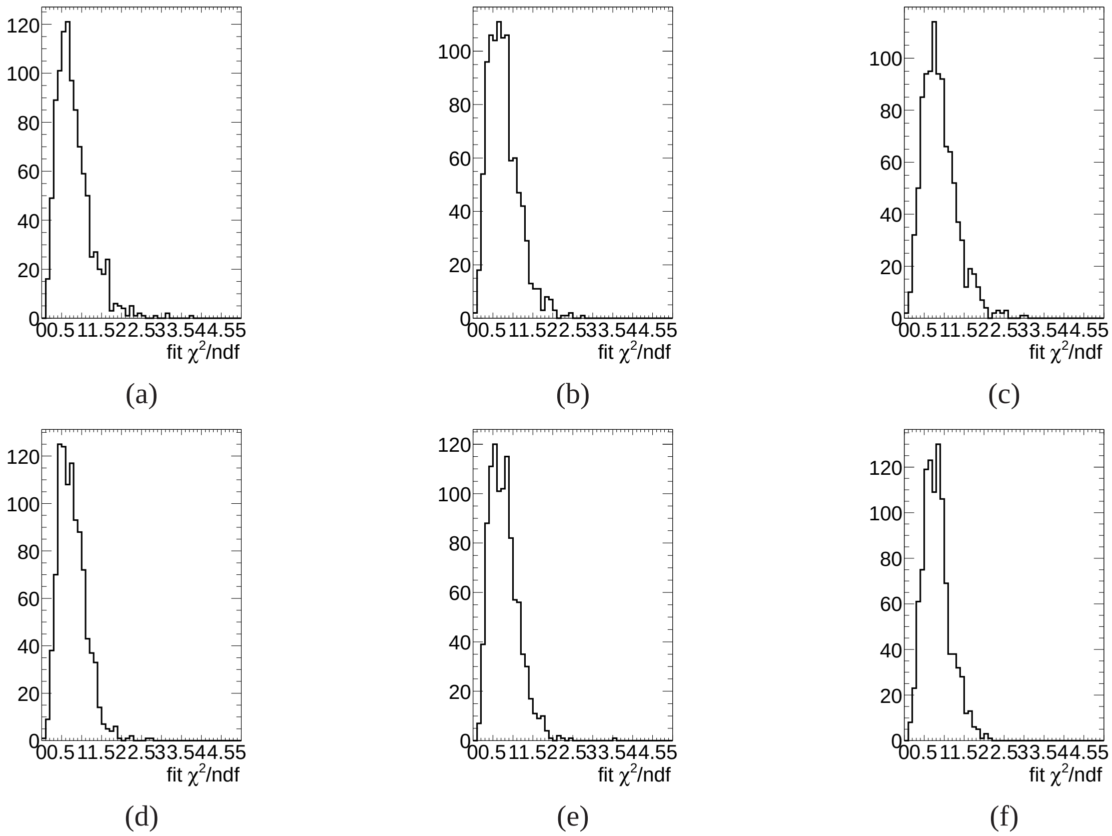

Figure 129: χ^2 tests for the differential $Z + bb$ fits. In all fitted bins of m_{bb}, (a) $10 < m_{bb} < 45 GeV$, (b) $45 < m_{bb} < 65 GeV$, (c) $65 < m_{bb} < 85 GeV$, (d) $85 < m_{bb} < 115 GeV$, (e) $115 < m_{bb} < 165 GeV$ and (f) $165 < m_{bb} < 350 GeV$

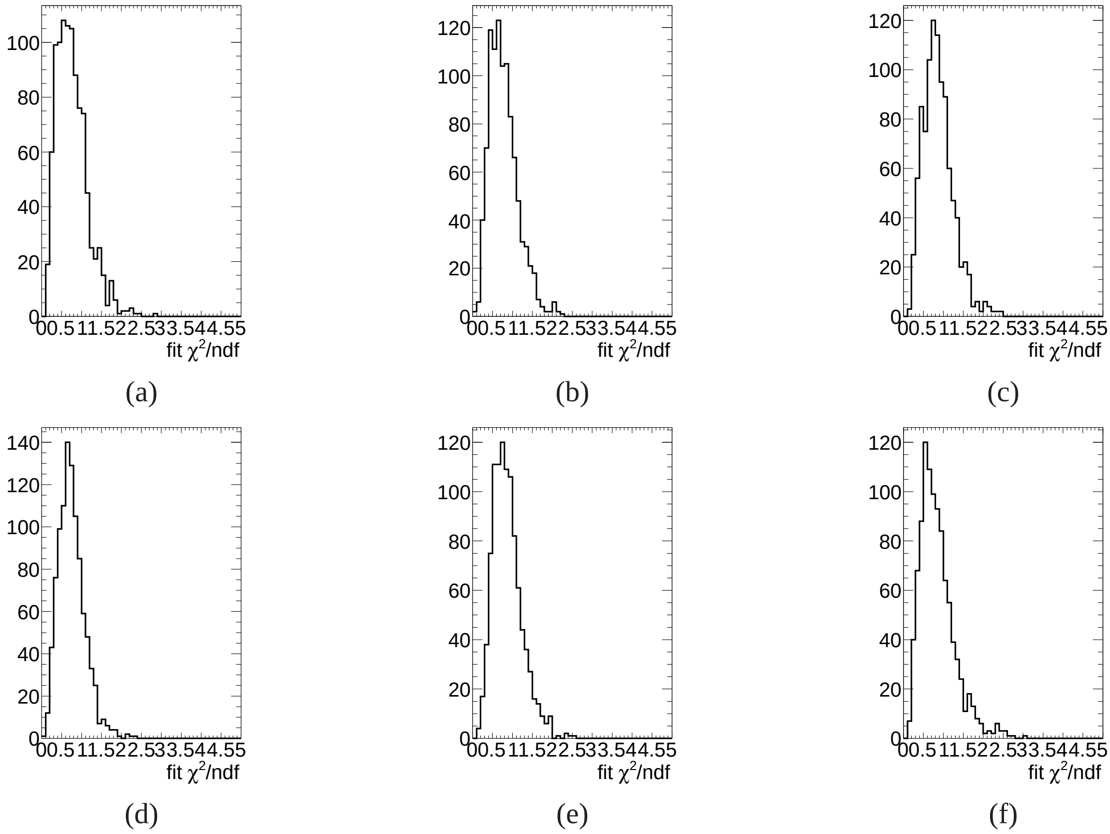

Figure 130: χ^2 tests for the differential $Z + bb$ fits. In all fitted bins of $p_{T,Z}$, (a) $p_{T,Z} < 20 GeV$, (b) $20 < p_{T,Z} < 40 GeV$, (c) $40 < p_{T,Z} < 60 GeV$, (d) $60 < p_{T,Z} < 80 GeV$, (e) $80 < p_{T,Z} < 110 GeV$ and (f) $110 < p_{T,Z} < 250 GeV$

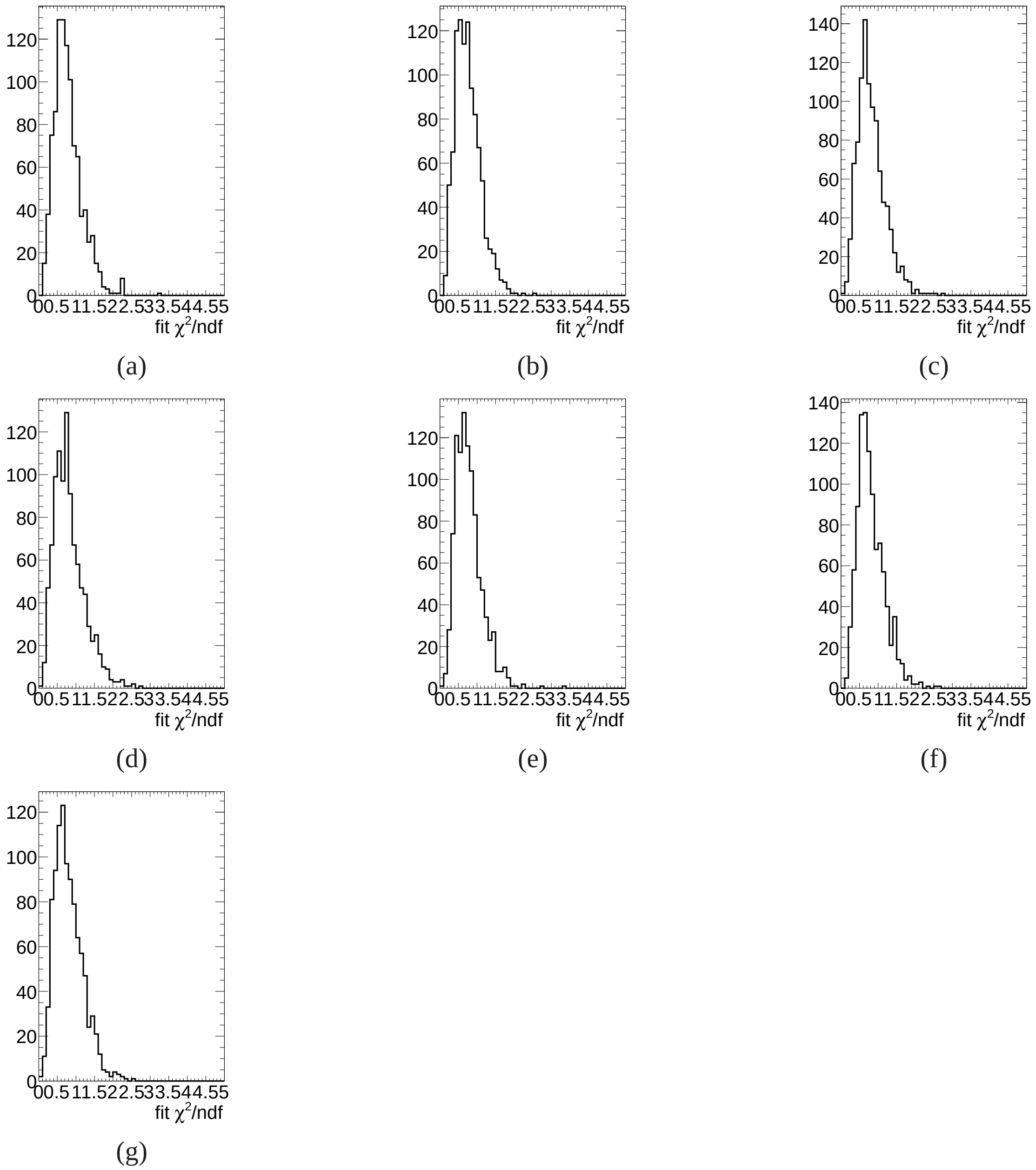

Figure 131: χ^2 tests for the differential $Z + bb$ fits. In all fitted bins of $Z|y|$, (a) $0 < Z|y| < 0.2$, (b) $0.2 < Z|y| < 0.4$, (c) $0.4 < Z|y| < 0.6$, (d) $0.6 < Z|y| < 0.8$, (e) $0.8 < Z|y| < 1.2$, (f) $1.2 < Z|y| < 1.6$ and (g) $1.6 < Z|y| < 2.5$

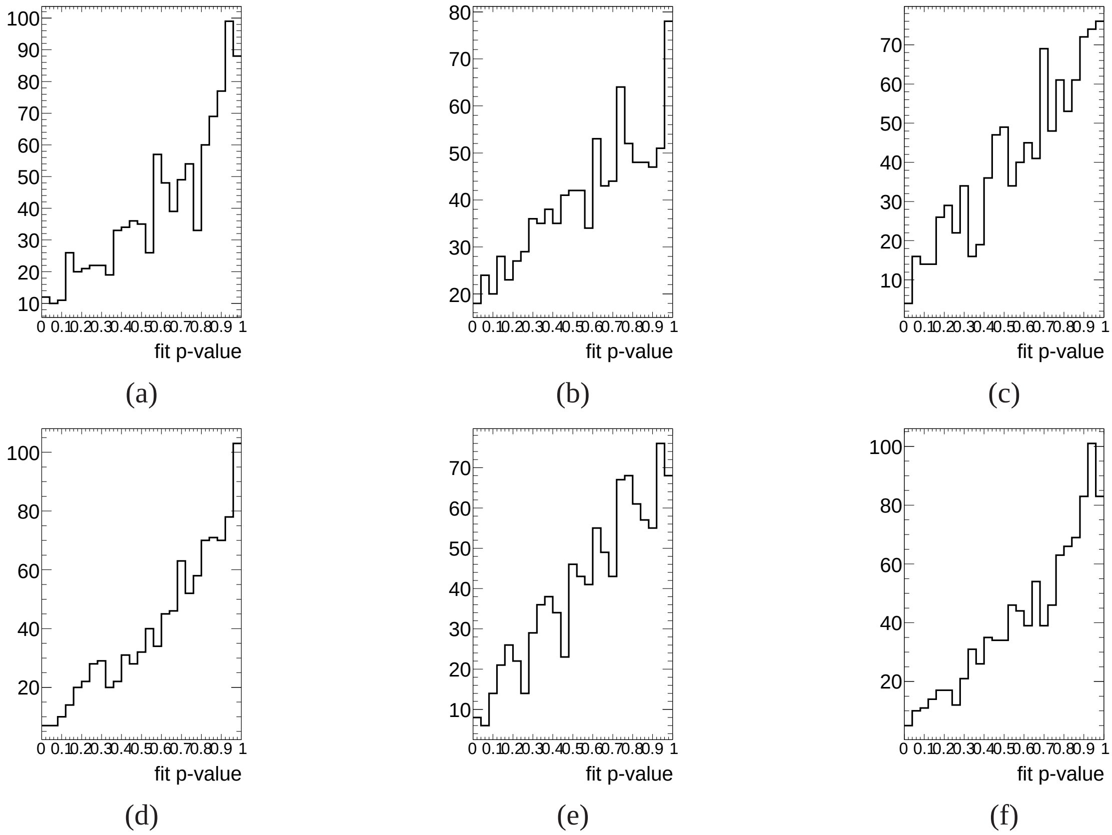

Figure 132: P-value tests for the differential $Z + bb$ fits. In all fitted bins of ΔR_{bb}, (a) $0.4 < \Delta R_{bb} < 1.15$, (b) $1.15 < \Delta R_{bb} < 1.9$, (c) $1.9 < \Delta R_{bb} < 2.4$, (d) $2.4 < \Delta R_{bb} < 2.8$, (e) $2.8 < \Delta R_{bb} < 3.2$ and (f) $3.2 < \Delta R_{bb} < 5$

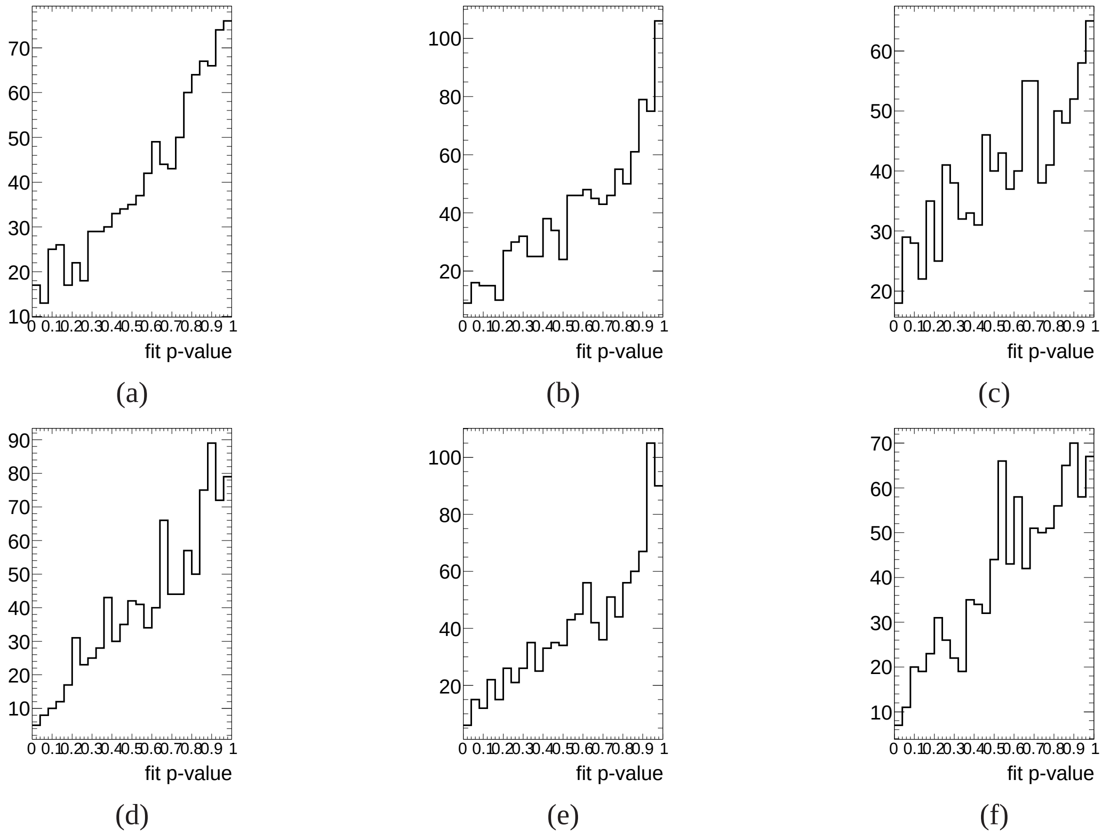

Figure 133: P-value tests for the differential $Z + bb$ fits. In all fitted bins of m_{bb}, (a) $10 < m_{bb} < 45GeV$, (b) $45 < m_{bb} < 65GeV$, (c) $65 < m_{bb} < 85GeV$, (d) $85 < m_{bb} < 115GeV$, (e) $115 < m_{bb} < 165GeV$ and (f) $165 < m_{bb} < 350GeV$

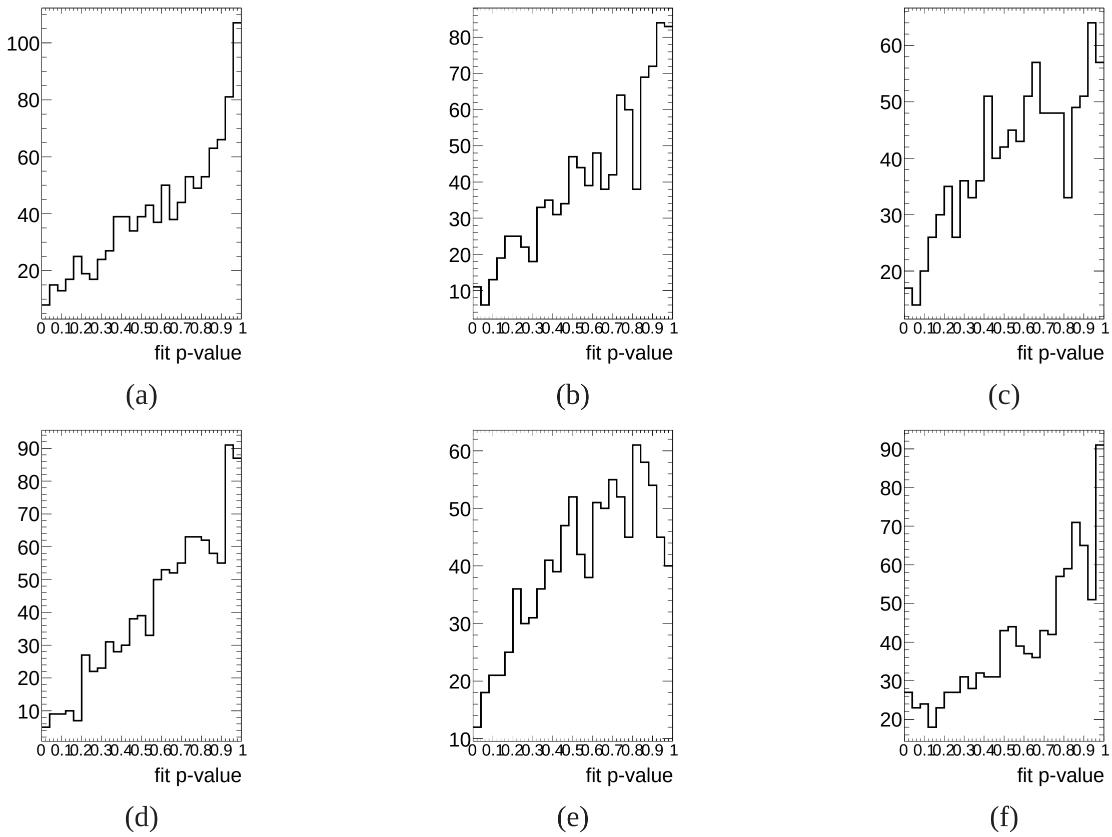

Figure 134: P-value tests for the differential $Z + bb$ fits. In all fitted bins of $p_{T,Z}$, (a) $p_{T,Z} < 20GeV$, (b) $20 < p_{T,Z} < 40GeV$, (c) $40 < p_{T,Z} < 60GeV$, (d) $60 < p_{T,Z} < 80GeV$, (e) $80 < p_{T,Z} < 110GeV$ and (f) $110 < p_{T,Z} < 250GeV$

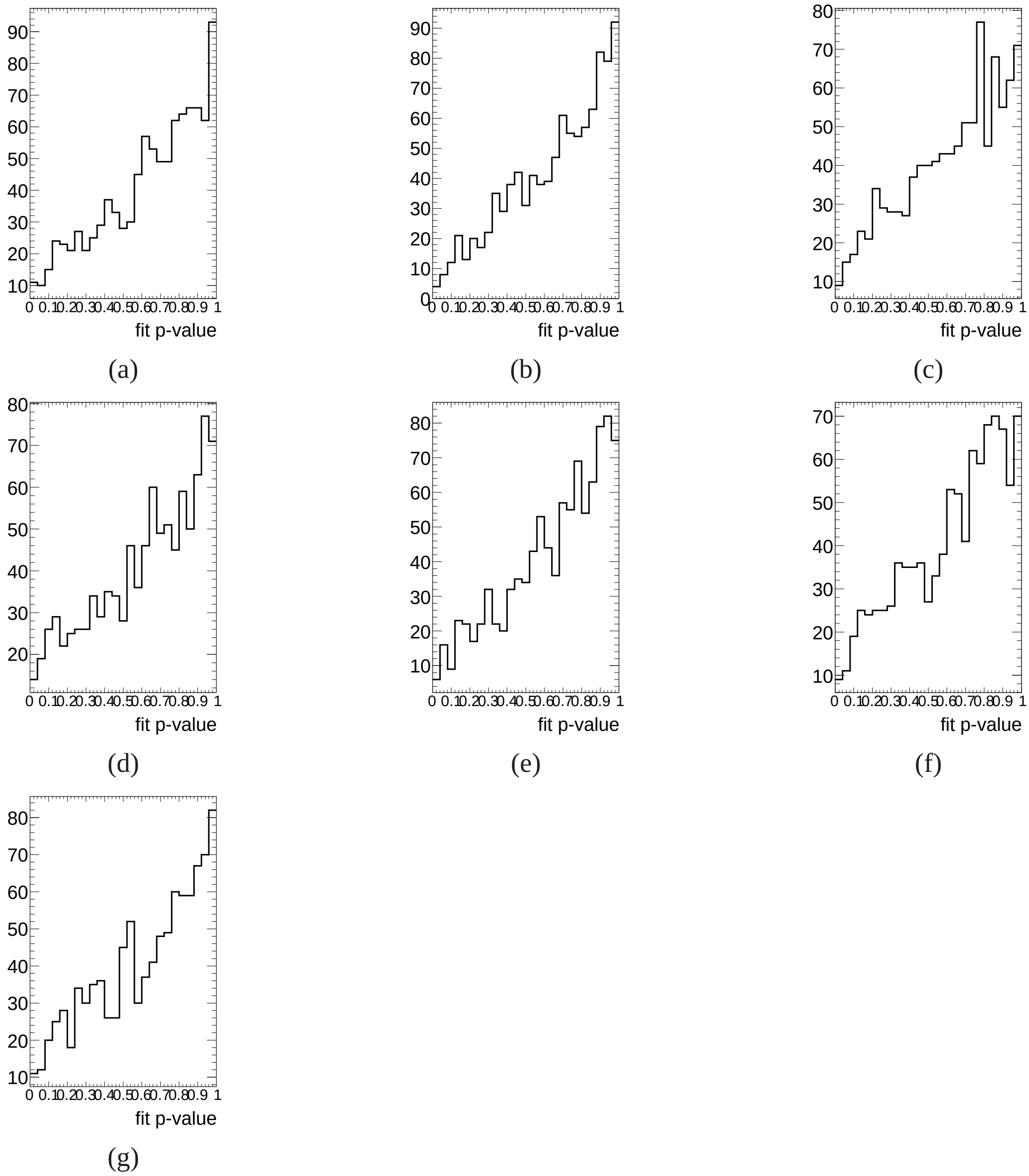

Figure 135: P-value tests for the differential $Z + bb$ fits. In all fitted bins of $Z|y|$, (a) $0 < Z|y| < 0.2$, (b) $0.2 < Z|y| < 0.4$, (c) $0.4 < Z|y| < 0.6$, (d) $0.6 < Z|y| < 0.8$, (e) $0.8 < Z|y| < 1.2$, (f) $1.2 < Z|y| < 1.6$ and (g) $1.6 < Z|y| < 2.5$